

Flexion in gravitation and cosmology

A Thesis

Submitted to the Faculty

of

Drexel University

by

Evan J. Arena

in partial fulfillment of the

requirements for the degree

of

Doctor of Philosophy

June 2024



© Copyright 2024
Evan J. Arena.

This work is licensed under the terms of the Creative Commons Attribution-ShareAlike license Version 3.0. The license is available at
<http://creativecommons.org/licenses/by-sa/3.0/>.

Dedications

*“... and teach me how
To name the bigger light, and how the less,
That burn by day and night:
and then I loved thee”*

William Shakespeare, the Tempest

For my mother, my light.

Acknowledgments

To my friends and family, who have all sacrificed in some way for me to be here – thank you. To my mother, Terre, my father, James, and my grandmother, Carole, for their unconditional love; to my Aunt Donna and Uncle Mike for giving me the opportunity to go to college; to my brother, Mike; and to Lauren, for your never-ending support throughout the most challenging parts of my Ph.D. and my future career search. I love you all.

I'd like to thank all of the people who helped me get to graduate school. To my Stony Brook friends: Anthony Bader, Aaron Seymour, Naveed An-Noor, Dr. Samantha Scibelli, and Andrew Klampert. I would never have had the confidence to pursue a Ph.D. without each and every one of you encouraging me throughout my undergraduate experience. To my formal and informal undergraduate advisors at Stony Brook and Brookhaven: Dr. Paul Stankus, Dr. Neelima Sehgal, Dr. Aňze Slosar, Dr. Erin Sheldon and Dr. Brant Johnson – thank you.

I am eternally grateful to my fellow graduate students at Drexel: Dr. Sean Lewis, Dr. Brian Andrews, Dr. Weixiang Yu, and Dr. Rebecca Phillipson. To those in my research group, thank you: to Dr. Joseph Fabritius II for serving as a mentor, to Jacob Shpiece for learning about flexion with me from the ground floor and always being supportive and constructive, and to Jeimin Garibnavajwala for continuing my work.

I would also like to thank Anthony and Sean for imparting to me nearly all of my knowledge about computer science and super-computer science, respectively. This work would have been impossible without their generosity of time and teaching – and their patience with my learning.

I'd like to thank the Dark Energy Survey for making this work possible. In particular, thank you to Dr. Judit Prat, Dr. Robert Gruendl, Dr. Erin Sheldon, Dr. Tom Diehl, and Dr. Gary Bernstein.

Thank you to Dr. Gordon Richards, Dr. Michelle Dolinski, and Dr. Steve McMillan for agreeing to serve on my thesis committee. Throughout my Ph.D., you have kept me on course and greatly improved my work. Michelle – thank you for providing me with endless advice during my years-long

job search, and Gordon – thank you for including me in the monthly telescope open houses which I will miss. I'd also like to thank Lisa Ferrara for her support throughout the years, for her help during my job search, and for all the advice I'm sure I'll seek as I begin my new job at Bryn Mawr College in my role as lab coordinator.

To my co-advisor Dr. David Bacon – I am immensely grateful for all you have done for me. Your warm encouragement throughout my Ph.D. was always appreciated, and often needed. Thank you for spending your valuable time as my co-advisor all the way from the UK, for giving me the opportunity to visit Portsmouth, and for a wonderful tour of your institute and city. My Ph.D. would not have been possible without you: from the theory you helped me build, to getting me in the Dark Energy Survey, to giving me time on the SCIAMA Supercomputer – you went above and beyond.

As I am set to embark on my next journey, as a lecturer at Bryn Mawr College, I often reflect on the fact that – in so many ways – I would not have become the teacher I am today without Dr. Rachael Kratzer. From the first day we met and on through my five years as Rachael's teaching assistant, Rachael saw in me a deep love of teaching and gave me every opportunity not only to teach, but to continually improve. Rachael always emphasized to me the importance of caring deeply about teaching, about giving everything to our students, and being able to communicate complicated concepts clearly and simply. Rachael taught me not only how to teach, but also how to do evidence-based teaching. Rachael – I am a better educator, communicator of science, and more empathetic teacher and person because of you.

Finally, I'd like to acknowledge the best advisor I could have possibly asked for. When I came to Dave with the idea for my thesis, he heard it with an open mind and allowed for me to pursue it. He always struck the right balance between letting me figure things out, adding his own insights – without which this work would have been impossible – all while keeping me on track. Dave – I admire – and always try to emulate – the way in which you are able to break down the most complicated of problems into the simplest of parts in research and teaching, and the good humor with which you do it. I look forward to continuing to work with, and learn from, you in the future.

This work was partially funded by the National Science Foundation Grant AST-2306989.

Table of Contents

LIST OF TABLES	xi
LIST OF FIGURES	xii
ABSTRACT	xix
1. COSMOLOGY AND GRAVITATIONAL LENSING	2
1.1 The Λ CDM universe	3
1.1.1 General Relativity	3
1.1.2 The cosmological principle	5
1.1.3 The ingredients of the Universe and the Big Bang	7
1.1.4 Distances and redshift	13
1.1.5 Structure formation	16
1.2 Weak Gravitational Lensing	31
1.2.1 The deflection of light	33
1.2.2 The lens equation	38
1.2.3 Lensing potential and convergence	39
1.2.4 Weak lensing: convergence and shear	41
1.2.5 Higher-order weak lensing: flexion	43
1.2.6 Complex representation: introducing the weak lensing flexion fields	44
1.2.7 Mass-sheet degeneracy, reduced shear and flexion	50
1.2.8 Measuring weak lensing fields	51
1.2.9 Lens models, galaxy-galaxy lensing, and galaxy-cluster lensing	53
1.2.10 Sensitivity of flexion to small scales and substructure	57
1.2.11 Fourier space representation and mass reconstruction	58
1.3 Cosmological Weak Lensing	60
1.3.1 The cosmological effective convergence	60

1.3.2	Cosmic shear	66
1.3.3	Cosmic flexion	68
2.	MEASURING LENSING: LENSER	71
2.1	Measuring weak gravitational lensing	71
2.2	Flexion Measurement	72
2.2.1	Analytic Image Modeling (AIM)	73
2.2.2	Image moment analysis	74
2.3	Lenser pipeline	79
2.3.1	Installing Lenser	79
2.3.2	Overview of Lenser structure: modules and classes	79
2.3.3	Step 1: Inputting a galaxy image – the FITS class	80
2.3.4	Step 2: Preparing the input galaxy for analysis	81
2.3.5	Step 3: Initial guess from image moments	82
2.3.6	Step 4: Minimizing the parameter space with analytic image modeling	82
2.4	Example: Running Lenser	85
2.5	Testing the Lenser framework	90
2.5.1	Testing Lenser with Lenser – Single galaxy	90
2.5.2	Testing Lenser with a simulated catalogue	92
2.5.3	Covariance testing	95
2.5.4	Comparing Lenser parameter reconstruction across two different telescopes	99
2.6	Multi-band, multi-epoch fitting	102
2.6.1	Lenser multi-fit pipeline	103
2.6.2	Testing the Lenser multi-fit framework	107
2.6.3	Conclusions: why use multi-band, multi-epoch fitting?	120
3.	COSMIC FLEXION IN THEORY	123
3.1	Introduction	123
3.2	The Theory of Cosmic Flexion	124

3.2.1	Cosmic Lensing Power Spectra	124
3.2.2	Two-Point Correlation Functions: Cosmic Shear and Flexion	126
3.2.3	Relating the Correlation Functions to Power Spectra	130
3.2.4	Consequences of Mixed Spin Field Cross-Correlation	131
3.3	Measuring Cosmic Flexion	135
3.3.1	Practical Estimators for Cosmic Flexion	135
3.3.2	Cosmic Flexion Covariance	138
3.3.3	Testing Cosmic Flexion with a Gaussian Random Field	145
3.4	Stage III Forecast	148
3.4.1	Handling Infinities: Renormalization of Cosmic Flexion	149
3.4.2	Forecasts for the Dark Energy Survey	153
3.4.3	Discussion	156
4.	FLEXION IN THE DARK ENERGY SURVEY	157
4.1	DES	157
4.1.1	DES Y3 dataset	158
4.1.2	DES Y3 results: Shape catalogue, galaxy clustering and weak lensing	158
4.2	DES Y3 Flexion Catalogue	159
4.2.1	Lens _{er} Catalogue	159
4.2.2	Object Selection: Flexion Catalogue	160
4.2.3	Systematics in the DES Y3 Flexion Catalogue	163
4.3	DES Y3: Cosmic Flexion	172
4.3.1	F-SHARP: Measuring cosmic flexion 2PCFs	173
4.3.2	The cosmic flexion 2PSFs	175
4.3.3	The cosmic flexion 2PCFs	180
4.3.4	Results: Cosmic flexion 2PCF measurements	182
4.3.5	Discussion	188
5.	FLEXION IN VARIOUS SPACETIMES	190

5.1	Introduction	190
5.2	Single-lens metrics	191
5.2.1	The Schwarzschild metric	191
5.2.2	Exotic spacetime metric	192
5.3	Flexion in exotic spacetime metrics	193
5.3.1	Weak lensing in exotic spacetimes	193
5.3.2	Discussion of shear and flexion behavior	196
5.4	Cosmic flexion in modified gravity	201
5.4.1	Case 1: Scale-independent post-GR functions	204
5.4.2	Case 2: Scale-dependent post-GR functions	206
5.5	Conclusions	208
6.	FUTURE PROSPECTS	209
6.1	Future work: Stage III	209
6.1.1	Systematics	209
6.1.2	Computation of 2PCFs	210
6.1.3	Theoretical work	211
6.1.4	Other signals to measure	212
6.1.5	Other datasets and surveys	212
6.1.6	Constraints on cosmology	212
6.2	Flexion in Stage IV cosmology	213
6.2.1	New physics	213
6.2.2	Higher-order flexion signals	214
	BIBLIOGRAPHY	215
	APPENDIX A: DERIVING THE MODIFIED SÉRSIC PROFILE	227
	APPENDIX B: THE QUADRUPOLE-SÉRSIC RELATION	228
	APPENDIX C: DERIVING THE THEORETICAL 2PCFs	231
C.1	Shear-Shear	231

C.2	Flexion-Flexion	233
C.3	Shear-Flexion	235
APPENDIX D: PSF LEAKAGE INTO THE 2PCFs		237
VITA		240

List of Tables

1.1	2018 TT, TE, EE + lowE + lensing constraints for cosmological parameters appearing explicitly in the Friedmann equation. Note that I only present an approximation of Ω_r , which is not directly given in the Planck 2018 results but is inferred from other parameter constraints.	13
1.2	2018 TT, TE, EE + lowE + lensing constraints for cosmological parameters relating to the linear matter power spectrum.	25
2.1	Real galaxy and lensing parameters compared with Lenser-fit parameters for a simulated galaxy	91
4.1	Total number of galaxy pairs in each flexion-flexion angular separation bin, i.e. the length of each 2PSF, for the DES Y3 cosmic flexion analysis.	181
4.2	Total number of galaxy pairs in each shear-flexion angular separation bin – i.e. the length of each 2PSF for the DES Y3 cosmic flexion analysis.	181
4.3	Single parameter constraints on theoretical predictions from DES Y3 cosmic flexion measurements	188

List of Figures

1.1	Linear matter power spectrum, $\mathcal{P}_L(k, z)$ plotted for four different redshifts, given a Λ CDM cosmology described by Tables 1.1 and 1.2. The matter power spectrum is computed using the Einstein-Boltzmann code CLASS . Vertical dashed lines indicate $k_{\text{NL}}(z)$, as defined in Sec. 1.1.5. Figure adapted from Dodelson and Schmidt [1].	26
1.2	Cartoon illustration of the 2-halo and 1-halo contributions to the nonlinear matter power spectrum. Figure adapted from Dodelson and Schmidt [1].	29
1.3	<i>Top panel:</i> Nonlinear matter power spectrum for $z = 0$, labelled P^{HM} , computed using the halofit halo model inside the Einstein-Boltzmann code CLASS . Also plotted are the 2-halo and 1-halo power spectra, along with the linear matter power spectrum for comparison. <i>Bottom panel:</i> Ratio of the halo model power spectrum to a power spectrum measured in N-body simulations using the CosmicEmu code [2]. All power spectra assume a Λ CDM cosmology. Figure adapted from Dodelson and Schmidt [1].	30
1.4	Galaxy cluster SMACS J0723.3-7327 as imaged by the James Webb Space Telescope (JWST; see: https://webb.nasa.gov/). Both strong and weak gravitational lensing effects are evident in this image: arced, multiply imaged galaxies are a strong lensing effect, while the minor shape distortions of galaxies at large radial distances away from the cluster arise from weak lensing. Note that the cluster itself is located at the center of the image.	32
1.5	Geometry of the lens system described by the lens equation. Figure from Michael Sachs, Wikimedia Commons: https://en.wikipedia.org/wiki/Gravitational_lensing_formalism	38
1.6	Weak lensing convergence, shear, \mathcal{F} -flexion, and \mathcal{G} -flexion applied individually to an unlensed, circularly symmetric, Gaussian galaxy. Spin-values of the weak lensing fields increase from left to right: convergence is spin-0, \mathcal{F} -flexion is spin-1, shear is spin-2, and \mathcal{G} -flexion is spin-3. The magnitudes of these fields are unrealistically large for the weak lensing regime, and are exaggerated only for visualization purposes. These images were created using Lenser (see Chapter 2).	47
1.7	Weak lensing convergence, shear, \mathcal{F} -flexion, and \mathcal{G} -flexion applied consecutively to an unlensed, circularly symmetric, Gaussian galaxy. The resulting field is arc- or banana-shaped. The magnitudes of these fields are unrealistically large for the weak lensing regime, and are exaggerated only for visualization purposes. These images were created using Lenser (see Chapter 2).	48
1.8	Prominent arcing of a source object in the Abell 2744 cluster. The red arrow indicates the direction to the nearest cluster galaxy. Here, the arcing is clearly “pointing” in the same direction as the arrow, indicating that the flexion shear is tangentially aligned along, and flexion pointing towards, the massive lens. Image is a best-fit Sérsic model from Lenser of object at RA 00:14:27.284, dec -30:23:55.18 (see Chapter 2). Figure adapted from Fabritius II [3].	49

1.9 Shear (upper), \mathcal{F} -flexion (lower-left) and \mathcal{G} -flexion (lower-right) induced by a simulated galaxy cluster. The cluster's underlying convergence map is plotted underneath the other weak lensing fields. The spin-2 shear field is represented by lines, the spin-1 \mathcal{F} -flexion by arrows (vectors), and the spin-3 \mathcal{G} -flexion by tri-edge markers. Figure adapted from BGRT.	57
1.10 Propagation of two light rays converging on an observer on the left. The red line along the bottom is taken to be the “fiducial” light ray, which will be denoted with the superscript (0) , defined by $\theta^{(0)} = 0$. The first light ray is drawn by the red line at the top. While both of these light rays are deflected by a deflector located at χ' from the observer, only the first ray has drawn the path the light would take with and without the presence of the deflector (the bottom and top branches, respectively). In this figure, $x(\chi)$ points from the bottom fiducial ray to the unperturbed top, first ray and $dx(\chi)$ points from the unperturbed to the perturbed top first ray. The deflection angle associated with the top ray points in the same direction as $dx(\chi)$, in the opposite direction of the transverse gradient of the gravitational potential. The dashed lines indicate the apparent direction of the light rays, converging on the observer at an observed angle θ . The dotted lines show the unperturbed geodesics, defining the angle β under which the unperturbed transverse comoving separation x is seen. Figure adapted from Kilbinger [4].	61
1.11 Cartoon of cosmic shear: gravitational lensing of source galaxies by large-scale structure causes coherent, tangential alignment of galaxy ellipticities around large-scale structure matter overdensities. Figure adapted from Karouzos [5].	68
1.12 Cartoon of cosmic flexion: gravitational lensing of source galaxies by large-scale structure causes coherent, radial alignment of \mathcal{F} -flexion (represented here as vectors) around large-scale structure matter overdensities.	70
2.1 Schematic of the <code>Lenser</code> pipeline.	84
2.2 FITS files for a galaxy in the COSMOS catalogue (which we refer to as galaxy number 1664) in the F814W band. <i>Top left</i> : the postage stamp science image of the galaxy, referred to as the data map. <i>Top right</i> : the noise map (root-mean square noise level measured in HST for this postage stamp). <i>Bottom left</i> : The segmentation map for this postage stamp, generated using <code>Source Extractor</code> . The value 0 refers to background pixels, 1 refers to the galaxy pixels, and 2 refers to some other object, visible in the data map, which appears to be some other galaxy in the background. <i>Bottom right</i> : the PSF map for the HST in this field. For details on the PSF model, see Koekemoer [6].	86
2.3 Masks for a galaxy in the COSMOS catalogue (which we refer to as galaxy number 1664) in the F814W band. <i>Left</i> : the übersegmentation bitmask mask created by the <code>FITS()</code> class <i>Right</i> : the elliptical bitmask produced by the <code>Image().generateEllipticalMask()</code> function.	88
2.4 Image reconstruction for a galaxy in the COSMOS catalogue (which we refer to as galaxy number 1664) in the F814W band. <i>Left</i> : the masked image of the galaxy. The applied mask is the combination (see Eq. (2.28)) of both masks given in Fig. 2.3. <i>Middle</i> : the model image of the galaxy, produced using the bestfit model parameters given in the example bash output. <i>Right</i> : The residual between the galaxy and model images.	88
2.5 The left panel shows a simulated galaxy image with known parameters and randomly generated noise, the middle panel shows the best-fit model, and the right panel shows the residual difference between the simulated galaxy image and the best-fit model. The reduced χ^2 for this fit is $\simeq 1.02$	91

2.6 Reconstructed versus input image centroids, θ_0^1 and θ_0^2 with errorbars computed from the χ^2 minimization in Lenser . The units of the centroids are pixels. The red line is a unity line ($y = x$), not a fit to the data.	95
2.7 Reconstructed versus input image Sérsic index, n_s and characteristic radius, θ_s , with errorbars computed from the χ^2 minimization in Lenser . n_s is dimensionless and θ_s has units of pixels. The red line is a unity line ($y = x$), not a fit to the data.	96
2.8 Reconstructed versus input image axis ratio, q , and orientation angle, ϕ , θ_0^1 and θ_0^2 with errorbars computed from the χ^2 minimization in Lenser . q is dimensionless and ϕ has units of radians. The red line is a unity line ($y = x$), not a fit to the data. We note that, due to the shear/ellipticity degeneracy in the presence of nonzero input shear as we have here, the true input q and ϕ will not be reconstructed by Lenser . We estimate the “input” q and ϕ analytically by adding the true input intrinsic ellipticity and shear components together.	96
2.9 Reconstructed versus input flexion terms, ψ_{ijk} , with errorbars computed from the χ^2 minimization in Lenser . The units of ψ_{ijk} are pixels $^{-1}$. The red line is a unity line ($y = x$), not a fit to the data.	97
2.10 Reconstructed versus input image normalization, I_0 . I_0 is not a Lenser fit parameter, but is estimated during using the bestfit χ^2 values of the parameters and Eq. (2.31). The units of I_0 are arbitrary. The red line is a unity line ($y = x$), not a fit to the data.	98
2.11 Covariance matrix for a stamp collection of 1000 images, with a noise map that matches that of the COSMOS catalogue. Here, we show 1σ and 2σ confidence ellipses below the diagonal (darker and lighter shades, respectively), 1σ Gaussians along the diagonal, and the locations of (p_i, p_j) denoted by white plus signs. The galaxy in each postage stamp is chosen to be canonically elliptical ($n_s = 4$). The galaxy also has realistic, nonzero ellipticity, shear, and flexion values. The centroid is dithered within a single pixel and hence is randomized for each image. We note that, due to the shear/ellipticity degeneracy in the presence of nonzero input shear as we have here, q and ϕ will not be reconstructed by Lenser . Hence, the location of the white plus sign for these values is estimated analytically by adding the input intrinsic ellipticity and shear components together. The centroid and θ_s are in units of pixels, ϕ is in units of radians, n_s and q are dimensionless, and the ψ_{ijk} flexion terms have units of pixels $^{-1}$	100
2.12 Ellipticity, ϵ_i and dimensionless flexion, $a\mathcal{F}_i$ and $a\mathcal{G}_i$, 1- and 2-components for source galaxies in Abell 2744 imaged by JWST versus HST. In these plot legends, ρ is the Pearson correlation coefficient. The red line is a best-fit to $y = mx + b$, and the best-fit slope and y -intercept values are given in the legend of each plot.	101
2.13 Schematic of the single-fit (left) and multi-fit (right) Lenser pipelines.	104
2.14 Ellipticity, ϵ_i , measurements for the subsample of galaxies in the COSMOS catalogue. The twelve panels in the plot are the twelve different combinations of the four Lenser runs. In these plot legends, ρ is the Pearson correlation coefficient. The red line is a best-fit to $y = mx + b$, and the best-fit slope and y -intercept values are given in the legend of each plot.	109

2.15 \mathcal{F} -flexion, \mathcal{F}_i , measurements for the subsample of galaxies in the COSMOS catalogue. The twelve panels in the plot are the twelve different combinations of the four Lenser runs. In these plot legends, ρ is the Pearson correlation coefficient. The red line is a best-fit to $y = mx + b$, and the best-fit slope and y -intercept values are given in the legend of each plot. The units of \mathcal{F}_i are inverse pixels.	110
2.16 \mathcal{G} -flexion, \mathcal{G}_i , measurements for the subsample of galaxies in the COSMOS catalogue. The twelve panels in the plot are the twelve different combinations of the four Lenser runs. In these plot legends, ρ is the Pearson correlation coefficient. The red line is a best-fit to $y = mx + b$, and the best-fit slope and y -intercept values are given in the legend of each plot. The units of \mathcal{G}_i are inverse pixels.	111
2.17 Dimensionless \mathcal{F} -flexion, $a\mathcal{F}_i$, measurements for the subsample of galaxies in the COSMOS catalogue. The twelve panels in the plot are the twelve different combinations of the four Lenser runs. In these plot legends, ρ is the Pearson correlation coefficient. The red line is a best-fit to $y = mx + b$, and the best-fit slope and y -intercept values are given in the legend of each plot.	112
2.18 Dimensionless \mathcal{G} -flexion, $a\mathcal{G}_i$, measurements for the subsample of galaxies in the COSMOS catalogue. The twelve panels in the plot are the twelve different combinations of the four Lenser runs. In these plot legends, ρ is the Pearson correlation coefficient. The red line is a best-fit to $y = mx + b$, and the best-fit slope and y -intercept values are given in the legend of each plot.	113
2.19 Ellipticity, ϵ_i , measurements for the subsample of galaxies in the DES Y3 dataset. The twelve panels in the plot are the twelve different combinations of the four Lenser runs. In these plot legends, ρ is the Pearson correlation coefficient. The red line is a best fit to $y = mx + b$, and the best-fit slope and y -intercept values are given in the legend of each plot.	114
2.20 \mathcal{F} -flexion, \mathcal{F}_i , measurements for the subsample of galaxies in the DES Y3 dataset. The twelve panels in the plot are the twelve different combinations of the four Lenser runs. In these plot legends, ρ is the Pearson correlation coefficient. The red line is a best fit to $y = mx + b$, and the best-fit slope and y -intercept values are given in the legend of each plot. The units of \mathcal{F}_i are inverse pixels.	115
2.21 \mathcal{G} -flexion, \mathcal{G}_i , measurements for the subsample of galaxies in the DES Y3 dataset. The twelve panels in the plot are the twelve different combinations of the four Lenser runs. In these plot legends, ρ is the Pearson correlation coefficient. The red line is a best fit to $y = mx + b$, and the best-fit slope and y -intercept values are given in the legend of each plot. The units of \mathcal{G}_i are inverse pixels.	116
2.22 Dimensionless \mathcal{F} -flexion, $a\mathcal{F}_i$, measurements for the subsample of galaxies in the DES Y3 dataset. The twelve panels in the plot are the twelve different combinations of the four Lenser runs. In these plot legends, ρ is the Pearson correlation coefficient. The red line is a best fit to $y = mx + b$, and the best-fit slope and y -intercept values are given in the legend of each plot.	117
2.23 Dimensionless \mathcal{G} -flexion, $a\mathcal{G}_i$, measurements for the subsample of galaxies in the DES Y3 dataset. The twelve panels in the plot are the twelve different combinations of the four Lenser runs. In these plot legends, ρ is the Pearson correlation coefficient. The red line is a best fit to $y = mx + b$, and the best-fit slope and y -intercept values are given in the legend of each plot.	118

2.24 Plotted is the distribution of the magnitude of dimensionless flexion, $a \mathcal{F} $ for each of the four DES Y3 dataset subsample runs. In the legend are the per-component scatter in $a\mathcal{F}_i$ for each run.	120
2.25 A subsample of 772 galaxies from the DES Y3 dataset run through <code>Lenser</code> in single-band r , i and z as well as an (i, z) multi-band run. The scatter of flexion estimates (σ in the legend) about $y = x$ in the single-band r fit versus (i, z) multi-band fit is smaller than either individually. We also see that the Pearson correlation coefficient (ρ in the legend) is highest for (i, z) multi-band fit versus single-band r fit.	121
3.1 Sketch of the rotated two-point coordinate system for the case of the \mathcal{F} -flexion for two galaxies located at ϑ and $\vartheta + \theta$. The axes (without arrows) for the rotated flexion components: \mathcal{F}'_1 and \mathcal{F}'_2 are shown on the galaxy located at $\vartheta + \theta$. Note how \mathcal{F}'_1 is oriented along the separation vector θ	128
3.2 A galaxy pair (i, j) with separation θ and polar angle $\varphi_{ij} = 0$ perturbed by a nearby mass distribution (on the left). In this case, the overdensity is along the line of the separation vector such that we have pure tangential shear, γ'_1 and radial flexion, \mathcal{F}'_1 (we assume that there is no intrinsic ellipticity or flexion in this case). The shear is represented by the ellipses and the spin-1 \mathcal{F} -flexion by the vectors. As galaxy (i) is closer to the overdensity, we see how the magnitude of the shear and flexion is larger for galaxy (i) than (j) . This cartoon illustrates how, for a given galaxy pair, flexion and shear are coupled between the objects, and to each other.	130
3.3 Three different galaxy-galaxy flexion scenarios. In each scenario, the flexion has only a 1-component and points radially toward the overdensity shown by the convergence κ^i . From top to bottom, we refer to these as scenarios 1, 2, and 3. The separation vector $\vec{\theta}$ in scenarios 1 and 2 points from left to right, along the 1-axis, and from right to left in scenario 3. The polar angle φ (i.e. the angle between the 1-axis and the separation vector) is 0 radians for scenarios 1 and 2, and $-\pi$ radians for the scenario 3. Using Eq. (3.10), the flexion $\mathcal{F}'_1{}^j$ is $+ \mathcal{F}^j $ for scenarios 1 and 3, and $- \mathcal{F}^j $ for scenario 2.	133
3.4 Theoretical cosmic flexion-flexion correlation functions $\xi_{\pm}^{\mathcal{FF}}$, $\xi_{\pm}^{\mathcal{GG}}$, and $\xi_{\pm}^{\mathcal{F}\rightarrow\mathcal{G}}$ for a delta-function convergence Gaussian random field. The solid (blue) lines are the ‘+’ theoretical correlation functions, and the dash-dotted (red) lines are the ‘-’ correlations. We see that the measurements of the ‘+’ and ‘-’ correlation functions are consistent with the theoretical curves. We also see that the so-called “cross” (‘ \times ’) correlation functions, which vanish due to parity-symmetry, are consistent with zero. Angular separation, θ , has units of arcseconds, and the flexion-flexion correlation functions have units of [radians] $^{-2}$	146
3.5 Theoretical cosmic shear-flexion correlation functions $\xi_{\pm}^{\gamma\rightarrow\mathcal{F}}$, $\xi_{\pm}^{\mathcal{F}\rightarrow\gamma}$, and $\xi_{\pm}^{\mathcal{G}\rightarrow\gamma}$ for a delta-function convergence Gaussian random field. The solid (blue) lines are the ‘+’ theoretical correlation functions, and the dash-dotted (red) lines are the ‘-’ correlations. We also see that the so-called “cross” (‘ \times ’) correlation functions, which vanish due to parity-symmetry, are consistent with zero. From these plots, we see that $\xi_{\pm}^{\mathcal{F}\rightarrow\gamma} = -\xi_{\pm}^{\gamma\rightarrow\mathcal{F}}$, which verifies Eqs. (3.27) and (3.28). Angular separation, θ has units of arcseconds, and the shear-flexion correlation functions have units of [radians] $^{-1}$	147
3.6 The cosmic flexion power spectrum expected for the DES Y3 lensing sample using a Planck 18 cosmology. The shaded region is the response of the power spectrum to varying σ_8 over ten times the TT,TE,EE+lowE+lensing 68% interval. The small width of this region is a consequence of the (very) tight constraints of the current Planck estimates. This does not, however, include variations of modeling approaches to highly nonlinear substructure.	149

3.7 The cosmic convergence-flexion power spectrum expected for the DES Y3 using a Planck 18 cosmology. The shaded region is the response of the power spectrum to varying σ_8 over ten times the TT,TE,EE+lowE+lensing 68% interval.	150
3.8 In the top panel, we show the integrand of the flexion-flexion correlation function $\xi_{-}^{\mathcal{F}\mathcal{F}}$ as a function of ℓ for $\theta = 10$ arcseconds. We see that after the first peak, there is a rapid oscillation of the cosine envelope. This ringing makes numerical integration very computationally expensive. The vertical dashed line is located at the second local maximum, ℓ_s . In the middle panel, we show the renormalized integrand, given by Eq. (3.76). The bottom panel shows the results of integrating the non-renormalized integrand (solid, gray line) and the normalized integrand (tightly dashed, red line). Additionally, we show the result of integration via the double-exponential transform of Eq. (3.77) (loosely dashed, blue line).	151
3.9 The theoretical cosmic flexion \mathcal{F} - \mathcal{F} auto-correlation (top row) and \mathcal{F} - \mathcal{G} cross-correlation functions (bottom row) with forecast errors for DES Y3. Note that the data points are equal to the theoretical values and do not represent a measurement. Here, we anticipate a higher S/N for the \mathcal{F} - \mathcal{G} cross-correlation than the \mathcal{F} - \mathcal{F} auto-correlation. Note that $\xi_{\pm}^{\mathcal{F}\mathcal{G}}$ here represents the combined use of both $\xi_{\pm}^{\mathcal{F}\rightarrow\mathcal{G}}$ and $\xi_{\pm}^{\mathcal{G}\rightarrow\mathcal{F}}$	154
3.10 The theoretical cosmic shear-flexion γ - \mathcal{F} (top row) and \mathcal{G} - γ (bottom row) cross-correlation functions with forecast errors for DES Y3. Note that the data points are equal to the theoretical values and do not represent a measurement. Here, we anticipate a much higher S/N for shear-flexion than flexion-flexion. Note that $\xi_{\pm}^{\gamma\mathcal{F}}$ here represents the combined use of both $\xi_{\pm}^{\gamma\rightarrow\mathcal{F}}$ and $\xi_{\pm}^{\mathcal{F}\rightarrow\gamma}$ (and similarly for $\xi_{\pm}^{\mathcal{G}\gamma}$).	155
4.1 Histograms of measured flexion in the DES Y3 Flexion Catalogue.	162
4.2 <i>Left:</i> Histograms of the measured ellipticity in the DES Y3 Flexion Catalogue. <i>Right:</i> Comparison of the ellipticity measured in the DES Y3 Flexion Catalogue to ellipticity measurements from the DES Y3 Shape Catalogue.	163
4.3 \mathcal{F} -flexion of sources in the DES Y3 Flexion Catalogue across the DES Y3 survey footprint.	165
4.4 \mathcal{G} -flexion of sources in the DES Y3 Flexion Catalogue across the DES Y3 survey footprint.	166
4.5 Ellipticity of sources in the DES Y3 Flexion Catalogue across the DES Y3 survey footprint.	167
4.6 DES Y3 \mathcal{F} -flexion maps smoothed with a 1° Gaussian filter.	168
4.7 DES Y3 \mathcal{G} -flexion maps smoothed with a 1° Gaussian filter.	169
4.8 DES Y3 ellipticity maps smoothed with a 1° Gaussian filter.	170
4.9 Histogram plots of the EE-mode flexion-flexion 2PSFs in five logarithmically spaced angular separation bins centered around the interval 1 to 100 arcseconds. The units on the x -axis are radians $^{-2}$	175
4.10 Histogram plots of the EB-mode flexion-flexion 2PSFs in five logarithmically spaced angular separation bins centered around the interval 1 to 100 arcseconds. The units on the x -axis are radians $^{-2}$	176

4.11 Histogram plots of the EE-mode shear-flexion 2PSFs in eight logarithmically spaced angular separation bins centered around the interval 1 arcsecond to 10 arcminutes. The units on the x -axis are radians $^{-1}$	177
4.12 Histogram plots of the EB-mode shear-flexion 2PSFs in eight logarithmically spaced angular separation bins centered around the interval 1 arcsecond to 10 arcminutes. The units on the x -axis are radians $^{-1}$	178
4.13 Measured DES Y3 flexion-flexion 2PCFs scaled by θ , such that the y -axis has units of radians $^{-1}$. The green line indicates the theoretical predictions from the fiducial cosmology, as described in AGB.	183
4.14 Measured DES Y3 EB-mode flexion-flexion 2PCFs scaled by θ , such that the y -axis has units of radians $^{-1}$	183
4.15 Measured DES Y3 shear-flexion 2PCFs scaled by θ , such that the y -axis is dimensionless. The green line indicates the theoretical predictions from the fiducial cosmology, as described in AGB.	184
4.16 Measured DES Y3 EB-mode shear-flexion 2PCFs scaled by θ , such that the y -axis is dimensionless.	184
5.1 Here we plot the amplitudes as a function of n for convergence, shear, \mathcal{F} -flexion, and \mathcal{G} -flexion for the cases $\varepsilon > 0$ (top) and $\varepsilon < 0$ (bottom). The signs of each amplitude for shear and flexion indicate alignment around a lens (for $\phi = 0$), whereas the sign on the amplitude for convergence indicates positive or negative convergence. Here we see how the \mathcal{F} -flexion is coupled to the convergence and the \mathcal{G} -flexion to the shear for $n > 1$. Specifically, we note that the \mathcal{F} -flexion behaves opposite to that of the shear in the presence of an $n > 1$ lens.	198
5.2 The behavior of shear and \mathcal{F} -flexion for two source (background) galaxies on opposite sides ($\phi = 0$ and $\phi = \pi$ radians) of three different lenses. <i>Top</i> : a typical scenario of lensing by a nonexotic mass defined by $\varepsilon > 0$ and $-1 < n < 1$ (we exclude the $n = 1$ Schwarzschild case where convergence and \mathcal{F} -flexion vanish). The shear has a tangential alignment around the lens and the \mathcal{F} -flexion points radially toward the lens (radial alignment). <i>Middle</i> : lensing by some exotic object ($\kappa < 0$) defined by $\varepsilon < 0$ and $-1 < n < 1$. Here, shear has tangential anti-alignment and \mathcal{F} -flexion points radially outward (radial anti-alignment). <i>Bottom</i> : lensing by some exotic object ($\kappa < 0$) defined by $\varepsilon > 0$ and $n > 1$. Here, shear has tangential alignment and \mathcal{F} -flexion points radially outward.	200

Abstract

Flexion in gravitation and cosmology

Evan J. Arena

David M. Goldberg, Ph.D. and David J. Bacon, Ph.D.

Cosmic flexion, like cosmic shear, is a weak gravitational lensing correlation function whose signal originates from the large-scale structure of the Universe. Building on the observational success of cosmic shear, along with the unprecedented quality of large-scale cosmological datasets, the time is ripe to explore the practical constraints from cosmic flexion. Unlike cosmic shear, which probes a broad region of the matter power spectrum, cosmic flexion is sensitive to small scales ($1 \text{ } h \text{ Mpc}^{-1} \lesssim k \lesssim 10^2 \text{ } h \text{ Mpc}^{-1}$) and therefore can uniquely place constraints on the small-scale matter power spectrum. I present a theoretical formalism I have developed for cosmic flexion, which includes novel flexion-flexion and shear-flexion two-point correlations. Using observations from the first three years (Y3) of Dark Energy Survey (DES) observations, I present the DES Y3 Flexion Catalogue built using the **Lenser** flexion measurement pipeline. With flexion measurements for $\sim 45\text{M}$ galaxies across the DES Y3 footprint, this is the largest such catalogue to date. I use this catalogue to measure cosmic flexion for the first time, where I detect a cosmic shear-flexion signal that is consistent with theoretical predictions to within $\sim 1\sigma$ and rejects the null hypothesis to $\sim 3\sigma$.

In addition to weak gravitational lensing flexion in general relativity and ΛCDM cosmology, I also examine the behavior of flexion due to exotic, single-lens metrics and the cosmological implications of flexion in a modified gravity context. I find that directional flexion can distinguish between the case of a positive or negative convergence where directional shear cannot, and therefore can provide a unique lensing signature for exotic objects with Ellis wormhole-type metrics, which act as gravitational lenses. I also find cosmic flexion to be a unique probe of parametric models of modified gravity, particularly in the case of scale-dependent phenomenological post-general relativity functions.

Preface

This thesis consists of six chapters. Chapter 1 serves as an introduction to cosmology and weak gravitational lensing. This introduction is heavily referenced by the other chapters throughout this thesis. Chapter 2 is an overview of a flexion measurement code I wrote called **Lenser**. The first part of this chapter is a summary of **Lenser** version 1, which was introduced in a second-author paper I wrote with Joseph M. Fabritius II and David M. Goldberg. The second part of this chapter focuses on **Lenser** version 2, to be published alongside the work presented in Chapter 4. Chapter 3 outlines the theory of cosmic flexion, as presented in a first-author paper I wrote with David M. Goldberg and David J. Bacon, hereafter AGB. In Chapter 4, I present the first measurements of cosmic flexion, using the Dark Energy Survey (DES) Year 3 (Y3) data. This chapter has two main parts: first, the DES Y3 Flexion Catalogue; second, measurements of the cosmic flexion signals. This work will be published with David M. Goldberg, David J. Bacon, and the DES Collaboration. Chapter 5 is based on a theoretical single-author paper I wrote that considers two topics: first, the flexion signal in exotic single-lens metrics; and second, cosmic flexion in modified gravity. In Chapter 6, I conclude with a summary discussion and comment on the prospects of using cosmic flexion as a probe in future cosmology surveys.

- Chapter 2: Fabritius, J. M., **Arena, E. J.**, and Goldberg, D. M. “*Shape, color, and distance in weak gravitational flexion,*” Mon.Not.Roy.Astron.Soc. **501**, 4103 (2021) [[arXiv:2006.03506](#)].
- Chapter 3: **Arena, E. J.**, Goldberg, D. M., and Bacon, D. J., “*Cosmic flexion,*” Phys.Rev.D **105**, 123521 (2022) [[arXiv:2203.12036](#)].
- Chapter 4: **Arena, E. J.**, Goldberg, D. M., Bacon, D. J., and the Dark Energy Survey Collaboration, “*Evidence for cosmic flexion in the Dark Energy Survey Year 3 data,*” in preparation.
- Chapter 5: **Arena, E. J.**, “*Weak gravitational flexion in various spacetimes: Exotic lenses and modified gravity,*” Phys.Rev.D **106**, 064019 (2022) [[arXiv:2207.07784](#)].

Chapter 1: Cosmology and gravitational lensing

"It is indifferent to me where I am to begin, for there I shall return again."

Parmenides, Frag. B 5, quoted by Proclus,

Commentary on the Parmenides, 708

Physics is the science of matter and energy. Among the many branches of physics are astronomy/astrophysics, which studies the physics of celestial bodies in our Universe such as planets, stars, black holes, and galaxies. Cosmology, on the other hand, concerns itself with the physics of the Universe itself. It attempts to understand and explain the nature of the very spacetime that astronomical objects are embedded in, how the matter and energy in the Universe affect the nature of spacetime and, in turn, how spacetime affects the matter and energy. Cosmology is able to describe what the Universe looks like today, what it looked like in the past, and what it will look like in the future.

A cosmological model is a predictive one, able to explain the time-evolution of the Universe from the Big Bang onward, including the expansion of spacetime and the growth of structure from tiny fluctuations in the primordial soup to the large-scale structure of the Universe we see today. The best cosmological model we currently have is one that is consistent with our numerous and varied cosmological observations. That model is the Λ CDM model, which says that the Universe can be described in terms of structure formation by cold dark matter (CDM), accelerated expansion by a nonzero cosmological constant (Λ) which we understand as dark energy, and is governed by Einstein's theory of General Relativity.

The main goal of this thesis is to lay the theoretical groundwork for a collection of novel probes of gravitation and cosmology, as well as offering the first measurements of some of them. This thesis

works, primarily, toward the goal of adding a few more items to the long list of observations we can take to stress-test the Λ CDM model of the universe and the theory of general relativity more broadly. This collection of probes is based upon a weak gravitational lensing signal known as *flexion*. To this end, this Chapter offers a brief overview of our current understanding of gravitation and cosmology, as well as an introduction to gravitational lensing.

1.1 The Λ CDM universe

1.1.1 General Relativity

Gravitation describes the formation of all major celestial bodies in our Universe and governs their dynamics. Gravitation describes not only the dynamics of objects within our Universe (the Earth orbiting around the Sun, for instance), but also the dynamics and evolution of the Universe *itself*.

The fundamental theory of gravitation in astrophysics and cosmology is General Relativity (GR) [7, 8]. In the Newtonian view, gravity is understood as a non-contact “force” that acts at a distance [9]. In GR, gravitation is interpreted as a property of spacetime (a four-dimensional quantity consisting of the three spatial dimensions we experience every day, plus a time component). In the language of GR, spacetime is a Riemannian manifold which is deformed by the presence of matter and energy. All particles travel on *geodesics* of this manifold. In the Newtonian view, particle trajectories are deflected from straight lines in the presence of the gravitational force acting on that particle due to a massive body. In GR, the gravitational deflection of particle trajectories is understood as an alteration of the geodesics with respect to empty space. The curvature of the Riemann manifold is described by the so-called Riemann tensor, $R^{\mu}_{\nu\lambda\rho}$, which depends on the *metric* and its various derivatives.

To understand the metric, it is useful to define it in terms of a line element, ds , or its invariant square, ds^2 , known as an *interval*. In GR, one can define a four-vector, x^μ , where Greek letters are indices running from 0 to 3, where 0 is the time component and $\{1, 2, 3\} = i \in \mu$ are the three spatial components, denoted by Latin letters. In general, two events in spacetime with coordinates

differing by dx^μ (one-form gradients of x^μ) are separated by ds , with

$$ds^2 = g_{\mu\nu} dx^\mu dx^\nu \quad (1.1)$$

where $g_{\mu\nu}$ is the metric tensor, and where summation over components is implied, such that $g_{\mu\nu} dx^\mu dx^\nu = \sum_{\mu,\nu=0}^3 g_{\mu\nu} dx^\mu dx^\nu$. The metric tensor also describes the relationship between raised and lowered indices in GR – namely, $x_\mu = g_{\mu\nu} x^\nu$.

The relationship between spacetime geometry and the matter embedded in it is described by the (covariant) Einstein field equations:

$$G_{\mu\nu} + \Lambda g_{\mu\nu} = \frac{8\pi G}{c^2} T_{\mu\nu}. \quad (1.2)$$

On the left-hand-side of the field equations, Λ is the cosmological constant, and the Einstein tensor is defined as

$$G_{\mu\nu} \equiv R_{\mu\nu} - \frac{1}{2} g_{\mu\nu} R, \quad (1.3)$$

where $R_{\mu\nu} \equiv R^\alpha_{\mu\alpha\nu}$ is the Ricci tensor (a contraction of the Riemann tensor)¹ and $R \equiv g^{\mu\nu} R_{\mu\nu} = R^\mu_\mu$ is the Ricci scalar. On the right-hand side of the field equations, G is Newton's gravitational constant, c is the speed of light, and $T_{\mu\nu}$ is the stress-energy tensor, describing the matter and energy-momentum content. In summary, $G_{\mu\nu}$ describes the curvature of spacetime, while $T_{\mu\nu}$ describes the energy content and flow in a region of space.

Solutions for the Einstein field equations are notoriously non-trivial to find, and only in a handful of special cases for the form of $T_{\mu\nu}$ and $g_{\mu\nu}$ is this possible. One can construct metrics that satisfy these equations for specific astronomical objects, such as a point mass given by the Schwarzschild metric [10]. In this case, one finds a local solution to the field equations. As we will see in the following subsections, though, one can also construct a metric for the entire Universe itself – this is the basis of the first building block of cosmology: general relativity applied to the whole Universe.

¹The Ricci tensor can be expressed in terms of the Christoffel symbols, $\Gamma^\alpha_{\mu\nu}$ and their derivatives, which in turn can be expressed in terms of the metric and its derivatives.

For a review of GR and cosmology, I refer the reader to Misner et al. [11] and Dodelson and Schmidt [1], respectively.

1.1.2 The cosmological principle

The cosmological principle states that: *on large scales, the Universe is homogeneous and isotropic.* By “large scales,” we mean on the order of 100 Mpc; by homogeneous, we mean that the Universe looks the same at all places, and isotropic means it looks the same in all directions. This is to say that there are no special locations or directions in the Universe.

Returning to Eq. (1.1), we can interpret the metric in the context of a homogenous and isotropic Universe. Here, we take the signature of the metric to be $(+, -, -, -)$ – this is known as the “mostly minus” signature.

The proper time of an observer who travels ds changes by ds/c . It is useful to define spatial coordinates that are constant for “fundamental” observers – these are known as *comoving coordinates*. In these coordinates, the mean motion is described by $dx^i = 0$, and hence, $ds^2 = g_{00}dt^2$. If we require that the proper time of the fundamental observers equals the cosmic time, then $g_{00} = c^2$. Isotropy requires that the space-time components of the metric vanish: $g_{0i} = 0$, as the off-diagonal terms of the metric would imply a preferred direction in space. Eq. (1.1) then becomes $ds^2 = c^2dt^2 + g_{ij}dx^i dx^j$, where g_{ij} is the metric of spatial hypersurfaces. Isotropy and homogeneity require that the spatial metric take the form of (the square of) a time-dependent scale factor, $a(t)$. To not violate isotropy, the spatial metric can only isotropically expand or contract. To not violate homogeneity, this scale factor is a function of time only (different expansions/contractions at different places violates homogeneity). The metric then becomes

$$ds^2 = c^2dt^2 - a^2(t)d\ell^2 \quad (1.4)$$

where $d\ell$ is the line element of the homogeneous and isotropic 3-space. The metric given by Eq. (1.4) is equivalent to the Minkowski metric, $\eta_{\mu\nu} = \text{diag}(+1, -1, -1, -1)$, in the case that $d\ell$ is Euclidean and $a(t)$ is constant. Typically, the normalization $a(t_0) = a_0 = 1$ is taken, where t_0 is the present

epoch, such that $0 \leq a(t) < 1$ for all times $t < t_0$.

The spatial hypersurfaces whose geometry is described by $d\ell$ can either be flat (Euclidean) or curved (non-Euclidean). Isotropy only requires them to be spherically symmetric – i.e. spatial surfaces a constant distance from an arbitrary point need to be 2-spheres. Homogeneity allows us to choose an arbitrary point as the origin of our coordinate system. We construct a coordinate system such that the polar angle, θ , and the azimuthal angle, ϕ , uniquely identify positions on the unit sphere around our chosen origin, and χ is chosen to be the *radial comoving coordinate*. We further define $f_K(\chi)$ to be the *comoving angular distance*, such that K is the curvature of the hypersurface:

$$f_K(\chi) = \begin{cases} K^{-1/2} \sin(K^{1/2}\chi) & \text{for } K > 0 \text{ (spherical)} \\ \chi & \text{for } K = 0 \text{ (flat)} \\ (-K)^{-1/2} \sinh[(-K)^{1/2}\chi] & \text{for } K < 0 \text{ (hyperbolic)} \end{cases} \quad (1.5)$$

In this coordinate system, we can therefore write

$$d\ell^2 = d\chi^2 + f_K^2(\chi)[d\theta^2 + \sin^2 \theta d\phi^2] \equiv d\chi^2 + f_K^2(\chi)d\Omega^2. \quad (1.6)$$

The metric given by Eq. (1.4), together with Eq. (1.6), is referred to as the Friedmann–Lemaître–Robertson–Walker (FLRW) metric, describing a homogeneous and isotropic Universe [12, 13, 14, 15].

Now that we have a metric for the homogeneous and isotropic Universe, the next step is to obtain the energy-momentum tensor, $T_{\mu\nu}$. Unsurprisingly, the cosmological principle dictates that the tensor describe a homogeneous and isotropic perfect fluid, which can be expressed as $T_{\mu\nu} = (\frac{p}{c^2} + \rho) U_\mu U_\nu - pg_{\mu\nu}$ in the *cosmic rest frame*, where $U^\mu = dx^\mu/d\tau$ is the 4-velocity of the fluid such that $d\tau = (-ds^2)^{-1/2}$, ρ is the density of the fluid, and p is the pressure of the fluid. As to not violate homogeneity or isotropy, ρ and p are functions of time (or scale factor) only. By lowering one index, this takes the simple form

$$T^\mu{}_\nu = \text{diag}(\rho c^2, -p, -p, -p). \quad (1.7)$$

Using the FLRW metric and the energy-momentum tensor given by Eq. (1.7), the Einstein field equations yield the *first and second Friedmann equations*:

$$\left(\frac{\dot{a}}{a}\right)^2 + \frac{Kc^2}{a^2} = \frac{8\pi G}{3}\rho + \frac{\Lambda}{3} \quad (1.8)$$

$$\frac{\ddot{a}}{a} = -\frac{4\pi G}{3}\left(\rho + \frac{3p}{c^2}\right) + \frac{\Lambda}{3}, \quad (1.9)$$

where the dot represents the time derivative. These equations describe the dynamics of the Universe as a function of time. Using the first Friedmann equation, the second Friedmann equation can be re-expressed as:

$$\dot{\rho} + 3\frac{\dot{a}}{a}\left(\rho + \frac{p}{c^2}\right) = 0 \quad (1.10)$$

which is known as the *fluid equation* or the *adiabatic equation*, where the latter name derives from the fact that this is a statement of the first law of thermodynamics as applied to cosmology.

1.1.3 The ingredients of the Universe and the Big Bang

The energy-momentum content of the Universe can be separated into three different *species*: matter, radiation, and dark energy. Each species (s) obeys the equation of state:

$$p_s = w_s c^2 \rho_s \quad (1.11)$$

such that each species has a unique equation-of-state parameter, w_s . The Friedmann equations can be solved for each species individually, and then the adiabatic equation yields the solution:

$$\rho_s(a) = \rho_{s,0} a^{-3(1+w_s)} \quad (1.12)$$

where $\rho_{s,0}$ is the energy density of the species at the present epoch, and $\rho_s(a)$ is its time evolution.

Matter: Baryonic and cold dark matter

In cosmology, we are interested in two types of non-relativistic² matter: baryonic matter and cold dark matter. Both baryonic and cold dark matter take the form of a pressureless ($w = 0$) “dust.”

In the language of particle physics, baryons are hadrons generally (composite particles composed of two or more quarks) and fermions specifically (composite particles composed of three quarks). The basic building blocks of the matter that makes up stars, planets, and you and me are the proton (a baryon), the neutron (also a baryon), and the electron (a lepton).³ Given their relative masses, the energy density of electrons is only a small perturbation to that of the proton and neutron.⁴ For this reason, in cosmology, we refer to the matter component of the Universe made of ions, atoms, and molecules as *baryonic matter*.

Both astrophysical and cosmological observations, in addition to theoretical considerations, indicate the existence of *dark matter* in our Universe, so called due to the fact that it does not emit electromagnetic radiation, only interacting gravitationally with ordinary matter and therefore falling outside of the standard model of particle physics (see Dodelson and Schmidt [1]). Evidence for the existence of dark matter was first put forth after observations of the Coma cluster showed that the velocity dispersion of member galaxies was too high to remain gravitationally bound without the presence of additional gravitation [16]. Subsequently, a number of observations of galactic rotation curves were found to violate Kepler’s Third Law if the only matter in the galaxies was the luminous matter of stars and gas [17, 18, 19, 20]. The apparent flattening of the rotation curve at large distances from the galaxy center is explainable if there is a large dark-matter component of the galaxy at those distances that obeys the expected rotational dynamics. Among the most compelling astrophysical evidence for the existence of dark matter is that of the “Bullet Cluster”

²Relativistic and non-relativistic refer to special relativity. Relativistic particles are those moving at speeds of $\gtrsim 0.85c$, at which their kinematics are described by special relativity. Examples of relativistic particles are: light, neutrinos, and any of the particles of the standard model that have a kinetic energy comparable to or exceeding their rest mass mc^2 .

³All of the particles in the standard model are essential to building a full picture of three of the four fundamental forces: the electromagnetic force, the weak force, and the strong force. However, it is the proton, neutron, and electron that are found in the elements of the periodic table and in a sense are the particles that make up all of the matter that we can see.

⁴On large scales, the Universe is electrically neutral. The proton has a charge of $+e$, where e is the elementary charge, and the neutron carries no charge. This implies that there is an equal number of protons and electrons (charge $-e$). However, the masses of the proton and neutron ($m_p c^2 = 938.27$ MeV and $m_n c^2 = 939.57$ MeV, respectively) are significantly larger than that of the electron ($m_e c^2 = 0.511$ MeV).

[21, 22]. This cluster, in the midst of a collision, has the bulk of its mass – observed indirectly via gravitational lensing measurements (see Sec. 1.2) – in a spatially distinct location from the luminous, hot, baryonic, X-ray emitting gas portion of the cluster.

The assumption of *cold*⁵ dark matter (CDM) is crucial to the Λ CDM model of the Universe. Baryonic matter alone is insufficient to form the large-scale structure of the Universe we see today. A CDM component is needed in the equations of structure formation, and – as it turns out – the majority of matter in the Universe is CDM.

Radiation: The CMB and CNB

Photons originating from the surface of “last scattering” are one of the main radiation components of the Universe.⁶ The surface of last scattering is dubbed the *Cosmic Microwave Background* due to the fact that the redshifted photons (see Sec. 1.1.4) that left it have microwave wavelength by the time they reach Earth today [23]. By analogy, there also exists a *Cosmic Neutrino Background* (CNB).⁷ While the neutrinos do have nonzero mass, it is very small compared to their kinetic energy, making them relativistic. As such, we treat these neutrinos as the other main radiation component of the Universe. The relativistic particles on both the CMB and CNB have an equation of state parameter of $w = 1/3$.

Dark energy

The physical mechanism of dark energy, responsible for the accelerated expansion of the Universe [24, 25], remains entirely a mystery. With current constraints, dark energy can be described by an equation of state parameter $w = -1$, such that it takes the form of a vacuum energy that is time independent (see Eq. 1.12) and the same for all fundamental observers [26]. This makes dark energy equivalent to a pure cosmological constant, Λ , in the Einstein field equations.⁸ Deviations

⁵*Cold* simply refers to the speed of the dark matter particles. Cold refers to slow moving or low kinetic energy particles at the present epoch – in other words, non-relativistic.

⁶After the Big Bang, the early hot, dense Universe was full of photons scattering within a plasma of protons and electrons. As the Universe expanded and cooled, the rapidly moving ions and electrons slowed to a speed where neutral Hydrogen atoms could be formed. The previously opaque Universe becomes transparent to the scattering photons upon this “recombination” period $\sim 380,000$ years after the Big Bang. This last-scattering surface behaves as a *blackbody* emitting photons.

⁷The Universe becomes transparent to neutrinos much earlier than the CMB, at roughly one second after the Big Bang.

⁸The cosmological constant is so called because it was introduced by Einstein in order to allow a static Universe (which he thought our Universe must be) to be a solution to the field equations, after Lemaître demonstrated that

from $w = -1$ are considered by various models of modified gravity, where dark energy is taken to be time and/or scale-dependent. This leads to modifications to the growth rate of large-scale structure, which can be measured by cosmological surveys using probes such as gravitational lensing (see Chapter 5).

The Friedmann equation revisited

It is useful to introduce the *Hubble parameter*:

$$H(a) \equiv \frac{\dot{a}}{a} \quad (1.13)$$

which describes the expansion history of the Universe. The *Hubble constant* $H_0 = H(t_0)$ is simply the Hubble parameter at the present epoch and is typically reported by $H_0 = 100h \text{ km s}^{-1} \text{ Mpc}^{-1}$, where h is one of many “cosmological parameters” constrained by various observations.⁹ For a fiducial cosmology, I will take the results from Planck 2018 [28], for which $h \simeq 0.67$ (see Table 1.1 for the Planck 2018 cosmology).

The total density ρ , summed over all species, can take a special value known as the *critical density*, ρ_{crit} . This is simply the density the Universe would have were it flat ($K = 0$). Its value at the present epoch is:

$$\rho_{\text{crit},0} = \frac{3H_0^2}{8\pi G} = 1.879 \times 10^{-26} h^2 \text{ kg m}^{-3} \quad (1.14)$$

Spherical and hyperbolic Universes have densities of $\rho > \rho_{\text{crit}}$ and $\rho < \rho_{\text{crit}}$, respectively. We introduce the *density parameter* for each species, defined as

$$\Omega_s \equiv \frac{\rho_{s,0}}{\rho_{\text{crit},0}} \quad (1.15)$$

where, unless written explicitly as $\Omega_s(a)$, density parameters are interpreted at the present epoch

the Einstein field equations (without a cosmological constant) implied an expanding Universe. Einstein would go on to discard Λ after Hubble’s discovery that the Universe really *is* expanding [27] (see the subsection below on Hot Big Bang and expansion history). With the discovery that this expansion is actually accelerating [24, 25] (see Sec. 1.1.3), Λ was reintroduced in order to describe this phenomenon.

⁹At the time I am writing this thesis, there is a tension in the values of cosmological parameters such as h from different cosmological and astrophysical probes.

such that $\Omega_s = \Omega_{s,0}$ implicitly.

Let us return our attention to the first Friedmann equation of Eq. (1.8). Recall that $\rho(a)$ is the density of the homogeneous and isotropic perfect fluid, defined in Eq. (1.7). This fluid is understood to be composed of the matter and radiation terms only, as the cosmological constant appears explicitly here, and explicitly in the Einstein field equations themselves. There is, of course, nothing preventing us from moving the cosmological constant term to the right-hand side of Eq. (1.2), such that the cosmological constant can be interpreted as another component of the cosmological fluid: $T_{(\Lambda)}^{\mu\nu} = -\frac{\Lambda}{8\pi G}\delta^{\mu\nu} = \text{diag}(-\rho_\Lambda, -\rho_\Lambda, -\rho_\Lambda, -\rho_\Lambda)$. where $\delta^{\mu\nu}$ is the Kronecker-delta tensor, and the dark energy component of the density is defined to be $\rho_\Lambda \equiv \Lambda/8\pi G$. Based on the form of this energy-momentum tensor, and comparing it to Eq. (1.7) it is clear that $p_\Lambda = -c^2\rho_\Lambda$, which defines ($w_\Lambda = -1$) as the equation of state parameter in Eq. (1.11). In this case, the first Friedmann equation can be written $(\frac{\dot{a}}{a})^2 = -\frac{Kc^2}{a^2} + \frac{8\pi G}{3}\sum_{s=m,r,\Lambda}\rho_s$. Using the Hubble parameter of Eq. (1.13), the density parameters of Eq. (1.15), the critical density given by Eq. (1.14), and the density evolution of Eq. (1.12) along with the equation of state parameters for matter ($w_m = 0$), radiation ($w_r = 1/3$) and dark energy ($w_\Lambda = -1$) one can write said first Friedmann equation as

$$\frac{H^2(a)}{H_0^2} = \frac{\Omega_r}{a^4} + \frac{\Omega_m}{a^3} + \frac{1 - \Omega_r - \Omega_m - \Omega_\Lambda}{a^2} + \Omega_\Lambda \quad (1.16)$$

where the curvature of the Universe is $K = (\frac{H_0}{c})^2(\Omega_r + \Omega_m + \Omega_\Lambda - 1)$. Interestingly, if one is to compare the three forms of the first Friedmann equation, one notices that there exists the relationship $\Omega_\Lambda = \Lambda/3H_0^2$.

Hot Big Bang and expansion history

In the 1920s, Edwin Hubble made the observation that apparent velocity of galaxies moving away from us was proportional to their redshift, z (see Sec. 1.1.4). This observation, known as Hubble's Law¹⁰, has the simple linear relationship (distance to galaxy) = cz/H_0 .¹¹ Hubble's original observations have been verified by various measurements, and today, we observe that all objects whose

¹⁰Hubble's Law is now sometimes called the Hubble-Lemaître Law, due to the role played by Lemaître on the theory front.

¹¹This distance is equivalent to any of the four distances defined in Sec. 1.1.4 in the limit of low redshift.

peculiar velocity is small relative to the Hubble flow are receding from us. This observation seems to imply, on its face, that we *are* in some special location in the Universe, violating the cosmological principle. How could it be that there are no special locations or directions in the Universe if we observe that all galaxies¹² are receding from us? As it turns out, *all fundamental observers observe Hubble's Law*. This implies that the Universe is expanding with time: $\dot{a}(t_0) > 0$.

If the right-hand side of Eq. (1.16) is not zero for some time earlier than the present epoch, then $\dot{a}(t) > 0$ for all $t < t_0$, implying that the Universe expanded from an initial singularity at $t = 0$. This moment at $t = 0$ is known as the *Big Bang*. The age of the Universe can be estimated by the Hubble time, H_0^{-1} , and solved for explicitly using the Friedmann equation. See Table 1.1 for the age of the Universe given current Planck 2018 constraints, the limits on the density parameters at the current epoch, as well as the Hubble constant.¹³

The expansion history of the Universe can be fully described by the Friedmann equation (Eq. 1.16)¹⁴, along with an additional framework known as *inflation*, which postulates that 10^{-35} seconds after the Big Bang the scale factor undergoes tens of *e-foldings* of expansion [29].¹⁵

¹²The only galaxy not receding from us is the Andromeda galaxy, the nearest neighbor to our galaxy – the Milky Way.

¹³With these parameters, one finds that the Λ CDM Universe has zero curvature ($K = 0$). This perfectly flat curvature is known as the “flatness problem” in cosmology, because it seems to imply a certain level of fine-tuning of the cosmological parameters.

¹⁴The Friedmann equation tells us which components of the Universe dominate the energy-density as a function of time – one need only look at the powers of $a(t)$ in Eq. (1.16). At very early times, the Universe was radiation dominated and expanded as $a \propto t^{1/2}$. Using the Stefan-Boltzmann law, $\rho \propto T^4$ and the fact that $\rho_r \propto a^{-4}$, we see that $T \propto a^{-1}$. This implies that the early Universe was very hot (the so-called *Hot Big Bang* model) and cooled as the Universe expanded. At roughly 50,000 years after the Big Bang, matter-radiation equality occurs, and matter becomes the dominant term in the Friedmann equation, slowing the expansion down to $a \propto t^{2/3}$. The Universe continues to cool, and eventually, photons decouple from the hot plasma, leaving behind an imprint of the early Universe at 380,000 years after the Big Bang – the CMB. The matter domination phase of the Universe lasts up until around 10 Gyr after the Big Bang. During the era of matter domination, the large-scale structures of the Universe form, creating the galaxies, stars, and planets we see today (see Sec. 1.1.5 for a detailed description of structure formation). After the matter-dominated phase comes the final stage of the Universe – the era of dark energy domination. In the 1990s, cosmologists discovered that the expansion of the Universe is *accelerating* – namely $\ddot{a}(t_0) > 0$ – explainable by dark energy, in the form of the cosmological constant. This dictates the ultimate fate of our Universe: it will be ever expanding and asymptotically de Sitter, with an expansion of $a \propto e^{\sqrt{\Lambda/3}t}$.

¹⁵Without inflation, the picture of expansion history leaves three problems unaddressed. The first is the so-called “flatness problem”. In addition to this, grand unified theories predict that, in the very early Universe, phase transitions create a very high density of magnetic monopoles. The fact that we observe none of these magnetic monopoles today, despite the fact that our theories of physics predict their existence, is known as the “monopole problem.” The third problem is known as the “horizon problem.” The temperature of the CMB is measured to be isotropic to within one part in 10^5 , in agreement with the cosmological principle. These tiny fluctuations actually turn out to be vitally important, though, and are in some sense imprints of the *seeds* that allow for the formation of large-scale structure. We observe, however, that regions of the CMB on opposite sides of the sky obey an isotropy that cannot be explained by our picture of the Universe so far, due to the fact that these regions had not been in causal contact with each other prior to recombination. All three of these problems are addressed by a framework known as *inflation* [29]. Inflation postulates that at a time of 10^{-35} seconds after the Big Bang, there was a very short period in which the Universe expanded exponentially, where the scale factor undergoes tens of *e-foldings* of expansion. The Universe inside the current horizon originated out of a very small, causally linked, pre-inflationary region, solving the “horizon problem.” The density of magnetic monopoles is reduced via inflation to a level that is consistent with the fact that we do

Table 1.1: 2018 TT, TE, EE + lowE + lensing constraints for cosmological parameters appearing explicitly in the Friedmann equation. Note that I only present an approximation of Ω_r , which is not directly given in the Planck 2018 results but is inferred from other parameter constraints.

Cosmological Parameter	Planck 2018 Measurement
h	0.6736 ± 0.0054
Age [Gyr]	13.797 ± 0.023
Ω_m	0.3153 ± 0.0073
$\Omega_{\text{cdm}}h^2$	0.1200 ± 0.0012
$\Omega_b h^2$	0.02237 ± 0.00015
$\Omega_r h^2$	$\simeq 4 \times 10^{-5}$
Ω_Λ	0.6847 ± 0.0073

1.1.4 Distances and redshift

Redshift

Photons are affected by the expansion of the Universe as they are propagating to us from some source. A photon emitted from a comoving source at some time t_e will have some wavelength λ_e . At some later time, t_0 , the wavelength of the same photon that reaches some comoving observer, λ_0 , will be different from λ_e in an expanding Universe. This is simply the *Doppler effect* where the source and observer are moving relative to each other as a consequence of the Universe expanding. Now, we know that photons travel on *null geodesics* ($ds = 0$). Along the spatial geodesic between the observer and source, the angle (θ, ϕ) is constant, and thus $d\ell = a(t)d\chi$. Hence, we can say that the FLRW metric becomes $0 = -c^2dt^2 + a(t)^2d\chi^2$, and hence $d\chi = (cdt)/a(t)$. Integrating over this,

$$c \int_{t_e}^{t_0} dt \frac{1}{a(t)} = \text{constant}, \quad (1.17)$$

where we have noted that the comoving distance between a source and observer is constant. Differentiating with respect to t_e , the time dilation can be expressed as $dt_0/dt_e = a(t_0)/a(t_e)$. Recognizing that dt_0/dt_e is equivalent to the ratio of the period of the light wave at t_0 to its period at t_e , we can

not observe them today, solving the “monopole problem.” Any initial curvature that the Universe may have had is flattened during inflation, solving the fine-tuning “flatness problem.”

also write this in terms of frequency, ν , and wavelength via $c = \nu\lambda$:

$$\frac{dt_0}{dt_e} = \frac{a(t_0)}{a(t_e)} = \frac{\nu_e}{\nu_0} = \frac{\lambda_0}{\lambda_e} \equiv 1 + z, \quad (1.18)$$

where z is defined as the cosmological *redshift*¹⁶. In an expanding Universe, $a(t)$ is increasing with time, which has the effect of redshifting the wavelength of light as it propagates.

Cosmological distances

In cosmology, the concept of “distance” is a nontrivial one. Back on Earth, we understand that two objects may be separated by some distance – say, one meter – that can be measured by extending a tape measure from the first object to the second. In cosmology, however, there are multiple interpretations of distance. First, we recall that spacetime may not be Euclidean, and a simple linear distance is not sufficient to describe the separation between objects. More complicated still, we know that the Universe can expand, which can be thought to either increase the distance between two objects (the so-called *proper distance*), or we can choose our coordinates so that the distance between the two objects is fixed and choose to have the markings on the tape measure itself increase in separation as the Universe expands (the so-called *comoving distance*). Additionally, there are two other useful distance measures: *angular-diameter distance* and *luminosity distance*.

We will define these four distance measures using the FLRW metric. We will consider the distances between two points: one at redshift z_e where a photon is emitted (the source), and the other at redshift z_0 where the photon is observed (the observer). Our coordinate system will be chosen such that the observer is at the origin, and distances are measured from the observer (from the origin) to the source.

The *proper distance* $D_{\text{prop}}(t)$ between two points is equal to the length of the spatial geodesic between them when the scale factor is fixed at the value $a(t)$. In other words, it is defined by the

¹⁶Here, z refers to z_e specifically, and $z_0 = 0$ is implied.

travel time of a photon between redshifts z_e and z_0 :

$$dD_{\text{prop}} = -cdt = -c \frac{da}{\dot{a}} = -c \frac{da}{aH(a)} \quad (1.19)$$

where this minus sign arises from the fact that cosmic time, t , increases as the photon is propagating from z_e to z_0 , but the distance is measured from z_0 to z_e , so that the observer is at the coordinate origin, and distances are measured from the origin. Upon integration from z_0 to z_e , we have $D_{\text{prop}}(z_0, z_e) = -c \int_{a(z_0)}^{a(z_e)} da/aH(a)$. Using the definition of the Friedmann equation given by Eq. (1.16), and flipping the bounds of integration, we can express the proper distance as

$$D_{\text{prop}}(z_0, z_e) = \frac{c}{H_0} \int_{a(z_e)}^{a(z_0)} da [a^{-2}\Omega_r + a^{-1}\Omega_m + (1 - \Omega_r - \Omega_m - \Omega_\Lambda) + a^2\Omega_\Lambda]^{-1/2} \quad (1.20)$$

The *comoving distance* D_{com} is simply the radial distance, χ , between two objects in the comoving coordinate system, such that the two objects follow the Hubble flow. Again, we will refer to the FLRW metric, as was done in the derivation of cosmological redshift. Again, for null geodesics, we have $ds = 0$, and $d\ell = a(t)d\chi$ for constant (θ, ϕ) . Again, we can say that the FLRW metric becomes $0 = -c^2dt^2 + a(t)^2d\chi^2$. This time, we choose the negative solution upon taking the square root, $cdt = -a(t)d\chi$. As with proper distance, the minus sign indicates the fact that distances measured from the origin to a source are measured backwards in time. Thus,

$$dD_{\text{com}} = d\chi = -\frac{cdt}{a} = -\frac{cda}{\ddot{a}a} = -\frac{cda}{a^2H(a)} \quad (1.21)$$

Upon integration, and using Eq. (1.16), we obtain

$$D_{\text{com}}(z_0, z_e) = \chi(z_0, z_e) = \frac{c}{H_0} \int_{a(z_e)}^{a(z_0)} da [\Omega_r + a\Omega_m + a^2(1 - \Omega_r - \Omega_m - \Omega_\Lambda) + a^4\Omega_\Lambda]^{-1/2} \quad (1.22)$$

Looking at Eqs. (1.19) and (1.21), one notices that there is an explicit relationship between proper

and comoving distances – namely,

$$dD_{\text{prop}} = a(t)dD_{\text{com}}. \quad (1.23)$$

The *angular diameter distance*, $D_{\text{ang}}(t)$, is the generalization of distance to an object of some physical size δL that subtends some angle $\delta\theta$ on the sky to a non-Euclidean metric. In the Euclidean case, we know that (via the small angle approximation) $\delta\theta = \delta L/D_{\text{ang}}$. Imagine that this object is a light-emitting yardstick, such that it is a source of light at z_e that we observe at z_0 . The comoving coordinates of the two ends of the yardstick, at the time the light was emitted, are (χ, θ, ϕ) and $(\chi, \theta + \delta\theta, \phi)$. In the FLRW metric, ds represents the distance between the two ends of the yardstick. From the coordinates of the ends of the yardstick, we note that $d\chi = d\phi = 0$ and also $dt = 0$, since light takes the same time to travel from both ends of the yardstick to us. The FLRW metric then becomes $ds^2 = a^2(t)f_K^2(\chi(z_0, z_e))\delta\theta^2$. However, for a standard yardstick whose length ℓ is known, we can set $ds = \delta L$ and thus find that

$$D_{\text{ang}}(z_0, z_e) = a(z_e)f_K(\chi(z_0, z_e)) \quad (1.24)$$

Note that, in general, $D_{\text{ang}}(z_1, z_2) \neq D_{\text{ang}}(z_2, z_1)$. Angular diameter distance is commonly used in gravitational lensing (see Sec. 1.2).

1.1.5 Structure formation

In the pre-inflationary period of the Universe, quantum fluctuations existed in the hot, dense, early Universe. These fluctuations grew with inflation, leading to over- and under-dense regions in the Universe. This is the beginning of the formation of large-scale structure in our Universe.

If we relax the assumption of the cosmological principle, we can analyze how density fluctuations in the Universe evolve with time. Considering scalar perturbations, the perturbed FLRW metric is

defined by (see e.g. Ma and Bertschinger [30]):

$$ds^2 = \left(1 + \frac{2\Psi}{c^2}\right) c^2 dt^2 - a^2(t) \left(1 - \frac{2\Phi}{c^2}\right) dl^2. \quad (1.25)$$

where dl^2 is given by Eq. (1.6), as before. This is known as the *Newtonian gauge*. The two Bardeen potentials, $\Psi(\mathbf{x}, t)$ and $\Phi(\mathbf{x}, t)$, are considered to describe weak fields, $\Psi, \Phi \ll c^2$ [31]. In GR, the two Bardeen potentials are equal to each other:

$$\Phi_N = \Phi = \Psi, \quad (1.26)$$

where Φ_N is the Newtonian gravitational potential defined via the Poisson equation. In modified gravity, these potentials need not be equivalent. It is often convenient to work in the *conformal Newtonian gauge*, where the *conformal time* is related to the cosmic time via $d\tau = a^{-1}dt$. Thus,

$$ds^2 = a^2(\tau) \left[\left(1 + \frac{2\Psi}{c^2}\right) c^2 d\tau^2 - \left(1 - \frac{2\Phi}{c^2}\right) dl^2 \right]. \quad (1.27)$$

The equations of the theory of gravitation at perturbation level relate the metric perturbations (the Bardeen potentials) to the perturbations of the cosmological fluid: the density contrast,

$$\delta \equiv \frac{\delta\rho}{\bar{\rho}}, \quad (1.28)$$

where $\delta = \delta(\mathbf{x}, \tau)$, $\rho = \rho(\mathbf{x}, \tau)$, $\bar{\rho} = \bar{\rho}(\tau)$, $\delta\rho = \rho - \bar{\rho}$; the pressure perturbation, $\delta p = p - \bar{p}$; the fluid velocity, v ; and the stress or anisotropic pressure, σ . In GR, these equations are the linearized Einstein field equations. Computing the Einstein field equations is most easily done in Fourier space, where we exchange spatial derivatives with powers of $i\mathbf{k}$, where k is the comoving wavenumber. We will use the convention:

$$\delta(\mathbf{x}, a) = \int \frac{d^3x}{(2\pi)^3} e^{i\mathbf{k}\cdot\mathbf{x}} \tilde{\delta}(\mathbf{k}, a) \iff \tilde{\delta}(\mathbf{k}, a) = \int d^3x e^{-i\mathbf{k}\cdot\mathbf{x}} \delta(\mathbf{x}, a) \quad (1.29)$$

and hence

$$\frac{\partial}{\partial x^i} \delta(\mathbf{x}, a) \rightarrow ik_i \tilde{\delta}(\mathbf{k}, a). \quad (1.30)$$

Given that we are dealing with scalar perturbations, we can anticipate that the $0 - 0$ and scalar component of the $i - j$ Einstein equations will be relevant. We will solve the Einstein equations using the conformal Newtonian gauge. Furthermore, we take $c = 1$ for simplicity in the rest of this section. The Einstein equations, in Fourier space, are as follows [30]:

$$\begin{aligned} (0 - 0) : \quad & k^2 \tilde{\Phi} + 3 \frac{\dot{a}}{a} \left(\dot{\tilde{\Phi}} + \frac{\dot{a}}{a} \tilde{\Psi} \right) = 4\pi G a^2 \delta T^0_0 \\ (0 - j) : \quad & k^2 \left(\dot{\tilde{\Phi}} + \frac{\dot{a}}{a} \tilde{\Psi} \right) = 4\pi G a^2 (\bar{\rho} + \bar{p}) \theta \\ (i - i) : \quad & \ddot{\tilde{\Phi}} + \frac{\ddot{a}}{a} \left(\dot{\tilde{\Psi}} + 2\dot{\tilde{\Phi}} \right) + \left(2 \frac{\ddot{a}}{a} \tilde{\Psi} - \frac{\dot{a}^2}{a^2} \right) \tilde{\Psi} + \frac{k^2}{3} \left(\tilde{\Phi} - \tilde{\Psi} \right) = \frac{4\pi}{3} G a^2 \delta T^i_i \\ (i - j) : \quad & k^2 \left(\tilde{\Phi} - \tilde{\Psi} \right) = 12\pi G a^2 (\bar{\rho} + \bar{p}) \sigma \end{aligned} \quad (1.31)$$

where δT^μ_ν is the perturbed energy-momentum tensor, and where there exists a summation over the various species – i.e. $(\bar{\rho} + \bar{p})\theta = \sum_s (\bar{\rho}_s + \bar{p}_s)\theta_s$ and $(\bar{\rho} + \bar{p})\sigma = \sum_s (\bar{\rho}_s + \bar{p}_s)\sigma_s$. In these equations, θ and σ are defined such that $(\bar{\rho} + \bar{p})\theta \equiv ik^j \delta T^0_j$ and $(\bar{\rho} + \bar{p})\sigma \equiv -(\hat{\mathbf{k}}_i \cdot \hat{\mathbf{k}}_j - \frac{1}{3}\delta_{ij}\Sigma^i_j)$; and $\Sigma^i_j \equiv T^i_j - \frac{1}{3}\delta^i_j T^k_k$ denotes the traceless component of T^i_j . For a fluid moving with a small coordinate velocity, $v^i \equiv dx^i/d\tau$, (relative to the cosmological rest frame defined by the perfect fluid of Eq. 1.7), v^i can be treated as a perturbation of the same order as $\delta\rho$, δp , and the metric perturbations. Then, to linear order in the perturbations, the energy-momentum tensor is given by

$$\begin{aligned} T^0_0 &= -(\bar{\rho} + \delta\rho), \\ T^0_i &= (\bar{\rho} + \bar{p})v_i = -T^i_0, \\ T^i_j &= (\bar{p} + \delta p)\delta^i_j + \Sigma^i_j, \quad \Sigma^i_i = 0, \end{aligned} \quad (1.32)$$

where there is an anisotropic shear perturbation Σ^i_j in T^i_j . From this, we note that θ , as defined earlier, is the divergence of the fluid velocity $\theta \equiv ik^j v_j$.

The Poisson equation

By inserting the $(0 - j)$ equation into the $(0 - 0)$ one, we obtain $k^2\tilde{\Phi} + 3\frac{\dot{a}}{a}\frac{1}{k^2}[4\pi Ga^2\delta T^0_0] = 4\pi Ga^2\delta T^0_0$. Using Eq. (1.13), Eq. (1.11), and recognizing that $\delta = -\delta T^0_0/\bar{\rho}$, this becomes $k^2\tilde{\Phi} = -4\pi Ga^2\bar{\rho}\left[\tilde{\delta} + \frac{3H(a)(1+w)\theta}{k^2}\right]$. It is often useful to define the *comoving density perturbation*:

$$\tilde{\Delta} = \tilde{\delta} + \frac{3H(a)(1+w)\theta}{k^2} \quad (1.33)$$

such that we are left with the *generalized Poisson equation*.

$$k^2\tilde{\Phi} = -4\pi Ga^2\bar{\rho}\tilde{\Delta} \quad (1.34)$$

This is the first of the evolution equations of the Bardeen potentials.

The Boltzmann, Continuity, and Euler equations

Two more evolution equations for the Bardeen potentials, the *continuity equation* and *Euler equation*, come from a statistical treatment of the particles in the cosmological fluid [30]. We begin by considering a phase space, described by six variables: three positions, x^i , and their conjugate momenta, P_i . The conjugate momenta are simply the spatial part of the 4-momentum with lower indices – i.e., for a particle of mass m , $P_i = mU_i$, where $U_i = dx_i/(-ds^2)^{1/2}$. The conjugate momentum is related to the proper momentum $p^i = p_i$ in the conformal Newtonian gauge by $P_i = a(1 - \Phi)p_i$. The phase-space distribution of the particles gives the number of particles in a differential volume $dx^1dx^2dx^3dP_1dP_2dP_3$:

$$f(x^i, P_j, \tau)dx^1dx^2dx^3dP_1dP_2dP_3 = dN. \quad (1.35)$$

The energy-momentum tensor can be expressed in terms of the distribution function and the 4-momentum components as

$$T_{\mu\nu} = \frac{1}{\sqrt{-g}} \int dP_1dP_2dP_3 \frac{P_\mu P_\nu}{P^0} f(x^i, P_j, \tau), \quad (1.36)$$

where g is the determinant of the metric tensor. It is convenient to replace P_j by $q_j = ap_j$, such that q_j is defined as the comoving 3-momentum. We can furthermore define it in terms of its magnitude and direction: $q_j = qn_j$, where $n^i n_i = \delta_{ij} n^i n^j$. The phase-space variables then change, and we replace $f(x^i, P_j, \tau) \rightarrow f(x^i, q, n_j, \tau)$. The phase-space distribution evolves according to the *Boltzmann equation*:

$$\frac{Df}{d\tau} = \frac{\partial f}{\partial \tau} + \frac{dx^i}{d\tau} \frac{\partial f}{\partial x^i} + \frac{dq}{d\tau} \frac{\partial f}{\partial q} + \frac{dn_i}{d\tau} \frac{\partial f}{\partial n_i} = \left(\frac{\partial f}{\partial \tau} \right)_C \quad (1.37)$$

where the right-hand side involves terms due to collisions.

From the perturbed part of the energy-momentum conservation equations, $\partial_\mu T^{\mu\nu} + \Gamma^\nu{}_{\alpha\beta} T^{\alpha\beta} + \Gamma^\alpha{}_{\alpha\beta} T^{\nu\beta} = 0$, along with the Boltzmann equation, one is able to solve for the continuity and Euler equation in the conformal Newtonian gauge in Fourier space. If we want to write down these equations for matter, we need to separate the matter component into a collisionless cold dark matter (such that the right-hand side of the Boltzmann equation vanishes) and a baryonic component which has collisions with the photon fluid. The continuity and Euler equations for cold dark matter and baryons, respectively, are:

$$\dot{\tilde{\delta}}_{\text{cdm}} = -\theta_{\text{cdm}} + 3\dot{\tilde{\Phi}} \quad (1.38)$$

$$\dot{\theta}_{\text{cdm}} = -H(a)\theta_{\text{cdm}} + k^2\tilde{\Psi} \quad (1.39)$$

$$\dot{\tilde{\delta}}_b = -\theta_b + 3\dot{\tilde{\Phi}} \quad (1.40)$$

$$\dot{\theta}_b = -H(a)\theta_b + c_s^2 k^2 \tilde{\delta}_b + \frac{4\bar{\rho}_\gamma}{3\bar{\rho}_b} a n_e \sigma_T (\theta_\gamma - \theta_b) k^2 \tilde{\Psi} \quad (1.41)$$

where γ refers to the photon fluid, n_e is the proper mean electron number density, σ_T is the electron Thompson-scattering cross-section, and the square of the baryon sound speed is $c_s^2 = \frac{\dot{\rho}_b}{\dot{\rho}_b} = \frac{k_B T_b}{\mu} \left(1 - \frac{1}{3} \frac{d \ln T_b}{d \ln a} \right)$, where $T_b(a)$ is the time-dependent temperature of the baryon fluid, k_B is the Boltzmann constant, and μ is the mean molecular weight of electrons and ions.

While there exist continuity and Euler equations for the remaining species of the cosmological

fluid, we will only be interested in how matter, via gravitational instability, evolves into the large-scale structure of the Universe in the following sections.

Initial conditions from inflation

Next, we turn to the mechanism that is responsible for generating the perturbations about the FLRW metric in the first place: inflation. Quantum-mechanical fluctuations in the very early Universe are first produced when the relevant scales are causally connected. These perturbations are then smoothed out of the horizon by inflation, re-entering later in order to serve as the initial conditions for the growth of structure in the Universe. These perturbations will be described in terms of the Fourier modes of the gravitational potential, $\tilde{\Phi}(\mathbf{k})$. While the mean of a given Fourier mode is zero – i.e. $\langle \tilde{\Phi}(\mathbf{k}) \rangle$ – a given mode has nonzero variance:

$$\langle \tilde{\Phi}(\mathbf{k}) \tilde{\Phi}^*(\mathbf{k}') \rangle = \mathcal{P}_\Phi(k) (2\pi)^3 \delta_D^{(3)}(\mathbf{k} - \mathbf{k}'), \quad (1.42)$$

where the Dirac-delta function enforces the independence of the modes. In the case of scalar perturbations¹⁷, the *power spectrum* for the gravitational potential is given by $\mathcal{P}_\Phi(k) = \frac{8\pi G}{9k^3} \frac{H^2}{\epsilon_{\text{sr}}} \Big|_{aH=k}$ where $\epsilon_{\text{sr}} = -\dot{H}/aH^2$ is the slow-roll parameter (see e.g. Dodelson and Schmidt [1]). The scalar perturbations during inflation can be parameterized in terms of the gauge-invariant curvature perturbation $\mathcal{R}(\mathbf{k}, \tau) \equiv \frac{ik_i T^i_0 a^2 H(a)}{k^2(\rho+p)} - \tilde{\Psi}(\mathbf{k}, \tau)$ whose power spectrum is given by

$$\mathcal{P}_{\mathcal{R}}(k) = \frac{2\pi}{k^3} \frac{H^2}{m_{\text{Pl}} \epsilon_{\text{sr}}} \Big|_{aH=k} \equiv \frac{(2\pi)^2 A_s}{k^3} \left(\frac{k_p}{k} \right)^{n_s - 1} \quad (1.43)$$

where m_{Pl} is the Planck mass, A_s is the variance of curvature perturbations in a logarithmic wavenumber interval centered around the pivot scale k_p (which we take to be 0.05 Mpc^{-1} ; see Aghanim et al. [28]), and n_s is the scalar spectral index. The Planck 2018 TT, TE, EE + lowE + lensing constraints of the cosmological parameters A_s and n_s are shown in Table 1.2. The power spectrum for \mathcal{R} is conserved on super-horizon scales, regardless of whether matter or radiation

¹⁷Inflation also produces tensor perturbations, in the form of gravitational waves. We have ignored tensor perturbations in the metric because our primary interest are the scalar perturbations which lead to the formation of large-scale structure

dominates, making it a useful place to build from.

The growth of structure: linear theory

Gravitational instability is responsible for the growth of large-scale structure in our Universe. As the Universe evolves, matter falls into these initially small gravitational potential wells. As the evolution continues, matter further accumulates in these wells, forming over-dense (and under-dense) regions where the matter is (and is not). Eventually, the large-scale structures of the Universe we see today are formed as a consequence (see Dodelson and Schmidt [1] for a review).

The evolution of the perturbations in the cosmological fluid can be broken into three stages. It is important to note that different wavelength modes, k , will evolve differently. Large-scale modes are of order $k < 0.01 \text{ Mpc}^{-1}$, intermediate scales of order $0.01 < k < 1 \text{ Mpc}^{-1}$, and small scales of order $k > 1 \text{ Mpc}^{-1}$. In the very early Universe, shortly after inflation, all of the modes are outside of the horizon, and the potential Φ is constant. At intermediate times, the wavelengths enter the horizon, and the universe evolves from radiation domination ($a \ll a_{\text{eq}}$) to matter domination ($a \gg a_{\text{eq}}$), where a_{eq} denotes matter-radiation equality. Large-scale modes, which enter the horizon well after a_{eq} , evolve much differently from the small-scale modes that enter prior to a_{eq} . At late times deep into matter domination, $a > a_{\text{late}}$, all modes evolve identically again, remaining constant. In this section, we will describe the growth of structure up until this point; however, it is worth pointing out that all modes will decay during the epoch of dark-energy domination.

For $a > a_{\text{late}}$, the gravitational potential is related to the primordial curvature perturbation \mathcal{R} generated during inflation by $\tilde{\Phi}(\mathbf{k}, a) = \frac{3}{5}\mathcal{R}(\mathbf{k})T(k)D_+(a)$, where $T(k)$ is the *transfer function* and $D_+(a)$ is the *growth factor*. The transfer function describes the evolution of perturbations through the epochs of horizon crossing, to matter-radiation equality, to late times. It is defined conventionally as

$$T(k) \equiv \frac{\tilde{\Phi}(\mathbf{k}, a_{\text{late}})}{\Phi_{\text{large-scale}}(\mathbf{k}, a_{\text{late}})} \quad (1.44)$$

where $\tilde{\Phi}_{\text{large-scale}}$ is the gravitational potential for modes that entered the horizon well into the matter-dominated epoch. As it turns out, this is equal to 9/10 the primordial gravitational potential

from inflation. The growth factor describes the wavelength-independent growth at late times, defined as $\frac{\tilde{\Phi}(\mathbf{k}, a)}{\Phi(\mathbf{k}, a_{\text{late}})} \equiv \frac{D_+(a)}{a}$ for $a > a_{\text{late}}$. During matter-domination, the potential is constant, such that $D_+(a) = a$. This allows us to write

$$\tilde{\Phi}(\mathbf{k}, a) = \frac{3}{5} T(k) \frac{D_+(a)}{a} \quad (a > a_{\text{late}}). \quad (1.45)$$

The evolution of the cold dark matter overdensity, $\tilde{\delta}_{\text{cdm}}$, follows from the evolution of $\tilde{\Phi}$. As we will see, despite the fact that $D_+(a) = a$ at late times, leading to a constant gravitational potential, the overdensity grows as $\tilde{\delta}_{\text{cdm}} \propto D_+(a)$, which is where the name-growth factor comes from.¹⁸

In the late Universe, baryons closely follow the evolution of cold dark matter; as such, we can describe the evolution of the total matter overdensity, $\tilde{\delta}_m$. In terms of the matter overdensity only, the Poisson equation of Eq. (1.34) is

$$k^2 \tilde{\Phi}(\mathbf{k}, a) = -4\pi G a^2 \bar{\rho}_m(a) \tilde{\Delta}_m(\mathbf{k}, a) \quad (a > a_{\text{late}}). \quad (1.46)$$

Here, we are interested in the evolution at large-scales, $k \gg aH$. In this case, the comoving density perturbation of Eq. (1.33) becomes $\tilde{\Delta} \simeq \tilde{\delta}$. From Eqs. (1.12) and (1.15), we know that $\rho_m = \Omega_m \rho_{\text{crit},0}/a^3$, and from Eq. (1.14), $4\pi G \rho_{\text{crit},0} = 3H_0^2/2$. Then $\tilde{\delta}_m(\mathbf{k}, a) = \frac{2k^2 a}{3\Omega_m H_0^2} \tilde{\Phi}(\mathbf{k}, a)$ for $a > a_{\text{late}}$ and $k \gg aH$. Using Eq. (1.45), we can express the total matter overdensity as

$$\tilde{\delta}_m(\mathbf{k}, a) = \frac{2k^2}{5\Omega_m H_0^2} \mathcal{R}(\mathbf{k}) T(k) D_+(a) \quad (a > a_{\text{late}}, k \gg aH). \quad (1.47)$$

After a prolonged throat clearing, we are finally ready to define the quantity that we have been building to for this entire chapter – the *linear matter power spectrum* at late times:

$$\langle \tilde{\delta}(\mathbf{k}, a) \tilde{\delta}^*(\mathbf{k}', a) \rangle = \mathcal{P}_L(k, a) (2\pi)^3 \delta_D^{(3)}(\mathbf{k} - \mathbf{k}'). \quad (1.48)$$

¹⁸It is actually the case that $\tilde{\delta}_{\text{cdm}}$ is a linear combination of the growth factor, $D_+(a)$ as well as a *decay factor*, $D_-(a)$. Density perturbations associated with the decay factor quickly decay and play no role in structure formation.

Evaluating the left-hand side of this expression, inserting Eq. (1.47), and further replacing the $\langle \mathcal{R}(\mathbf{k})\mathcal{R}(\mathbf{k}') \rangle$ term that appears with the primordial power spectrum from inflation given by Eq. (1.43), we are left with the following expression:

$$\mathcal{P}_L(k, a) = \frac{8\pi^2}{25} \frac{A_s}{\Omega_m^2} D_+^2(a) T^2(k) \frac{k^{n_s}}{H_0^4 k_p^{n_s - 1}} \quad (1.49)$$

where we note that this power spectrum has dimensions of [length]³.

The evolution of the cold dark matter and baryonic matter overdensities, starting with the seeds of inflation, are described by the Einstein equations of Eq. (1.31), and the full set of Boltzmann equations, including those for cold dark matter and baryons given by Eqs. (1.38) - (1.41), as well as those not reported here for the remaining species of the cosmological fluid, along with the Poisson equation. While approximate analytic solutions can be obtained for these in some special cases, there is no analytic solution valid for all scales and at all times. As such, it is common practice in the field of cosmology today to (i) encode the details of the evolution of the matter overdensity in $T(k)$ and $D_+(a)$, and (ii) solve them numerically using one of two Einstein-Boltzmann codes such as CAMB¹⁹ [32] or CLASS²⁰ [33].

Computing $T(k)$ involves a substantial amount of physics inside of these Einstein-Boltzmann solvers. Calculating $D_+(a)$, on the other hand, is relatively straightforward. A combination of the continuity, Euler, and Poisson equations for the matter overdensity yields the ordinary differential equation

$$\frac{d^2 \tilde{\delta}_m}{da^2} + \frac{d \ln(a^3 H)}{da} \frac{d \tilde{\delta}_m}{da} - \frac{3 \Omega_m H_0^2}{2 a^5 H^2} \tilde{\delta}_m = 0. \quad (1.50)$$

Upon the numerical integration of this differential equation done by the Einstein-Boltzmann solvers, one can solve for $D_+(a)$.

Before moving on, it is useful to define a cosmological parameter that will be relevant later on. The overall amplitude and shape of the linear matter power spectrum is often characterized by A_s and n_s , respectively. Another common way to describe the amplitude is by the parameter σ_8 , which

¹⁹<https://camb.info/>

²⁰https://lesgourg.github.io/class_public/class.html

Table 1.2: 2018 TT, TE, EE + lowE + lensing constraints for cosmological parameters relating to the linear matter power spectrum.

Cosmological Parameter	Planck 2018 Measurement
$10^9 A_s$	2.100 ± 0.030
n_s	0.9649 ± 0.0042
σ_8	0.8111 ± 0.0060

defines the root-mean square overdensity in a sphere of comoving radius $R = 8 h^{-1}$ Mpc. For some general radius R [1],

$$\sigma_R \equiv \langle \delta_{\text{m},R}^2(\mathbf{x}) \rangle, \quad (1.51)$$

where

$$\delta_{\text{m},R}(\mathbf{x}) \equiv \int d^3x' \delta_{\text{m}}(\mathbf{x}') W_R(|\mathbf{x} - \mathbf{x}'|) \quad (1.52)$$

where $W_R(x)$ is a top-hat window function, equal to $3/(4\pi R^3)$ for $x < R$ and 0 otherwise.

In Fig. 1.1, the linear matter power spectrum is plotted for four different redshifts, given a Λ CDM cosmology described by Tables 1.1 and 1.2. The overall shape of the linear-matter power spectrum is well described as a power law for low k and high k . For $T(k) = 1$ at large scales, the power spectrum goes as k^{n_s} . For small scales, as $T(k)$ becomes small, the power spectrum turns over and goes as k^{n_s-1} .

Nonlinear evolution

In the previous section, we constructed the linear matter power spectrum by considering small perturbations to the FLRW metric. This works remarkably well for large scales (small k); however, there is a scale beyond which nonlinearities cannot be ignored, k_{NL} , where the linear matter power spectrum no longer accurately follows the matter distribution in our Universe. The regime where the matter overdensity is small with respect to unity, or equivalently, where the dimensionless linear matter power spectrum $(k^3/2\pi^2)\mathcal{P}_{\text{L}}(k, a) \ll 1$ corresponds to the linear regime, where perturbations can be well described by linear theory. $(k^3/2\pi^2)\mathcal{P}_{\text{L}}(k, a) \gtrsim 1$, on the other hand, is the nonlinear regime. Solving the condition $(k^3/2\pi^2)\mathcal{P}_{\text{L}}(k_{\text{NL}}, a) = 1$, we find $k_{\text{N}}(a = 1) \simeq 0.25h \text{ Mpc}^{-1}$.

The linear large scales we have discussed provide an accurate description of the CMB; however,

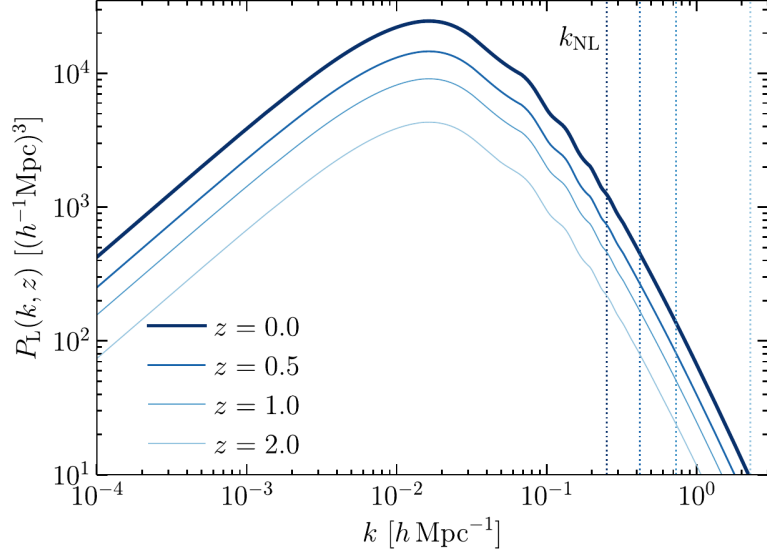


Figure 1.1: Linear matter power spectrum, $\mathcal{P}_L(k, z)$ plotted for four different redshifts, given a Λ CDM cosmology described by Tables 1.1 and 1.2. The matter power spectrum is computed using the Einstein-Boltzmann code **CLASS**. Vertical dashed lines indicate $k_{NL}(z)$, as defined in Sec. 1.1.5. Figure adapted from Dodelson and Schmidt [1].

this approach is an insufficient description of the late Universe and its galaxy clusters, galaxies, and stars. This is precisely the regime that is probed by cosmological weak lensing – we therefore need to extend our analysis beyond linear order. Even in the nonlinear regime, we are still able to work with the assumption of weak gravity, such that the metric perturbations are still small, and the FLRW metric is still applicable. We can therefore work to linear order in the metric perturbations while being fully nonlinear in the matter overdensity.

In our treatment of the nonlinear scales, we will still make the assumption that baryons follow cold dark matter and can be treated as collisionless, as before. At *very* small scales ($k \gtrsim 1 h \text{ Mpc}^{-1}$), this assumption, too, breaks down – we address this in the following subsection. For now, we focus on larger, yet nonlinear, scales.

The idea here is relatively straightforward: perturbations are small on large scales and large on nonlinear scales. Structure can be deemed “nonlinear” when it “collapses,” which first occurs at these smaller, nonlinear scales. These structures *hierarchically* assemble into larger structures as the Universe evolves. The nonlinear structure can be well described by *halos* – bound cold dark matter

structures (with baryons following the cold dark matter). One of the main methods for describing nonlinear structure is that of N-body simulations plus the “halo model,” which is the focus of this subsection. The other method, perturbation theory, is not discussed here.

The first relevant equation for the nonlinear evolution of collisionless cold dark and baryonic matter is the *Vlasov* equation (see e.g. Dodelson and Schmidt [1]):

$$\frac{Df_m}{D\tau} = \frac{\partial f_m}{\partial \tau} + \frac{P_i}{ma} \frac{\partial f_m}{\partial x^i} - am \frac{\partial \Psi}{\partial x^i} \frac{\partial f_m}{\partial P_i} = 0 \quad (1.53)$$

where m is the mass of the matter particle. The Vlasov equation for cold matter is derived from the collisionless Boltzmann equation extended to nonlinear order. The second relevant equation is the Poisson equation for the total matter overdensity. Choosing to work in terms of Ψ , as the perturbation to the time-time component of the metric is what physically governs the motion of the matter (and remembering that $\Phi = \Psi$ in GR), the Poisson equation can be written as $k^2 \tilde{\Psi}(\mathbf{k}, a) = -4\pi G a^2 \bar{\rho}_m(a) \tilde{\delta}_m(\mathbf{k}, a)$ such that $\tilde{\Delta}_m(\mathbf{k}, a) \simeq \tilde{\delta}_m(\mathbf{k}, a)$. Taking the Fourier transform of this, such that $-k^2 = (ik_i)(ik^i) \rightarrow \nabla^2$, the Poisson equation becomes $\nabla^2 \tilde{\Psi}(\mathbf{x}, \tau) = 4\pi G a^2 \bar{\rho}_m(a) \tilde{\delta}_m(\mathbf{x}, \tau)$, where we have chosen to have functions of τ rather than a . From Eq. (1.28), we know that $\bar{\rho}_m \delta_m = \rho_m - \bar{\rho}_m$. We also know that $\rho_m = \int dP_1 dP_2 dP_3 f_m(x^i, P_j, \tau)$. Using these two substitutions, we can write the Poisson equation as:

$$\nabla^2 \Psi = 4\pi G a^2 \left[\int dP_1 dP_2 dP_3 f_m(x^i, P_j, \tau) - \bar{\rho}_m \right]. \quad (1.54)$$

Eqs. (1.53) and (1.54) constitute the *Vlasov-Poisson* system. This system can be solved for f_m numerically via N-body simulations, in which the phase space is discretized such that the “particles” are chunks of the phase space occupied by matter. As an input, N-body simulations therefore need (i) the matter density, determined by Ω_m ; (ii) the expansion history $H(a)$; and (iii) the linear matter power spectrum from which to generate initial conditions. The output of the N-body simulation is a collection of particle²¹ positions and velocities at different “snapshots” of time. Assigning these

²¹Again, “particle” here refers to a chunk of phase space, not an individual dark matter particle.

particles to a grid, we are then able to reconstruct the underlying density field. The nonlinear matter power spectrum can then be calculated from the statistics of this density field.

There is additional information to be found in N-body simulations beyond the density field itself. Within the density field, one can identify dark matter halos – this simply involves finding the densest parts of the field, as well as evaluating which nearby particles are gravitationally bound. Each particle is assigned to one, and only one, halo. Under the assumption that all matter is enclosed by halos, each with their own mass, the matter density field can be built from the density field of the halos, along with a model for their internal structure. This is known as the *halo model*.

From early N-body simulations, it was found that dark matter halos exhibit approximately universal spherically averaged density profiles, known as the NFW profile [34, 35, 36].

$$\rho(r) = \frac{\rho_{\text{crit}}(z)\Delta_c}{(r/r_s)(1+r/r_s)^2} \quad (1.55)$$

where Δ_c is a dimensionless scaling density and r_s is the *scale radius*. For $r \ll r_s$, $\rho \propto r^{-1}$ and for $r \gg r_s$, $\rho \propto r^{-3}$, so r_s can be thought of as the radius where the slope of the profile changes. The virial mass, M_{200} , is defined as the mass contained within a region, $r \leq r_{200}$, where the average density is 200 times the critical density (see Eq. 1.14) at redshift z : $M_{200} = \frac{4\pi}{3} r_{200}^3 \times 200\rho_{\text{crit}}(z) = 4\pi \int_0^{r_{200}} dr \frac{\rho_s}{(r/r_s)(1+r/r_s)^2}$ such that the dimensionless scaling density can be expressed as $\Delta_c = \frac{200}{3} \frac{c^3}{\ln(1+c)-c/(1+c)}$, where the concentration parameter is defined as $c \equiv r_{200}/r_s$. The NFW parameters can be used as fitting parameters and constrained by astrophysical observations such as weak gravitational lensing.

It is worth noting that there is an approximation to this profile, known as the Singular Isothermal Sphere (SIS) model [37],

$$\rho(r) = \frac{\sigma_v^2}{2\pi G r^2} \quad (1.56)$$

where σ_v is the velocity dispersion of the particles. The lensing properties of the SIS and NFW models are discussed in Sec. 1.2.9.

Also obtainable from N-body simulations is the *halo mass function*, $dn/d\ln M$, which is the

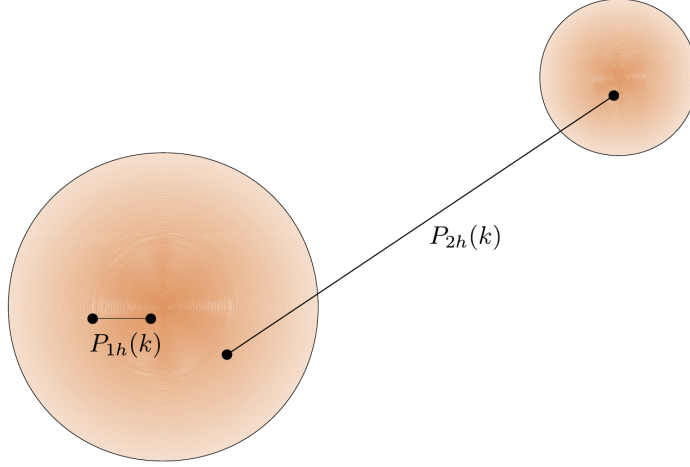


Figure 1.2: Cartoon illustration of the 2-halo and 1-halo contributions to the nonlinear matter power spectrum. Figure adapted from Dodelson and Schmidt [1].

number density of halos within some mass bin, and the *halo clustering*, which is simply the power spectrum of the halo overdensity, δ_h .

The halo model consists of taking a halo density profile, halo mass function, and halo clustering to model the statistics of the nonlinear matter density in the Universe. The nonlinear matter power spectrum, in this model, can be expressed as

$$\mathcal{P}_{\text{NL}}(k) = \mathcal{P}^{(2-h)}(k) + \mathcal{P}^{(1-h)}(k) \quad (1.57)$$

where the 2-halo term is related to the large-scale clustering of halos and very closely follows the linear matter power spectrum, and the 1-halo term involves mass elements *within* a halo and can be thought of as the halo shot-noise convolved with its profile (see Fig. 1.2). Halo model codes, such as `halofit`, are capable of calculating the nonlinear matter power spectrum using the halo model. `halofit` is incorporated into popular Einstein-Boltzmann codes such as `CLASS`. Fig. 1.3 shows a comparison of the various power spectra, where we see the domination of the 2-halo term on large scales and the 1-halo term at nonlinear scales.

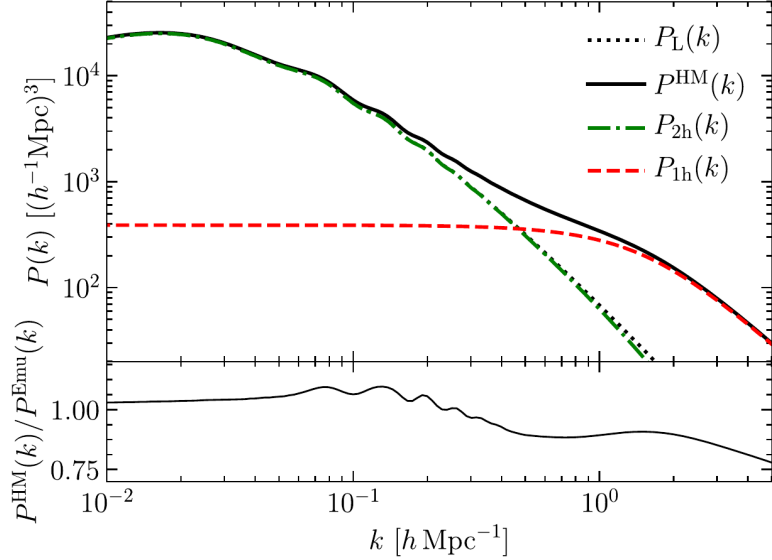


Figure 1.3: *Top panel:* Nonlinear matter power spectrum for $z = 0$, labelled P^{HM} , computed using the `halofit` halo model inside the Einstein-Boltzmann code `CLASS`. Also plotted are the 2-halo and 1-halo power spectra, along with the linear matter power spectrum for comparison. *Bottom panel:* Ratio of the halo model power spectrum to a power spectrum measured in N-body simulations using the `CosmicEmu` code [2]. All power spectra assume a Λ CDM cosmology. Figure adapted from Dodelson and Schmidt [1].

The small-scale power spectrum: baryonic effects

The small-scale matter power spectrum, or the baryonic nonlinear matter power spectrum, is defined by scales beyond which neither N-body simulations and the halo model nor perturbation theory are able to accurately model the distribution of matter in the Universe – namely, $k \gtrsim 1 h \text{ Mpc}^{-1}$ (see e.g. Dodelson and Schmidt [1]). This is due to the fact that both of the approaches for modeling the nonlinear matter power spectrum are *gravity only* approaches, treating baryons as collisionless and following the evolution of cold dark matter. In fact, at small scales, baryon collisions are highly significant.

The baryonic physics at small scales are a source of considerable uncertainty and are poorly constrained. Probes such as cosmological weak lensing are sensitive to these scales, and as such, it is an area of active research among cosmologists. *Baryonic feedback* is a mechanism by which the growth of structure is suppressed. Examples of this include the feedback from active galactic nuclei (AGN) and supernovae, which heat up the halo environment and suppress the clustering of matter.

On the other hand, metal enrichment can offer cooling channels that increase power at these scales.

There do exist hydrodynamical N-body simulations such as OWLS-AGN [38], as opposed to the gravity-only N-body simulations we discussed above, to model some of these effects, as well as codes for computing the small-scale matter power spectrum, such as `Baccoemu` [39]. The parameters of the baryonic effects, however, are poorly constrained, so many modern cosmological analyses simply discard the small-scale information plagued by this theoretical uncertainty (see e.g. Abbott et al. [40]).

As will be discussed, the main drive of this thesis is to offer novel weak lensing cosmology probes that directly probe these small scales, hoping to offer a path forward toward constraining the small-scale power spectrum.

1.2 Weak Gravitational Lensing

As light propagates through an inhomogeneous gravitational field, photons travel on null geodesics ($ds^2 = 0$) in four-dimensional spacetime, while being deflected from straight paths in three-dimensional space. This phenomenon, known as gravitational lensing – so called because it is analogous to the effect optical lenses have on light rays – is one of the most powerful tools in astrophysics and cosmology. Observations of gravitational lensing through telescopes allow us to probe the invisible dark matter in the Universe that is responsible for deflecting light as it travels to us from far-away galaxies.

Gravitational lensing can be divided into two classes: *strong* and *weak*. The arcs that appear in telescope images of galaxy clusters, such as those shown in Fig. 1.4, are examples of strongly lensed background galaxies. In the regime of strong lensing, extremely massive foreground lenses, such as galaxy clusters, can produce multiple “images” of background galaxies. Strong lensing can be used to measure the mass of a lens, where both parametric and nonparametric approaches have been used successfully.

This thesis focuses exclusively on weak lensing. As the name suggests, weak lensing refers to a weaker gravitational lensing effect, producing more modestly distorted single images as compared to the prominent arcs and multiple images that are characteristic of strong lensing. In weak lensing,



Figure 1.4: Galaxy cluster SMACS J0723.3-7327 as imaged by the James Webb Space Telescope (JWST; see: <https://webb.nasa.gov/>). Both strong and weak gravitational lensing effects are evident in this image: arced, multiply imaged galaxies are a strong lensing effect, while the minor shape distortions of galaxies at large radial distances away from the cluster arise from weak lensing. Note that the cluster itself is located at the center of the image.

a matter distribution produces a coherent distortion across a field of background galaxies. Measurement of weak lensing, therefore, is inherently statistical. Through observation of the lensing of multiple background galaxies, one can reconstruct the underlying mass field.

1.2.1 The deflection of light

In gravitational lensing, a “lens” can be described by its Newtonian gravitational potential, Φ_N , such that in the weak-field, its metric is given by (see Bartelmann and Schneider [41])

$$ds^2 = \left(1 + \frac{2\Phi_N}{c^2}\right) c^2 dt^2 - \left(1 - \frac{2\Phi_N}{c^2}\right) dl^2, \quad (1.58)$$

where $dl^2 = dx_i dx^i$, such that this is a perturbed Minkowski metric (or a flat FLRW metric with constant scale factor and $\Phi_N = \Phi = \Psi$). Light rays travel on null geodesics ($ds^2 = 0$), in which case the metric gives us $dt/dl = (1/c)\sqrt{1 - 2\Phi_N/c^2}/\sqrt{1 + 2\Phi_N/c^2}$. As we are in the weak-field limit, $\Phi_N \ll c^2$, we can Taylor expand the term $\sqrt{(1-x)/(1+x)} \simeq 1 - x + \dots$, and we are left with

$$\frac{dt}{dl} \simeq \frac{1}{c} \left(1 - \frac{2\Phi_N}{c^2}\right). \quad (1.59)$$

Using the analogy of light refracting in some medium, the speed of light within the gravitational field is $c' = dl/dt$, such that the index of refraction

$$n = \frac{c}{c'} = c \frac{dt}{dl} = 1 - \frac{2\Phi_N}{c^2}. \quad (1.60)$$

We are interested in finding the *deflection angle*, describing the deflection of the light ray from a straight path in three-space. This is a variational problem where we apply the Fermat principle, stating that $\delta t = 0$. We are therefore looking for the light path, l , which satisfies $\delta \int dl n = 0$. We can describe this in terms of a Lagrangian, $\mathcal{L}(\dot{\mathbf{l}}, \mathbf{l}, \lambda)$, where λ is an arbitrary curve parameter and dots represent derivatives with respect to λ , such that we want to minimize the action:

$$\delta S = \delta \int_{\lambda_S}^{\lambda_O} d\lambda \mathcal{L}(\dot{\mathbf{l}}, \mathbf{l}, \lambda) = 0; \quad \mathcal{L}(\dot{\mathbf{l}}, \mathbf{l}, \lambda) = n[\mathbf{l}(\lambda)] \frac{dl}{d\lambda} = n[\mathbf{l}(\lambda)] \dot{\mathbf{l}} \quad (1.61)$$

where S and O refer to the source of the light and the observer. The corresponding Euler-Lagrange equations can be written as

$$\frac{d}{d\lambda} \frac{\partial \mathcal{L}}{\partial \dot{\mathbf{l}}} - \frac{\partial \mathcal{L}}{\partial \mathbf{l}} = 0. \quad (1.62)$$

The individual terms of the Euler-Lagrange equation become

$$\frac{\partial \mathcal{L}}{\partial \mathbf{l}} = |\dot{\mathbf{l}}| \frac{\partial n}{\partial \mathbf{l}} + n \frac{\partial |\dot{\mathbf{l}}|}{\partial \mathbf{l}} = |\dot{\mathbf{l}}| \frac{\partial n}{\partial \mathbf{l}} = |\dot{\mathbf{l}}| \nabla n \quad (1.63)$$

$$\frac{\partial \mathcal{L}}{\partial \dot{\mathbf{l}}} = |\dot{\mathbf{l}}| \frac{\partial n}{\partial \dot{\mathbf{l}}} + n \frac{\partial |\dot{\mathbf{l}}|}{\partial \dot{\mathbf{l}}} = n \frac{\partial |\dot{\mathbf{l}}|}{\partial \dot{\mathbf{l}}} = n \hat{\mathbf{l}} = n \frac{\dot{\mathbf{l}}}{|\dot{\mathbf{l}}|} \quad (1.64)$$

such that the Euler-Lagrange equation can be written as

$$\frac{d}{d\lambda} \left(n \frac{\dot{\mathbf{l}}}{|\dot{\mathbf{l}}|} \right) - |\dot{\mathbf{l}}| \nabla n = 0. \quad (1.65)$$

We understand $\dot{\mathbf{l}}$ to be a tangent vector to the light path \mathbf{l} , which we can assume to be normalized by a suitable choice for λ . We thus take $|\dot{\mathbf{l}}| = 1$, and the Euler-Lagrange equation becomes

$$\frac{d}{d\lambda} (n \dot{\mathbf{l}}) - \nabla n = 0. \quad (1.66)$$

We see that

$$\frac{dn}{d\lambda} = \frac{d\mathbf{l}}{d\lambda} \frac{dn}{d\mathbf{l}} = \dot{\mathbf{l}} \cdot \nabla n \quad (1.67)$$

$$\implies \frac{d}{d\lambda} (n \dot{\mathbf{l}}) = \frac{dn}{d\lambda} \dot{\mathbf{l}} + n \frac{d\dot{\mathbf{l}}}{d\lambda} = \dot{\mathbf{l}} (\nabla n \cdot \dot{\mathbf{l}}) + n \ddot{\mathbf{l}} \quad (1.68)$$

which yields for the Euler-Lagrange equation

$$n \ddot{\mathbf{l}} = \nabla n - \dot{\mathbf{l}} (\nabla n \cdot \dot{\mathbf{l}}). \quad (1.69)$$

The gradient can be decomposed into two parts:

$$\nabla = \nabla_{\parallel} + \nabla_{\perp} \quad (1.70)$$

where ∇_{\parallel} is the derivative along the light path, such that $\nabla_{\parallel} n = (\nabla n \cdot \hat{\mathbf{i}}) \hat{\mathbf{i}} = (\nabla n \cdot \dot{\mathbf{i}}) \dot{\mathbf{i}}$ where the last term comes from the normalization $|\dot{\mathbf{i}}| = 1$. Therefore, $\nabla_{\perp} = \nabla n - \nabla_{\parallel} n = \nabla n - \dot{\mathbf{i}}(\nabla n \cdot \dot{\mathbf{i}})_{xcvb}$ is the gradient perpendicular to the light path. Hence, the Euler-Lagrange equation becomes

$$n \ddot{\mathbf{l}} = \nabla_{\perp} n \implies \ddot{\mathbf{l}} = \frac{1}{n} \nabla_{\perp} n = \nabla_{\perp} \ln n \quad (1.71)$$

In the weak-field limit, where $\Phi_N \ll c^2$, $n = 1 - 2\Phi_N/c^2 \ll 1$. We can therefore Taylor expand: $\ln(1 + x) \simeq x$, and we are left with

$$\ddot{\mathbf{l}} = -\frac{2}{c^2} \nabla_{\perp} \Phi_N \quad (1.72)$$

The total deflection angle over the light path, $\hat{\boldsymbol{\alpha}} = -(\dot{\mathbf{l}}_O - \dot{\mathbf{l}}_S)$ is now the integral over $\ddot{\mathbf{l}}$ along the light path:

$$\hat{\boldsymbol{\alpha}} = -\frac{2}{c^2} \int_{\lambda_S}^{\lambda_O} d\lambda \nabla_{\perp} \Phi_N \quad (1.73)$$

or, in other words, the integral over the “pull” of the gravitational potential perpendicular to the light path. Note that $\nabla_{\perp} \Phi_N$ points *toward* the lens center, so $\hat{\boldsymbol{\alpha}}$ points in the opposite direction.

As it stands, the equation for the deflection angle is not useful, as we would have to integrate over the actual light path, which is unknown by definition. However, in the weak-field limit $\Phi_N \ll c^2$, we expect the deflection angle to be small. We therefore are justified in adopting the *Born approximation*, where we can integrate over the unperturbed light path.

The Schwarzschild lens

The Schwarzschild metric [10] is a spherically symmetric solution of the Einstein Field Equations for a point mass M

$$g_{\mu\nu} = \begin{pmatrix} -(1 - R_s/r) & 0 & 0 & 0 \\ 0 & (1 - R_s/r)^{-1} & 0 & 0 \\ 0 & 0 & r^2 & 0 \\ 0 & 0 & 0 & r^2 \sin^2 \theta \end{pmatrix} \quad (1.74)$$

where $R_s = 2GM/c^2$ is the Schwarzschild radius. In the weak-field limit $r \gg R_s$, the line element of the metric simply becomes

$$ds^2 \simeq -\left(1 - \frac{R_s}{r}\right)c^2 dt^2 + \left(1 + \frac{R_s}{r}\right)dr^2 + r^2 d\Omega^2, \quad (1.75)$$

Through a transform $R = r(1 + GM/2rc^2)^2$, as well as a coordinate transform from spherical to Cartesian coordinates, $\mathbf{R} = (x^2, x^2, x^3)$, it can be shown that the Schwarzschild metric can be written in the form of the general lens metric given by Eq. (1.58), such that the gravitational potential for the Schwarzschild lens is

$$\Phi_N = -\frac{GM}{R} \quad (1.76)$$

and therefore, taking x^3 to be along the unperturbed light path,

$$\nabla_{\perp} \Phi_N = \begin{pmatrix} \frac{\partial \Phi_N}{\partial x^1} \\ \frac{\partial \Phi_N}{\partial x^2} \end{pmatrix} = \frac{GM}{R^3} \begin{pmatrix} x^1 \\ x^2 \end{pmatrix} = \frac{GM}{R^3} \boldsymbol{\xi} \quad (1.77)$$

where we have defined the impact parameter $\boldsymbol{\xi} \equiv (x^1, x^2)$, which is perpendicular to the x^3 -direction that defines the unperturbed light path. With this definition, we can write $R = \sqrt{\xi^2 + (x^3)^2}$. We choose a lens system such that we place the source at ∞ , the lens at $x^3 = 0$, and the observer at $-\infty$. Therefore, using the Born approximation and integrating along the unperturbed light path x^3 ,

the deflection angle becomes (see Bartelmann and Schneider [41]):

$$\hat{\alpha} = -\frac{2GM}{c^2}\xi \int_{\infty}^{-\infty} dx^3 \frac{1}{(\xi^2 + (x^3)^2)^{3/2}} = \frac{4GM}{c^2\xi} \frac{\xi}{\xi^2}. \quad (1.78)$$

The thin lens approximation

The next step beyond a single point mass lens would be a distribution of point masses, m_i . If $\xi \gg R_s$, as is the case with the single point-mass lens, then the deflection angle is the sum of the deflection angles from each individual lens [41]:

$$\hat{\alpha}(\xi) = \frac{4G}{c^2} \sum_i m_i(\xi_i, x_i^3) \frac{\xi - \xi_i}{|\xi - \xi_i|^2}. \quad (1.79)$$

Treating this as a continuous mass distribution of density ρ , this becomes

$$\hat{\alpha}(\xi) = \frac{4G}{c^2} \int d^2\xi' \int dx'^3 \rho(\xi', x'^3) \frac{\xi - \xi'}{|\xi - \xi'|^2} \quad (1.80)$$

We introduce the *surface mass density*,

$$\Sigma(\xi) = \int dx^3 \rho(\xi, x^3). \quad (1.81)$$

such that Eq. (1.80) becomes

$$\hat{\alpha}(\xi) = \frac{4G}{c^2} \int d^2\xi' \Sigma(\xi') \frac{\xi - \xi'}{|\xi - \xi'|}. \quad (1.82)$$

This expression is valid under the *thin lens/screen approximation* – the assumption that the extent of the mass distribution along the line of sight, constituting the lens, is much smaller than the distances between the source, lens, and observer. This approximation holds under the common astrophysical applications of gravitational lensing, such as galaxy-galaxy and galaxy-cluster lensing (see Sec. 1.2.9). It does not hold, however, in the context of weak lensing by the large-scale structure of the Universe (see Sec. 1.3).

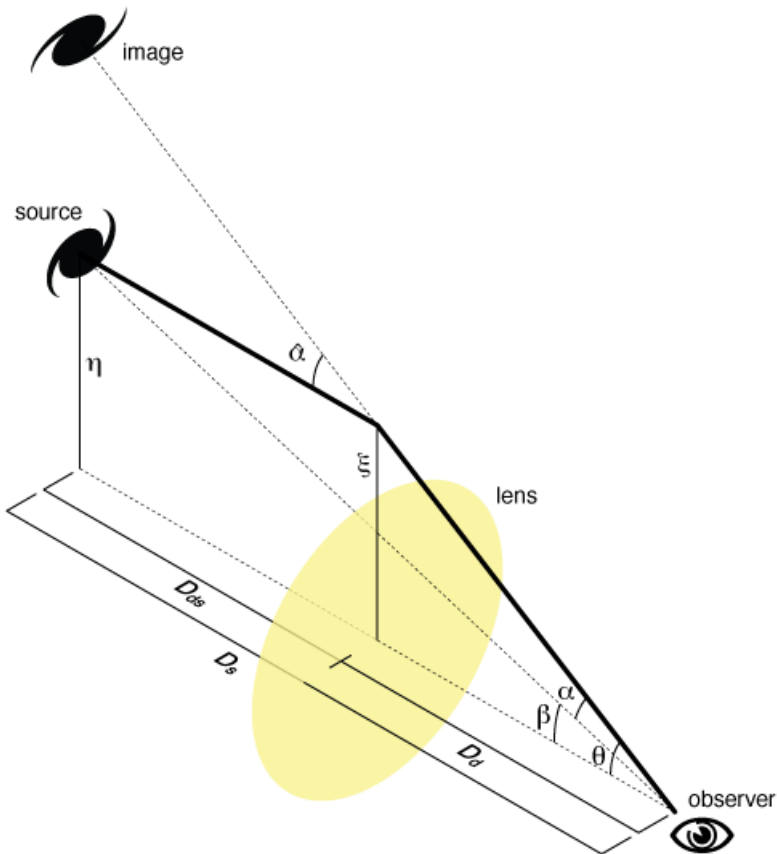


Figure 1.5: Geometry of the lens system described by the lens equation. Figure from Michael Sachs, Wikimedia Commons: https://en.wikipedia.org/wiki/Gravitational_lensing_formalism

1.2.2 The lens equation

We now wish to use the observed deflection of light in order to write an equation relating the true position of a source on the sky to its observed position. The *optical axis* is defined as a line of sight connecting an observer to the lens. We can define a *source plane* and *lens plane*, both perpendicular to the optical axis, which define the planes where the source and lens (under the thin lens approximation) are located, respectively. Figure 1.5 shows a sketch of the geometry for such a system. As before, ξ is the impact parameter in the lens plane. We can similarly define η as the distance along the source plane from the optical axis to the location of the source. We define the following angular diameter distances: D_d is the distance from the observer to the lens or “deflector,” D_s is the distance from the observer to the source, and D_{ds} is the distance between the lens and the

source. From the geometry of Fig. 1.5, the intercept theorem tells us that $D_d/D_s = \xi/(\eta + D_{ds}\hat{\alpha}(\xi))$, where $D_{ds}\hat{\alpha}(\xi)$ comes from the small angle approximation. We can therefore write

$$\boldsymbol{\eta} = \frac{D_s}{D_D} \boldsymbol{\xi} - D_{ds}\hat{\alpha}(\xi) \quad (1.83)$$

Using the small-angle approximation again, we can define the two-dimensional source-plane coordinate

$$\boldsymbol{\beta} = (\beta^1, \beta^2) \equiv \frac{\boldsymbol{\eta}}{D_s} \quad (1.84)$$

and lens-plane coordinate

$$\boldsymbol{\theta} = (\theta^1, \theta^2) \equiv \frac{\boldsymbol{\xi}}{D_d}, \quad (1.85)$$

where 1 and 2 refer to the directions defined by x^1 and x^2 . This leaves us with the *lens equation*:

$$\boldsymbol{\beta} = \boldsymbol{\theta} - \boldsymbol{\alpha}(\boldsymbol{\theta}), \quad (1.86)$$

where we have defined the scaled deflection angle

$$\boldsymbol{\alpha}(\boldsymbol{\theta}) \equiv \frac{D_{ds}}{D_s} \hat{\alpha}(D_d \boldsymbol{\theta}). \quad (1.87)$$

It is important to note that the lens plane, while a distance D_d from the observer, is the image that the observer will see (since there is no additional deflection of light from the lens to the observer). Therefore, the lens plane and observed/image plane are equivalent.

The observed image position, $\boldsymbol{\theta}$, is taken to be the solution of the lens equation for a given source position, $\boldsymbol{\beta}$, and deflection angle, $\boldsymbol{\alpha}$ determined by a given mass distribution. The number of solutions to the lens equation corresponds to the number of images produced.

1.2.3 Lensing potential and convergence

In the formalism of source and lens planes, we can interpret $\Sigma(D_d \boldsymbol{\theta})$ of Eq. (1.81) as the projected surface density of the lens. We can further define a *dimensionless projected surface mass density*

(see e.g. Bartelmann and Schneider [41]):

$$\kappa(\boldsymbol{\theta}) \equiv \frac{\Sigma(D_d \boldsymbol{\theta})}{\Sigma_{\text{crit}}}, \quad (1.88)$$

also known as the *convergence*, where the *critical surface mass density* is defined as

$$\Sigma_{\text{crit}} \equiv \frac{c^2}{4\pi G} \frac{D_s}{D_d D_{ds}}. \quad (1.89)$$

A mass distribution with convergence $\kappa \geq 1$ at some position $\boldsymbol{\theta}$ produces multiple images provided there is a source at an appropriate $\boldsymbol{\beta}$. Therefore, the strong lensing regime is defined by $\kappa \geq 1$.

Using Eq. (1.89), (1.87), and (1.80), the scaled deflection angle can be written as

$$\boldsymbol{\alpha}(\boldsymbol{\theta}) = \frac{1}{\pi} \int d^2\theta' \kappa(\boldsymbol{\theta}') \frac{\boldsymbol{\theta} - \boldsymbol{\theta}'}{|\boldsymbol{\theta} - \boldsymbol{\theta}'|^2}. \quad (1.90)$$

The deflection angle is defined as the gradient of the deflection potential or *lensing potential*,

$$\boldsymbol{\alpha}(\boldsymbol{\theta}) \equiv \nabla_{\boldsymbol{\theta}} \psi(\boldsymbol{\theta}), \quad (1.91)$$

where $\nabla_{\boldsymbol{\theta}}$ is the gradient with respect to the two-dimensional lens-plane coordinate $\boldsymbol{\theta}$. Using Eqs. (1.90) and (1.91), the lensing potential can be expressed as

$$\psi(\boldsymbol{\theta}) = \frac{1}{\pi} \int d^2\theta' \kappa(\boldsymbol{\theta}') \ln |\boldsymbol{\theta} - \boldsymbol{\theta}'| \quad (1.92)$$

and we note that the lensing potential satisfies the two-dimensional Poisson equation

$$\nabla_{\boldsymbol{\theta}}^2 \psi(\boldsymbol{\theta}) = 2\kappa(\boldsymbol{\theta}). \quad (1.93)$$

It is also useful to express the lensing potential as a two-dimensional projection of the Newtonian

potential. Starting with Eqs. (1.73) and (1.87), we can write

$$\boldsymbol{\alpha} = -\frac{2}{c^2} \frac{D_{ds}}{D_s} \int_{\lambda_s}^{\lambda_o} d\lambda \nabla_{\perp} \Phi_N. \quad (1.94)$$

Using the Born approximation, we take $\lambda = x^3$, as before. This also implies that $\nabla_{\perp} = \nabla_{\xi}$. Since $\xi = D_d \boldsymbol{\theta}$, then $\nabla_{\theta} = D_d \boldsymbol{\theta}$. Therefore,

$$\boldsymbol{\alpha}(\boldsymbol{\theta}) = -\frac{2}{c^2} \frac{D_{ds}}{D_s D_d} \int_{x_s^3}^{x_o^3} dx^3 \nabla_{\theta} \Phi_N(D_d \boldsymbol{\theta}, x^3). \quad (1.95)$$

By pulling ∇_{θ} in front of the right-hand side of the above expression, we recognize that by Eq. (1.91),

$$\psi(\boldsymbol{\theta}) = -\frac{2}{c^2} \frac{D_{ds}}{D_s D_d} \int_{x_s^3}^{x_o^3} dx^3 \Phi_N(D_d \boldsymbol{\theta}, x^3). \quad (1.96)$$

1.2.4 Weak lensing: convergence and shear

Next, we wish to consider the gravitational lensing of extended objects, such as galaxies, rather than point sources. In this gravitational lens system, we imagine a background galaxy in the source plane and a thin lens. In this case, we consider the fact that deflection of light differs slightly across the image of a galaxy, leading to an observable distortion in its shape.

As a consequence of Liouville's theorem, gravitational lensing conserves surface brightness. Hence, if $I^{(s)}(\boldsymbol{\beta})$ is the surface brightness distribution in the source plane, we know that the observed surface brightness distribution in the lens plane must be equal to this. It is useful to think of gravitational lensing as a coordinate transform between the source and lens plane. If the transformation between the source plane position, $\boldsymbol{\beta}$, and lens plane position, $\boldsymbol{\theta}$, is a well defined function $\boldsymbol{\beta}(\boldsymbol{\theta})$, then the observed surface brightness is given by (see e.g. Bartelmann and Schneider [41])

$$I(\boldsymbol{\theta}) = I^s(\boldsymbol{\beta}(\boldsymbol{\theta})). \quad (1.97)$$

If the angular extent of the source is smaller than the scale over which the lens properties change,

the function $\beta(\boldsymbol{\theta})$ can be linearized via a Taylor expansion of β around some $\boldsymbol{\theta}_{(0)}$:

$$\boldsymbol{\beta} - \boldsymbol{\beta}_{(0)} = \mathcal{A}(\boldsymbol{\theta}_{(0)}) \cdot (\boldsymbol{\theta} - \boldsymbol{\theta}_{(0)}) \quad (1.98)$$

where

$$\mathcal{A}_{ij}(\boldsymbol{\theta}) \equiv \frac{\partial \beta_i}{\partial \theta_j} = \delta_{ij} - \frac{\partial \alpha_i}{\partial \theta_j} = \delta_{ij} - \frac{\partial^2 \psi(\boldsymbol{\theta})}{\partial \theta_i \partial \theta_j} \quad (1.99)$$

is the *distortion matrix*, which has been defined through the lens equation (Eq. 5.3) and where the final term comes from the definition of the lensing potential (Eq. 1.91). The symmetric, Jacobian distortion matrix can be parameterized with the convergence and *shear*. The distortion matrix can be written as

$$\mathcal{A}_{ij} = \begin{pmatrix} 1 - \kappa - \gamma_1 & -\gamma_2 \\ -\gamma_2 & 1 - \kappa + \gamma_1 \end{pmatrix} \quad (1.100)$$

where the convergence in this context is understood as a spin-0 weak lensing field, and the two-component shear $\gamma = (\gamma_1, \gamma_2)$ is a spin-2 field. We note that a field of spin m transforms identically under rotations by an angle of $2\pi/m$ for $m \neq 0$, and is rotationally invariant for $m = 0$.

If we choose our coordinate system such that $\boldsymbol{\beta}_{(0)} = \boldsymbol{\theta}_{(0)} = 0$, then we can express the coordinate mapping as

$$\beta^i = \mathcal{A}^i{}_j \theta^j. \quad (1.101)$$

At this point, it is convenient to use the comma-derivative notation. In terms of the weak lensing equation, indices that appear after commas refer to derivatives with respect to the lens plane coordinate:

$$\psi_{,i} \equiv \frac{\partial}{\partial \theta_i} \psi(\boldsymbol{\theta}). \quad (1.102)$$

We can therefore rewrite Eq. (1.99) in terms of second derivatives of the lensing potential:

$$\mathcal{A}_{ij} = \begin{pmatrix} 1 - \psi_{,11} & -\psi_{,12} \\ -\psi_{,12} & 1 - \psi_{,22} \end{pmatrix}. \quad (1.103)$$

Comparing the definitions of the distortion matrix given by Eq. (1.100) and Eq. (1.103), we see that the convergence and shear can be expressed in terms of the second derivatives of the lensing potential:

$$\kappa = \frac{1}{2}(\psi_{,11} + \psi_{,22}) \quad (1.104)$$

$$\gamma_1 = \frac{1}{2}(\psi_{,11} - \psi_{,22}) \quad (1.105)$$

$$\gamma_2 = \psi_{,12} \quad (1.106)$$

1.2.5 Higher-order weak lensing: flexion

Beyond convergence and shear, there exists higher-order lensing known as *flexion*, which arises from the convergence and shear not being constant across an image [42, 43, 44, 45]. Working in the weak lensing regime, defined by $|\kappa| \ll 1$ and $|\gamma| \ll 1$, flexion arises from Taylor expanding the lens equation given by Eq. (1.101) to second order:

$$\beta^i = \mathcal{A}^i{}_j \theta^j + \frac{1}{2} \mathcal{D}^i{}_{jk} \theta^j \theta^k \quad (1.107)$$

where

$$\mathcal{D}_{ijk} = \mathcal{A}_{ij,k} \quad (1.108)$$

is the *flexion tensor*. From Eqs. (1.104) - (1.106), derivatives of the convergence are related to derivatives of shear via [46]

$$\kappa_{,1} = \gamma_{1,1} + \gamma_{2,2} \quad (1.109)$$

$$\kappa_{,2} = -\gamma_{1,2} + \gamma_{2,1}. \quad (1.110)$$

Using these relations and Eq. (1.100) the flexion tensor (Eq. 1.108), can be expressed as

$$\mathcal{D}_{ij1} = \begin{pmatrix} -2\gamma_{1,1} - \gamma_{2,2} & -\gamma_{2,1} \\ -\gamma_{2,1} & -\gamma_{2,2} \end{pmatrix} \quad (1.111)$$

$$\mathcal{D}_{ij2} = \begin{pmatrix} -\gamma_{2,1} & -\gamma_{2,2} \\ -\gamma_{2,2} & 2\gamma_{1,2} - \gamma_{2,1} \end{pmatrix}. \quad (1.112)$$

1.2.6 Complex representation: introducing the weak lensing flexion fields

We begin by defining the shorthand

$$\partial_i = \frac{\partial}{\partial \theta_i} \quad (1.113)$$

in order to introduce the complex gradient operator (see e.g. Bacon et al. [43], hereafter referred to as BGRT):²²

$$\partial \equiv \partial_1 + i\partial_2 \quad (1.114)$$

where i is the imaginary number. This operator can be thought of as a derivative with an amplitude and direction down the slope of a surface at any point. Furthermore, it transforms under rotations as a vector: $\partial \rightarrow \partial e^{i\phi}$, where ϕ is the angle of rotation. Applying this operator to the spin-0 (i.e. scalar) lensing potential, we generate the spin-1 (i.e. vector) lensing displacement field

$$\alpha = \alpha_1 + i\alpha_2. \quad (1.115)$$

Thus, ∂ can be interpreted as a spin-raising operator. Its complex conjugate, ∂^* , behaves as a spin-lowering operator. Applying these operators consecutively gives us the spin-0 two-dimensional Laplacian in the lens plane:

$$\partial\partial^* = \partial^*\partial = \nabla_\theta^2 \quad (1.116)$$

where we note that ∂ and ∂^* commute. Applying the spin-lowering operation to the displacement

²²This can be compared with the covariant derivative formalism for weak lensing on the curved sky [47].

field, we find that the spin is lowered to the spin-0 convergence field:

$$\kappa = \frac{1}{2} \partial^* \alpha = \frac{1}{2} \partial^* \partial \psi \quad (1.117)$$

where the final term is equivalent to the definition of convergence given by Eq. (1.93). We can express the shear in the following way:

$$\gamma = \gamma_1 + i\gamma_2 = \frac{1}{2} \partial \partial \psi = |\gamma| e^{2i\phi} \quad (1.118)$$

where the final term is expressed as the magnitude and direction of the shear, where we see how the spin-2 rotational properties are encoded in the $e^{2i\phi}$ term.

We are finally ready to introduce the weak lensing flexion fields. There are two of them – the *first flexion* and *second flexion*, respectively:

$$\mathcal{F} = \mathcal{F}_1 + i\mathcal{F}_2 = \frac{1}{2} \partial \partial^* \partial \psi = \partial \kappa = \partial^* \gamma = |\mathcal{F}| e^{i\phi} \quad (1.119)$$

$$\mathcal{G} = \mathcal{G}_1 + i\mathcal{G}_2 = \frac{1}{2} \partial \partial \partial \psi = \partial \gamma = |\mathcal{G}| e^{3i\phi} \quad (1.120)$$

also referred to as the spin-1 \mathcal{F} -flexion and spin-3 \mathcal{G} -flexion. The components of the flexions can be expressed in terms of the derivatives of the lensing potential:

$$\mathcal{F}_1 = \frac{1}{2} (\psi_{,111} + \psi_{,122}) \quad (1.121)$$

$$\mathcal{F}_2 = \frac{1}{2} (\psi_{,112} - \psi_{,222}) \quad (1.122)$$

$$\mathcal{G}_1 = \frac{1}{2} (\psi_{,111} - 3\psi_{,122}) \quad (1.123)$$

$$\mathcal{G}_2 = \frac{1}{2} (3\psi_{,112} - \psi_{,222}). \quad (1.124)$$

Furthermore, the flexion fields can be related to the flexion tensor, by re-expressing it as the sum of two terms:

$$\mathcal{D}_{ijk} = \mathcal{F}_{ijk} + \mathcal{G}_{ijk} \quad (1.125)$$

such that

$$\mathcal{F}_{ij1} = -\frac{1}{2} \begin{pmatrix} 3\mathcal{F}_1 & \mathcal{F}_2 \\ \mathcal{F}_2 & \mathcal{F}_1 \end{pmatrix} \quad (1.126)$$

$$\mathcal{F}_{ij2} = -\frac{1}{2} \begin{pmatrix} \mathcal{F}_2 & \mathcal{F}_1 \\ \mathcal{F}_1 & 3\mathcal{F}_2 \end{pmatrix} \quad (1.127)$$

$$\mathcal{G}_{ij1} = -\frac{1}{2} \begin{pmatrix} \mathcal{G}_1 & \mathcal{G}_2 \\ \mathcal{G}_2 & -\mathcal{G}_1 \end{pmatrix} \quad (1.128)$$

$$\mathcal{G}_{ij2} = -\frac{1}{2} \begin{pmatrix} \mathcal{G}_2 & -\mathcal{G}_1 \\ -\mathcal{G}_1 & -\mathcal{G}_2 \end{pmatrix}. \quad (1.129)$$

It is important to note that while the convergence and shear are dimensionless, this is not the case for the flexion fields, which have dimensionality of inverse length or inverse sky angle. Rather, the product of image size, a , and the magnitudes of the flexions $|\mathcal{F}|$ and $|\mathcal{G}|$, is a dimensionless quantity which characterizes the contribution of flexion to the coordinate transformation described by the lens equation.

Finally, with these definitions in place, we note that the coordinate mapping/lens equation to higher-order (Eq. 1.107) can be most compactly written in terms of the derivatives of the lensing potential:

$$\beta_i = \delta_{ij}\theta^j - \psi_{,ij}\theta^j - \frac{1}{2}\psi_{,ijk}\theta^j\theta^k. \quad (1.130)$$

Now that we have defined all of the weak lensing fields of interest – the convergence, shear, \mathcal{F} -flexion, and \mathcal{G} -flexion – it is useful to describe what these fields actually *look* like, given the fact that the goal is to observe them. Figure 1.6 shows the effect of each weak lensing field individually on a unlensed, circularly symmetric, Gaussian source galaxy. Here, we see that the convergence is an isotropic distortion, while the shear is an anisotropic, elliptical stretching of the source image. The \mathcal{F} -flexion effect is a skewing distortion which manifests as a centroid shift, whereas the \mathcal{G} -flexion is a trefoil distortion resulting in a triangularization of the source image.

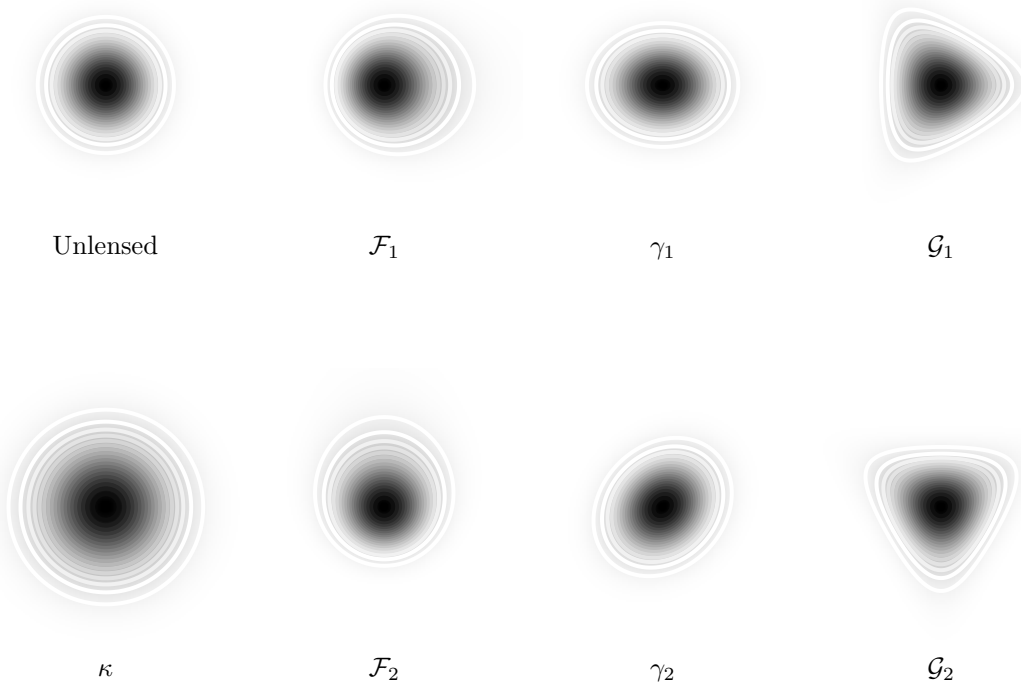


Figure 1.6: Weak lensing convergence, shear, \mathcal{F} -flexion, and \mathcal{G} -flexion applied individually to an unlensed, circularly symmetric, Gaussian galaxy. Spin-values of the weak lensing fields increase from left to right: convergence is spin-0, \mathcal{F} -flexion is spin-1, shear is spin-2, and \mathcal{G} -flexion is spin-3. The magnitudes of these fields are unrealistically large for the weak lensing regime, and are exaggerated only for visualization purposes. These images were created using **Lenser** (see Chapter 2).

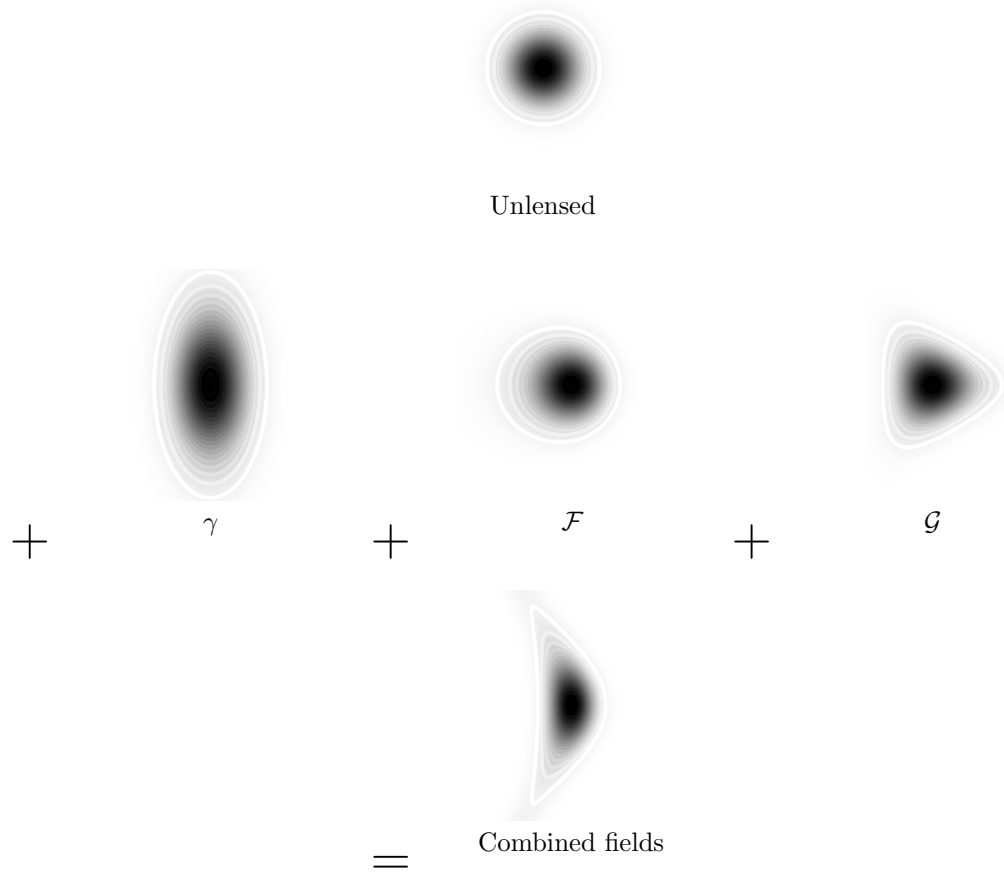


Figure 1.7: Weak lensing convergence, shear, \mathcal{F} -flexion, and \mathcal{G} -flexion applied consecutively to an unlensed, circularly symmetric, Gaussian galaxy. The resulting field is arc- or banana-shaped. The magnitudes of these fields are unrealistically large for the weak lensing regime, and are exaggerated only for visualization purposes. These images were created using `Lenser` (see Chapter 2).

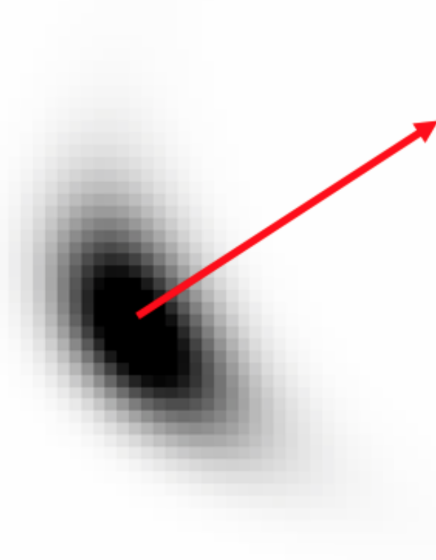


Figure 1.8: Prominent arcing of a source object in the Abell 2744 cluster. The red arrow indicates the direction to the nearest cluster galaxy. Here, the arcing is clearly “pointing” in the same direction as the arrow, indicating that the flexion shear is tangentially aligned along, and flexion pointing towards, the massive lens. Image is a best-fit Sérsic model from `Lenser` of object at RA 00:14:27.284, dec -30:23:55.18 (see Chapter 2). Figure adapted from Fabritius II [3].

When we observe a lensed galaxy, we will observe the combined effects of all of the lensing fields.

In Fig. 1.7, we show how the combination of all lensing fields together leads to an arc- or banana-shaped image. We note that the magnitudes of the lensing fields used in Figs. 1.6 and 1.7 are exaggerated for visualization purposes. In the regime of weak lensing, these effects are all modest, as to collectively lead to modest arcing of lensed galaxies.

Occasionally in weak lensing scenarios, this arcing can be rather prominent. Figure 1.8 shows a prominent arcing of source galaxy that is being weakly lensed by the galaxy cluster Abell 2744. As we will discuss in the following sections, a massive lens causes the spin-2 shear field to “tangentially” align itself around the lens, and the flexion fields point “radially” toward the lens. The combined effect is that the galaxy “arcs” around the lens. It is important to note that while this banana-ness may be reminiscent of the strong lensing arcs, this is a different effect – the arcing from the combination of shear and flexion here is a much more modest weak lensing effect.

1.2.7 Mass-sheet degeneracy, reduced shear and flexion

For a general lens system, the object in the source plane is, by definition, unobservable. Its position in the source plane, β , its size, and its luminosity²³, are unknown. This leads to a non-uniqueness in the projected surface mass density of the lens, such that there exists a family of models [48],

$$\kappa_\lambda = (1 - \lambda) + \lambda\kappa, \quad (1.131)$$

that rescales the convergence by a multiplicative factor λ and adds a constant ‘‘mass-sheet’’ $(1 - \lambda)$ to it, reproduces the observational constraints of the lens system in both the weak and strong lensing regime. This is known as the *mass-sheet degeneracy*. This family satisfies the Poisson equation (Eq. 1.93): $\nabla_\theta^2\psi_\lambda(\theta) = 2\kappa_\lambda(\theta)$ with $\psi_\lambda(\theta) = (1 - \lambda)\theta^2/2 + \lambda\psi(\theta)$. By Eq. (1.91), the corresponding family of deflection angles is $\alpha_\lambda(\theta) = \nabla_\theta\psi_\lambda(\theta) = (1 - \lambda)\theta + \alpha(\theta)$. Inserting this into the lens equation (Eq. (5.3)), we obtain

$$\beta_\lambda = \theta - \alpha_\lambda(\theta) = \lambda(\theta - \alpha(\theta)) \quad (1.132)$$

and find that the lens equation is rescaled by λ . This rescales the shear and flexions by the same factor: $\gamma_\lambda = \lambda\gamma$, $\mathcal{F}_\lambda = \lambda\mathcal{F}$, and $\mathcal{G}_\lambda = \lambda\mathcal{G}$. The consequence of the mass-sheet degeneracy is that the shear and flexion are unobservable – there exists a family of these weak lensing fields that satisfy the lens system. What is observable, however, are the invariant versions of these fields, known as the *reduced shear*

$$g = \frac{\gamma}{1 - \kappa} \quad (1.133)$$

and the *reduced flexions* [45]

$$F \equiv \partial g = \frac{\mathcal{F} + g\mathcal{F}^*}{1 - \kappa} \quad (1.134)$$

$$G \equiv \partial^* g = \frac{\mathcal{G} + g\mathcal{F}}{1 - \kappa}. \quad (1.135)$$

²³Except in the case of a standard candle such as a Type-Ia supernova

In the weak lensing regime $\kappa \ll 1$ and $|\gamma| \ll 1$, the reduced shear is simply equal to the shear

$$g \simeq \gamma. \quad (1.136)$$

Extending this to flexion, noting that the weak lensing regime is also defined further by $a|\mathcal{F}| \ll 1$ and $a|\mathcal{G}| \ll 1$, where a is the size of the galaxy,

$$F \simeq \mathcal{F}, \quad G \simeq \mathcal{G}. \quad (1.137)$$

1.2.8 Measuring weak lensing fields

In fact, we are unable to observe a single galaxy, measure its ellipticity, and claim a detection of shear. When we look through a telescope and see an elliptical galaxy, how do we know whether (i) that galaxy is elliptical because it was once a circular source and was sheared into an ellipse though gravitational lensing, or (ii) that there is absolutely no gravitational lensing, and the galaxy actually just *is* elliptical? The answer is that we don't know – this is referred to as the shear/ellipticity degeneracy. In general, the observed ellipticity of a galaxy is a combination of its intrinsic ellipticity (how elliptical it actually is) and the additional ellipticity from shear, assuming the galaxy is weakly lensed. We begin by defining the observed ellipticity of a galaxy as (see e.g. Bartelmann and Schneider [41])

$$\epsilon = \frac{a - b}{a + b} e^{2i\phi} \quad (1.138)$$

where a and b are the semimajor and semiminor axes of the ellipse, respectively, and ϕ is the position/orientation angle of the ellipse. In the weak lensing regime, $\kappa \ll 1$ and $|\gamma| \ll 1$ the observable ellipticity of a galaxy image is related to the galaxy's intrinsic ellipticity and the lensing shear, so long as $|\epsilon^s| \lesssim 1/2$, via [49]

$$\epsilon = \epsilon^s + \gamma. \quad (1.139)$$

Under the assumption that the orientation of the intrinsic ellipticities of galaxies, which is justifiable

by the statistical isotropy of the large-scale structure of the Universe,²⁴ the expectation value of the intrinsic ellipticity vanishes, $\langle \epsilon^s \rangle = 0$. The observed ellipticity averaged over a sample of galaxies is therefore an estimator of the shear in that region,

$$\langle \epsilon \rangle = \gamma. \quad (1.140)$$

This idea extends to flexion as well – galaxies have intrinsic properties that have spin-1 and spin-3 behavior. For a detailed study of intrinsic flexion, see our paper [50]. With ellipticity, we have two different words to distinguish between the spin-2 intrinsic and observed ellipticities versus the spin-2 weak lensing shear. This is not the case with flexion, however, and here we will refer to the *observed flexion*, *intrinsic flexion*, and *lensing flexion*. In the weak lensing regime defined by $\kappa \ll 1$, $|\gamma| \ll 1$, $a|\mathcal{F}| \ll 1$, and $a|\mathcal{G}| \ll 1$ The relationship between these quantities is given by

$$\mathcal{F}^o = \mathcal{F}^s + \mathcal{F}, \quad \mathcal{G}^o = \mathcal{G}^s + \mathcal{G}, \quad (1.141)$$

where the superscript “o” denotes the observed flexion, the superscript “s” denotes the intrinsic flexion, and the term with no superscript denotes the lensing flexion. As is the case with intrinsic ellipticity, $\langle \mathcal{F}^s \rangle = 0$ and $\langle \mathcal{G}^s \rangle = 0$ and hence

$$\langle \mathcal{F}^o \rangle = \mathcal{F}, \quad \langle \mathcal{G}^o \rangle = \mathcal{G}. \quad (1.142)$$

In Chapter 2, I describe the process for measuring the observed ellipticity and observed flexions for individual galaxies. Once you have a catalogue of these observed ellipticities and flexions, ensemble averages can be calculated to reconstruct the shear and lensing flexions.

As we will see, the ensemble averaging is not nearly as simple as described by Eqs. (1.140) and (1.142). In galaxy-cluster or galaxy-galaxy lensing (see Sec. 1.2.9), averages need to be taken with a

²⁴In reality, the intrinsic ellipticities and flexions of galaxies are not truly random, due to the correlated intrinsic alignment of galaxies with the gravitational tidal field of large-scale structure or in local environments with the intrinsic alignment of other galaxies. This effect needs careful treatment in, for example, high S/N measurements of cosmic shear. It can, however, be ignored in most circumstances as a higher-order effect. I will ignore intrinsic alignments throughout this work.

particular coordinate system in mind, such that each source galaxy has a coordinate system defined by the location of the lens – either a galaxy cluster or a lens galaxy in the cases of galaxy-cluster and galaxy-galaxy lensing, respectively.

1.2.9 Lens models, galaxy-galaxy lensing, and galaxy-cluster lensing

In this section, we first describe two models for lenses in a gravitational lens system: the singular isothermal sphere (SIS) and Navarro-Frenk-White (NFW) lenses. Then, we will present analytic expressions for the weak lensing fields that are induced by these lenses. We reiterate that both the SIS and NFW profiles are circularly symmetric.

As was discussed in Sec. 1.1.3, the rotation curves of spiral galaxies are observed to be approximately flat out to the largest radii where they can be measured, which can be understood if galactic disks are embedded in a dark halo with density profile that scales as $\rho \propto r^{-2}$ for large r . This profile can be obtained by assuming that the velocity dispersion of the dark matter profiles is spatially constant, and hence, they are called *isothermal profiles*. An example of this profile is the SIS profile of Eq. (1.56), introduced in Sec. 1.1.5, where we discussed density profiles of dark matter halos. At this point, it is important to note that an SIS can model both a single galaxy’s density profile – where the particles rotating are the stars in the galaxy and the dark matter particles in the galaxy’s halo – and a galaxy cluster’s density profile, where the particles orbiting are the galaxies in the cluster as well as the dark matter particles throughout.

This is all to say that an SIS can be used to model the density profile of single galaxy as well as an entire galaxy cluster. Similarly, NFW profiles, introduced in Eq. (1.55), can also be applied to single galaxies and galaxy clusters.

Galaxy-galaxy lensing and galaxy-cluster lensing

In gravitational lens systems, a background galaxy in the source plane is lensed by a foreground object – a lens – in the lens plane. When a background galaxy is lensed by a foreground galaxy, this is known as *galaxy-galaxy lensing*. *Galaxy-cluster lensing* occurs when a background galaxy is lensed by a galaxy cluster in the foreground.

In the remainder of this section, we discuss the weak lensing fields that are induced in galaxy-galaxy and galaxy-cluster lensing, modeling the lenses with SIS and NFW profiles. We choose a coordinate system where the origin is placed at the center of the lens. Source galaxies are mapped from their background positions in the source plane to a position (θ_1, θ_2) in the lens plane. We define a complex sky position vector, $\boldsymbol{\theta} = \theta_1 + i\theta_2$ pointing from the origin to the location of a source in the lens plane. We can then make use of polar coordinates, where $\theta = \sqrt{(\theta_1)^2 + (\theta_2)^2}$ is the modulus of the complex sky position vector and $\phi = \arctan(\theta_2/\theta_1)$. This is sufficient to describe the weak lensing fields as a function of θ and ϕ .

SIS Lens

Using Eq. (1.56) and Eq. (1.81), the projected surface mass density of an SIS is given by

$$\Sigma(D_d \boldsymbol{\theta}) = \frac{\sigma_v^2}{2GD_d \theta} \frac{\boldsymbol{\theta}}{\theta} \quad (1.143)$$

which, by Eqs. (1.88) and (1.89), gives a corresponding convergence of

$$\kappa(\boldsymbol{\theta}) = \frac{\theta_E}{2\theta} \quad (1.144)$$

where we have defined the *Einstein radius* as

$$\theta_E \equiv 4\pi \left(\frac{\sigma_v}{c} \right)^2 \frac{D_{ds}}{D_s} \quad (1.145)$$

and we note that the spin-0 convergence depends only on the modulus of $\boldsymbol{\theta}$. From Eq. (1.90), we see that $\alpha = \theta_E$, and by Eq. (1.91), $\psi = \theta_E \theta$. Therefore, by using the relationships between the components of the shear and the derivatives of the lensing potential (see Eqs. 1.105, 1.106, and 1.118),

$$\gamma(\boldsymbol{\theta}) = -\frac{\theta_E}{2\theta} e^{2i\phi}. \quad (1.146)$$

Similarly, from Eqs. (1.119) and (1.120), the flexion fields induced by an SIS lens are

$$\mathcal{F}(\boldsymbol{\theta}) = -\frac{\theta_E}{2\theta^2} e^{i\phi}, \quad (1.147)$$

$$\mathcal{G}(\boldsymbol{\theta}) = \frac{3\theta_E}{2\theta^2} e^{3i\phi}. \quad (1.148)$$

NFW Lens

The NFW density profile given by Eq. (1.55) implies that the convergence is given by [51]

$$\kappa(\boldsymbol{\theta}) = 2\kappa_s \frac{f(y)}{y^2 - 1} \quad (1.149)$$

where we have defined $\kappa_s \equiv \rho_{\text{crit}}(z)\Delta_c r_s/\Sigma_{\text{crit}}$, $y \equiv \xi/r_s = \theta D_{\text{d}}/r_s$, and

$$f(y) = \begin{cases} 1 - \frac{2}{\sqrt{1-y^2}} \operatorname{arctanh} \sqrt{\frac{1-y}{1+y}} & y < 1 \\ 0 & y = 1 \\ 1 - \frac{2}{\sqrt{y^2-1}} \operatorname{arctan} \sqrt{\frac{y-1}{y+1}} & y > 1. \end{cases} \quad (1.150)$$

The shear is given by

$$\gamma(\boldsymbol{\theta}) = -\kappa_s g(y) e^{2i\phi} \quad (1.151)$$

where the magnitude of this signal was derived in Wright and Brainerd [52], and I've added the directional component, and where

$$g(y) \equiv \begin{cases} \frac{8\operatorname{arctanh}\frac{1-y}{1+y}}{y^2\sqrt{1-y^2}} + \frac{4}{y^2} \ln\left(\frac{y}{2}\right) - \frac{2}{y^2-1} + \frac{4\operatorname{arctanh}\frac{1-y}{1+y}}{(y^2-1)\sqrt{1-y^2}} & y < 1 \\ \frac{10}{3} + 4\ln\left(\frac{1}{2}\right) & y = 1 \\ \frac{8\operatorname{arctan}\frac{y-1}{y+1}}{y^2\sqrt{y^2-1}} + \frac{4}{y^2} \ln\left(\frac{y}{2}\right) - \frac{2}{y^2-1} + \frac{4\operatorname{arctan}\frac{y-1}{y+1}}{(y^2-1)^{3/2}} & y > 1. \end{cases} \quad (1.152)$$

The \mathcal{F} -flexion for the NFW profile can be computed by taking the derivative of the convergence,

$\mathcal{F} = \nabla_\theta \kappa = \frac{\partial y}{\partial \theta} \frac{\partial}{\partial y} \kappa$, which becomes [43]

$$\mathcal{F}(\theta) = -\frac{2\mathcal{F}_s}{(y^2 - 1)^2} [2yf(y) - f'(y)] e^{i\phi}, \quad (1.153)$$

where we have defined $\mathcal{F}_s \equiv \kappa_s D_d / r_s$, and from Eq. (1.150),

$$f'(y) = \frac{df}{dy} = \begin{cases} \frac{2y}{\sqrt{1-y^2}} \operatorname{arctanh} \sqrt{\frac{1-y}{1+y}} - \frac{1}{y} & y < 1 \\ 0 & y = 1 \\ \frac{2y}{\sqrt{y^2-1}} \operatorname{arctan} \sqrt{\frac{y-1}{y+1}} - \frac{1}{y} & y > 1. \end{cases} \quad (1.154)$$

The \mathcal{G} -flexion can be expressed as [43]

$$\mathcal{G}(\theta) = 2\mathcal{F}_s \left[\frac{8}{y^3} \ln \left(\frac{y}{2} \right) + \frac{\frac{3}{y}(1-2y^2) + h(y)}{(y^2-1)^2} \right] e^{3i\phi} \quad (1.155)$$

where

$$h(y) = \begin{cases} \left(\frac{8}{y^3} - \frac{20}{y} + 15y \right) \frac{2}{\sqrt{1-y^2}} \operatorname{arctanh} \sqrt{\frac{1-y}{1+y}} & y < 1 \\ 0 & y = 1 \\ \left(\frac{8}{y^3} - \frac{20}{y} + 15y \right) \frac{2}{\sqrt{y^2-1}} \operatorname{arctanh} \sqrt{\frac{y-1}{y+1}} & y > 1. \end{cases} \quad (1.156)$$

Directional behavior of shear and flexion

We can study the behavior of the shear and flexion lensing fields by considering the simple example of a source (background) galaxy located at polar angle $\phi = 0$ around the lens. Then, the direction of the field is encoded in the sign of the lensing field amplitude. Around such a lens, there exists “tangential” alignment of galaxy ellipticities, such that the spin-2 shear, for both the SIS and NFW cases, $\gamma < 0$ (again, for $\phi = 0$). \mathcal{F} -flexion, which has the spin properties of a vector, points radially toward the lens, such that $\mathcal{F} < 0$. \mathcal{G} -flexion oscillates around the lens as a spin-3 quantity; however, its behavior could also be described as a type of radial alignment, but where $\mathcal{G} > 0$.

This behavior is illustrated in Fig. 1.9, where we see the “tangential” alignment of shear around

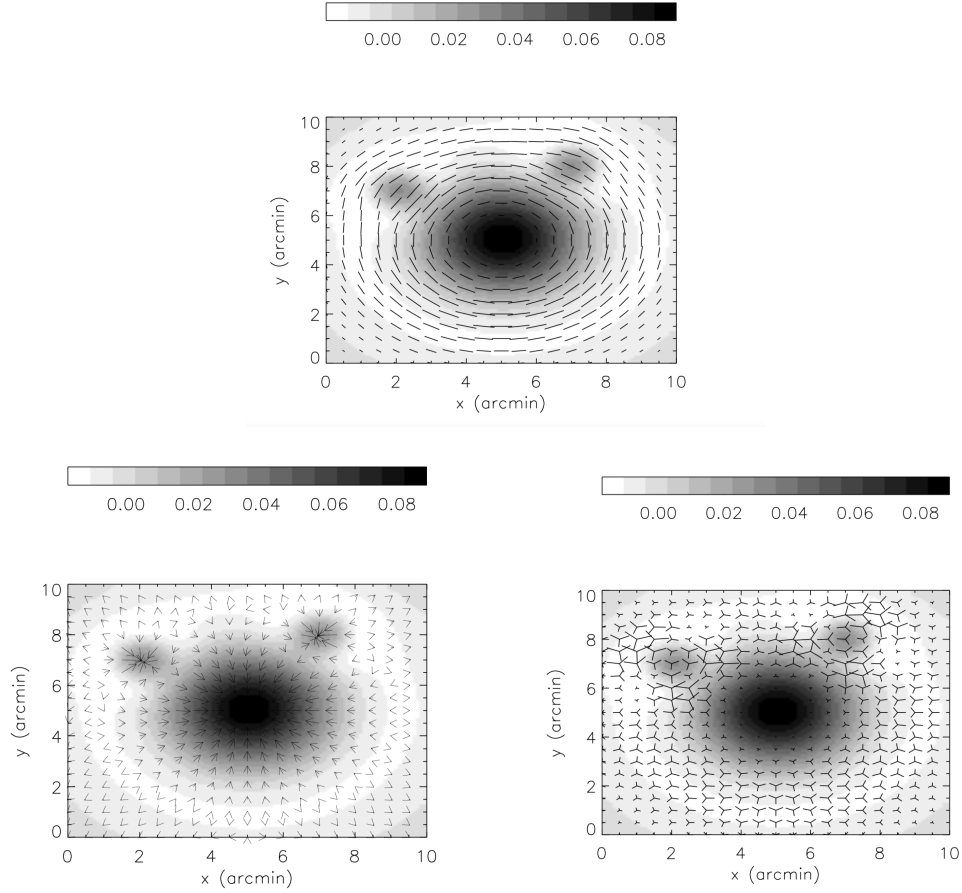


Figure 1.9: Shear (upper), \mathcal{F} -flexion (lower-left) and \mathcal{G} -flexion (lower-right) induced by a simulated galaxy cluster. The cluster's underlying convergence map is plotted underneath the other weak lensing fields. The spin-2 shear field is represented by lines, the spin-1 \mathcal{F} -flexion by arrows (vectors), and the spin-3 \mathcal{G} -flexion by tri-edge markers. Figure adapted from BGRT.

a simulated galaxy cluster lens. The \mathcal{F} -flexion, represented as a vector, points radially *toward* the lens, and the \mathcal{G} -flexion is “radially” aligned (again, as a spin-3 quantity).

1.2.10 Sensitivity of flexion to small scales and substructure

As flexion is a higher-order lensing effect, related to the third derivatives of the lensing potential, it is sensitive to smaller scales than is shear, which is related to the second derivative of the lensing potential.

As an illustrative example of this, we can examine Fig. 1.9. This simulation of a galaxy cluster does not consist of one single dark matter halo; instead, there is a large central halo, as well as

two smaller subhalos. These subhalos represent *substructure* of the galaxy cluster. As we see in the figure, the directional behavior of the shear is such that it is tangentially aligned around the large, central halo, but it does not respond to the small-scale substructure. \mathcal{F} -flexion, on the other hand, is clearly very sensitive to the small-scale substructure. \mathcal{F} -flexion responds *locally* to the density gradient, whereas \mathcal{G} -flexion responds nonlocally while still giving large signals near the substructure.

Flexion has been shown to be a probe of small scales unavailable to shear measurement in various contexts. In Refs. [42, 53], galaxy-galaxy flexion signals were shown to peak at scales smaller than that of galaxy-galaxy shear, in agreement with the SIS and NFW lens models given in Sec. 1.2.9. In various studies of galaxy clusters (see. Refs. [54, 55, 56]), the small-scale structure of subhalos that do not appear through mass reconstruction maps created using shear measurement have been identified through measurements of flexion (see Sec. 1.2.11 for a description of mass reconstruction using weak lensing fields). Finally, as is the subject of most of my work, I will demonstrate that *cosmic flexion* probes the matter power spectrum at much smaller scales than that of cosmic shear (see Sec. 1.3 for an introduction to cosmic shear and cosmic flexion).

1.2.11 Fourier space representation and mass reconstruction

The observable weak lensing fields – shear and flexion – can be related to the lensing convergence field in Fourier space. Remembering that the convergence is also the dimensionless projected mass density, it can then be used to reconstruct a two-dimensional surface density map of the matter distribution that constitutes the lens.

First, we adopt a sign convention where the relationship between the lensing potential in real and Fourier space is given by

$$\psi(\boldsymbol{\theta}) = \frac{1}{(2\pi)^2} \int_0^\infty d^2\ell \tilde{\psi}(\ell) e^{-i\ell \cdot \boldsymbol{\theta}} \iff \tilde{\kappa}(\ell) = \int_0^\infty d^2\theta \kappa(\theta) e^{i\ell \cdot \theta} \quad (1.157)$$

and hence, the derivatives with respect to $\boldsymbol{\theta}$ are given in Fourier space by

$$\frac{\partial}{\partial \theta^i} \psi(\boldsymbol{\theta}) = \psi_{,i}(\boldsymbol{\theta}) \rightarrow i\ell_i \tilde{\psi}(\ell). \quad (1.158)$$

such that the n^{th} derivative corresponds to a factor of $(i\ell_i)^n$. Here, $i \in \{1, 2\}$ and $\boldsymbol{\ell} = (\ell_1, \ell_2)$ is the *two-dimensional wavevector* – the Fourier-conjugate of $\boldsymbol{\theta} = (\theta_1, \theta_2)$.

Taking the Fourier transform of Eq. (1.104), we find that the convergence can be represented in Fourier space via

$$\tilde{\kappa}(\boldsymbol{\ell}) = -\frac{1}{2}\ell^2\tilde{\psi}(\boldsymbol{\ell}) \quad (1.159)$$

where $\ell^2 = \ell_1^2 + \ell_2^2$. By taking the Fourier transform of Eqs. (1.105) and (1.106), we find that $\tilde{\gamma}_1 = -\frac{1}{2}(\ell_1^2 - \ell_2^2)\tilde{\psi}$ and $\tilde{\gamma}_2 = -\ell_1\ell_2\tilde{\psi}$. Relating this to Eq. (1.159), the shear is related to the convergence in Fourier space by [57, 58, 4]²⁵

$$\tilde{\gamma}_1 = \frac{(\ell_1^2 - \ell_2^2)}{\ell^2}\tilde{\kappa}, \quad (1.160)$$

$$\tilde{\gamma}_2 = \frac{2\ell_1\ell_2}{\ell^2}\tilde{\kappa} \quad (1.161)$$

Similarly, by taking the Fourier transform of Eqs. (1.121) - (1.124), we find that²⁶ $\tilde{\mathcal{F}}_1 = -\frac{i}{2}\ell_1\ell^2\tilde{\psi}$, $\tilde{\mathcal{F}}_2 = -\frac{i}{2}\ell_2\ell^2\tilde{\psi}$, $\tilde{\mathcal{G}}_1 = -\frac{i}{2}(\ell_1^3 - 3\ell_1\ell_2^2)\tilde{\psi}$, and $\tilde{\mathcal{G}}_2 = -\frac{i}{2}(3\ell_1^2\ell_2 - \ell_2^3)\tilde{\psi}$. Relating this to Eq. (1.159), the flexion is related to the convergence in Fourier space by (see BGRT and AGB)

$$\tilde{\mathcal{F}}_1 = i\ell_1\tilde{\kappa} \quad (1.162)$$

$$\tilde{\mathcal{F}}_2 = i\ell_2\tilde{\kappa} \quad (1.163)$$

$$\tilde{\mathcal{G}}_1 = \frac{i(\ell_1^3 - 3\ell_1\ell_2^2)}{\ell^2}\tilde{\kappa} \quad (1.164)$$

$$\tilde{\mathcal{G}}_2 = \frac{i(3\ell_1^2\ell_2 - \ell_2^3)}{\ell^2}\tilde{\kappa} \quad (1.165)$$

The relations for shear and flexion can be inverted, and optimized, in order to construct an estimate

²⁵In the literature, k and ℓ are sometimes used interchangeably, as in BGRT. This is simply a matter of notation – in that context, \mathbf{k} is understood to be the 2D Fourier-conjugate of $\boldsymbol{\theta}$ rather than the 3D Fourier-conjugate of \mathbf{x} , as in Eq. (1.30).

²⁶These have the opposite sign convention from that in BGRT. I also correct for a missing factor of two in the \mathcal{G} -flexion, which was first presented in AGB.

for the convergence field:

$$\tilde{\kappa}_\gamma = \frac{\ell_1^2 - \ell_2^2}{\ell^2} \tilde{\gamma}_1 + \frac{2\ell_1\ell_2}{\ell^2} \tilde{\gamma}_2 \quad (1.166)$$

$$\tilde{\kappa}_{\mathcal{F}} = \frac{i\ell_1}{\ell^2} \tilde{\mathcal{F}}_1 + \frac{i\ell_2}{\ell^2} \tilde{\mathcal{F}}_2 \quad (1.167)$$

$$\tilde{\kappa}_{\mathcal{G}} = \frac{i(\ell_1^3 - 3\ell_1\ell_2^2)}{\ell^4} \tilde{\mathcal{G}}_1 + \frac{i(\ell_2^3 - 3\ell_1\ell_2)}{\ell^4} \tilde{\mathcal{G}}_2. \quad (1.168)$$

Such is the prescription of Kaiser and Squires [57] and BGRT: measure the shear and flexion fields, take the Fourier transform, calculate $\tilde{\kappa}$, and then take the inverse Fourier transform to find κ .

1.3 Cosmological Weak Lensing

Cosmological weak lensing refers to gravitational lensing by the large-scale structure of the Universe. In this lens system, background source galaxies are gravitationally lensed by the large-scale structure, characterized by the perturbed FLRW metric, that exists between the source galaxies and us (the observer). As the light from these source galaxies makes its way to us, the path of the light is continuously perturbed by large-scale structure. As such, the thin lens approximation is no longer valid in this context.

1.3.1 The cosmological effective convergence

Here, we consider the propagation of light through an inhomogeneous Universe, described by the perturbed FLRW metric of Eq. (1.27) with Eq. (1.6) (see Refs. [41, 4] for a review). Thus, we will quantify the relation between the deflection of light and the underlying gravitational potential, Φ_N , on cosmological scales. To describe the differential propagation of rays within an infinitesimally thin light bundle, we consider the difference between two neighboring geodesics. In this section, we will again take $\mathbf{x} = (x^1, x^2)$ to refer to physical (i.e. not angular) coordinates on the sky. We take these to be comoving coordinates, such that the coordinate perpendicular to \mathbf{x} is given by the radial comoving coordinate, χ (see Eq. 1.5). In a homogeneous FLRW Universe, the transverse comoving separation, \mathbf{x}_0 , between two light rays as a function of comoving distance from the observer, χ , is

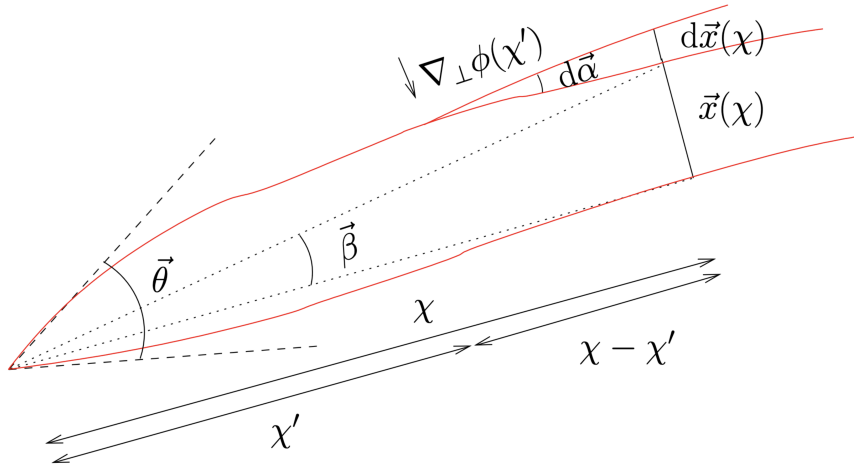


Figure 1.10: Propagation of two light rays converging on an observer on the left. The red line along the bottom is taken to be the “fiducial” light ray, which will be denoted with the superscript (0) , defined by $\theta^{(0)} = 0$. The first light ray is drawn by the red line at the top. While both of these light rays are deflected by a deflector located at χ' from the observer, only the first ray has drawn the path the light would take with and without the presence of the deflector (the bottom and top branches, respectively). In this figure, $x(\chi)$ points from the bottom fiducial ray to the unperturbed top, first ray and $d\vec{x}(\chi)$ points from the unperturbed to the perturbed top first ray. The deflection angle associated with the top ray points in the same direction as $d\vec{x}(\chi)$, in the opposite direction of the transverse gradient of the gravitational potential. The dashed lines indicate the apparent direction of the light rays, converging on the observer at an observed angle θ . The dotted lines show the unperturbed geodesics, defining the angle β under which the unperturbed transverse comoving separation x is seen. Figure adapted from Kilbinger [4].

proportional to the comoving angular distance $f_K(\chi)$ (see Eq. 1.5):

$$\mathbf{x}_0(\chi) = f_K(\chi)\boldsymbol{\theta} \quad (1.169)$$

where the separation vector \mathbf{x}_0 is seen by the observer under the (small) observed angle $\boldsymbol{\theta}$ (previously referred to as the lens plane angle). Using Eq. (1.73), we can express the deflection angle in this comoving frame, such that a light ray is deflected by an amount

$$d\hat{\boldsymbol{\alpha}} = -\frac{2}{c^2} \boldsymbol{\nabla}_{\perp} \Phi_N(\mathbf{x}, \chi') d\chi' \quad (1.170)$$

in the presence of the potential Φ_N (i.e. the “lens”) at a distance of χ' from the observer. From Fig. 1.10, we see that the observer sees the induced change in the separation vector at source comoving distance χ as

$$d\mathbf{x} = f_K(\chi' - \chi) d\hat{\boldsymbol{\alpha}}. \quad (1.171)$$

Lensing deflections modify the paths of both light rays. Denoting the fiducial ray with the superscript (0) , and calculating the total separation by integrating $d\mathbf{x}(\chi)$ along the line of sight χ' , we find

$$\mathbf{x}(\chi) + \int d\mathbf{x} = \mathbf{x}^{(0)}(\chi) + \int d\mathbf{x}^{(0)}. \quad (1.172)$$

Substituting Eqs. (1.169), (1.171), and (1.170), we have

$$\mathbf{x}(\chi) = f_K(\chi)\boldsymbol{\theta} - \frac{2}{c^2} \int_0^\chi d\chi' f_K(\chi - \chi') \left[\boldsymbol{\nabla}_{\perp} \Phi_N(\mathbf{x}(\chi'), \chi') - \boldsymbol{\nabla}_{\perp} \Phi_N^{(0)}(\chi') \right] \quad (1.173)$$

where we have flipped the bounds of integration from those defined in Eq. (1.73) to be from the observer to the source. In the absence of lensing, the separation vector \mathbf{x} would be seen by the observer under an angle $\boldsymbol{\beta} = \mathbf{x}(\chi)/f_K(\chi)$. The difference between the apparent angle, $\boldsymbol{\theta}$, and $\boldsymbol{\beta}$ is

the total scaled deflection angle, α , as defined by the lens equation given by Eq. (1.86). Thus,

$$\boldsymbol{\alpha} = \frac{2}{c^2} \int_0^\chi d\chi' \frac{f_K(\chi - \chi')}{f_K(\chi)} \left[\boldsymbol{\nabla}_\perp \Phi_N(\mathbf{x}(\chi'), \chi') - \boldsymbol{\nabla}_\perp \Phi_N^{(0)}(\chi') \right]. \quad (1.174)$$

Now, assuming that the change of the comoving separation vector between the two actual rays, \mathbf{x} , is small compared to the comoving separation of the unperturbed rays, $\mathbf{x}^{(0)}(\chi) = f_K(\chi)\boldsymbol{\theta}$, i.e.

$$\frac{|\mathbf{x}(\boldsymbol{\theta}, \chi') - f_K(\chi')\boldsymbol{\theta}|}{|f_K(\chi')\boldsymbol{\theta}|} \ll 1, \quad (1.175)$$

we can replace $\mathbf{x}(\boldsymbol{\theta}, \chi')$ by the zeroth-order solution $\mathbf{x}^{(0)}(\chi') = f_K(\chi')\boldsymbol{\theta}$ in the integrand of Eq. (1.174) to arrive at a much simpler expression – this corresponds to the Born approximation of small-angle scattering. Next, we use the definition of the amplification matrix given by Eq. (1.99),

$$\begin{aligned} \mathcal{A}_{ij} &\equiv \frac{\partial \beta_i}{\partial \theta_j} = \delta_{ij} - \frac{\partial \alpha_i}{\partial \theta_j} \\ &= \delta_{ij} - \frac{2}{c^2} \int_0^\chi \frac{\partial}{\partial \theta_j} \left(d\chi' \frac{f_K(\chi - \chi')}{f_K(\chi)} \boldsymbol{\nabla}_\perp \Phi_N(f_K(\chi')\boldsymbol{\theta}, \chi') \right) \end{aligned} \quad (1.176)$$

where we have noted that $\frac{\partial}{\partial \theta_j} \left(\boldsymbol{\nabla}_\perp \Phi_N^{(0)}(\chi') \right) = 0$, since $\Phi_N^{(0)}(\chi')$ does not depend on $\boldsymbol{\theta}$. Next, we note that the relationship between the gradient with respect to angle on the sky and the gradient with respect to physical distance is given by

$$\partial_i = \frac{\partial}{\partial \theta_i} = f_K(\chi) \frac{\partial}{\partial x_i} \iff \frac{\partial}{\partial x_i} = \frac{1}{f_K(\chi)} \frac{\partial}{\partial \theta_i}. \quad (1.177)$$

This allows us to write

$$\mathcal{A}_{ij} = \delta_{ij} - \frac{2}{c^2} \int_0^\chi d\chi' \frac{f_K(\chi - \chi')}{f_K(\chi)f_K(\chi')} \frac{\partial^2}{\partial \theta_i \partial \theta_j} \Phi_N(f_K(\chi')\boldsymbol{\theta}, \chi'). \quad (1.178)$$

Furthermore, recognizing that from Eq. (1.99), $\mathcal{A}_{ij} = \delta_{ij} - \frac{\partial^2 \psi(\boldsymbol{\theta})}{\partial \theta_i \partial \theta_j}$, we can write the lensing potential

as

$$\psi(\boldsymbol{\theta}, \chi) = \frac{2}{c^2} \int_0^\chi d\chi' \frac{f_K(\chi - \chi')}{f_K(\chi)f_K(\chi')} \Phi_N(f_K(\chi')\boldsymbol{\theta}, \chi'). \quad (1.179)$$

Now, we recall that, in the thin lens approximation, the convergence and lensing potential are related by (see Eq. 1.104) $\kappa(\boldsymbol{\theta}) = \frac{1}{2} \frac{\partial^2}{\partial \theta_i \partial \theta_i} \psi(\boldsymbol{\theta})$, where the summation over (i) is implied. In exact analogy, an effective convergence can be defined for cosmological weak lensing – the *cosmological effective convergence*:

$$\kappa_{\text{eff}}(\boldsymbol{\theta}, \chi) = \frac{1}{c^2} \int_0^\chi d\chi' \frac{f_K(\chi - \chi')}{f_K(\chi)f_K(\chi')} \frac{\partial^2}{\partial \theta_i \partial \theta_i} \Phi_N(f_K(\chi')\boldsymbol{\theta}, \chi'). \quad (1.180)$$

Now, using Eq. (1.177), $\frac{\partial}{\partial \theta_i} \Phi_N(f_K(\chi')\boldsymbol{\theta}, \chi') = f_K(\chi') \frac{\partial}{\partial x_i} \Phi_N(f_K(\chi')\boldsymbol{\theta}, \chi')$, and hence we can write

$$\kappa_{\text{eff}}(\boldsymbol{\theta}, \chi) = \frac{1}{c^2} \int_0^\chi d\chi' \frac{f_K(\chi - \chi')f_K(\chi')}{f_K(\chi)} \frac{\partial^2}{\partial x_i \partial x_i} \Phi_N(f_K(\chi')\boldsymbol{\theta}, \chi'). \quad (1.181)$$

Now, since the convergence is related to the lensing potential via the two-dimensional Poisson equation, it can be interpreted as a projected surface density. We can apply the two-dimensional Laplacian of the lensing potential to the three-dimensional potential Φ_N and add the second-order derivative along the comoving coordinate, $\frac{\partial^2}{\partial \chi^2}$, such that

$$\nabla^2 = \frac{\partial^2}{\partial x_1^2} + \frac{\partial^2}{\partial x_2^2} + \frac{\partial^2}{\partial \chi^2}. \quad (1.182)$$

This additional term $\frac{\partial^2}{\partial \chi^2}$ vanishes, since positive and negative contributions cancel out to a good approximation when integrating along the line of sight. Thus,

$$\kappa_{\text{eff}}(\boldsymbol{\theta}, \chi) = \frac{1}{c^2} \int_0^\chi d\chi' \frac{f_K(\chi - \chi')f_K(\chi)}{f_K(\chi)} \nabla^2 \Phi_N(f_K(\chi')\boldsymbol{\theta}, \chi'). \quad (1.183)$$

Now, we recognize that the term $\nabla^2 \Phi_N$ in the above expression is the left-hand side of the Poisson equation. In terms of the matter overdensity only, the Poisson equation of Eq. (1.34) is given by Eq. (1.46). From Eqs. (1.12) and (1.15), we know that $\rho_m = \Omega_m \rho_{\text{crit},0}/a^3$, and from Eq. (1.14), $4\pi G \rho_{\text{crit},0} = 3H_0^2/2$. Then, taking the inverse Fourier transform, the Poisson equation in real space

can be expressed as

$$\nabla^2 \Phi_N = \frac{3}{2} \Omega_m H_0^2 a^{-1} \Delta. \quad (1.184)$$

where Δ is the comoving total matter density perturbation. Substituting this into Eq. (1.183), the cosmological effective convergence can be written as

$$\kappa_{\text{eff}}(\boldsymbol{\theta}, \chi) = \frac{3}{2} \Omega_m \left(\frac{H_0}{c} \right)^2 \int_0^\chi d\chi' \frac{f_K(\chi - \chi') f_K(\chi)}{f_K(\chi) a(\chi')} \Delta(f_K(\chi') \boldsymbol{\theta}, \chi'). \quad (1.185)$$

Eq. (1.185) gives the cosmological effective convergence for a fixed source redshift corresponding to the comoving distance χ . When the sources are distributed in comoving distance, the cosmological effective convergence needs to be averaged over the (normalized) source distribution, $n(\chi)$, such that

$$\int_0^\infty d\chi n(\chi) = 1. \quad (1.186)$$

This is to say that

$$\kappa_{\text{eff}}(\boldsymbol{\theta}) = \int_0^{\chi_H} d\chi n(\chi) \kappa_{\text{eff}}(\boldsymbol{\theta}, \chi) \quad (1.187)$$

where χ_H is the horizon distance, defined as the comoving distance obtained for infinite redshift.

This allows us to write

$$\kappa_{\text{eff}}(\boldsymbol{\theta}) = \frac{3}{2} \Omega_m \left(\frac{H_0}{c} \right)^2 \int_0^{\chi_H} d\chi n(\chi) \int_\chi^{\chi_H} d\chi' \frac{f_K(\chi - \chi') f_K(\chi)}{f_K(\chi) a(\chi')} \Delta(f_K(\chi') \boldsymbol{\theta}, \chi'). \quad (1.188)$$

where we have rearranged the bounds of integration. By defining the *lensing efficiency function*,

$$q(\chi) = \frac{3}{2} \Omega_m \left(\frac{H_0}{c} \right)^2 \frac{f_K(\chi)}{a(\chi)} \int_\chi^{\chi_H} d\chi' n(\chi') \frac{f_K(\chi' - \chi)}{f_K(\chi')}, \quad (1.189)$$

we can express the cosmological effective convergence as

$$\kappa_{\text{eff}}(\boldsymbol{\theta}) = \int_0^{\chi_H} d\chi q(\chi) \Delta(f_K(\chi') \boldsymbol{\theta}, \chi'). \quad (1.190)$$

The cosmological effective convergence therefore describes the matter density, projected along the line of sight, and depends on a given cosmology.

1.3.2 Cosmic shear

In cosmology, we are interested in statistical descriptions of underlying physical quantities. After all, we simply can't know the value of the matter overdensity at every location in the Universe at every point in time. In practice, measurements of large-scale structures are compressed into statistics, such as the matter-power spectrum.

Here, we are interested in the statistics of the cosmological effective convergence. By definition, the expectation value of the matter overdensity, $\langle \Delta \rangle = 0$. As such, the expectation value of the cosmological effective convergence vanishes as well. Therefore, the first non-trivial statistical measure of the distribution of the convergence is the second moment.

Let us first discuss the second moment of the distribution of convergence in real, or “configuration,” space. Imagine two positions on the sky, separated by some distance $\boldsymbol{\theta}$. These two positions can then be described by $\boldsymbol{\vartheta}$ and $\boldsymbol{\vartheta} + \boldsymbol{\theta}$. The basic second-order function of Eq. (1.190) is then $\langle \kappa(\boldsymbol{\vartheta})\kappa(\boldsymbol{\vartheta} + \boldsymbol{\theta}) \rangle$, where the brackets denote an ensemble average which can be replaced by a spatial average over angular separation $\boldsymbol{\theta}$. A second-order function of this kind is known as a *two-point correlation function* (2PCF). As a consequence of the cosmological principle – i.e. the matter overdensity field, Δ , is homogeneous and isotropic on large scales – so too is the cosmological effective convergence. Therefore, the convergence 2PCF is invariant under translation and rotation, depending only on θ – the modulus of the separation vector between two lines of sight.

Expressed in Fourier-space, the 2PCF can be interpreted as an expression of the variance of the modes $\tilde{\kappa}(\boldsymbol{\ell})$. As we know from Eq. (1.42), this can be used to define the *convergence power spectrum*

$$\langle \tilde{\kappa}(\boldsymbol{\ell})\tilde{\kappa}^*(\boldsymbol{\ell}') \rangle = (2\pi)^2 \delta_D(\boldsymbol{\ell} - \boldsymbol{\ell}') \mathcal{P}_\kappa(\boldsymbol{\ell}) \quad (1.191)$$

where again, due to statistical homogeneity and isotropy, the convergence power spectrum depends only on the modulus of the two-dimensional wavevector $\boldsymbol{\ell}$.

Limber's equation/approximation states that, for two quantities, g_a and g_b of the form $g_a = \int_0^{\chi_H} d\chi h_a(\chi) X(f_K(\chi)\boldsymbol{\theta}, \chi)$ where X is some field – e.g. the density contrast – the cross-power spectrum of g_a and g_b is [41, 59, 60]

$$\mathcal{P}_{ab}(\ell) = \int_0^{\chi_H} d\chi \frac{h_a(\chi)h_b(\chi)}{f_K^2(\chi)} \mathcal{P}_X \left(k = \frac{\ell + 1/2}{f_K(\chi)}, \chi \right). \quad (1.192)$$

It should be noted that, in addition to the Limber approximation whereby correlations of modes along the line of sight are neglected, and we only consider correlations in the plane of the sky, we are also assuming the small-angle approximation and the flat-sky approximation.

If one sets $h_a = h_b = q(\chi)$ in the Limber equation, we obtain an expression for the convergence power spectrum

$$\mathcal{P}_\kappa(\ell) = \int_0^{\chi_H} d\chi \frac{q^2(\chi)}{f_K^2(\chi)} \mathcal{P}_\Delta \left(k = \frac{\ell + 1/2}{f_K(\chi)}, \chi \right) \quad (1.193)$$

where $\mathcal{P}_\Delta(k, z)$ is the (nonlinear) matter power spectrum.

From Eqs. (1.160) and (1.161), we can write

$$\tilde{\gamma}(\boldsymbol{\ell}) = \frac{(\ell_1 + i\ell_2)^2}{\ell^2} \tilde{\kappa}(\boldsymbol{\ell}) = e^{2i\beta} \tilde{\kappa}(\boldsymbol{\ell}) \quad (1.194)$$

where we have used the fact that $\ell_1 = \ell \cos \beta$ and $\ell_2 = \ell \sin \beta$ along with Euler's formula, such that β is the polar angle of $\boldsymbol{\ell}$. From this, we see that $\langle \tilde{\gamma}(\boldsymbol{\ell}) \tilde{\gamma}^*(\boldsymbol{\ell}') \rangle = \langle \tilde{\kappa}(\boldsymbol{\ell}) \tilde{\kappa}^*(\boldsymbol{\ell}') \rangle$ and therefore, by Eq. (1.193)

$$\mathcal{P}_\gamma(\ell) = \mathcal{P}_\kappa(\ell) \quad (1.195)$$

that is, the shear power spectrum is equivalent to the convergence power spectrum.

The fact that there exists a shear power spectrum, which can be understood in real space as a shear two-point correlation function, implies the existence of a coherent shear signal arising from the large-scale structure of the Universe. This measurable signal is known as *cosmic shear*. As will be discussed in Chapter 3, this signal is typically measured in real space on pairs of galaxies.

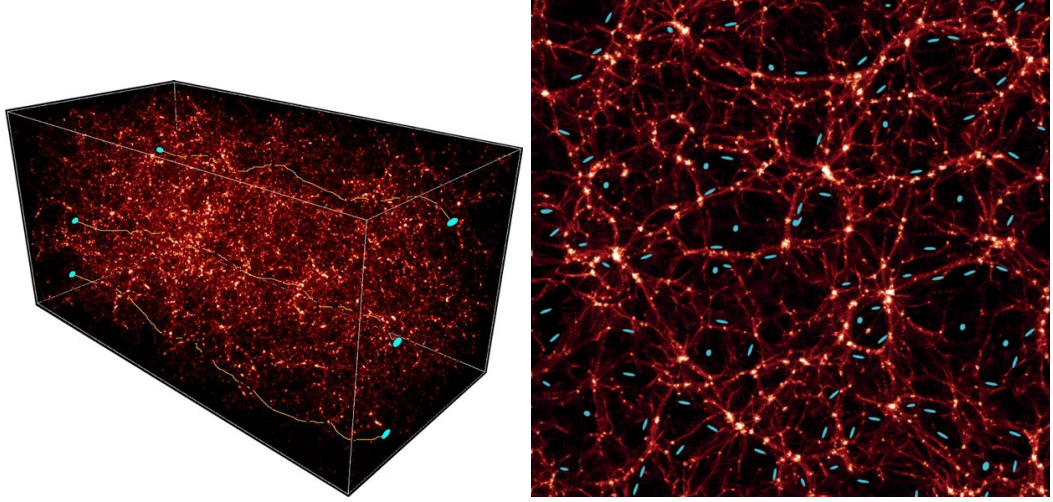


Figure 1.11: Cartoon of cosmic shear: gravitational lensing of source galaxies by large-scale structure causes coherent, tangential alignment of galaxy ellipticities around large-scale structure matter overdensities. Figure adapted from Karouzos [5].

1.3.3 Cosmic flexion

Just as there is a coherent shear signal arising from large-scale structure, so too should there be a flexion signal. Here, we wish to obtain the cosmic flexion power spectrum (see BGRT and AGB). Making use of the definition of flexion given by Eq. (1.119) – i.e.

$$\mathcal{F}_i = \partial_i \kappa = \frac{\partial}{\partial \theta_i} \kappa = f_K(\chi) \frac{\partial}{\partial x_i} \kappa, \quad (1.196)$$

the cosmological effective flexion can be obtained from the cosmological effective convergence of Eq. (1.185):

$$\mathcal{F}_{\text{eff}}(\boldsymbol{\theta}, \chi) = \frac{3}{2} \Omega_{m,0} \left(\frac{H_0}{c} \right)^2 \int_0^\chi d\chi' \frac{f_K(\chi - \chi') f_K(\chi')}{f_K(\chi) a(\chi')} f_K(\chi') \Delta'(f_K(\chi') \boldsymbol{\theta}, \chi') \quad (1.197)$$

where Δ' is the transverse gradient of the density contrast. We therefore obtain

$$\mathcal{F}_{\text{eff}}(\boldsymbol{\theta}) = \int_0^{\chi_H} d\chi q(\chi) \Delta'(f_K(\chi) \boldsymbol{\theta}, \chi). \quad (1.198)$$

This time, we set $h_a = h_b = f_K(\chi)q(\chi)$ and obtain, via Limber's equation,

$$\begin{aligned}\mathcal{P}_{\mathcal{F}}(\ell) &= \int_0^{\chi_H} d\chi q^2(\chi) \mathcal{P}_{\Delta'} \left(k = \frac{\ell + 1/2}{f_K(\chi)}, \chi \right) \\ &= \ell^2 \mathcal{P}_\kappa(\ell)\end{aligned}\tag{1.199}$$

where we have noted that $|X'|^2 = |X|^2 k_i k^i$, and hence (taking $k = (\ell + 1/2)/f_K(\chi) \approx \ell/f_K(\chi)$) [43]

$$\mathcal{P}_{X'} \left(\frac{\ell}{f_K(\chi), \chi} \right) = \mathcal{P}_X \left(\frac{\ell}{f_K(\chi), \chi} \right) \frac{\ell^2}{f_K^2(\chi)}. \tag{1.200}$$

In addition to the cosmic-flexion power spectrum, we can also obtain the convergence-flexion cross spectrum (see BGRT and AGB). We again use Limber's equation, but this time, we work in terms of \mathcal{P}_Δ rather than $\mathcal{P}_{\Delta'}$. We set $h_\kappa = q(\chi)\Sigma(a(\chi))$ and $h_{\mathcal{F}} = q(\chi)\Sigma(a(\chi))\ell$ to obtain

$$\mathcal{P}_{\kappa\mathcal{F}}(\ell) = \ell \mathcal{P}_\kappa(\ell). \tag{1.201}$$

We note that, owing to the fact that shear and convergence statistics are the same – i.e. $\mathcal{P}_\gamma(\ell) = \mathcal{P}_\kappa(\ell)$ [4] – so too (because of the relations in Eq. 1.120) are the \mathcal{F} - and \mathcal{G} -flexion power spectra,

$$\mathcal{P}_{\mathcal{G}}(\ell) = \mathcal{P}_{\mathcal{F}}(\ell), \tag{1.202}$$

and similarly,

$$\mathcal{P}_{\kappa\mathcal{G}}(\ell) = \mathcal{P}_{\kappa\mathcal{F}}(\ell). \tag{1.203}$$

From this point on, I refer to the flexion power spectra and convergence-flexion cross spectra as a family of signals known as *cosmic flexion*. The bulk of this thesis contains the first full consideration of cosmic flexion as a probe of the small-scale matter power spectrum. In Chapter 3, I will present a full theoretical formalism for cosmic flexion, including real-space observables, as first laid out in my paper AGB. In Chapter 4, I present the first-ever measurement of cosmic flexion.

.....0.....

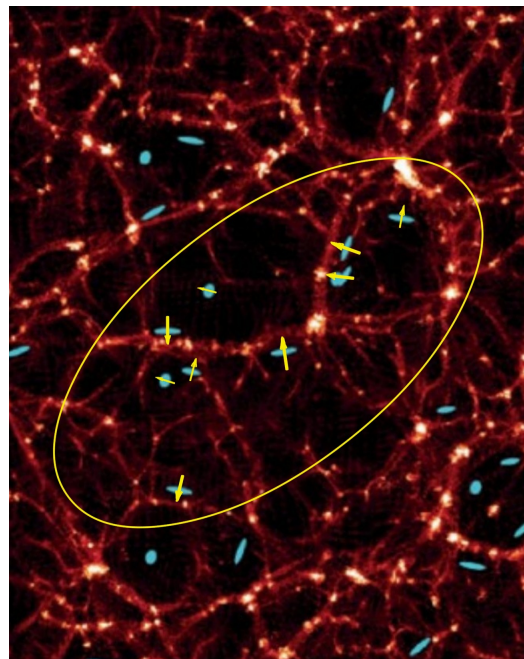


Figure 1.12: Cartoon of cosmic flexion: gravitational lensing of source galaxies by large-scale structure causes coherent, radial alignment of \mathcal{F} -flexion (represented here as vectors) around large-scale structure matter overdensities.

Chapter 2: Measuring lensing: Lenser

2.1 Measuring weak gravitational lensing

As discussed in Chapter 1, Sec. 1.2.8 in particular, in order to measure the effect of gravitational lensing, one needs to be able to measure the shapes of individual galaxies.¹ Here, *shape* refers to the combination of intrinsic ellipticity and flexion effects, as well as lensing shear and flexion effects.

In order to reconstruct an underlying weak gravitational lensing shear field, for example, this involves measuring the observed ellipticities of individual galaxies. The measurement of galaxy ellipticities has been well studied for nearly three decades. Methods for measuring ellipticity have traditionally included image moment analysis of the light distribution (see e.g. Bartelmann and Schneider [41]) and parameterized model fitting [63, 64, 65, 66, 67, 68, 69, 70, 71]. State-of-the-art measurement techniques, such as METACALIBRATION [72, 73] rely less on prior information about galaxy properties and do not require calibration from simulations.

Various methods of ellipticity measurement exist, with varying levels of accuracy and applicability, because of the fact that the measurement of a galaxy’s shape is not trivial. As we have discussed, a galaxy will have some unknown intrinsic shape, which is altered by gravitational lensing. This alone, however, is not what our observation of the galaxy looks like through a telescope. As the light from the galaxy passes through the telescope, the image is smeared. As an illustrative example of this, stars are understood to be point sources of light but appear as a smeared image when viewed through a telescope. We understand this smearing as a kernel, known as a point-spread function (PSF), that is convolved with the image of a star or galaxy. To complicate matters further, PSF effects are more pronounced for ground-based telescopes (as opposed to space-based), as the Earth’s atmosphere adds an additional smearing to the image. The sky also adds a roughly constant “background” noise to the image, for both space-based and ground-based telescopes. After the light passes

¹There do exist measurement techniques to infer a shear field that do not rely on a per-galaxy shape measurement, such as the Bayesian Fourier Domain method [61] or that of Schneider et al. [62]. In this thesis, I consider only shape measurement techniques for both shear and flexion.

through the telescope’s optics, it is collected by the instrument’s charged-coupling device (CCD) detector. The CCD sums the photons falling in each square detector element (pixel). While the CCD allows for galaxy images to be saved as digital images, it also pixelates said images. The CCD also introduces additional forms of noise in the image: Poisson noise, owing to the discrete nature of the photons arriving in each pixel; as well as Gaussian noise due to detector effects. Therefore, the observed shape of a galaxy as viewed through a telescope is influenced by its intrinsic shape, gravitational lensing, PSF convolution, noise, and pixelation. At the per-galaxy level, one can measure the observed shape (intrinsic shape plus lensing) of a galaxy to within a specific confidence, dictated by the noise and PSF effects within an image as well as a measurement technique’s ability to account for said effects.

2.2 Flexion Measurement

Studies on weak gravitational lensing flexion have made use of several techniques for per-galaxy flexion measurement. This has included moment analysis of light distribution [44, 74], decomposing images into “shaplet” basis sets [42, 74, 75], and exploring the local potential field through a forward-modeling, parameterized ray tracing known as Analytic Image Modeling (AIM) [55]. While flexion measurement techniques have existed for some time, ellipticity measurement long predates and has been much more well studied than that of flexion measurement.

In 2020, I – with contributions from Dr. Dave Goldberg and Dr. Joseph Fabritius II – publicly released a flexion measurement code called **Lenser**,² coinciding with the publication of Fabritius II et al. [50]. We wanted to address a need in the flexion community for a robust, fast, open-source, accessible Python tool that draws on the strengths of the most successful flexion measurement techniques.

Lenser is capable of measuring lensing signals from real survey data or realistically simulated images. The module forward models second-order lensing effects, performs a PSF convolution, and minimizes a parameter space. **Lenser** is intended as a hybrid approach, first using a moment analysis to localize a best-fit lensing model in parameter space and then performing a local minimization

²<https://github.com/DrexelLenser/Lenser>

on the model parameters (seven lensing potential parameters, six shape parameters) based on the AIM technique. Since the AIM technique relies on a local-minimization of a nominally thirteen-dimensional parameter space, I utilize image moments as an initial guess to ensure that the pipeline converges quickly. I present the details of this measurement technique in the following sections, include tests of its accuracy, and summarize updates that have been made to the code since its initial release.

2.2.1 Analytic Image Modeling (AIM)

Analytic Image Modeling (AIM) analysis explores lensing effects on simulated source galaxy images in real space through parameterized ray tracing [55]. From Liouville’s theorem (see Eq. 1.97), we know that gravitational lensing conserves surface brightness, which allows us to relate an observed surface brightness distribution in the lens plane at a lensing-plane coordinate position θ – i.e I , to the surface brightness distribution in the source plane at a source-plane coordinate position β , i.e. $I^{(s)}$:

$$I[\theta] = I^{(s)}[\beta(\theta)], \quad (2.1)$$

where $\beta(\theta)$ is the lensing coordinate transformation. The unlensed intensity profile of a galaxy can be well described by a particular model with a corresponding set of model parameters, $\{p_{\text{gal}}\}$ [76, 77]. The lensed model image is then

$$I_{\text{mod}}[\theta; \{p_{\text{gal}}\}, \{p_{\text{lens}}\}] = I^{(s)}[\beta(\theta, \{p_{\text{lens}}\}), \{p_{\text{gal}}\}] \quad (2.2)$$

where $\{p_{\text{lens}}\}$ is the parameter space of the lensing transformation. In Fabritius II et al. [50], we introduce a novel, generalized intensity profile for modeling galaxies, which is simply a modified Sérsic-type intensity profile (see Appendix A for a derivation):

$$I(\theta) = I_0 \exp \left[- \left(\frac{\theta'}{\theta_s} \right)^{1/n_s} \right], \quad (2.3)$$

where I_0 is the central brightness, θ_s is the “characteristic” radius, n_s is the Sérsic index (a measure

of curve steepness), and the radial coordinate θ' is given by

$$\theta' = \sqrt{(x/q)^2 + y^2}, \quad (2.4)$$

where x and y are the centroid-subtracted source-plane coordinates rotated appropriately by an orientation angle ϕ :

$$\begin{pmatrix} x \\ y \end{pmatrix} = \begin{pmatrix} [\beta_1(\theta_1 - \theta_0^1)]' \\ [\beta_2(\theta_2 - \theta_0^2)]' \end{pmatrix} = \begin{pmatrix} \cos \phi & \sin \phi \\ -\sin \phi & \cos \phi \end{pmatrix} \begin{pmatrix} \beta_1 \\ \beta_2 \end{pmatrix} \quad (2.5)$$

and where q is the semimajor-to-semiminor axis ratio of the galaxy ³. We recall that we can relate the unlensed and lensed coordinates by Eq. (1.130).

Equations 1.130, 2.3, as well as the centroid (θ_0^1, θ_0^2) , q , and ϕ , create a thirteen-parameter space to describe a galaxy (seven lensing potential parameters, six shape parameters). Recognizing the existence of the shear/ellipticity degeneracy, we initially set shear to zero ($\psi_{ij} = 0$) and absorb the degenerate parameters into the intrinsic ellipticity described by q and ϕ . In the context of smoothed mass mapping, the inferred shear can be used as a prior. This leaves us with a ten-parameter space given by

$$\{p_i\} = \{\theta_0^1, \theta_0^2, n_s, \theta_s, q, \phi, \psi_{,111}, \psi_{,112}, \psi_{,122}, \psi_{,222}\}.$$

2.2.2 Image moment analysis

In terms of the galaxy brightness distribution $I(\theta)$, assuming the galaxy image is isolated, the unweighted *raw* moments of the galaxy surface brightness are given by

$$M_{ij\dots k} = \int d^2\theta I(\theta) \theta_i \theta_j \dots \theta_k \quad (2.6)$$

³ $\theta' = \theta$ therefore corresponds to a circularly symmetric galaxy in the limit of no lensing.

With the raw moments, one can calculate the image centroid (θ_0^1, θ_0^2) as:

$$\begin{aligned}\theta_0^1 &= \frac{M_{10}}{M_{00}} \\ \theta_0^2 &= \frac{M_{01}}{M_{00}}\end{aligned}\quad (2.7)$$

where $M_{00} = \int d^2\theta I(\theta)$ is the unweighted integrated flux. The central moments are defined to be centroid-subtracted $\mu_{ij\dots k} = \int d^2\theta I(\theta)(\theta_i - \theta_0^i)(\theta_j - \theta_0^j) \cdots (\theta_k - \theta_0^k)$. We make use of the normalized central brightness moments $Q_{ij\dots k} \equiv \mu_{ij\dots k}/M_{00}$:

$$Q_{ij\dots k} = \frac{\int d^2\theta I(\theta)(\theta_i - \theta_0^i)(\theta_j - \theta_0^j) \cdots (\theta_k - \theta_0^k)}{\int d^2\theta I(\theta)} \quad (2.8)$$

It is possible to construct estimates of the remaining parameters in the Sérsic profile from image moments as well. A galaxy's ellipticity is a combination of q and ϕ that depends on the quadrupole moments. We can decompose q and ϕ using either of the following definitions of the ellipticity:

$$\epsilon = \frac{q-1}{q+1} e^{2i\phi} \quad (2.9)$$

$$\bar{\chi} = \frac{q^2-1}{q^2+1} e^{2i\phi} \quad (2.10)$$

In `Lenser`, I make use of the *complex ellipticity* [41]

$$\bar{\chi} \equiv \bar{\chi}_1 + i\bar{\chi}_2 = \frac{Q_{11} - Q_{22} + 2iQ_{12}}{Q_{11} + Q_{22}}. \quad (2.11)$$

Hence, we can construct an estimate of q in terms of image moments:

$$q = \sqrt{\frac{1 + \bar{\chi}^* \bar{\chi}}{1 - \bar{\chi}^* \bar{\chi}}}; \quad (2.12)$$

as well as an estimate of ϕ :

$$\phi = \frac{1}{2} \arctan \left(\frac{\bar{\chi}_2}{\bar{\chi}_1} \right) = \frac{1}{2} \arctan \left(\frac{2Q_{12}}{Q_{11} - Q_{22}} \right). \quad (2.13)$$

In Fabritius II et al. [50], I was able to find a relationship between n_s , θ_s , q , and image moments.

We start by quantifying the *size* of a galaxy image by

$$a \equiv \sqrt{|Q_{11} + Q_{22}|}. \quad (2.14)$$

Using this definition, the relationship between these quantities, which I refer to as the *quadrupole-Sérsic relation*, is given by

$$\theta_s = a \sqrt{\frac{2}{1+q^2} \frac{\Gamma(2n_s)}{\Gamma(4n_s)}} = \sqrt{\frac{2(|Q_{11} + Q_{22}|)\Gamma(2n_s)}{(1+q^2)\Gamma(4n_s)}}, \quad (2.15)$$

which I derive in Appendix B.

We now have estimates for all of the galaxy parameters, so let us turn to the lensing parameters. As stated above, there exists a degeneracy between shear and ellipticity. For this reason, it is not necessary to estimate the ψ_{ij} terms directly from the image moments. Flexion, however, is related to the octupole and hexadecapole moments. Estimators of the flexion can be found by the following inversion[44, 74]

$$\mathcal{M} \begin{pmatrix} \mathcal{F}_1 \\ \mathcal{F}_2 \\ \mathcal{G}_1 \\ \mathcal{G}_2 \end{pmatrix} = \begin{pmatrix} \zeta_1 \\ \zeta_2 \\ \delta_1 \\ \delta_2 \end{pmatrix} \quad (2.16)$$

where the HOLICs are defined as⁴

$$\zeta \equiv \frac{(Q_{111} + Q_{222}) + i(Q_{112} + Q_{222})}{\xi} \quad (2.17)$$

$$\delta \equiv \frac{(Q_{111} - 3Q_{122}) + i(3Q_{112} - Q_{222})}{\xi} \quad (2.18)$$

$$\xi \equiv Q_{1111} + 2Q_{1122} + Q_{2222}.$$

⁴Note that if a galaxy is otherwise perfectly circular (i.e. no ellipticity), and in the absence of noise, then the HOLICs may be directly related to estimators of the flexion: $\mathcal{F} \simeq \frac{4\zeta\xi}{9\xi - 6(Q_{11}^2 + Q_{22}^2)}$ and $\mathcal{G} \simeq \frac{4\delta}{3}$

and the matrix elements are

$$\begin{aligned}
\mathcal{M}_{11} &= \frac{1}{4}(9 + 8\eta_1) - \frac{33Q_{11}^2 + 14Q_{11}Q_{22} + Q_{22}^2 + 20Q_{12}^2}{4\xi} \\
\mathcal{M}_{12} &= 2\eta_2 - \frac{32Q_{12}Q_{22} + 32Q_{11}Q_{12}}{4\xi} \\
\mathcal{M}_{13} &= \frac{1}{4}(2\eta_1 + \lambda_1) - \frac{3Q_{11}^2 - 2Q_{11}Q_{22} - Q_{22}^2 - 4Q_{12}^2}{4\xi} \\
\mathcal{M}_{14} &= \frac{1}{4}(2\eta_2 + \lambda_2) - \frac{2Q_{11}Q_{12}}{\xi} \\
\mathcal{M}_{21} &= 2\eta_2 - \frac{32Q_{12}Q_{22} + 32Q_{11}Q_{12}}{4\xi} \\
\mathcal{M}_{22} &= \frac{1}{4}(-8\eta_1 + 9) - \frac{Q_{11}^2 + 14Q_{11}Q_{22} + 20Q_{12}^2 + 33Q_{22}^2}{4\xi} \\
\mathcal{M}_{23} &= \frac{1}{4}(-2\eta_2 + \lambda_2) - \frac{-2Q_{12}Q_{22}}{\xi} \\
\mathcal{M}_{24} &= \frac{1}{4}(2\eta_1 - \lambda_1) - \frac{Q_{11}^2 + 4Q_{12}^2 + Q_{11}Q_{22} - 3Q_{22}^2}{4\xi} \\
\mathcal{M}_{31} &= \frac{1}{4}(10\eta_1 + 7\lambda_1) - \frac{3(11Q_{11}^2 - 10Q_{11}Q_{22} - Q_{22}^2 - 20Q_{12}^2)}{4\xi} \\
\mathcal{M}_{32} &= \frac{1}{4}(-10\eta_2 + 7\lambda_2) - \frac{3(8Q_{11}Q_{12} - 32Q_{12}Q_{22})}{4\xi} \\
\mathcal{M}_{33} &= \frac{3}{4} - \frac{3(-2Q_{11}Q_{22} + Q_{11}^2 + Q_{22}^2 + 4Q_{12}^2)}{4\xi} \\
\mathcal{M}_{34} &= 0 \\
\mathcal{M}_{41} &= \frac{1}{4}(10\eta_2 + 7\lambda_2) - \frac{3(32Q_{11}Q_{12} - 8Q_{12}Q_{22})}{4\xi} \\
\mathcal{M}_{42} &= \frac{1}{4}(10\eta_1 - 7\lambda_1) - \frac{3(Q_{11}^2 + 20Q_{12}^2 + 10Q_{11}Q_{22} - 11Q_{22}^2)}{4\xi} \\
\mathcal{M}_{43} &= 0 \\
\mathcal{M}_{44} &= \frac{3}{4} - \frac{3(-2Q_{11}Q_{22} + Q_{11}^2 + Q_{22}^2 + 4Q_{12}^2)}{4\xi}
\end{aligned} \tag{2.19}$$

where

$$\eta \equiv \frac{(Q_{1111} - Q_{2222}) + 2i(Q_{1112} + Q_{1222})}{\xi} \tag{2.20}$$

$$\lambda \equiv \frac{(Q_{1111} - 6Q_{1122} + Q_{2222}) + 4i(Q_{1112} - Q_{12222})}{\xi}. \tag{2.21}$$

Therefore, we estimate the ψ_{ijk} terms as

$$\psi_{,111} = \frac{1}{2}(3\mathcal{F}_1 + \mathcal{G}_1) \quad (2.22)$$

$$\psi_{,112} = \frac{1}{2}(\mathcal{F}_2 + \mathcal{G}_2) \quad (2.23)$$

$$\psi_{,122} = \frac{1}{2}(\mathcal{F}_1 - \mathcal{G}_1) \quad (2.24)$$

$$\psi_{,222} = \frac{1}{2}(3\mathcal{F}_2 - \mathcal{G}_2). \quad (2.25)$$

Finally, it is important to note that the image moment analysis presented here, and implemented in `Lenser`, does not account for the PSF. The PSF is handled in the AIM portion of the `Lenser` pipeline, and we take the image moments to be an approximate estimate of the parameter space.

2.3 Lenser pipeline

In the following subsections, I present an overview of the `Lenser` pipeline.

2.3.1 Installing Lenser

To install `Lenser`, one can `git pull` from the `Lenser` homepage at:

<https://github.com/DrexelLenser/Lenser>

Additional documentation can be found at the `Lenser` homepage as well.

2.3.2 Overview of Lenser structure: modules and classes

Below is a list of the modules in `Lenser`, along with a description of their most important classes and functions:

- `lenser_fits.py` module: Takes galaxy science images as an input.
 - `FITS()` class: Prepares galaxy FITS files for use in `Lenser`.
- `lenser_galaxy.py` module: Holds a real galaxy image, or a model galaxy image and model parameters.
 - `Galaxy()` class: Holds the list of parameters used in the modified Sérsic model.

- `Galaxy().generateImage()` function: Holds the modified Sérsic model, points to the `Lens()` class and performs the lensing coordinate deprojection, points to the `Image()` class to create a two-dimensional image of the model, performs PSF convolution if a PSF is available.
- `Image()` class: Holds various two-dimensional arrays referred to as “maps” and “masks” e.g. data map, weight map, PSF map, übersegmentation mask, etc.
- `Lens()` class: Handles the lensing coordinate deprojection, temporarily holds the (up to) seven lens parameters before they are passed into the `Galaxy()` class.
- `lenser_aim.py` module: Estimates lensing signals from real survey data or realistically simulated images.
 - `aimModel()` class: Forward-models first- and second-order lensing effects via calling `lenser_galaxy`, convolves with a PSF, and minimizes a parameter space.

2.3.3 Step 1: Inputting a galaxy image – the `FITS` class

The first stage of `Lenser` involves the input of a galaxy image. A “postage stamp” is a `.FITS` file of dimensions (N_1, N_2) that is an image of a galaxy. The `FITS()` class takes as an input the path to a galaxy postage stamp (as well as galaxy name). `Lenser` assumes that the postage stamp, generated using `Source Extractor`, is centered at or near the galaxy centroid and has a buffer around the galaxy sufficiently large as to ensure that the flexion-susceptible galaxy wings and background are included. At the path location, `FITS()` also searches for additional `Source Extractor` outputs, such as a noise or weight (inverse variance) map and segmentation map. If no noise or weight map is provided, `FITS()` will search for a pickle file at the location `../*noise-info.pkl` that contains information in order to calculate one. If this pickle file does not exist, then a noisemap is calculated based on simple assumptions in the `lenser_galaxy` module.

The segmentation map is an array of integers, where a single integer is assigned for every pixel of the postage stamp. This map is generated using `Source Extractor`, which seeks to identify the background (and assign it a value 0); the main galaxy object (value 1); and any other foreground

objects that may be present in the postage stamp (value 2 for the first extraneous foreground object, 3 for the second, etc.), such as stars, bad pixels, etc.

`Lenser` then creates a segmentation *mask* – a bitmask wherein the background and galaxy get values of 1, and all other foreground objects get a value of 0 – i.e., they are *masked* out. If a segmentation map is absent, the assumption is that the input postage stamp includes only the background and galaxy, and hence, all pixels are viable. By default, `Lenser` also constructs a background mask (a bitmask where background pixels = 1 and all other pixels = 0) and an übersegmentation mask (a bitmask where any pixel that is closer to another object than the galaxy = 0) [78]. The übersegmentation mask acts to mask out light from any other nearby sources.

Next, `FITS` will also search for a PSF file associated with a given galaxy at the specified path.

Finally, a galaxy is instantiated in `Lenser` by calling the `Image()` class, which takes as arguments all of the “maps” and “masks” associated with the galaxy.

2.3.4 Step 2: Preparing the input galaxy for analysis

If a noise map is absent, `Lenser` will generate one that includes both sky and Poisson noise. If a PSF map is absent, `Lenser` will proceed without one.

After `Lenser` inputs the postage stamp and any other maps present, it proceeds to generating an elliptical mask. This first involves calculating and subtracting away the background, if one is present. To calculate a background map, I assume a simple gradient function and do a best fit of the gradient function on the background pixels only (by using the background mask). After the background is subtracted, we then proceed to computing an elliptical mask around the galaxy, to further remove any spurious light sources. The elliptical mask also serves to include only the pixels that are necessary for the `Lenser` pipeline. Including the elliptical mask reduces the number of pixels that are used in the analysis, which speeds up the overall run time of `Lenser`. The first iteration of computing this elliptical mask involves restricting ourselves to the portion of the postage stamp that satisfies

$$|f_i| > |N_\sigma n_i|, \quad (2.26)$$

where f_i is the datemap value at each pixel, n_i is the noisemap value at each pixel, and the parameter N_σ controls the size of the mask and can roughly be thought of as the number of standard deviations one wishes the mask to be above the noisemap. We heuristically take $N_\sigma = 2.5$. The remaining iterations make use of the definition of complex ellipticity given by Eq. (2.11). We thus iteratively compute the elliptical mask by locating the portion of the stamp that satisfies

$$\left(\frac{(\theta^1 - \theta_0^1)'}{\sqrt{|1 + \bar{\chi}^* \bar{\chi}|}} \right)^2 + \left(\frac{(\theta^2 - \theta_0^2)'}{\sqrt{|1 - \bar{\chi}^* \bar{\chi}|}} \right)^2 < N_\sigma^2(Q_{11} + Q_{22}), \quad (2.27)$$

where the prime indicates rotation by an angle given by Eq. (2.13).

At this stage, the input postage stamp has up to three available masks – a segmentation mask, an übersegmentation mask, and an elliptical mask. As the übersegmentation mask already incorporates the information from the segmentation mask, `Lenser` takes the “total” mask M , to be:

$$M_i = (\text{überseg})_i \times (\text{elliptical})_i \quad (2.28)$$

by default. The user has, however, the option to choose any combination of masks, including no masks.

2.3.5 Step 3: Initial guess from image moments

The second stage of `Lenser` calculates image moments as an initial guess for the galaxy model, as described in Section 2.2.2.

2.3.6 Step 4: Minimizing the parameter space with analytic image modeling

With initialized parameter estimates provided by the measured light moments, the final stage of the `Lenser` pipeline employs a two-step χ^2 minimization. This is to say that `Lenser` creates a model galaxy and performs a χ^2 minimization in order to find the best-fit parameters. The χ^2 function is given by

$$\chi^2 = \sum_i (f_i - I_0 g_i)^2 M_i w_i \quad (2.29)$$

and the reduced χ^2 is

$$\chi^2/\text{d.o.f} = \frac{\chi^2}{(\sum_i M_i) - N_p} \quad (2.30)$$

where we sum over each pixel, $y_i = I_0 g_i$ is the model image data map such that g_i is the normalized Sérsic profile and I_0 is the central brightness as described by Eq. (2.3), f_i is the real image data map, M_i is the total mask, w_i is the weight (which is simply the inverse variance such that $w_i = 1/n_i^2$), and N_p is the number of model parameters. It is necessary to have an estimate of I_0 in order to do the χ^2 minimization. Rather than add this to the parameter space, we can assume a prior of $I_0 = 1$ and calculate I_0 after each iteration of the minimization process. This is done by analytically assuming a value of I_0 that minimizes the χ^2 . Using Eq. (2.29),

$$\frac{\partial \chi^2}{\partial I_0} = \frac{\partial}{\partial I_0} \sum_i (f_i - I_0 g_i)^2 M_i w_i = 0$$

we find that

$$I_0 = \frac{\sum_i g_i f_i M_i w_i}{\sum_i g_i^2 M_i w_i}. \quad (2.31)$$

The two-step minimization is as follows:

(i) initially minimizing over the subspace $\{n_s, \theta_s\}$, which involves a brute-force tactic to decouple n_s and θ_s from each other. The method for this is as follows: we take the estimate of q from the image moments portion of the hybrid **Lenser** method, iterate over the range of reasonable n_s values for galaxies (which is taken to be 0.1 to 10), and make use of the relation in Eq. (2.15) in order to calculate θ_s at each iteration. This procedure provides estimates for $\{n_s, \theta_s\}$ before proceeding to the full local minimization.

(ii) a final local minimization over the entire parameter space. This local minimization is implemented with the `scipy` optimization function, which utilizes a Limited-memory Broyden-Fletcher-Goldfarb-Shanno Box-constraint algorithm (L-BFGS-B). This includes constraints on the parameter space to help reduce run time, as well as preventing an unrealistic minimization of model parameters.

During each iteration of the two-step minimization, the model image is convolved with the PSF, provided that one exists, using the Fast-Fourier-Transform (FFT) convolution algorithm in

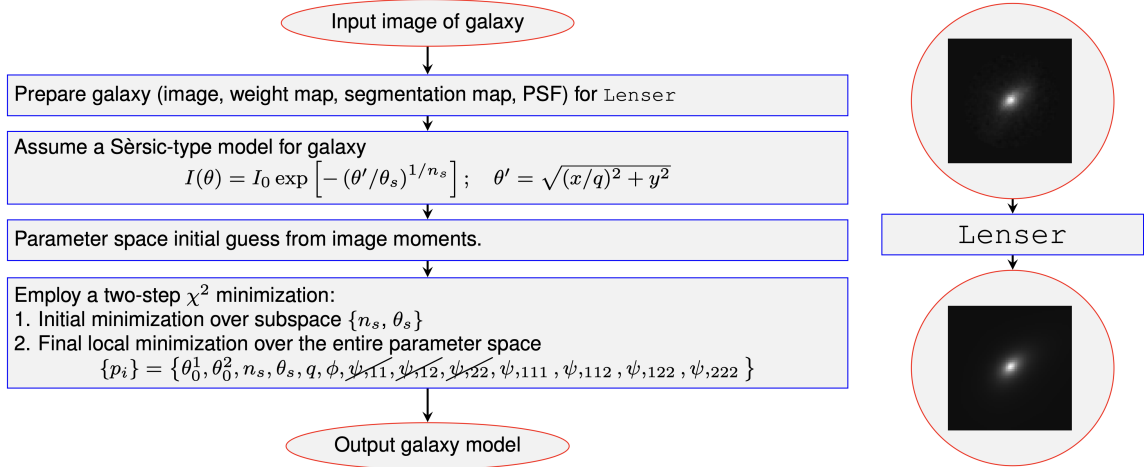


Figure 2.1: Schematic of the `Lenser` pipeline.

`astropy.convolution.convolve_fft`.

Additionally, `Lenser` has the option to exclude certain parameters from the minimization process.

By default, all of the ψ_{ij} parameters are not included and have values fixed to zero, due to the shear/ellipticity degeneracy. One could, in principle, choose to minimize over the ψ_{ij} parameters and exclude q and ϕ from the minimization.

It is important to note that, as a consequence of the mass sheet degeneracy, `Lenser` actually measures the *reduced* flexion (see Sec. 1.2.7). In the limit of weak lensing ($\kappa \ll 1$), we see that the mass-sheet-invariant fields g , F , and G , are equivalent to γ , \mathcal{F} , and \mathcal{G} , respectively. As `Lenser` operates exclusively in this regime, we define the observables to be the flexion rather than the reduced flexion.

The final output from `Lenser` includes the best-fit values for the shape and lensing parameters and their corresponding errors, which are estimated from the inverse Hessian matrix that is provided by `scipy.optimize.minimize` for the L-BFGS-B method, as well as the final $\chi^2/\text{d.o.f.}$, the estimated size of the galaxy image, a , the estimated central brightness, I_0 , and the datamap model generated from the best-fit parameters and I_0 .

The AIM portion of the hybrid `Lenser` method (AIM-L) builds on the original AIM method of Cain et al. [55] (AIM-C) in two major ways. First, while AIM-C uses an elliptical Gaussian

intensity profile for the modeling galaxies (i.e. n_s is fixed to 0.5), AIM-L uses the modified Sérsic-type profile of Eq. (2.3). Cain et al. [55] find that when a Sérsic profile is used, the modeling is not robust due to degeneracies between the image brightness normalization, image size, and n_s , as well as the parameter space simply being too large. The authors decided to only model the lensing distortions of the galaxy isophotes and accurately fit the flexion at the cost of poorly fitting the image normalization and image size, and not fitting n_s at all. In AIM-L, we fit n_s , but do not fit the image normalization. AIM-L therefore maintains the same size parameter space as AIM-C. Second, AIM-L uses a two-step minimization approach, as described above, whereas AIM-C only performs a single local minimization.

With AIM-L, we find that we are able to robustly fit our entire parameter space. This allows us to use fit n_s values as a simple way to classify galaxies by type, which is useful for flexion-based studies, such as the one we carried out in Fabritius II et al. [50].

2.4 Example: Running Lenser on a real galaxy image

Here, I demonstrate a simple example of using `Lenser`, where we input a galaxy from the COSMOS catalogue imaged with the Hubble Space Telescope (HST). For a description of this catalogue and postage stamps used, see Sec. 2.5.2 and our paper Fabritius II et al. [50].

Figure 2.2 shows the collection of `FITS` files for a galaxy in the COSMOS catalogue. These include the data map, a noise map, a segmentation map from `Source Extractor`, and a PSF map.

Below I show a snippet of Python code that can be used to run this galaxy through `Lenser`. This code is an example script provided in `Lenser` that can be found in

`/examples/run_real_gal/lenser_run_real_gal_single_fit.py`.

```

1 import sys
2 sys.path.append('..../')
3 from lenser import *
4 import numpy as np
5
6 # Read in image from FITS file. We will choose a galaxy from the COSMOS catalogue
7 # ... Specify path to science image

```

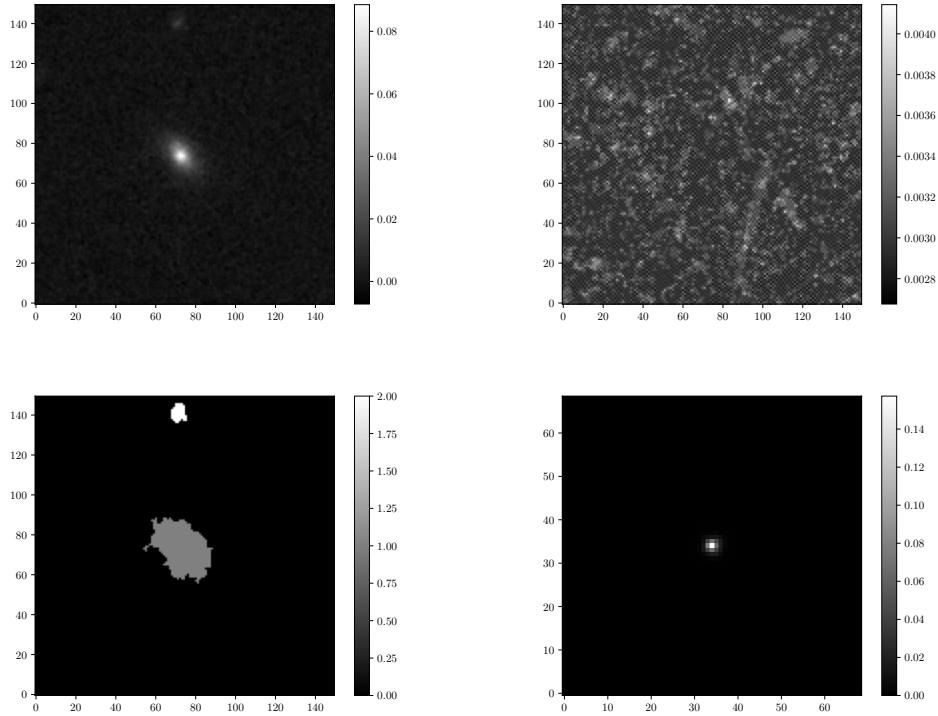


Figure 2.2: FITS files for a galaxy in the COSMOS catalogue (which we refer to as galaxy number 1664) in the F814W band. *Top left*: the postage stamp science image of the galaxy, referred to as the data map. *Top right*: the noise map (root-mean square noise level measured in HST for this postage stamp). *Bottom left*: The segmentation map for this postage stamp, generated using `Source Extractor`. The value 0 refers to background pixels, 1 refers to the galaxy pixels, and 2 refers to some other object, visible in the data map, which appears to be some other galaxy in the background. *Bottom right*: the PSF map for the HST in this field. For details on the PSF model, see Koekemoer [6].

```

8 path_to_image = '../Catalogues/COSMOS/Images_F814W/COSMOS_1664_F814W.fits',
9 # ... Get science image, noisemap, segmentation mask (uberseg by default),
10 #      psfmap, and background mask from lenser_fits:
11 f = FITS(path_to_image)
12 dat = f.get_FITS('data')
13 rms = f.get_FITS('noise')
14 seg = f.get_FITS('segmask')
15 psf = f.get_FITS('psf')
16 bg = f.get_FITS('bgmask')
17 # ... Get name of object from path_to_image (can be overridden)
18 image_name = path_to_image.split('/')[-1].split('.')[0]

```

```

19
20 # Create an Image instance
21 myImage = Image(name = image_name, datamap = dat, noisemap = rms,
22                  übersegmask = seg, psfmap = psf, bgmask = bg)
23 # .. Plot science image
24 myImage.plot(save=False, show=True)
25
26 # Generate elliptical mask and subtract background
27 myImage.generateEllipticalMask(subtractBackground=True)
28 # .. Plot the total mask (elliptical multiplied by seg)
29 myImage.plot(type='totalmask', save=False, show=True)
30
31 # Plot noisemap
32 myImage.plot(type='noise', save=False, show=True)
33
34 # Plot PSF
35 myImage.plot(type='psf', save=False, show=True)
36
37 # Initialize AIM model
38 myModel = aimModel(myImage)
39
40 # Run local minimization
41 myModel.runLocalMinRoutine()
42
43 # Plot the real galaxy image, the best-fit model, and the difference between the two
44 myModel.make_plot_compare(save=False, show=True)
45 # .. Zoom in for visual comparison
46 myModel.make_plot_compare(zoom=True, save=False, show=True)
47
48 # Reset the parameters to their default values
49 myModel.empty()

```

Figure 2.3 shows two masks used in the `Lenser` analysis – the übersegmentation mask created by the `FITS()` class, and the elliptical mask generated by `myImage.generateEllipticalMask()` in

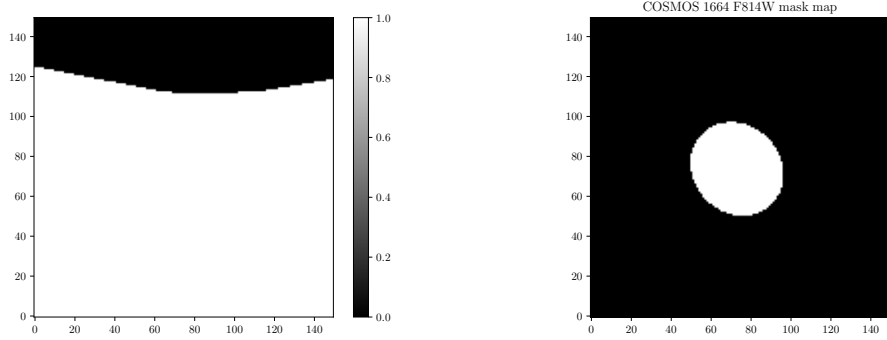


Figure 2.3: Masks for a galaxy in the COSMOS catalogue (which we refer to as galaxy number 1664) in the F814W band. *Left:* the übersegmentation bitmask mask created by the `FITS()` class *Right:* the elliptical bitmask produced by the `Image().generateEllipticalMask()` function.

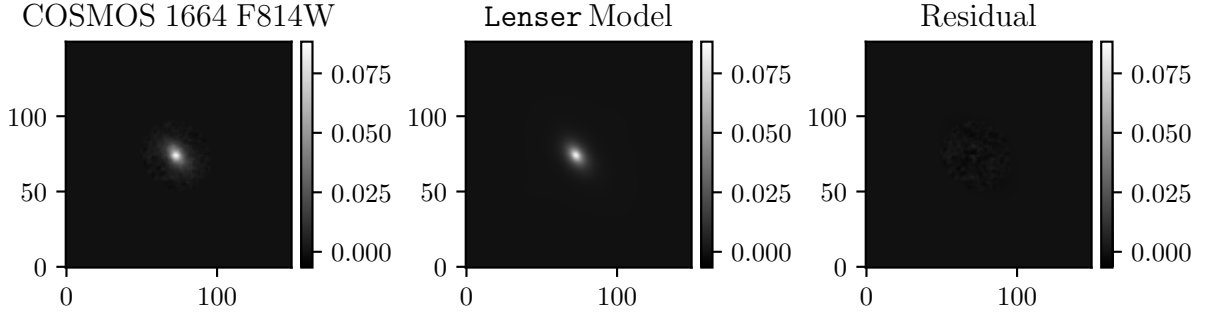


Figure 2.4: Image reconstruction for a galaxy in the COSMOS catalogue (which we refer to as galaxy number 1664) in the F814W band. *Left:* the masked image of the galaxy. The applied mask is the combination (see Eq. (2.28)) of both masks given in Fig. 2.3. *Middle:* the model image of the galaxy, produced using the bestfit model parameters given in the example bash output. *Right:* The residual between the galaxy and model images.

the above Python snippet code.

Figure 2.4 shows the output plot given by produced by `myModel.make_plot_compare()` in the python script. This includes the masked postage-stamp image of the galaxy , the model image generated from the best-fit parameter space, and the residual between the galaxy image and the model image. Below, I give the corresponding output that is printed in the bash shell for this galaxy. This includes the initial guess of the parameter values the best-fit parameter values after the full local minimization, as well as the errors on these parameters, and the $\chi^2/\text{d.o.f.}$ of the fit:

```

1 ****
2 *          Welcome to LENSER! *
3 ****
4 Parameter subspace initial guess from image moments:
5 ... [ xc = -2.7394027972640487 ]
6 ... [ yc = -1.6122698223191065 ]
7 ... [ q = 1.4459503640672202 ]
8 ... [ phi = -0.822557960683524 ]
9 ... [ psi,111 = -0.0021813356235319734 ]
10 ... [ psi,112 = -0.0015964285243539223 ]
11 ... [ psi,122 = 0.0008336085242247166 ]
12 ... [ psi,222 = 0.001531155827114365 ]
13 ... [ Chisqr = 10.759857483069352 ]
14 Brute force subspace minimization best-fit values:
15 ... [ ns = 1.2000000000000002 ]
16 ... [ rs = 2.0878569081246696 ]
17 ... [ Chisqr = 0.5397420606374749 ]
18 L-BFGS-B local minimization best-fit values:
19 ... [ xc = -3.042740397213897 ]
20 ... [ yc = -1.4395617015848432 ]
21 ... [ ns = 1.255598771531636 ]
22 ... [ rs = 1.8823539491516617 ]
23 ... [ q = 1.6207957723606636 ]
24 ... [ phi = -0.9356827151902667 ]
25 ... [ psi,11 = 0.0 ]
26 ... [ psi,12 = 0.0 ]
27 ... [ psi,22 = 0.0 ]
28 ... [ psi,111 = 0.007470043619177005 ]
29 ... [ psi,112 = 0.00020287195397455186 ]
30 ... [ psi,122 = 0.0020170224673287853 ]
31 ... [ psi,222 = 0.001097699460032259 ]
32 ... [ Chisqr = 0.4273407176787629 ]
33 1sigma errors on parameters:
34 ... [ error on xc = 0.009310273923579221 ]

```

```

35 ... [ error on yc = 0.011518419804286164 ]
36 ... [ error on ns = 0.0031384024451667296 ]
37 ... [ error on rs = 0.00851722875021398 ]
38 ... [ error on q = 0.0024080991726882998 ]
39 ... [ error on phi = 0.0019939808213823144 ]
40 ... [ error on psi,11 = 0.0 ]
41 ... [ error on psi,12 = 0.0 ]
42 ... [ error on psi,22 = 0.0 ]
43 ... [ error on psi,111 = 0.0012266155615447676 ]
44 ... [ error on psi,112 = 0.00045543405847244065 ]
45 ... [ error on psi,122 = 0.000346159306123415 ]
46 ... [ error on psi,222 = 0.00039323810680246603 ]

```

2.5 Testing the Lenser framework

In Sections 2.5.1 - 2.5.3, I test the ability of `Lenser` to reconstruct known input parameters using simulated galaxy images. In Sec. 2.5.4, I test the robustness of `Lenser` by comparing the reconstruction of parameters across two different telescopes: HST and JWST.

2.5.1 Testing Lenser with Lenser – Single galaxy

Since `Lenser` is a forward-modeling code, the user can specify a set of input parameters and create an image of a lensed galaxy. In other words, we can use `Lenser` in order to simulate a postage stamp of a galaxy. In this case, the galaxy itself is modeled using the modified Sérsic-type intensity profile, some sky background b is added to the image, and randomly generated noise is added, such that each pixel i in the stamp has a value given by

$$f_i = I_i(\theta_i) + n_i * \text{numpy.random.normal(size=(N_1, N_2))} + b_i, \quad (2.32)$$

where the noisemap

$$n_i = \sqrt{n_{a,i}^2 + (n_{b,i}\sqrt{I_i})^2}, \quad (2.33)$$

where $n_{a,i}$ is the sky noise and $n_{b,i}\sqrt{I_i}$ is the Poisson noise.

Once a galaxy image and noisemap are simulated, `Lenser` can export both of them and clear local variables. Since `Lenser` is now blind to the parameter space it used in order to generate this image, one can test the ability of the code to reconstruct known parameters.

For a simple toy demonstration of `Lenser`'s accuracy, I randomly choose some input parameters for a galaxy and use them to create a postage stamp of the galaxy image and a noisemap. This simulated galaxy is then run through `Lenser`. Fig. 2.5 shows the visual fit to a simulated galaxy image, while Table 2.1 shows a comparison of the corresponding known and reconstructed parameter space. We see that there exists reasonable agreement between the simulated galaxy image and its model for this simple toy problem of one galaxy.

The code for this toy problem can be found in

`/examples/run_sim_gal/lenser_run_sim_gal_single_fit.py`.

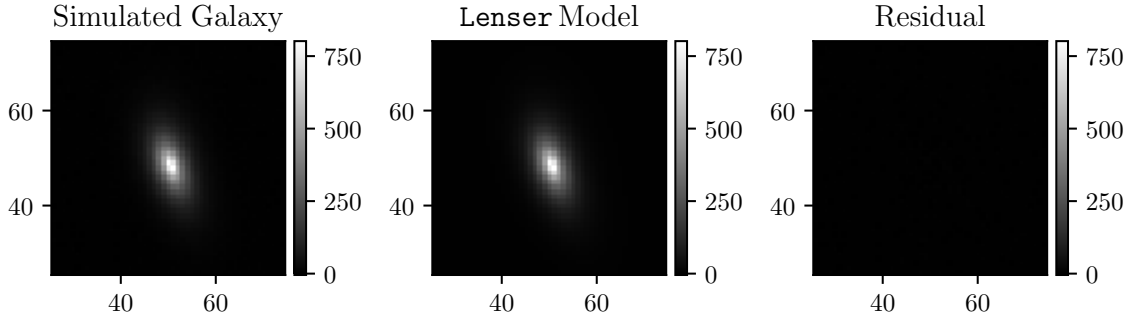


Figure 2.5: The left panel shows a simulated galaxy image with known parameters and randomly generated noise, the middle panel shows the best-fit model, and the right panel shows the residual difference between the simulated galaxy image and the best-fit model. The reduced χ^2 for this fit is $\simeq 1.02$

Table 2.1: Real galaxy and lensing parameters compared with `Lenser`-fit parameters for a simulated galaxy

	θ_0^1	θ_0^2	n_s	θ_s	q	ϕ
Real	0	0	1.0	2.0	2.0	1.25
<code>Lenser</code>	3.9703e-3	2.9707e-3	0.9996	2.0031	1.9985	1.2509
	$\psi_{,11}$	$\psi_{,12}$	$\psi_{,22}$	$\psi_{,111}$	$\psi_{,112}$	$\psi_{,122}$
Real	0	0	0	1e-2	-3e-3	7e-3
<code>Lenser</code>	0.0000	0.0000	0.0000	9.5930e-3	-3.0942e-3	6.8563e-3
						-2.8864e-3

2.5.2 Testing Lenser with a simulated catalogue

Next, I test the ability of `Lenser` to reconstruct known parameters for a simulated galaxy “catalogue.” Using the code provided in `examples/sim_cat/lenser_sim_cat.py`. A number of desired galaxies N_{gal} is specified, galactic and lensing parameters are randomly generated for each galaxy, an image is generated for each galaxy, and the resulting N_{gal} postage stamps are exported to the path `'/examples/Catalogues/Simulated_(insert time)/'`.

Input catalogue parameters

In creating a simulated galaxy catalogue, the properties given to each galaxy – including the shape and lensing parameters, as well as the size of each postage stamp and the noise within it – are chosen to reflect a given telescope imaging survey.

The CANDELS Program [6] contains a large catalogue of high-redshift ($z = 0.15$ to 8) deep-imaging galaxies using the Hubble Space Telescope (HST) WFC3/IR and ACS camera systems (which operate at a pixel scale of 0.03 arcsec/pixel). This large program is a collection of observations across multiple fields In Fabritius II et al. [50], we used a subset of galaxies from the COSMOS field for a flexion study. The catalogue used in our paper will be referred to throughout this work as the “COSMOS” catalogue.

For this simulated catalogue, the postage stamp size, galaxy size a , peak brightness I_0 , and the noisemaps are all chosen to mimic the COSMOS catalogue. As both the postage stamp and galaxy sizes reflect the COSMOS catalogue, the simulated catalogue also has the same pixel scale, by definition.

The non-fit parameter properties of the simulated galaxy catalogue are described below:

1. A total of 100 galaxies are generated
2. The postage stamp sizes are 150×150 .
3. Every galaxy is chosen to have a size of $a = 10$ pixels.⁵

⁵It is important to note here that an input a shares a degeneracy with various parameters such as I_0 , n_s , θ_s , and q . When generating an image in `Lenser`, its size is defined by θ_s , as a function of a , q , and n_s , using Eq. (2.15). After the image is generated, a , is then “measured” by the quadrupole moments as given by Eq. (2.14). The result of this is that input a and measured a do not always match or have the same physical meaning. I find that for

4. The peak brightness, I_0 is drawn from a uniform distribution between 0.1 and 10.
5. The noisemaps (see Eq. 2.33) are generated with $n_{a,i} = 1.3 \times 10^{-3}$ and $n_{b,i} = 0$.
6. The background is chosen to be zero.

Input shape parameters

- The centroid, (θ_0^1, θ_0^2) , is dithered within the four central pixels – i.e., each coordinate can take values between -1 and 1 .
- The Sérsic index, n_s , is drawn from a uniform distribution between 0.2 and 5. This range covers all reasonable values that n_s can take. We note that, canonically, $n_s = 1$ for spiral galaxy profiles and $n_s = 4$ for elliptical galaxy profiles.
- The axis ratio, q , is calculated via

$$q = \frac{1 + |\epsilon^{(s)}|}{1 - |\epsilon^{(s)}|} \quad (2.34)$$

where the intrinsic ellipticity, $\epsilon^{(s)}$, is drawn from the probability distribution [79]:

$$p_s(\epsilon^{(s)}) = \frac{1}{\pi\sigma_\epsilon(1 - e^{-1/\sigma_\epsilon^2})} e^{-|\epsilon^{(s)}|^2/\sigma_\epsilon^2} \quad (2.35)$$

where $\sigma_\epsilon = 0.2$.

- The orientation angle, ϕ is drawn from a uniform distribution between 0 and 2π .
- The characteristic radius, θ_s is not drawn from a random distribution. It is instead generated in the following way. First, we note that the characteristic size of a galaxy is given by Eq. (2.14). Galaxy size, a , is not a fit parameter, although it will be set to a specific input value for each of the catalogues below. This is done in order to calculate the characteristic radius, θ_s , as it is coupled to n_s , a , and q , as given by Eq. (2.15).

values of n_s corresponding to $0.2 \leq n_s < 2$, input and measured a do match. For larger values of n_s , however, the Sérsic profile becomes more dispersed and centrally concentrated, and the input value of $a = 10$ does not match the measured value. To deal with this, I make the following adjustments: for galaxies with $2 < n_s \leq 3$, I set input $a = 2 \times (10 \text{ pixels})$, for galaxies with $3 < n_s \leq 4$, I set input $a = 4 \times (10 \text{ pixels})$, and for galaxies with $4 < n_s \leq 5$, I set input $a = 8 \times (10 \text{ pixels})$. I find empirically that this yields measured values of $a \simeq 10$ for all galaxies.

Input lensing parameters

- We generate the shear, γ_1 and γ_2 , from Gaussian distributions, with means of zero and standard deviations of 0.25. For convenience, we set the convergence $\kappa = 0$ (this choice is arbitrary due to the mass-sheet degeneracy). We then compute $\psi_{,ij}$ via the relations:

$$\psi_{,11} = \kappa + \gamma_1; \quad \psi_{,12} = -\gamma_2; \quad \psi_{,22} = \kappa - \gamma_1 \quad (2.36)$$

- We generate the first flexion, \mathcal{F}_1 and \mathcal{F}_2 , from Gaussian distributions with means of zero and standard deviations of $(5 \times 10^{-4})/\sqrt{2}$ pixels $^{-1}$.
- Now, we have to be careful when generating the \mathcal{G} flexion, because $\psi_{,ijk}$ are not independent from one another. We therefore do the following:

1. Generate \mathcal{F}_1 and \mathcal{F}_2 from Gaussian distributions.
2. Assume a particular analytic lens model, which in this case is a singular isothermal sphere (SIS). This allows us to relate first and second flexion in an analytic way. The flexions are given by

$$\mathcal{F} = -\frac{\theta_E}{2\theta^2} e^{i\phi}; \quad \mathcal{G} = \frac{3\theta_E}{2\theta^2} e^{3i\phi}$$

3. Use \mathcal{F}_1 and \mathcal{F}_2 to calculate the lens position ϕ (not to be confused with the **Lenser** parameter ϕ). With \mathcal{F}_1 and \mathcal{F}_2 defined, we can simply calculate $\phi = \arctan(\mathcal{F}_2/\mathcal{F}_1)$.
4. With ϕ defined, we then calculate \mathcal{G}_1 and \mathcal{G}_2 via

$$\mathcal{G}_1 = -\frac{3 \cos 3\phi}{\cos \phi} \mathcal{F}_1; \quad \mathcal{G}_2 = -\frac{3 \sin 3\phi}{\sin \phi} \mathcal{F}_2 \quad (2.37)$$

- Finally, we calculate $\psi_{,ijk}$ via the relations:

$$\psi_{,111} = \frac{1}{2}(3\mathcal{F}_1 + \mathcal{G}_1); \quad \psi_{,112} = \frac{1}{2}(\mathcal{F}_2 + \mathcal{G}_2); \quad \psi_{,122} = \frac{1}{2}(\mathcal{F}_1 - \mathcal{G}_1); \quad \psi_{,222} = \frac{1}{2}(3\mathcal{F}_2 - \mathcal{G}_2). \quad (2.38)$$

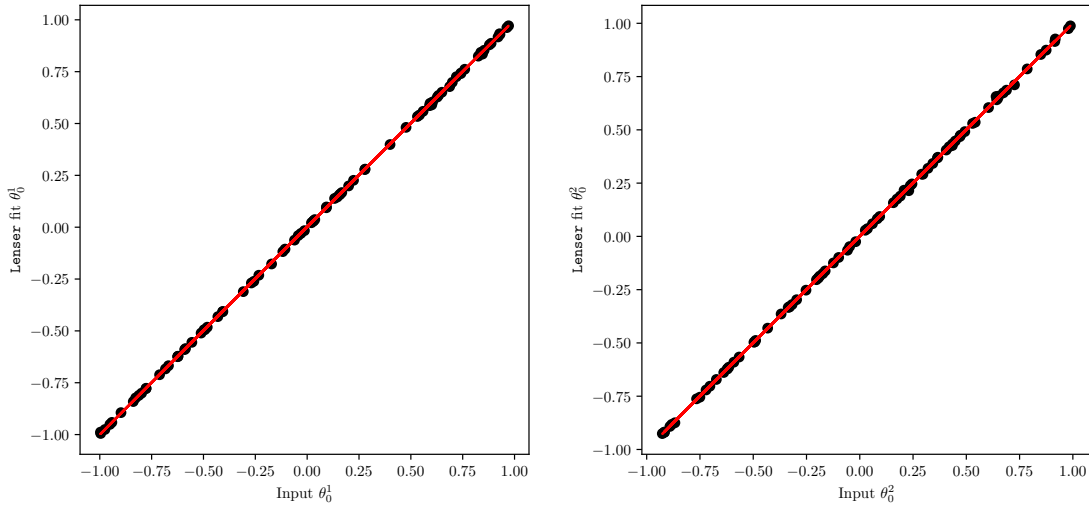


Figure 2.6: Reconstructed versus input image centroids, θ_0^1 and θ_0^2 with errorbars computed from the χ^2 minimization in `Lenser`. The units of the centroids are pixels. The red line is a unity line ($y = x$), not a fit to the data.

Fit results

With an input catalogue of galaxies created, I run all of them through `Lenser` using the catalogue manager in `/examples/run_cat/lenser_run_cat_single_fit.py`.

Figures 2.6 - 2.9 show the `Lenser` fit parameters as compared to the truth input parameters for the simulated COSMOS-like catalogue. I impose only two data cuts here: first, I choose only fits where $\chi^2/\text{d.o.f} < 1.5$ (in keeping with various flexion studies such as Cain et al. [55] and Fabritius II et al. [50]) and I choose only fits where $a\mathcal{F} \leq 1$ (where we recall that this quantity should be small with respect to unity). From these figures, it is clear that `Lenser` is able to reconstruct every parameter in the parameter space. `Lenser` is even able to adequately reconstruct non-fit parameters such as I_0 , as defined by Eq. (2.31), shown in Fig. 2.10.

2.5.3 Covariance testing

Finally, we wish to test the response of `Lenser` to noise, to verify the robustness of the parameter reconstruction. Since `Lenser` is a forward-modeling code, the user can specify a set of input parameters and create an image of a lensed galaxy. It is therefore possible to use `Lenser` in order to

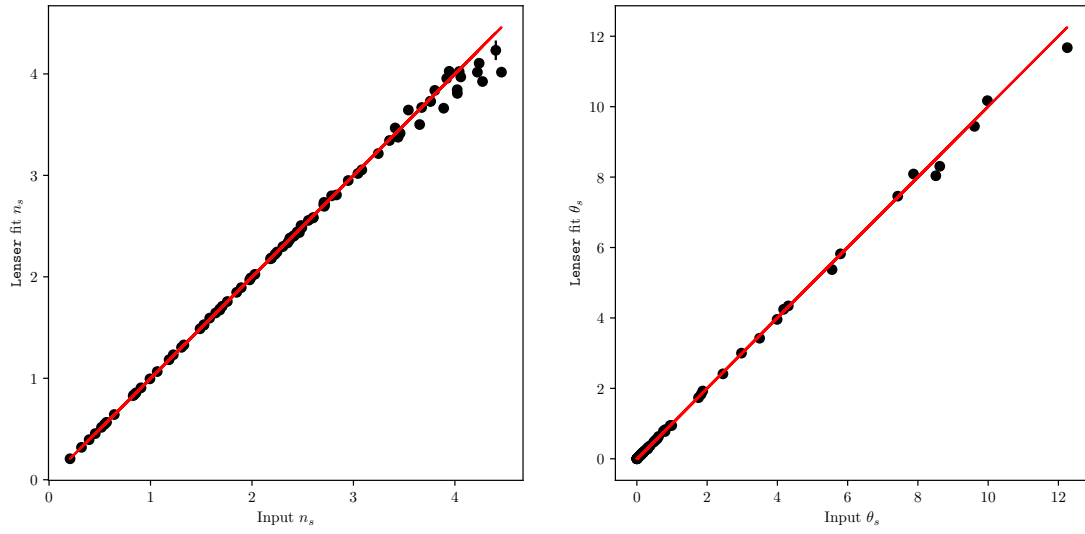


Figure 2.7: Reconstructed versus input image Sérsic index, n_s and characteristic radius, θ_s , with errorbars computed from the χ^2 minimization in **Lenser**. n_s is dimensionless and θ_s has units of pixels. The red line is a unity line ($y = x$), not a fit to the data.

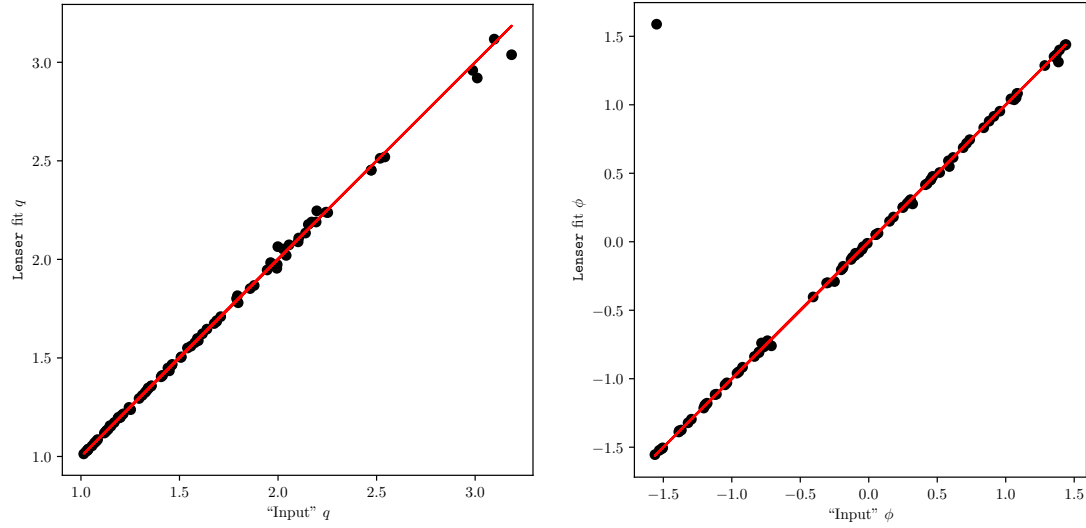


Figure 2.8: Reconstructed versus input image axis ratio, q , and orientation angle, ϕ , θ_0^1 and θ_0^2 with errorbars computed from the χ^2 minimization in **Lenser**. q is dimensionless and ϕ has units of radians. The red line is a unity line ($y = x$), not a fit to the data. We note that, due to the shear/ellipticity degeneracy in the presence of nonzero input shear as we have here, the true input q and ϕ will not be reconstructed by **Lenser**. We estimate the "input" q and ϕ analytically by adding the true input intrinsic ellipticity and shear components together.

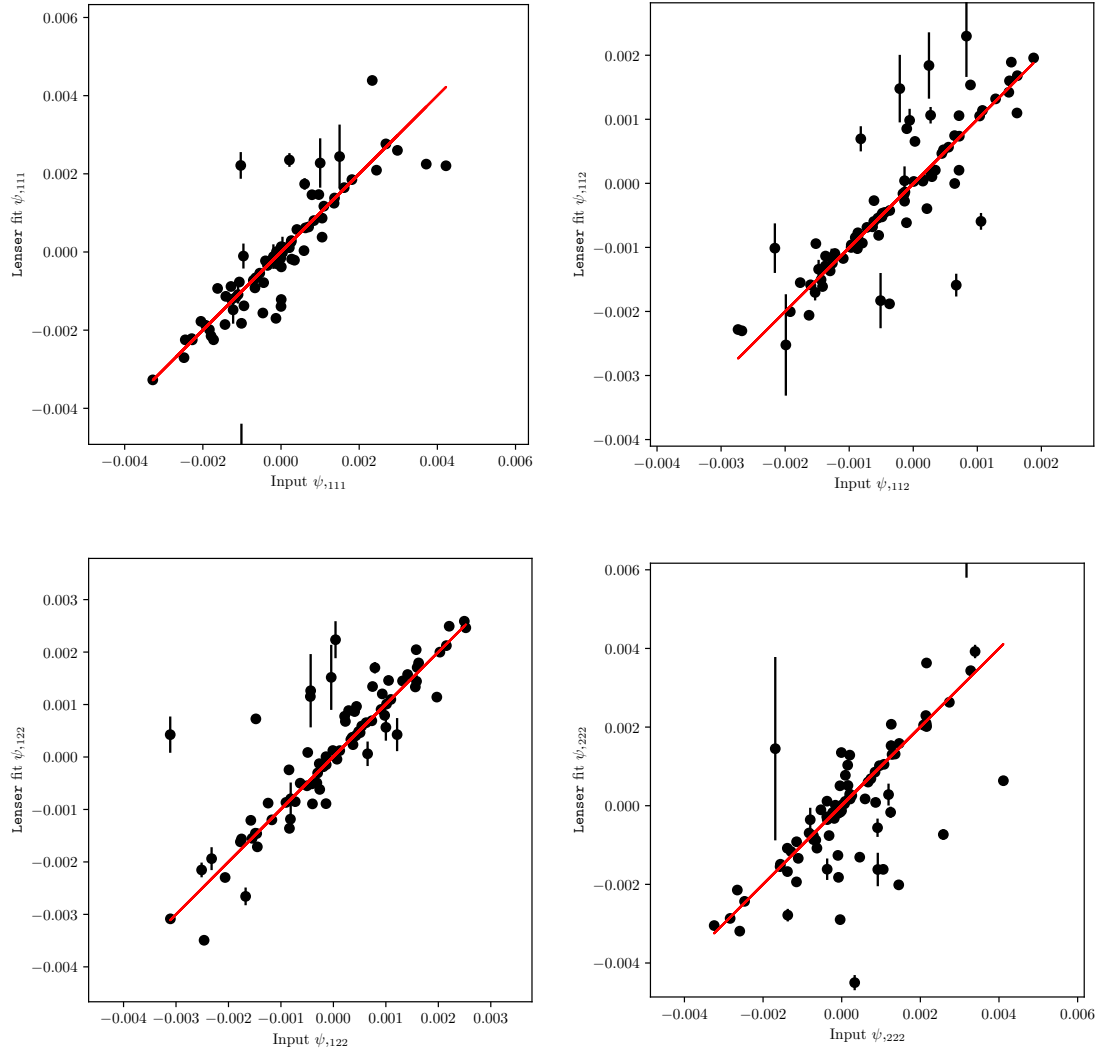


Figure 2.9: Reconstructed versus input flexion terms, ψ_{ijk} , with errorbars computed from the χ^2 minimization in **Lenser**. The units of ψ_{ijk} are pixels $^{-1}$. The red line is a unity line ($y = x$), not a fit to the data.

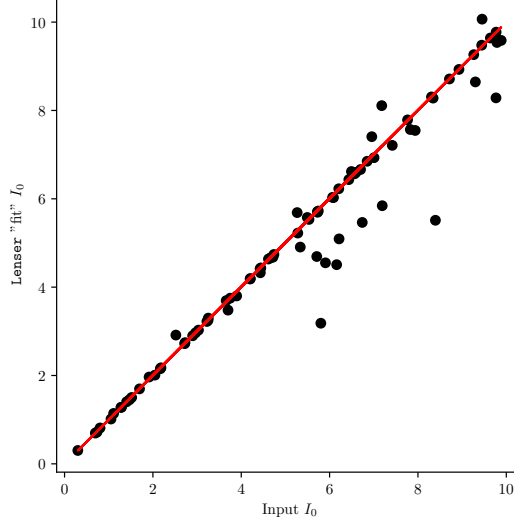


Figure 2.10: Reconstructed versus input image normalization, I_0 . I_0 is not a `Lenser` fit parameter, but is estimated during using the bestfit χ^2 values of the parameters and Eq. (2.31). The units of I_0 are arbitrary. The red line is a unity line ($y = x$), not a fit to the data.

compute a covariance matrix for our parameter space by simulating an ensemble of postage stamp images (a "stamp collection") with known input parameters, p_i , and noise, and then running each of the postage stamps through `Lenser` for fitting. To test the response of `Lenser` to noise, each postage stamp has identical input parameters and noise maps, but additional, unique Gaussian noise injected into each. The covariance matrix is given by $\sigma_{ij}^2 = \langle (\hat{p}_i - \langle \hat{p}_i \rangle)(\hat{p}_j - \langle \hat{p}_j \rangle) \rangle$, where \hat{p}_i are the reconstructed parameters. Once the covariance matrix is calculated, we are able to compute the marginalized 1σ uncertainty on each parameter simply by taking the square root of the diagonal: $\sigma_i = \sqrt{\sigma_{ii}^2}$.

Fig. 2.11 shows the 1σ and 2σ confidence ellipses (and 1σ Gaussians along the diagonal) for the covariance matrix of a particular stamp collection. Additionally, since the input parameters are known, we can display them on top of the error ellipses to explicitly compare each p_i to $\langle \hat{p}_i \rangle$. The white plus sign in each matrix element (i,j) indicates the location of (p_i, p_j) . Successful fits will have white plus signs that fall within the error ellipses. We clearly see from Fig. 2.11 that `Lenser` is able to appropriately reconstruct the input parameter space.⁶ It is also evident that reasonable

⁶For the set of parameters used in the covariance analysis of Fig. 2.11, we note that (n_s, θ_s) falls outside the error ellipse. When using `Lenser` to create the images for the stamp collection, the user needs to specify additional input values outside of the parameter space, such as I_0 and a , where the latter is used to derive θ_s from n_s . We attribute

correlations exist in the parameter space. For example, we see that n_s and θ_s are anticorrelated, as expected.

2.5.4 Comparing Lenser parameter reconstruction across two different telescopes

Unlike for a simulated galaxy, it is challenging to test the ability of **Lenser** to correctly measure a real galaxy’s shape and lensing parameters, given the fact that the truth values of the parameter space are inherently unknown.

Abell 2744 is a well studied galaxy cluster that has been observed both by HST and JWST. In Fabritius and Goldberg [80], Joseph Fabritius used **Lenser** to measure the shape and lensing parameters of the source galaxies in Abell 2744. This analysis was done using images from HST in the F814W filter.⁷ Recently, Drexel graduate student Jeimin Garibnavajwala has used **Lenser** to measure the parameters of the Abell 2744 source galaxies using the images from JWST in the F115W filter.⁸ Due to a number of reasons, which include the fact that these two observations from HST and JWST are in different bands, have differing fields of view, different maximum redshift depth, and different pixel coordinate systems relative to the World Coordinate System (WCS) – right-ascension (RA) and declination (Dec) – the HST and JWST images of Abell 2744 will not be a one-to-one comparison. They will not both contain the exact same source galaxies. Drexel graduate student Jacob Shpiece created a catalogue of source galaxies that (i) appear in both the HST and JWST images and (ii) are successfully fit by **Lenser**. He also applied coordinate rotations so that both the HST and JWST catalogues are oriented along the WCS.

With this catalogue, we can compare the **Lenser** fit results. A description of the data cuts applied to the **Lenser** output for the HST sample can be found in Fabritius and Goldberg [80], and the same cuts are applied to the JWST sample. The final sample of galaxies used here are those that simultaneously pass the applied data cuts for both the HST and JWST **Lenser** fits. If **Lenser** is truly measuring the flexion and ellipticities of the source galaxies correctly, then there should

the discrepancy in n_s versus $\langle n_s \rangle$ to the degeneracies that exist between image brightness normalization, n_s , and image size that occur for large $n_s / \theta_s \ll a$. Despite this, since I_0 and a are not in the parameter space, a robust fit is still achieved.

⁷See <http://svo2.cab.inta-csic.es/theory/fps/> for a description of the filters used by HST and JWST.

⁸This work is part of a larger study on using **Lenser** multi-band fitting measurements of flexion (see Sec. 2.6) to analyze structure in galaxy clusters imaged by JWST. We plan on publishing this work after my Ph.D.

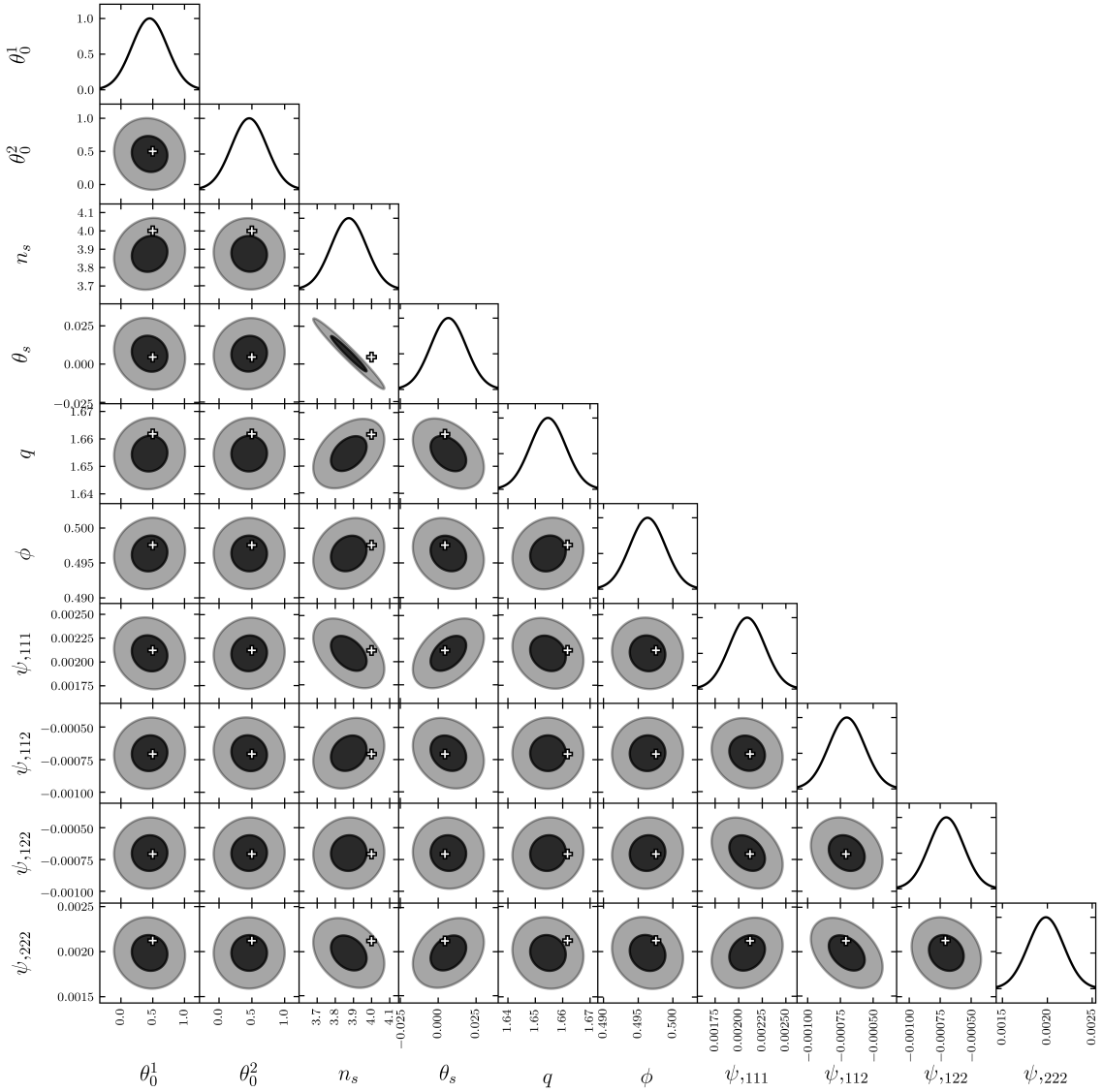


Figure 2.11: Covariance matrix for a stamp collection of 1000 images, with a noise map that matches that of the COSMOS catalogue. Here, we show 1σ and 2σ confidence ellipses below the diagonal (darker and lighter shades, respectively), 1σ Gaussians along the diagonal, and the locations of (p_i, p_j) denoted by white plus signs. The galaxy in each postage stamp is chosen to be canonically elliptical ($n_s = 4$). The galaxy also has realistic, nonzero ellipticity, shear, and flexion values. The centroid is dithered within a single pixel and hence is randomized for each image. We note that, due to the shear/ellipticity degeneracy in the presence of nonzero input shear as we have here, q and ϕ will not be reconstructed by **Lenser**. Hence, the location of the white plus sign for these values is estimated analytically by adding the input intrinsic ellipticity and shear components together. The centroid and θ_s are in units of pixels, ϕ is in units of radians, n_s and q are dimensionless, and the $\psi_{,ijk}$ flexion terms have units of pixels $^{-1}$.

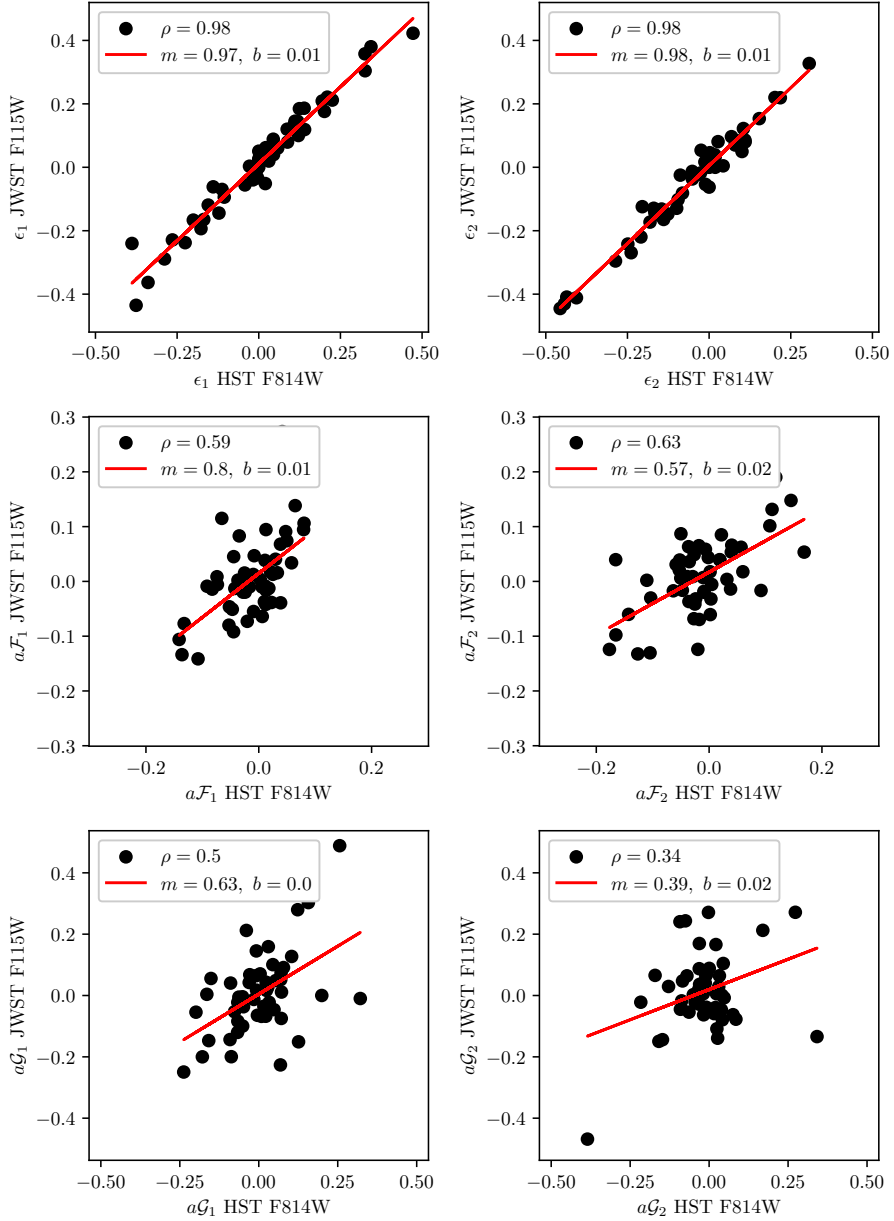


Figure 2.12: Ellipticity, ϵ_i and dimensionless flexion, $a\mathcal{F}_i$ and $a\mathcal{G}_i$, 1- and 2-components for source galaxies in Abell 2744 imaged by JWST versus HST. In these plot legends, ρ is the Pearson correlation coefficient. The red line is a best-fit to $y = mx + b$, and the best-fit slope and y -intercept values are given in the legend of each plot.

be a high correlation between, for example, the flexion measured of a galaxy in the HST image compared to the flexion measured of the same galaxy in the JWST image. This is an excellent test of the robustness of `Lenser` – we are comparing two different bands, images that are necessarily two different epochs since they were imaged about a decade apart, images with two entirely different noise realizations, and with two different instruments we have two different PSFs.

The results of this comparison are shown in Fig. 2.12. In this figure, I am comparing the dimensionless flexions $a\mathcal{F}_i$ and $a\mathcal{G}_i$, where a is defined in Eq. (2.14). Note that a is measured by `Lenser` and its output along with the `Lenser` parameter space. I also note that the \mathcal{F} - and \mathcal{G} -flexion are calculated from the `Lenser` best-fit parameters ψ_{ijk} by Eqs. (1.121) - (1.124). Similarly, the ellipticities ϵ_i are calculated from the `Lenser` best-fit parameters q and ϕ by Eq. (2.9). We see that there is good agreement for the ellipticity and flexion measurements across both telescopes. We do see, particularly for the flexion, that there is not perfect agreement. This is largely due to the fact that flexion is an inherently more difficult signal to measure than ellipticity. As will be discussed in Sec. 2.6, we also hypothesize that the (intrinsic) flexion signal *does* vary as a function of band. Even still, there is a clear, convincing correlation between the ellipticity and flexion reconstruction across both telescopes which indicates that `Lenser` is, indeed, a robust flexion measurement tool.

2.6 Lenser 2.0: Multi-band, multi-epoch fitting

In the previous section, I briefly discussed bands and epochs in the context of HST and JWST. Here, I'd like to first discuss these terms in more detail. An *epoch* refers to a single-exposure image taken by a telescope. Observational astronomers often wish to take multiple images of the same astronomical object at different points in time – these are referred to as multiple epochs. In the context of astronomical observation, a *band* refers to the photometric bandpass filter used by the telescope for observation. In photometry (which is used as an alternative to spectroscopy), filters are used on telescopes to only allow light within a specific wavelength range to enter the telescope. It is often the case that multiple observations (and hence multiple epochs) are taken in different bands (using different bandpass filters). For example, the HST WFC3/IR ACS and the JWST NIRCAM/MIRI camera systems have multiple available filters. Examples of filters used by HST

and JWST are F814W and F115W, respectively, as discussed in the previous section. Telescope surveys, such as the Sloan Digital Sky Survey, the Dark Energy Survey, and LSST make use of the Johnson/Morgan – Kron/Cousins filter system ($ugrizY$ filters). [add citations here]

The general idea behind multi-band, multi-epoch fitting is to make use of all available information for a particular galaxy in order to improve the overall quality of the model fit and hence improve the robustness of lensing measurements. Below, I describe the implementation of this in my `Lenser` code. The idea for this technique exists for ellipticity measurement in e.g. Jarvis et al. [78]. In the following sections, I build on this formalism and extend it to flexion measurement for the first time.

2.6.1 Lenser multi-fit pipeline

In addition to extracting flexion measurements by fitting a (modified Sérsic) model to a single image of a galaxy, `Lenser` has the capability of doing multi-band, multi-epoch fitting. It is the first, and currently only, code capable of doing this for flexion measurement.

In multi-epoch fitting, `Lenser` fits a single model to all available postage stamp images of a particular galaxy, where each postage stamp represents an epoch. In this case, the epochs could be multiple epochs within a single band, and/or they could be epochs across multiple bands. The latter would be an example of multi-band fitting. For a simple example of multi-band fitting, consider a galaxy imaged in the r , i , and z bands, such that there is one epoch per band. Multi-band fitting in this case would consist of a simultaneous fit to the (r, i, z) bands in multi-fit mode, rather than just fitting the r band in single-fit mode.

Here, I will discuss how the `Lenser` multi-fit pipeline builds off of and modifies the single-fit pipeline. Imagine that there are N_{epoch} available epochs for a galaxy – again, these could be epochs within one band and/or across multiple bands.

For Step 1 of the pipeline (see Sec. 2.3.3), the `FITS()` class needs to be called for each epoch. It is assumed that associated with each epoch is a unique data map, noise/weight map, segmentation map, and PSF map. The galaxy is then instantiated by using the `MultiImage()` class, which holds one `Image()` object per epoch.

In Step 2 (see Sec. 2.3.4), an elliptical mask is generated for each epoch individually, and a total

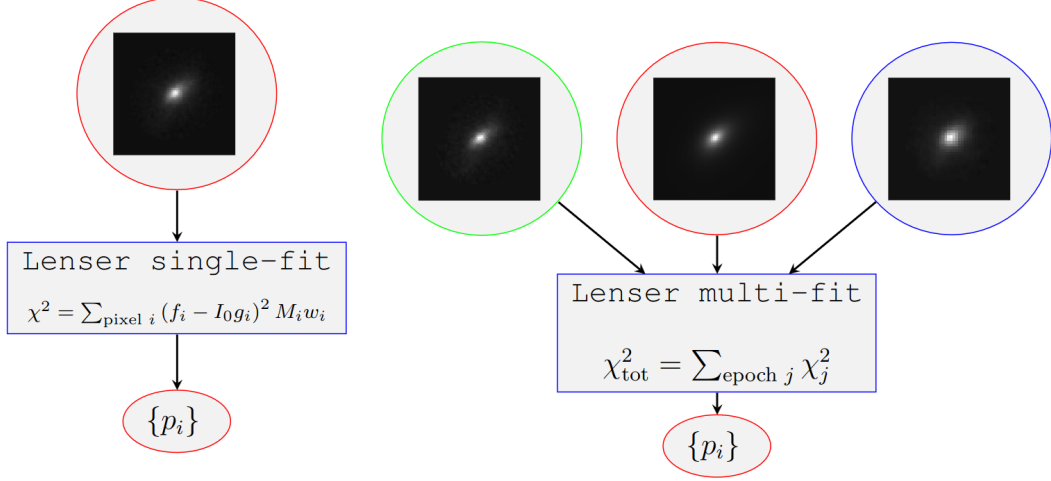


Figure 2.13: Schematic of the single-fit (left) and multi-fit (right) **LENSER** pipelines.

mask for each epoch is defined.

In Step 3 (see Sec. 2.3.5), image moments are calculated for each epoch in order to get estimates of $\{\theta_0^1, \theta_0^2, q, \phi, \psi_{ijk}\}$. This leaves us with N_{epoch} estimates of this parameter space. As the goal of multi-fit is to fit a single model to all epochs, I take as estimates of the parameter space to be the median of each parameter. For example, the estimate of q used in the next step of the **LENSER** pipeline is taken to be: $\text{median}(q_{(1)}, q_{(2)}, \dots, q_{(N_{\text{epoch}})})$. If for any epoch image moment calculations return NaN, this epoch is excluded from the median calculation for all parameters.

In Step 4 (see Sec. 2.3.6), the two-step χ^2 minimization is employed. For single-fit mode, the χ^2 is given by Eq. (2.29). In multi-fit mode, I define a total chi-squared:

$$\chi_{\text{tot}}^2 = \sum_{\text{epoch } j}^{N_{\text{epoch}}} \chi_j^2 \quad (2.39)$$

where χ_j^2 is the chi-squared value of fitting the multi-fit model to epoch j , and is given by Eq. (2.29), where f_i is the per-pixel value of the datamap of epoch j , g_i is the per-pixel normalized multi-fit model of the galaxy, and I_0 is calculated for each epoch. I define a reduced chi-squared:

$$\chi_{\text{tot}}^2 / \text{d.o.f.} = \frac{\chi_{\text{tot}}^2}{(\sum_j^{N_{\text{epoch}}} \sum_i M_i) - N_p} \quad (2.40)$$

such that $\sum_j^{N_{\text{epoch}}} \Sigma_i M_i$ is the total number of pixels across all available epochs.

While the `Lenser` parameter space is simultaneously fit to all available epochs, the non-fit parameter I_0 is allowed to vary across epochs. I_0 is simply calculated using Eq. (2.31) at each iteration of the minimization. `Lenser` then outputs the a list of the final I_0 values for each epoch.

Figure 2.13 shows a schematic of the `Lenser` multi-fit pipeline compared to the single-fit pipeline. Additionally, below I show a snippet of Python code that demonstrates how to run a single galaxy through the multi-fit pipeline. For this example, I use a galaxy from the COSMOS catalogue (from HST) with three epochs where each epoch is a different band – F814W, F606W, and F125W. This code is an example script provided in `Lenser` and can be found in

`/examples/run_real_gal/lenser_run_real_gal_multi_fit.py`.

```

1 import sys
2
3 sys.path.append('..')
4
5 from lenser import *
6
7 import numpy as np
8
9 from astropy.io import fits
10
11
12 # Read in images from FITS file. We will choose a galaxy from the COSMOS catalogue
13 # ... Band 1: F814W
14 # ... Specify path to science image
15 path_to_image = '../Catalogues/COSMOS/Images_F814W/COSMOS_5168_F814W.fits'
16 # ... Get science image, noisemap, segmentation mask (uberseg by default),
17 #      psfmap, and background mask from lenser_fits:
18 f = FITS(path_to_image)
19 dat_F814W = f.get_FITS('data')
20 rms_F814W = f.get_FITS('noise')
21 seg_F814W = f.get_FITS('segmask')
22 psf_F814W = f.get_FITS('psf')
23 bg_F814W = f.get_FITS('bgmask')
24
25 # ... Get name of object and band from path_to_image (can be overridden)
26 image_name_F814W = path_to_image.split('/')[-1].split('.')[0]
27 # ... Band 2: F606W
28 path_to_image = '../Catalogues/COSMOS/Images_F606W/COSMOS_5168_F606W.fits'

```

```

23 f = FITS(path_to_image)
24 dat_F606W = f.get_FITS('data')
25 rms_F606W = f.get_FITS('noise')
26 seg_F606W = f.get_FITS('segmask')
27 psf_F606W = f.get_FITS('psf')
28 bg_F606W = f.get_FITS('bgmask')
29 image_name_F606W = path_to_image.split('/')[-1].split('.')[0]
30 # ... Band 3: F125W
31 path_to_image = '../Catalogues/COSMOS/Images_F125W/COSMOS_5168_F125W.fits'
32 f = FITS(path_to_image)
33 dat_F125W = f.get_FITS('data')
34 rms_F125W = f.get_FITS('noise')
35 seg_F125W = f.get_FITS('segmask')
36 psf_F125W = f.get_FITS('psf')
37 bg_F125W = f.get_FITS('bgmask')
38 image_name_F125W = path_to_image.split('/')[-1].split('.')[0]
39
40 # Create a MultiImage instance
41 # ... Elliptical mask is generated and background subtracted by default
42 myMultiImage = MultiImage(namelist = [image_name_F814W, image_name_F606W,
43                                     image_name_F125W],
44                                     datalist = [dat_F814W, dat_F606W, dat_F125W],
45                                     noiselist = [rms_F814W, rms_F606W, rms_F125W],
46                                     uberseglist = [seg_F814W, seg_F606W, seg_F125W],
47                                     psflist = [psf_F814W, psf_F606W, psf_F125W],
48                                     bgmasklist = [bg_F814W, bg_F606W, bg_F125W])
49
50 # Initialize AIM model
51 myModel = aimModel(myMultiImage = myMultiImage)
52
53 # Run local minimization
54 myModel.runLocalMinRoutine()
55
56 # Reset the parameters to their default values

```

```
57 myModel.empty()
```

2.6.2 Testing the Lenser multi-fit framework

In order to test the robustness of the `Lenser` multi-fit pipeline, I make use of two different galaxy catalogues: the HST COSMOS catalogue and the Dark Energy Survey (DES) Year 3 (Y3) dataset. The DES Y3 dataset is the subject of Chapter 4. I ultimately use this dataset to create the DES Y3 Flexion Catalogue.

First, let us consider the COSMOS catalogue. I will make use of three different epochs for a sample of galaxies in the COSMOS catalogue. Each of the three epochs are three different bands: F814W, F606W, and F125W. I perform four different runs of the COSMOS catalogue through `Lenser`:

1. COSMOS single-band F814W fit
2. COSMOS single-band F606W fit
3. COSMOS single-band F125W fit
4. COMSOS multi-band (F814W, F606W, F125W) fit

With the output from `Lenser`, I calculate the ellipticity and flexion in each run as described in Sec. 2.5.4.

It is interesting to look at how measurements of \mathcal{F} -flexion, for example, compare across the four different `Lenser` runs. There are $N(N - 1) = 12$ different combinations of the $N = 4$ different `Lenser` runs – e.g. F814W versus F606W, F814W versus multi-fit, etc. For each of the 12 run combinations, one can look at the correlation of flexion measurements. We have already considered an example of comparing flexion measurements of a set of galaxies in Abell 2744 across two different bands in Sec. 2.5.4. We should therefore expect there to be some reasonable correlation between the flexion measurements in two different bands in the COSMOS catalogue, too. We also want to investigate, though, how single-band fits compare to the multi-band fit.

In Figs. 2.14 - 2.18, I show plots of the run combinations for ϵ_i , \mathcal{F}_i , \mathcal{G}_i , $a\mathcal{F}_i$, and $a\mathcal{G}_i$, respectively. The galaxies used in these plots are a subsample of those in the COSMOS catalogue. The subsample is drawn from the `Lenser` output, but it is restricted to only those galaxies that simultaneously pass a number of selection cuts in all four runs. These selection cuts are: $\chi^2/\text{d.o.f.} < 1.5$, $a|\mathcal{F}| < 0.4$, $a|\mathcal{G}| < 0.8$, and $a > 0.5$ pixels.

From these correlation plots, we notice a number of interesting things. First, there is very strong correlation of the ellipticity measurements across all four runs. The multi-band run tends to have a higher level of correlation with the single-band runs than the single-band runs do with each other. The flexion correlations are generally quite strong, although not as strong as the ellipticity measurements. Again, as discussed in Sec. 2.5.4, flexion is an inherently more difficult signal to measure than ellipticity, as it is a higher-order effect, and we therefore expect more scatter in these measurements. We also tend to see higher correlation for \mathcal{F} than \mathcal{G} . This is also unsurprising, given the fact that \mathcal{G} is a noisier signal and more difficult to measure given its complicated spin-3 property. That being said, it is still the case that flexion measurement in one band is correlated with flexion measurement in another, and flexion measurement in one band is correlated with a multi-band fit. The latter fact indicates that the multi-band fitting is reasonably incorporating the information from all available bands.

There is an additional interesting trend that can be noticed with the flexion correlations. Among the single-band fits, there is both a consistently higher correlation between F814W versus F606W compared to F814W versus F125W, as well as a slope closer to unity. The difference between the mean wavelength of the filters is larger for F814W–F125W than F814W–F606W. While underlying gravitational lensing signals are achromatic and therefore do not vary as a function of wavelength, I hypothesize that the intrinsic flexion *does* vary as a function of wavelength, and hence, a measured flexion signal varies as a function of band. If this were the case, it would explain why there is lower correlation between measured flexion signals across two bands as a function of wavelength separation between the bands.

Next, let us consider a similar analysis using the DES Y3 dataset. In the DES Y3 dataset,

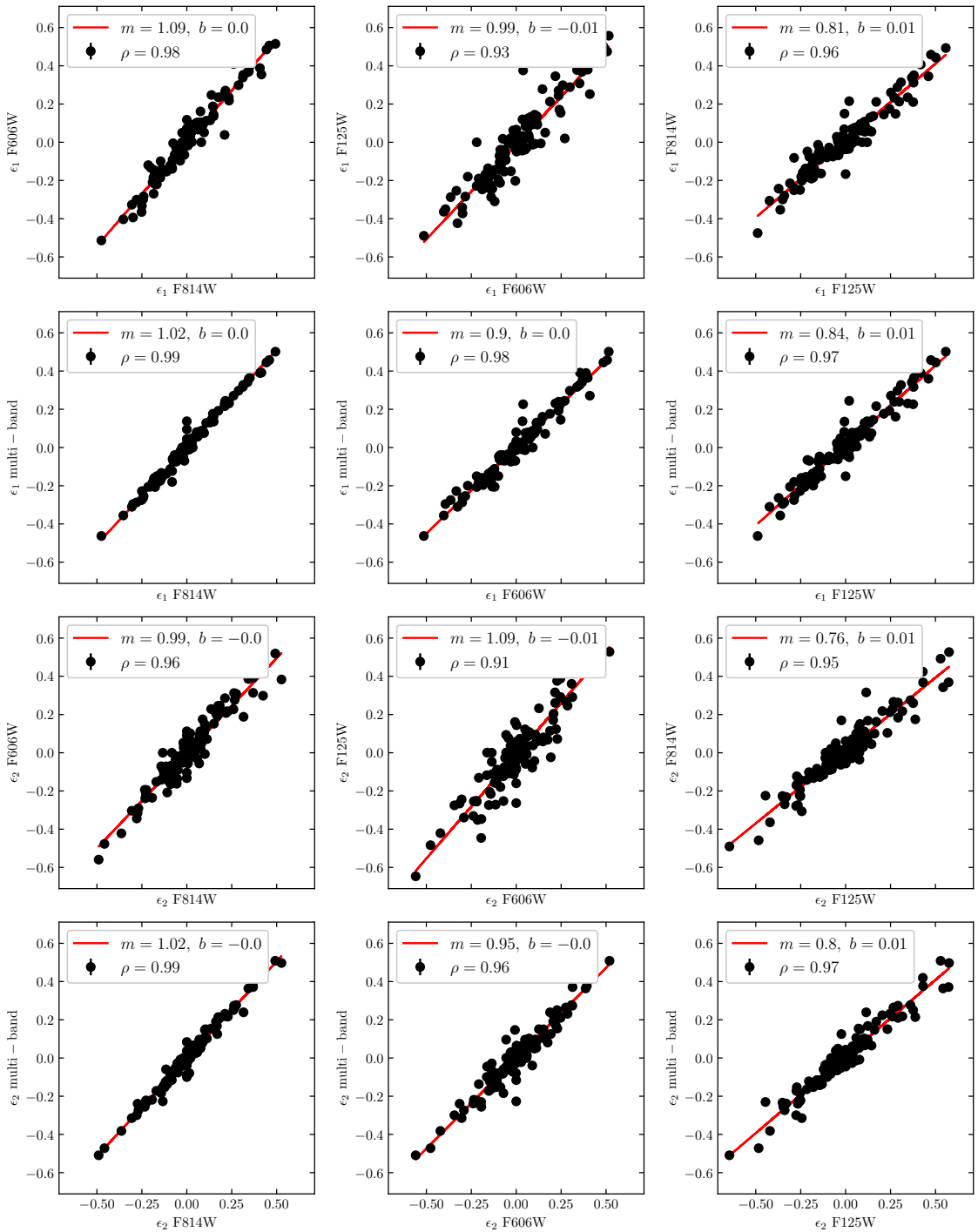


Figure 2.14: Ellipticity, ϵ_i , measurements for the subsample of galaxies in the COSMOS catalogue. The twelve panels in the plot are the twelve different combinations of the four LENSER runs. In these plot legends, ρ is the Pearson correlation coefficient. The red line is a best-fit to $y = mx + b$, and the best-fit slope and y -intercept values are given in the legend of each plot.

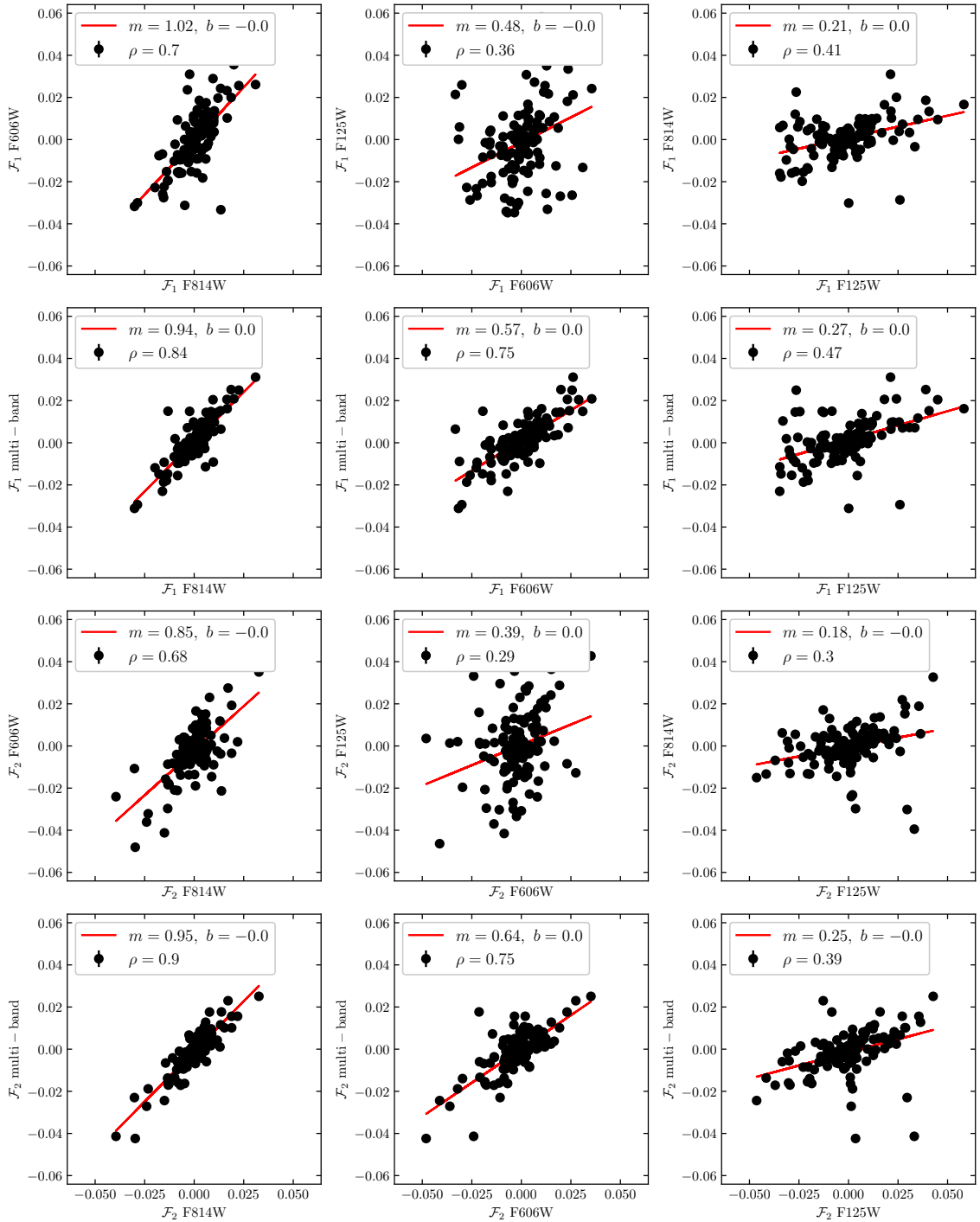


Figure 2.15: \mathcal{F} -flexion, \mathcal{F}_i , measurements for the subsample of galaxies in the COSMOS catalogue. The twelve panels in the plot are the twelve different combinations of the four **Lenser** runs. In these plot legends, ρ is the Pearson correlation coefficient. The red line is a best-fit to $y = mx + b$, and the best-fit slope and y -intercept values are given in the legend of each plot. The units of \mathcal{F}_i are inverse pixels.

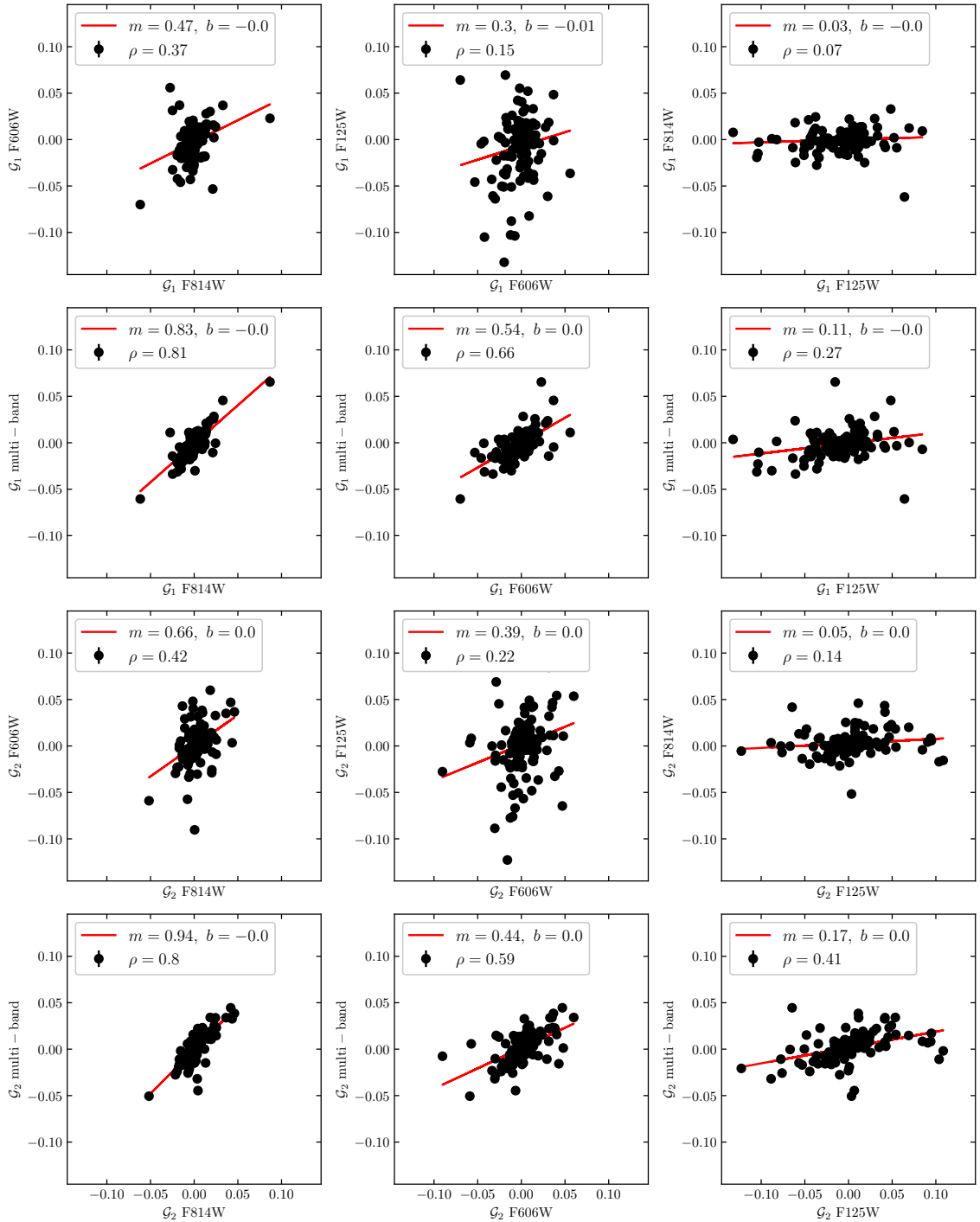


Figure 2.16: \mathcal{G} -flexion, \mathcal{G}_i , measurements for the subsample of galaxies in the COSMOS catalogue. The twelve panels in the plot are the twelve different combinations of the four Lenser runs. In these plot legends, ρ is the Pearson correlation coefficient. The red line is a best-fit to $y = mx + b$, and the best-fit slope and y -intercept values are given in the legend of each plot. The units of \mathcal{G}_i are inverse pixels.

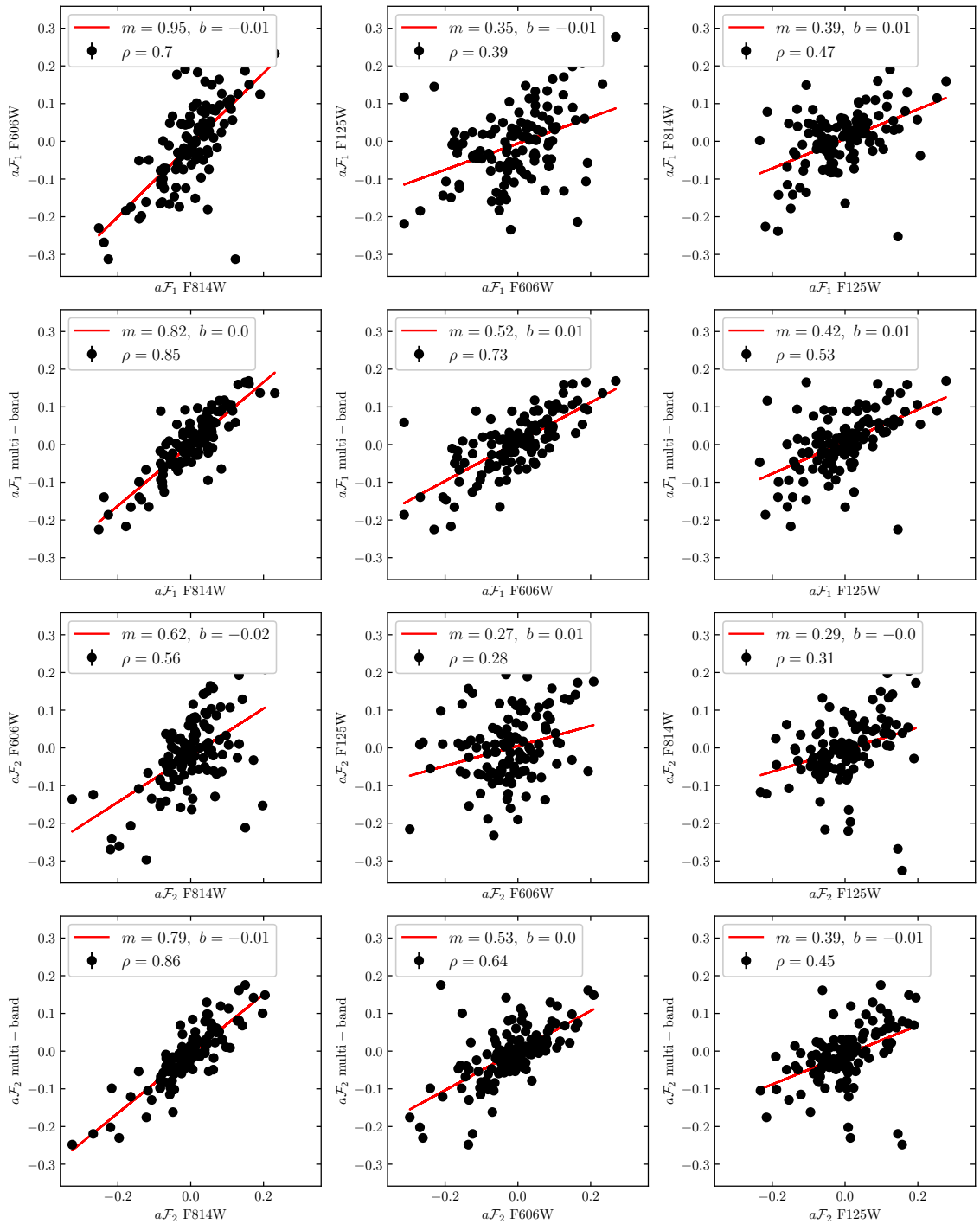


Figure 2.17: Dimensionless \mathcal{F} -flexion, $a\mathcal{F}_i$, measurements for the subsample of galaxies in the COSMOS catalogue. The twelve panels in the plot are the twelve different combinations of the four Lenser runs. In these plot legends, ρ is the Pearson correlation coefficient. The red line is a best-fit to $y = mx + b$, and the best-fit slope and y -intercept values are given in the legend of each plot.

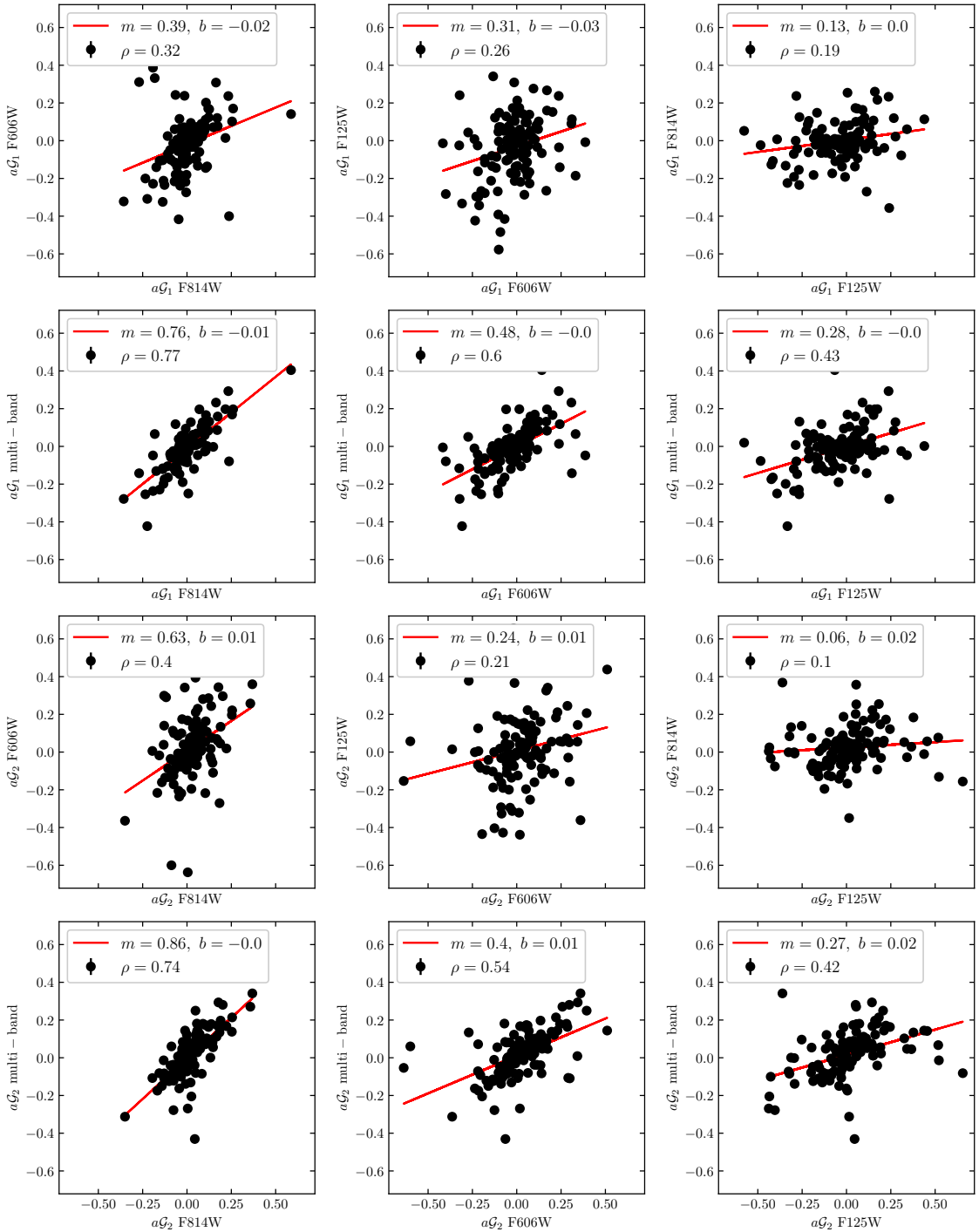


Figure 2.18: Dimensionless \mathcal{G} -flexion, $a\mathcal{G}_i$, measurements for the subsample of galaxies in the COSMOS catalogue. The twelve panels in the plot are the twelve different combinations of the four Lenser runs. In these plot legends, ρ is the Pearson correlation coefficient. The red line is a best-fit to $y = mx + b$, and the best-fit slope and y -intercept values are given in the legend of each plot.

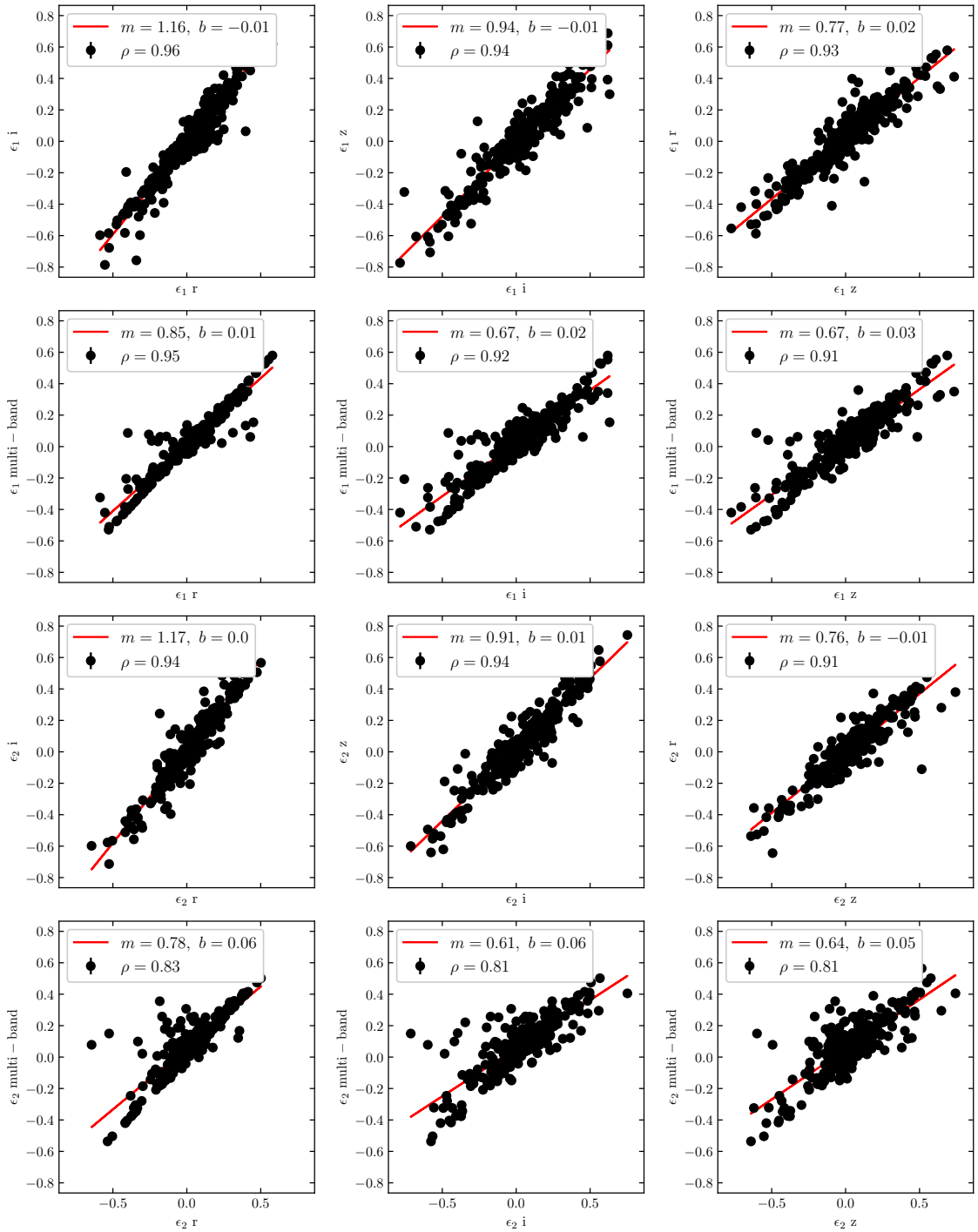


Figure 2.19: Ellipticity, ϵ_i , measurements for the subsample of galaxies in the DES Y3 dataset. The twelve panels in the plot are the twelve different combinations of the four LENSER runs. In these plot legends, ρ is the Pearson correlation coefficient. The red line is a best fit to $y = mx + b$, and the best-fit slope and y -intercept values are given in the legend of each plot.

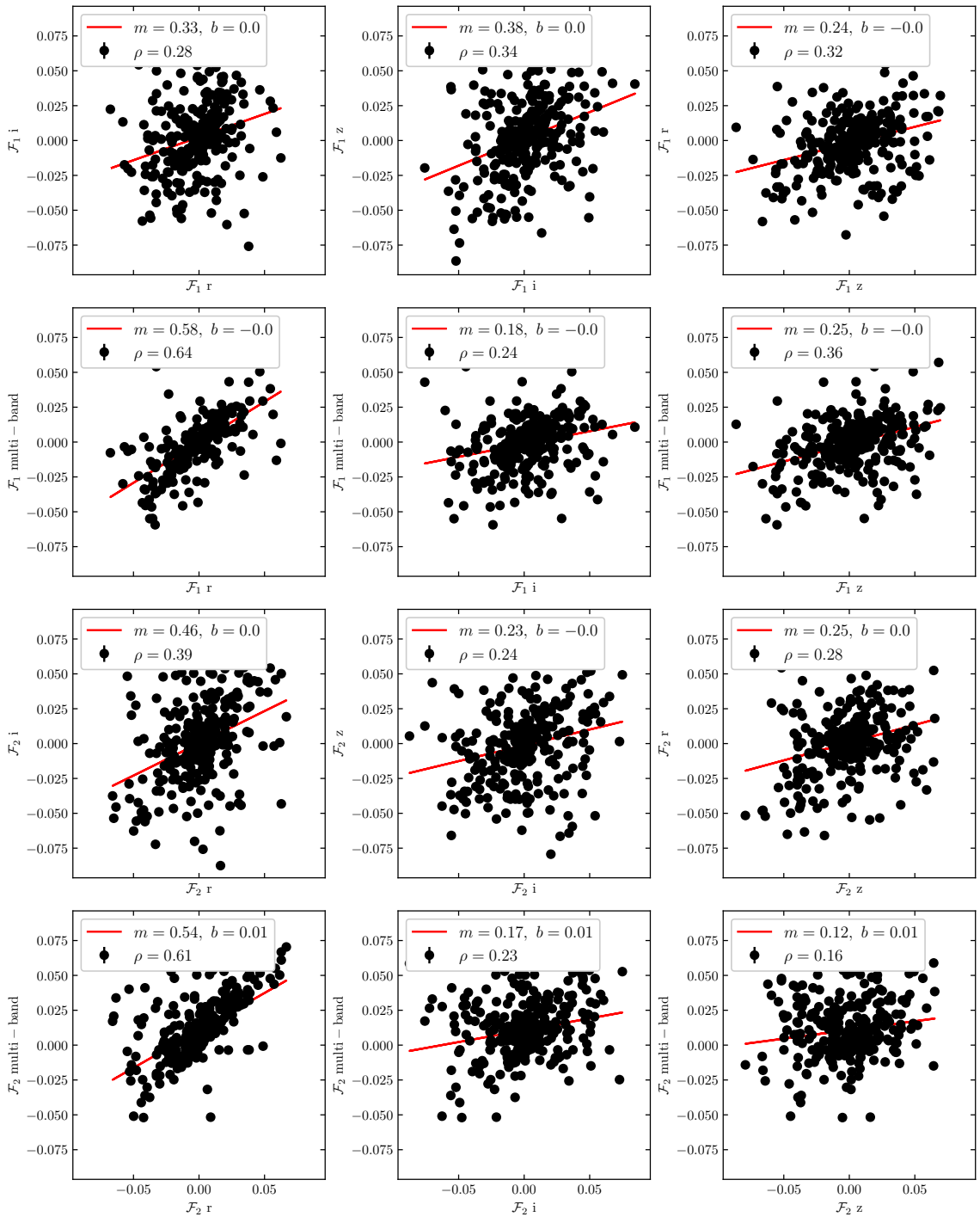


Figure 2.20: \mathcal{F} -flexion, \mathcal{F}_i , measurements for the subsample of galaxies in the DES Y3 dataset. The twelve panels in the plot are the twelve different combinations of the four **Lenser** runs. In these plot legends, ρ is the Pearson correlation coefficient. The red line is a best fit to $y = mx + b$, and the best-fit slope and y -intercept values are given in the legend of each plot. The units of \mathcal{F}_i are inverse pixels.

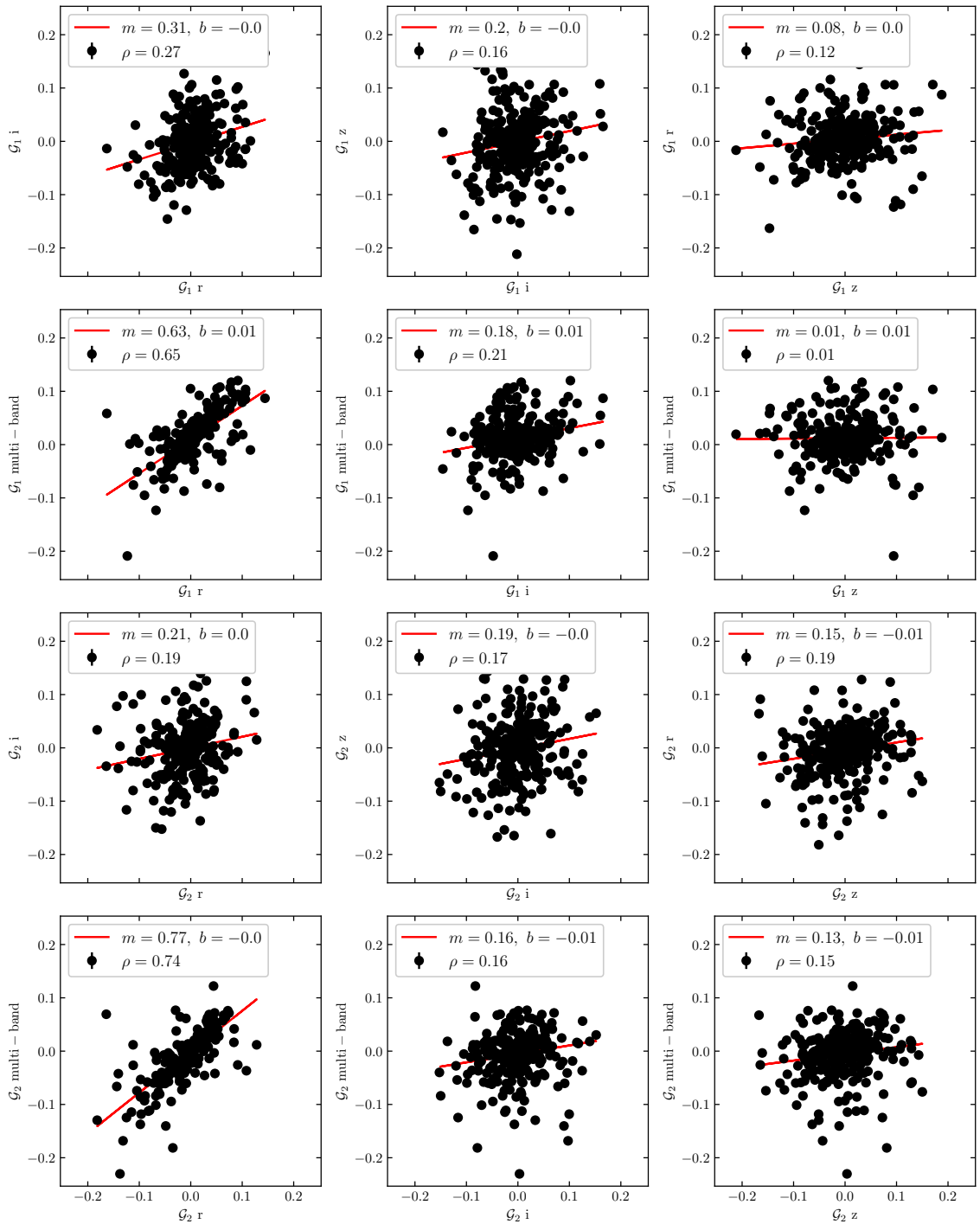


Figure 2.21: \mathcal{G} -flexion, \mathcal{G}_i , measurements for the subsample of galaxies in the DES Y3 dataset. The twelve panels in the plot are the twelve different combinations of the four **Lenser** runs. In these plot legends, ρ is the Pearson correlation coefficient. The red line is a best fit to $y = mx + b$, and the best-fit slope and y -intercept values are given in the legend of each plot. The units of \mathcal{G}_i are inverse pixels.

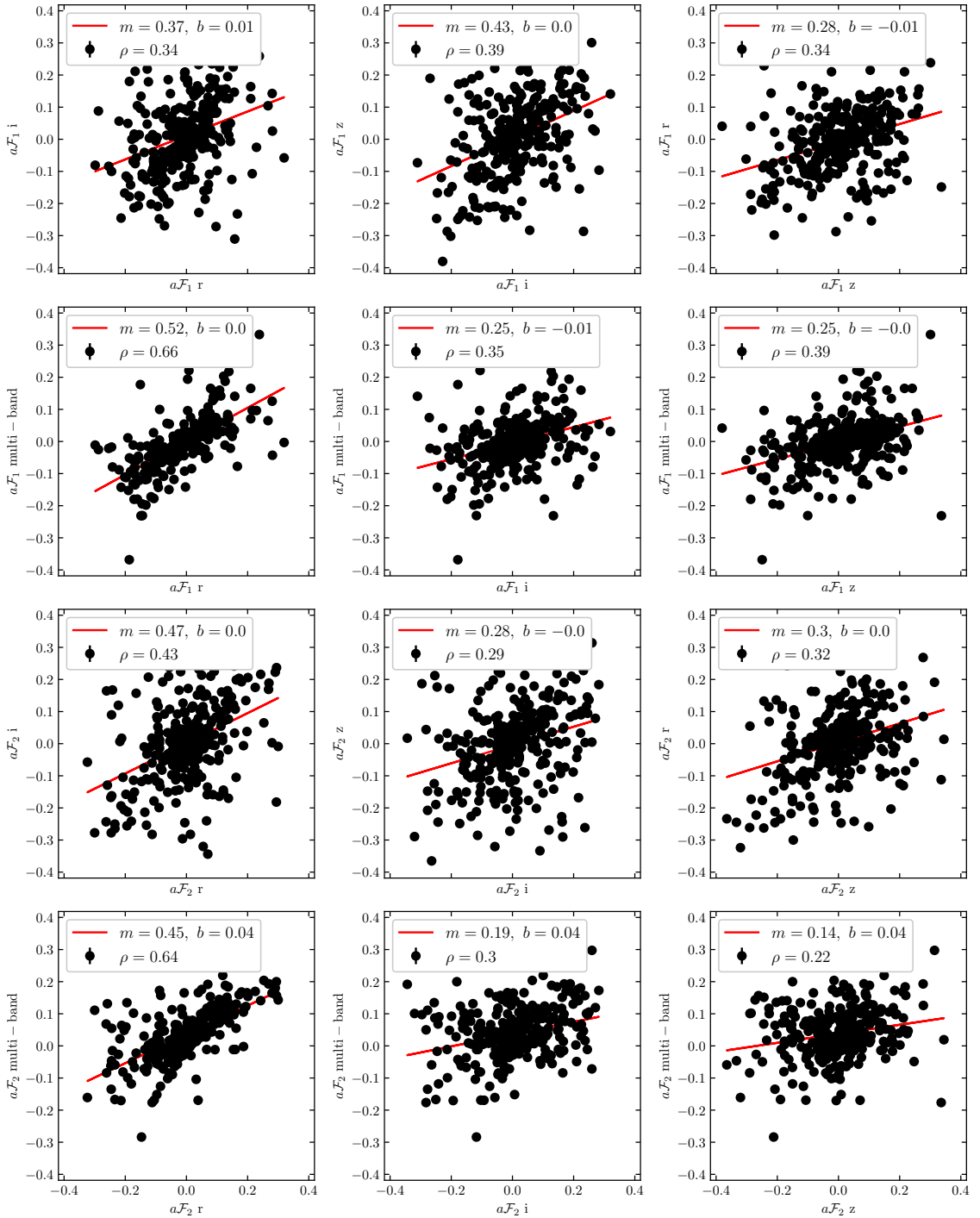


Figure 2.22: Dimensionless \mathcal{F} -flexion, $a\mathcal{F}_i$, measurements for the subsample of galaxies in the DES Y3 dataset. The twelve panels in the plot are the twelve different combinations of the four **Lenser** runs. In these plot legends, ρ is the Pearson correlation coefficient. The red line is a best fit to $y = mx + b$, and the best-fit slope and y -intercept values are given in the legend of each plot.

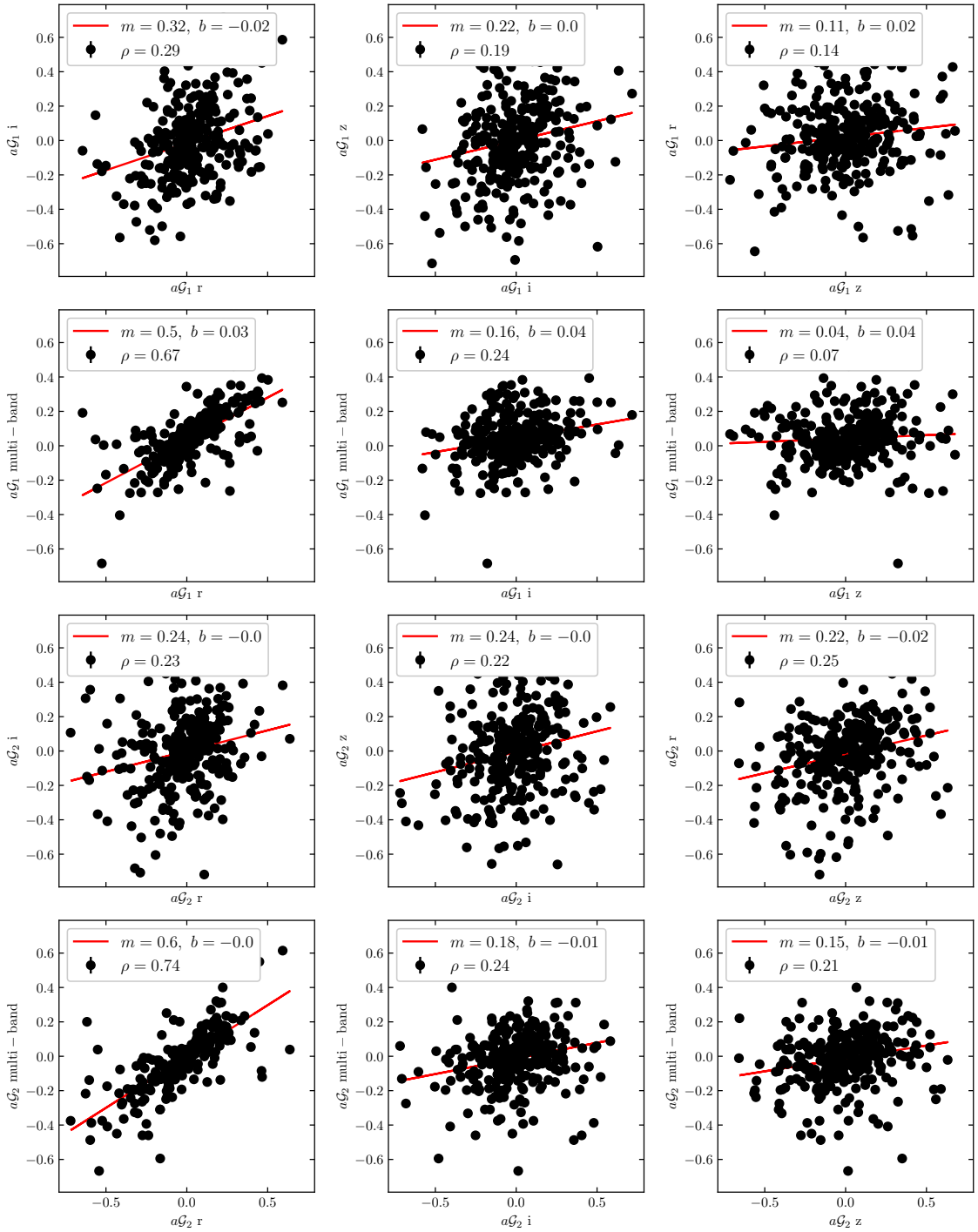


Figure 2.23: Dimensionless \mathcal{G} -flexion, $a\mathcal{G}_i$, measurements for the subsample of galaxies in the DES Y3 dataset. The twelve panels in the plot are the twelve different combinations of the four **Lenser** runs. In these plot legends, ρ is the Pearson correlation coefficient. The red line is a best fit to $y = mx + b$, and the best-fit slope and y -intercept values are given in the legend of each plot.

galaxies are imaged over multiple epochs and multiple bands. I choose to work with coadd rather than single-epoch images, and I make use of three different bands: r , i , and z . While the DES Y3 dataset contains ~ 400 M objects, ~ 100 M of which are galaxies that are successfully fit by the DES Y3 shear measurement pipeline, METACALIBRATION (see Chapter 4), I choose to work with a small subset – one DES tile of 23732 objects – in order to analyze single- and multi-band fitting.

Using this subset, I carried out the following runs:

1. DES single-band r fit
2. DES single-band i fit
3. DES single-band z fit
4. DES multi-band (r, i, z) fit

It is important to emphasize that not all of these objects in the subset are galaxies, and not all of those galaxies successfully made it through the METACALIBRATION pipeline and subsequent DES Y3 Shape Catalogue data cuts (see Sec. 4.2). After each of the four runs, I select only for objects that are galaxies passing the DES Y3 Shape Catalogue data cuts, as well my own selection cuts, described in Sec. 4.2.

In Figs. 2.19 - 2.18, I show plots of the run combinations for ϵ_i , \mathcal{F}_i , \mathcal{G}_i , $a\mathcal{F}_i$, and $a\mathcal{G}_i$, respectively. The galaxies used in these plots are from the DES Y3 subsample described above, further restricted to those galaxies that simultaneously pass selection cuts in all four runs. We notice that overall, the behavior of the correlation is largely similar to that of the COSMOS catalogue. Given the level of correlation between the multi-band fit and the single-band fits, this functions as an additional, independent verification that the multi-band fitting is reasonably incorporating all of the information from the three bands.

It is evident from the DES Y3 subsample correlations that the strongest correlation exists between the single-band r fit and the multi-band (r, i, z) fit, i versus (r, i, z) is the next strongest correlation, and z versus (r, i, z) is the weakest. As it turns out, the r band is the highest S/N of the three, and z is the weakest S/N [81]. This emphasizes an important feature of the **Lenser** multi-band, multi-

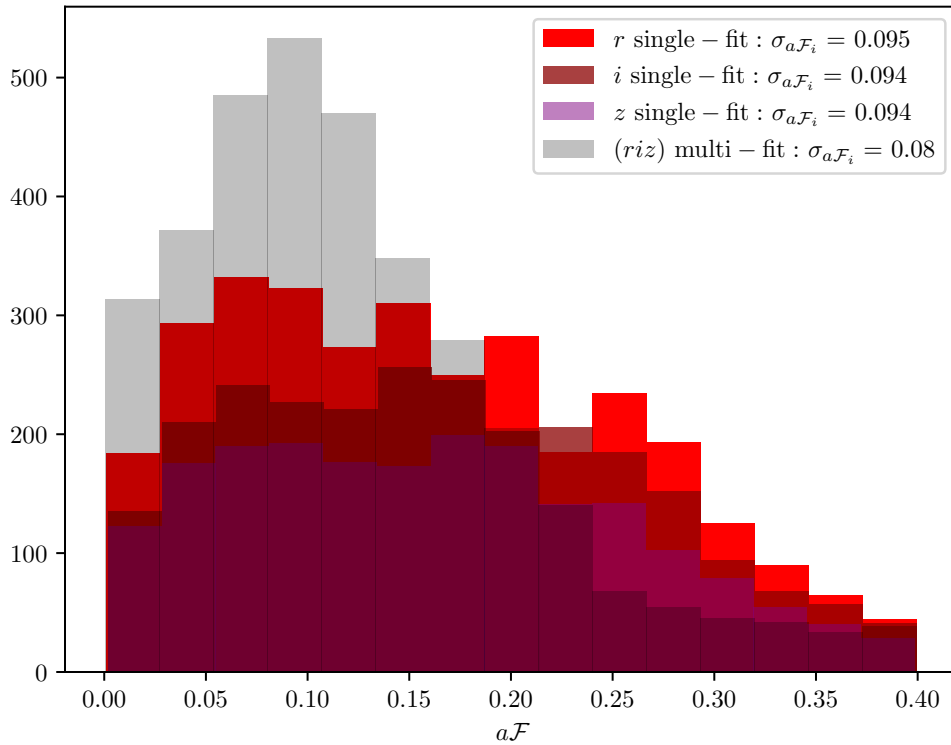


Figure 2.24: Plotted is the distribution of the magnitude of dimensionless flexion, $a|\mathcal{F}|$ for each of the four DES Y3 dataset subsample runs. In the legend are the per-component scatter in $a\mathcal{F}_i$ for each run.

epoch fitting framework: epochs and bands used in the multi-fit pipeline are weighted appropriately based on overall S/N by the total chi-squared figure of merit given by Eq. (2.39). This means that noisier epochs are automatically downweighted, and the user does not need to worry about noisy epochs degrading the overall shape measurement.

2.6.3 Conclusions: why use multi-band, multi-epoch fitting?

So far, it has been demonstrated that the `Lenser` multi-band, multi-epoch pipeline correctly makes use of all available epochs and bands, weights them appropriately, and reconstructs the shape and lensing parameters of galaxies. It is natural to ask the question: why make use of multi-band, multi-epoch fitting as opposed to simply making use of a single epoch or band? After all, one might reasonably expect that making use of N_{epochs} will increase the overall `Lenser` run-time by

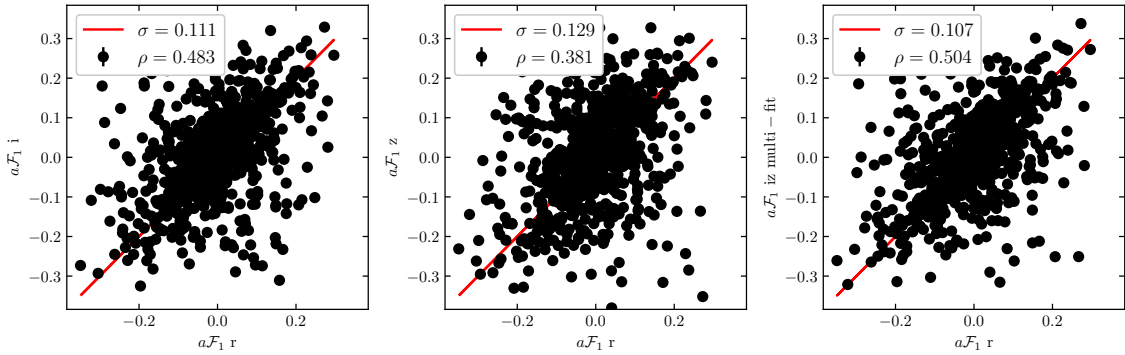


Figure 2.25: A subsample of 772 galaxies from the DES Y3 dataset run through `Lenser` in single-band r , i and z as well as an (i, z) multi-band run. The scatter of flexion estimates (σ in the legend) about $y = x$ in the single-band r fit versus (i, z) multi-band fit is smaller than either individually. We also see that the Pearson correlation coefficient (ρ in the legend) is highest for (i, z) multi-band fit versus single-band r fit.

introducing many more pixels that are used by the fitting routine. With the trade off of increasing the run time of `Lenser` reconstruction, in general, I find three benefits to multi-band, multi-epoch fitting for flexion measurement with `Lenser`.

First, I find that multi-band fitting yields successful fits for a slightly larger percentage of a sample of galaxies compared to single-fit mode. This can be seen by comparing the four different DES Y3 subsample runs. If I apply the selection cuts to the four runs individually and do not require that all galaxies pass selection cuts in all runs *simultaneously*, we get a different number of galaxies in each run. In the single-band fits, we are left with 3183, 2540, and 2003 galaxies after selection cuts for the r , i , and z bands, respectively. The fact that the r band achieves the largest number of successful fits while z the fewest is a consequence of r being the highest S/N band. For the multi-band fit, we successfully fit 3424 galaxies – a modest 3% increase relative to the r band only.

Second, I also find that multi-band fitting has a smaller intrinsic flexion scatter than single-band fitting. As shown in Fig. 2.24, I find, for example, a scatter in per-component intrinsic flexion of $\sigma_{a\mathcal{F}_i} \simeq 0.095$ in the r , i , and z bands in single-fit mode, but a smaller $\sigma_{a\mathcal{F}_i} = 0.08$ in a simultaneous (r, i, z) multi-band fit. This ancillary benefit allows for a stronger detection of gravitational flexion signals, as the dominant noise term in any flexion estimate is due to intrinsic flexion. Referring to

my earlier hypothesis of intrinsic flexion varying as a function of band, it may be the case that the multi-band fitting is able to average over this effect, minimizing the variance of intrinsic flexion over multiple bands.

Third, multi-band fitting offers a more accurate flexion measurement than single-band fitting. As long as the `Lenser` multi-fit pipeline is working correctly, it is not unsurprising that the flexion measurements from a multi-band (r, i, z) fit is correlated with those from single-band r fit – after all, the (r, i, z) fit uses information from the r band. If multi-band fitting is truly a more accurate flexion measurement technique than single-band fitting, then we should expect that a multi-band fit using (i, z) only is strongly correlated with a single-band r fit, more so than r versus i alone or z alone. As such, I ran a fifth DES Y3 dataset run, this time using an (i, z) multi-band fit. Shown in Fig. 2.25 is a comparison of three different runs: single-band r , single-band i , single-band z , and multi-band (i, z) . First, we see that the scatter of flexion measurements about $y = x$ in the single-band r fit versus (i, z) multi-band fit is smaller than that for single-band r versus single-band i and single-band r versus single-band z . We also see that the correlation is strongest for (i, z) multi-band fit versus single-band r fit. Indeed, multi-band fitting provides a more accurate flexion measurement than single-band fitting.

Chapter 3: Cosmic Flexion in Theory

3.1 Introduction

Cosmological studies of the Cosmic Microwave Background (CMB) have found that observations agree with the standard model of cosmology (Λ CDM) to remarkable accuracy [82, 24, 25, 28]. As we look at more recent parts of cosmic history, using tools such as weak lensing, Λ CDM still appears to be the law of the land. Subtle discrepancies are found, however, between these low-redshift observations and the high-redshift measurements of the CMB [83, 28, 84, 85]. These discrepancies could indicate that Λ CDM might not be sufficient to connect all parts of the cosmic history [86, 87, 88]. It is therefore necessary to have multiple cosmological probes that complement each other in order to get the full picture of cosmology across all length scales and cosmic times.

As was discussed in Secs. 1.2 and 1.3, gravitational lensing has become one of the quintessential cosmological and astrophysical probes of the last few decades. Lensing probes the gravitational potential and is therefore a useful measure of the total matter distribution. To this end, lensing has had a great impact at several different mass scales. From Sec. 1.2.9, we know that lensing is powerful for studying galaxy cluster mass distributions [89, 90]. Also from Sec. 1.2.9 we know that a weaker effect, known as galaxy-galaxy lensing, is the lensing of a background galaxy by a foreground galaxy. Specifically, galaxy-galaxy shear correlates the shapes of high-redshift “source” galaxies with positions of low-redshift “lensing” galaxies [91, 92]. Even weaker is the lensing by the large-scale structure of the Universe – specifically, the so-called cosmic shear – which probes the underlying matter power spectrum [93, 94, 95, 96], as discussed in Sec. 1.3. Finally, lensing of the CMB has also been detected at high significance [28], which has been a further useful probe of cosmological parameters.

In studies interested in using low-redshift lensing measurements to extract cosmological information, cosmic shear is often combined with galaxy-galaxy lensing, along with galaxy clustering, which allows for very high constraining power on cosmological parameters [83].

Beyond shear, there exists a higher-order lensing effect known as *flexion* [42, 43, 44, 45], which was introduced in Sec. 1.2.9. In this Chapter, we will consider the as-of-yet undetected cosmic flexion signal, the analogue to cosmic shear. Cosmic flexion is the flexion correlation function whose signal originates from the large-scale structure of the Universe. Cosmic shear has proven to be a highly valuable cosmological probe; cosmic flexion therefore warrants further investigation in order to determine the extent to which it is cosmologically useful. Cosmic flexion is much more difficult to detect than cosmic shear, owing to (i) its weaker signal-to-noise ratio (S/N) on the scale of typical galaxy-galaxy separation, (ii) the fact that it peaks at small, nonlinear scales, and (iii) the lack of an appropriate tool for measuring this signal – until now. We also consider cosmic shear-flexion – i.e., the cross-correlation between cosmic shear and flexion – which has a higher S/N than flexion-flexion, albeit at different angular scales.

We will first present the theory of cosmic flexion. We then consider the feasibility of detecting this signal in Stage III lensing surveys such as the Dark Energy Survey¹ (DES; [97]), the Kilo-Degree Survey² (KiDS; [98]) and the Hyper Suprime-Cam Subaru Strategic Program³ (HSC SSP; [99]), with the aim of constraining the normalization and slope of small-scale cosmic structure. We then comment on improvements from Stage IV surveys such as the Legacy Survey of Space and Time with the Vera C. Rubin Observatory⁴ (LSST; [100]), Euclid⁵ [101], and the Nancy Grace Roman Space Telescope⁶ [102], as well as physics that may be constrained by these results.

3.2 The Theory of Cosmic Flexion

3.2.1 Cosmic Lensing Power Spectra

Starting with the cosmological effective convergence as Bartelmann and Schneider [41], one can obtain the convergence power spectrum via Limber’s equation [59, 60]:

$$\mathcal{P}_\kappa(\ell) = \int_0^{\chi_H} d\chi \frac{q^2(\chi)}{\chi^2} \mathcal{P}_{\text{NL}} \left(k = \frac{\ell + 1/2}{\chi}, \chi \right) \quad (3.1)$$

¹<https://www.darkenergysurvey.org>

²<https://kids.strw.leidenuniv.nl>

³<https://hsc.mtk.nao.ac.jp/ssp>

⁴<https://www.lsst.org>

⁵<https://www.euclid-ec.org>

⁶<https://roman.gsfc.nasa.gov>

where the lensing efficiency function

$$q(\chi) = \frac{3}{2} \Omega_m \left(\frac{H_0}{c} \right)^2 \frac{\chi}{a(\chi)} \int_{\chi}^{\chi_H} d\chi' n(\chi') \frac{\chi' - \chi}{\chi'}. \quad (3.2)$$

In these expressions, H_0 is the Hubble constant, Ω_m is the matter density at the present epoch, c is the speed of light, χ is comoving distance, χ_H is the horizon distance, a is the scale factor, k is the comoving wavenumber, $\mathcal{P}_{\text{NL}}(k, z)$ is the (nonlinear) matter power spectrum⁷ as a function of k and redshift, z , and $n(\chi)$ is the effective number density of (source) galaxies as a function of χ , normalized such that $\int_0^\infty d\chi n(\chi) = 1$. The lensing efficiency function, and hence the power spectrum, depends on the redshift distribution of galaxies, $n(z)$, which is in turn dependent on the galaxies available for a particular cosmological survey. We note that the convergence power spectrum was derived in Sec. 1.3; however, in this Chapter we will consider a flat Universe for convenience, such that $f_K(\chi) = \chi$ (see Eq. 1.5).

As we recall from Sec. 1.3, in the case of cosmic shear, it is the shear that is measured from observed galaxy shapes, not the convergence. However, it is conveniently the case that [4]

$$\mathcal{P}_\gamma(\ell) = \mathcal{P}_\kappa(\ell). \quad (3.3)$$

From Sec. 1.3, we recall that in BGRT it was shown that a cosmic flexion power spectrum can be derived along the same lines, with the additional step of differentiating the cosmological effective convergence, and then making use of Limber's equation. From this, we obtain

$$\mathcal{P}_{\mathcal{F}}(\ell) = \ell^2 \mathcal{P}_\kappa(\ell). \quad (3.4)$$

We also recall from Sec. 1.3 that

$$\mathcal{P}_g(\ell) = \mathcal{P}_{\mathcal{F}}(\ell). \quad (3.5)$$

BGRT also introduced the idea of a convergence-flexion cross spectrum. Again following Limber's

⁷We caution the reader that the nonlinear matter power spectrum must be used, as the cosmic flexion signal exists in the small-scale, nonlinear regime.

equation, one finds

$$\mathcal{P}_{\kappa\mathcal{F}}(\ell) = \mathcal{P}_{\kappa\mathcal{G}}(\ell) = \ell\mathcal{P}_\kappa(\ell). \quad (3.6)$$

We will use these power spectra later in the calculation of measurable two-point correlation functions.

3.2.2 Two-Point Correlation Functions: Cosmic Shear and Flexion

While one can try to measure the cosmic flexion (or shear) power spectra defined in Fourier space, it is often more straightforward to take measurements in real space. One can calculate real-space two-point correlation functions by taking a Hankel transform of the power spectrum. BGRT did this; however, they considered what turns out to be only one out of six possible nonzero cosmic flexion correlation functions.

Coordinate System

The shear and flexion correlation functions are defined by considering pairs of positions of galaxy images on the sky, $\boldsymbol{\vartheta}$ and $\boldsymbol{\theta} + \boldsymbol{\vartheta}$, and defining a coordinate system along the line connecting the two galaxies [4]. For shear, $\gamma = \gamma_1 + i\gamma_2$; these components are conventionally referred to as the “tangential” and “cross” components. These are defined at position $\boldsymbol{\vartheta}$ for this pair as $\gamma_t = -\Re\{\gamma e^{-2i\varphi}\}$ and $\gamma_x = -\Im\{\gamma e^{-2i\varphi}\}$, respectively, where φ is the polar angle of the separation vector $\boldsymbol{\theta}$.

This spin-2 cosmic shear coordinate system can be generalized to any combination of spin fields. Let $a = a_1 + ia_2$ and $b = b_1 + ib_2$ be two fields with spins s_a and s_b . Define $a'(\boldsymbol{\vartheta}_i)$ and $b'(\boldsymbol{\vartheta}_j)$ as the fields a and b at locations $\boldsymbol{\vartheta}_i$ and $\boldsymbol{\vartheta}_j$ rotated such that the x -axis of the tangential coordinate systems at directions $\hat{\boldsymbol{\vartheta}}_i$ and $\hat{\boldsymbol{\vartheta}}_j$ become aligned with the vector connecting both points. (Note: $\hat{\boldsymbol{\vartheta}}_i \cdot \hat{\boldsymbol{\vartheta}}_j = \cos\theta$ and $\boldsymbol{\theta} = \boldsymbol{\vartheta}_j - \boldsymbol{\vartheta}_i$.) We may then define the components in this rotated coordinate system as

$$\begin{pmatrix} a'_1 \\ a'_2 \end{pmatrix} = \text{csgn}[(-i)^{s_a}] R(s_a\varphi) \begin{pmatrix} a_1 \\ a_2 \end{pmatrix} \quad (3.7)$$

where $\text{csgn}(z)$ is the complex signum function and the (passive) rotation matrix is defined as

$$R(s_a\varphi) = \begin{pmatrix} \cos s_a\varphi & \sin s_a\varphi \\ -\sin s_a\varphi & \cos s_a\varphi \end{pmatrix}. \quad (3.8)$$

We choose to adopt this $\text{SO}(2)$ formalism rather than the conventional real- and imaginary-component formalism from the literature, as we believe it more straightforwardly demonstrates that this is a rotated coordinate system. We see, then, that

$$\begin{pmatrix} \gamma'_1 \\ \gamma'_2 \end{pmatrix} = -R(2\varphi) \begin{pmatrix} \gamma_1 \\ \gamma_2 \end{pmatrix}. \quad (3.9)$$

In the same way, we can define the rotated components of the lensing flexions $\mathcal{F} = \mathcal{F}_1 + i\mathcal{F}_2$ and $\mathcal{G} = \mathcal{G}_1 + i\mathcal{G}_2$ as

$$\begin{pmatrix} \mathcal{F}'_1 \\ \mathcal{F}'_2 \end{pmatrix} = -R(\varphi) \begin{pmatrix} \mathcal{F}_1 \\ \mathcal{F}_2 \end{pmatrix} \quad (3.10)$$

$$\begin{pmatrix} \mathcal{G}'_1 \\ \mathcal{G}'_2 \end{pmatrix} = +R(3\varphi) \begin{pmatrix} \mathcal{G}_1 \\ \mathcal{G}_2 \end{pmatrix}. \quad (3.11)$$

In Fig. 3.1, we show a sketch of the rotated two-point coordinate system in the case of the spin-1 \mathcal{F} -flexion.

It should be pointed out that, in this work, the conventional tangential and cross components of the shear, (γ_t, γ_x) , are referred to as (γ'_1, γ'_2) . The conventional names refer to the fact that $\gamma'_1 > 0$ corresponds to tangential alignment of galaxies around an overdensity, and the cross-component is oriented along a 45° angle with respect to the line connecting the galaxy pair. With the spin-1 \mathcal{F} -flexion, however, there is radially inward alignment around an overdensity, such that a tangential \mathcal{F} -flexion is analogous to a cross shear. To avoid the confusion arising from these different directional alignments of various spin fields, we instead choose to refer rather plainly to rotated 1- and 2-components. Furthermore, $\text{csgn} [(-i)^{s_a}]$ is introduced such that the \mathcal{G} -flexion has what can roughly

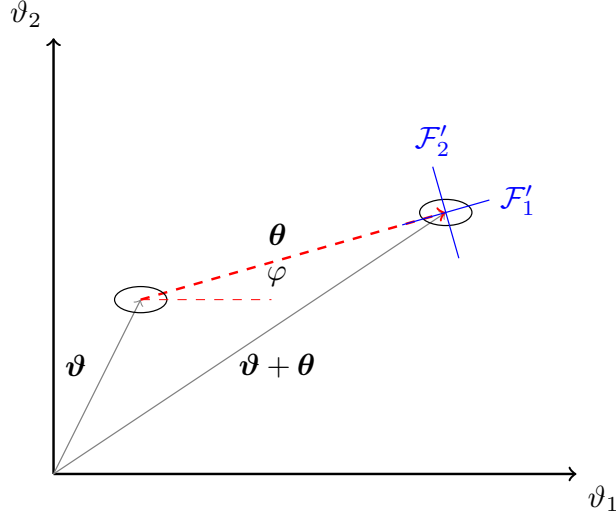


Figure 3.1: Sketch of the rotated two-point coordinate system for the case of the \mathcal{F} -flexion for two galaxies located at ϑ and $\vartheta + \theta$. The axes (without arrows) for the rotated flexion components: \mathcal{F}'_1 and \mathcal{F}'_2 are shown on the galaxy located at $\vartheta + \theta$. Note how \mathcal{F}'_1 is oriented along the separation vector θ .

be thought of as a radially outward alignment around an overdensity, as motivated by its behavior around a Singular Isothermal Sphere (SIS) lens (see 1.2.9, where $\gamma < 0$ and $\mathcal{F} < 0$ around an SIS lens, but $\mathcal{G} > 0$).

Real-Space Two-Point Correlation Functions

It is well known with cosmic shear that one can construct three two-point correlations from the two shear components, $\langle \gamma'_1 \gamma'_1 \rangle$, $\langle \gamma'_2 \gamma'_2 \rangle$, and $\langle \gamma'_1 \gamma'_2 \rangle$ [4]. The latter vanishes in a parity-symmetric Universe, since γ'_1 is parity invariant under a mirror transformation, but γ'_2 changes sign. The two nonzero correlations are then combined into the two components of the cosmic shear correlation functions.

In general, we can define two correlation functions [103]:

$$\xi_+^{ab}(\theta) = \Re \langle a'(\vartheta_i) b'^*(\vartheta_j) \rangle = \langle a'_1 b'_1 \rangle + \langle a'_2 b'_2 \rangle \quad (3.12)$$

$$\xi_-^{ab}(\theta) = \Re \langle a'(\vartheta_i) b'(\vartheta_j) \rangle = \langle a'_1 b'_1 \rangle - \langle a'_2 b'_2 \rangle. \quad (3.13)$$

where 1 and 2 refer to the components of each field and $\langle a'_1 b'_1 \rangle$ is shorthand for $\langle a'_1(\boldsymbol{\vartheta}_i) b'_1(\boldsymbol{\vartheta}_j) \rangle$.

Therefore, in addition to the well known cosmic shear correlation functions⁸

$$\xi_{\pm}^{\gamma\gamma}(\theta) = \langle \gamma'_1 \gamma'_1 \rangle \pm \langle \gamma'_2 \gamma'_2 \rangle, \quad (3.14)$$

we posit the existence of six cosmic flexion correlation functions. Firstly, there are the autocorrelations of each flexion field

$$\xi_{\pm}^{\mathcal{F}\mathcal{F}}(\theta) = \langle \mathcal{F}'_1 \mathcal{F}'_1 \rangle \pm \langle \mathcal{F}'_2 \mathcal{F}'_2 \rangle \quad (3.15)$$

$$\xi_{\pm}^{\mathcal{G}\mathcal{G}}(\theta) = \langle \mathcal{G}'_1 \mathcal{G}'_1 \rangle \pm \langle \mathcal{G}'_2 \mathcal{G}'_2 \rangle. \quad (3.16)$$

Secondly, there is a cross-correlation between the two flexion fields (we will see that this is nonzero in Section 3.2.4 below):

$$\xi_{\pm}^{\mathcal{F}\mathcal{G}}(\theta) = \langle \mathcal{F}'_1 \mathcal{G}'_1 \rangle \pm \langle \mathcal{F}'_2 \mathcal{G}'_2 \rangle. \quad (3.17)$$

Of these six possible correlations, only $\xi_{+}^{\mathcal{F}\mathcal{F}}(\theta)$ was considered in BGRT.

In addition to the shear-shear and flexion-flexion correlations listed above, we further posit the existence of shear-flexion cross-correlations, given by⁹

$$\xi_{\pm}^{\gamma\mathcal{F}}(\theta) = \langle \gamma'_1 \mathcal{F}'_1 \rangle \pm \langle \gamma'_2 \mathcal{F}'_2 \rangle \quad (3.18)$$

$$\xi_{\pm}^{\mathcal{G}\gamma}(\theta) = \langle \mathcal{G}'_1 \gamma'_1 \rangle \pm \langle \mathcal{G}'_2 \gamma'_2 \rangle. \quad (3.19)$$

Again, we will find these to be non-zero in Section 3.2.4. In Fig. 3.2, we show a cartoon of the auto- and cross-correlations of \mathcal{F} -flexion and shear for a galaxy pair in real space.

⁸ $\xi_{\pm}^{\gamma\gamma}$ is referred to simply as ξ_{\pm} in the cosmic shear literature, owing to the fact that it is currently the only lensing field correlation that is widely considered.

⁹One may be curious as to why we choose the ordering shear-flexion for $\gamma\mathcal{F}$, but flexion-shear for $\mathcal{G}\gamma$. Simply put, we choose to have a convention where the spin of the first field is greater than or equal to that of the second.

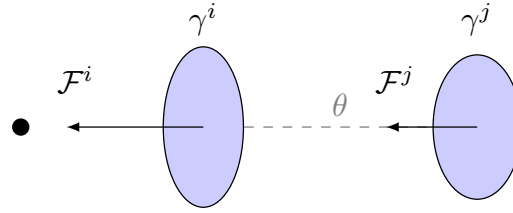


Figure 3.2: A galaxy pair (i, j) with separation θ and polar angle $\varphi_{ij} = 0$ perturbed by a nearby mass distribution (on the left). In this case, the overdensity is along the line of the separation vector such that we have pure tangential shear, γ'_1 and radial flexion, \mathcal{F}'_1 (we assume that there is no intrinsic ellipticity or flexion in this case). The shear is represented by the ellipses and the spin-1 \mathcal{F} -flexion by the vectors. As galaxy (i) is closer to the overdensity, we see how the magnitude of the shear and flexion is larger for galaxy (i) than (j) . This cartoon illustrates how, for a given galaxy pair, flexion and shear are coupled between the objects, and to each other.

3.2.3 Relating the Correlation Functions to Power Spectra

In the flat-sky approximation, the two-point correlation functions are related to the angular power spectra via [103, 104, 105]

$$\xi_{\pm}^{ab}(\theta) = (\pm 1)^{s_a} \int_0^\infty \frac{d\ell}{2\pi} \mathcal{P}_{ab}(\ell) J_{s_b \mp s_a}(\ell\theta) \quad (3.20)$$

where $J_n(x)$ is the Bessel function of the first kind, order n . We do not derive this general equation in this paper. Rather, it is a modified version of that presented in Chisari et al. [103], where we have swapped s_a and s_b (we refer the reader to Appendix C for the justification of this).

From this general expression, we recover the well known relationship between the cosmic shear correlation functions and the convergence power spectrum:

$$\xi_{\pm}^{\gamma\gamma}(\theta) = \int_0^\infty \frac{d\ell}{2\pi} \mathcal{P}_\kappa(\ell) J_{0,4}(\ell\theta) \quad (3.21)$$

where $J_0(\ell\theta)$ and $J_4(\ell\theta)$ refer to $\xi_+^{\gamma\gamma}$ and $\xi_-^{\gamma\gamma}$, respectively. The flexion-flexion correlation functions

are then given by

$$\xi_{\pm}^{\mathcal{FF}}(\theta) = \pm \int_0^{\infty} \frac{d\ell}{2\pi} \mathcal{P}_{\mathcal{F}}(\ell) J_{0,2}(\ell\theta) \quad (3.22)$$

$$\xi_{\pm}^{\mathcal{GG}}(\theta) = \pm \int_0^{\infty} \frac{d\ell}{2\pi} \mathcal{P}_{\mathcal{F}}(\ell) J_{0,6}(\ell\theta) \quad (3.23)$$

$$\xi_{\pm}^{\mathcal{FG}}(\theta) = \pm \int_0^{\infty} \frac{d\ell}{2\pi} \mathcal{P}_{\mathcal{F}}(\ell) J_{2,4}(\ell\theta) \quad (3.24)$$

and the shear-flexion correlation functions are

$$\xi_{\pm}^{\gamma\mathcal{F}}(\theta) = \mp \int_0^{\infty} \frac{d\ell}{2\pi} \mathcal{P}_{\kappa\mathcal{F}}(\ell) J_{1,3}(\ell\theta) \quad (3.25)$$

$$\xi_{\pm}^{\mathcal{G}\gamma}(\theta) = - \int_0^{\infty} \frac{d\ell}{2\pi} \mathcal{P}_{\kappa\mathcal{F}}(\ell) J_{1,5}(\ell\theta). \quad (3.26)$$

In Appendix C, we show how to derive some of these correlation functions from first principles and demonstrate that they are in agreement with Eq. (3.20).

3.2.4 Consequences of Mixed Spin Field Cross-Correlation

The correlation of two different lensing fields is not widely considered in the literature. Only combinations of the same lensing field are generally discussed (i.e. shear-shear correlation). Here, we discuss the implications of correlating lensing fields of different spin. Note that throughout this discussion, “spin combination” refers to the sum and/or difference of the spin fields of two correlated fields, $s_a \pm s_b$. As such, spin combination can either be even, as in the case of cosmic shear or any other two-point autocorrelation, or odd.

Consequence 1: Order Matters for Odd Spin Combinations, or the Noncommutativity of Weak Lensing

Let us first consider cosmic shear. One might intuitively guess that $\langle \gamma'_1 \gamma'_2 \rangle = 0$. After all, the tangential and cross components are, by definition, not activated in the same way gravitationally. Indeed, it turns out that $\langle \gamma'_1 \gamma'_2 \rangle$ vanishes due to the *parity symmetry* of the Universe. Roughly speaking, if one were to look at the Universe under a mirror transformation, the combinations

$\langle \gamma'_1 \gamma'_1 \rangle$ and $\langle \gamma'_2 \gamma'_2 \rangle$ would look the same (i.e. they are parity invariant), whereas $\langle \gamma'_1 \gamma'_2 \rangle$ would not. The fact that $\langle \gamma'_1 \gamma'_2 \rangle$ is not parity invariant means that it must be zero in our parity-symmetric Universe.

These arguments hold for cosmic flexion as well, for both \mathcal{F} and \mathcal{G} . One finds that $\langle \mathcal{F}'_1 \mathcal{F}'_1 \rangle$, $\langle \mathcal{F}'_2 \mathcal{F}'_2 \rangle$, $\langle \mathcal{G}'_1 \mathcal{G}'_1 \rangle$, $\langle \mathcal{G}'_2 \mathcal{G}'_2 \rangle$, $\langle \mathcal{F}'_1 \mathcal{G}'_1 \rangle$, $\langle \mathcal{F}'_2 \mathcal{G}'_2 \rangle$, etc., are parity-invariant combinations, whereas $\langle \mathcal{F}'_1 \mathcal{F}'_2 \rangle$, $\langle \mathcal{G}'_1 \mathcal{G}'_2 \rangle$, $\langle \mathcal{F}'_1 \mathcal{G}'_2 \rangle$, etc., are not and will equal zero.

One might suppose that parity-symmetry requirements could pose a problem for the existence of a shear-flexion cross-correlation. Consider a γ - \mathcal{F} correlation. There are four possible two-point correlations: $\langle \gamma'_1 \mathcal{F}'_1 \rangle$, $\langle \gamma'_2 \mathcal{F}'_2 \rangle$, $\langle \gamma'_1 \mathcal{F}'_2 \rangle$, and $\langle \gamma'_2 \mathcal{F}'_1 \rangle$. We should immediately expect that $\langle \gamma'_1 \mathcal{F}'_2 \rangle = \langle \gamma'_2 \mathcal{F}'_1 \rangle = 0$ due to parity symmetry. This is indeed the case.

However, it also could seem as though neither $\langle \gamma'_1 \mathcal{F}'_1 \rangle$ nor $\langle \gamma'_2 \mathcal{F}'_2 \rangle$ are parity invariant either. Recall that shear is spin-2, and \mathcal{F} and \mathcal{G} flexions are spin-1 and spin-3, respectively. The spin-combinations are even for both shear-shear and flexion-flexion correlation. Even spin implies a possible parity-invariant combination of components. But any shear-flexion correlation will always have an odd-spin combination. This might appear to be an argument for any shear-flexion cross-correlation vanishing in our Universe.

In reality, certain odd-spin constructions do not simply vanish in this way. In order to demonstrate this, consider first the example of galaxy-galaxy flexion (the flexion version of galaxy-galaxy shear). In galaxy-galaxy shear, there is a tangential alignment of galaxy ellipticities around a foreground lens. In galaxy-galaxy flexion, there is a radial alignment of background galaxy flexions around the lens. Fig. 3.3 shows three different galaxy-galaxy flexion scenarios. From top to bottom, let us refer to these as scenarios 1, 2, and 3, respectively. In scenario 1, there is an \mathcal{F} -flexion to the right of an overdensity, and in scenarios 2 and 3, the \mathcal{F} -flexion is to the left of the same overdensity.

We notice that the flexion in scenario 2 is the negative of the flexion in scenario 1. This sign difference might naively suggest that a galaxy-galaxy flexion signal vanishes (imagine adding these two flexions together), which we understand not to be the case – galaxy-galaxy flexion has been measured in multiple scenarios (see e.g. Refs. [42, 54, 53]). Conversely, the flexion in scenario 3 *does*

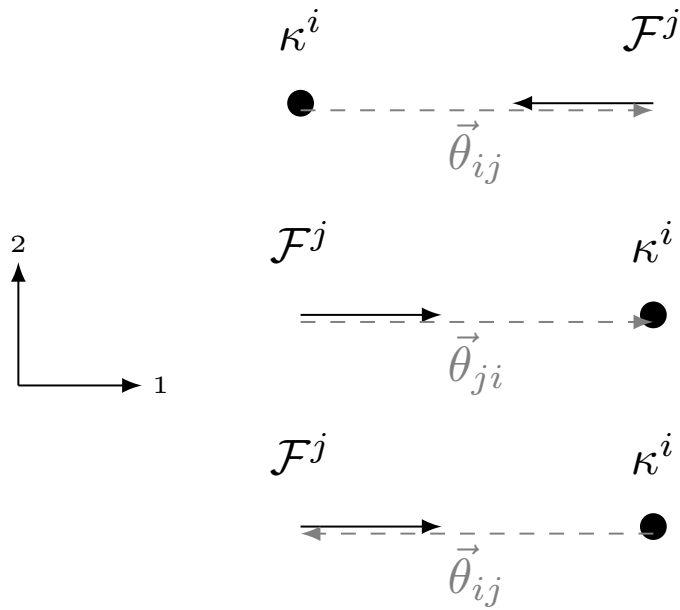


Figure 3.3: Three different galaxy-galaxy flexion scenarios. In each scenario, the flexion has only a 1-component and points radially toward the overdensity shown by the convergence κ^i . From top to bottom, we refer to these as scenarios 1, 2, and 3. The separation vector $\vec{\theta}$ in scenarios 1 and 2 points from left to right, along the 1-axis, and from right to left in scenario 3. The polar angle φ (i.e. the angle between the 1-axis and the separation vector) is 0 radians for scenarios 1 and 2, and $-\pi$ radians for the scenario 3. Using Eq. (3.10), the flexion \mathcal{F}'_1^j is $+|\mathcal{F}^j|$ for scenarios 1 and 3, and $-|\mathcal{F}^j|$ for scenario 2.

carry the same sign as that in scenario 1. The difference between scenarios 2 and 3 is simply the direction of the separation vector, which is a result of the order in which the pairing is constructed. In scenarios 1 and 3, the pairing is $i \rightarrow j$, but in scenario 2, the pairing is $j \rightarrow i$. The crucial point here is that the *order* in which one field is rotated and correlated with another matters for odd-spin combinations, whereas all three of these scenarios give the same sign for an even spin combination such as galaxy-galaxy shear. We therefore distinguish between $\kappa \rightarrow \mathcal{F}$ and $\mathcal{F} \rightarrow \kappa$ correlation. $\kappa \rightarrow \mathcal{F}'_k$ denotes $\langle \kappa \mathcal{F}'_k \rangle$ where the separation vector $\vec{\theta}$ used for rotation points from a first object for which we supply κ , to a second object for which we supply \mathcal{F}'_k . $\mathcal{F}'_k \rightarrow \kappa$ is defined in a similar way, with $\vec{\theta}$ pointing from a first object for which we supply \mathcal{F}'_k to a second object for which we supply κ . $\kappa \rightarrow \mathcal{F}'_k$ and $\mathcal{F}'_k \rightarrow \kappa$ turn out to be the negative, or the parity transforms, of each other.

This line of reasoning directly extends to shear-flexion cross-correlation. With this odd spin combination, we need to emphasize the difference between $\gamma \rightarrow \mathcal{F}$ and $\mathcal{F} \rightarrow \gamma$ correlation. Note that $\langle \gamma'_1 \rightarrow \mathcal{F}'_1 \rangle$ and $\langle \mathcal{F}'_1 \rightarrow \gamma'_1 \rangle$ are the parity transformations of each other, and carry opposite signs. The easiest way to visualize this is to recognize that γ'_1 is *itself* parity invariant, whereas \mathcal{F}'_1 is not. As before, when one does a mirror transform of \mathcal{F}'_1 , it is simply the negative of itself. Hence

$$\langle \mathcal{F}'_1 \rightarrow \gamma'_1 \rangle = -\langle \gamma'_1 \rightarrow \mathcal{F}'_1 \rangle. \quad (3.27)$$

This fact is also evident in the real-Fourier space relation. From Eq. (3.20), we see that

$$\xi_{\pm}^{\mathcal{F} \rightarrow \gamma}(\theta) = - \int_0^\infty \frac{d\ell}{2\pi} \mathcal{P}_{\kappa \mathcal{F}}(\ell) J_{-1,3}(\ell\theta) = -\xi_{\pm}^{\gamma \rightarrow \mathcal{F}}(\theta) \quad (3.28)$$

where we have used

$$J_{-n}(x) = (-1)^n J_n(x). \quad (3.29)$$

This is all to say that parity invariance for $\gamma - \mathcal{F}$ cross-correlation may be preserved through *fixed-ordered* pairing $i \rightarrow j$, and hence by distinguishing between $\gamma \rightarrow \mathcal{F}$ and $\mathcal{F} \rightarrow \gamma$.

As a final point, we note that *non-ordered* parity invariance is achieved by the fact that, while

$\langle \mathcal{F}'_1 \rightarrow \gamma'_1 \rangle$ is nonzero (and hence measurable), it is indeed the case that the sum $\langle \mathcal{F}'_1 \rightarrow \gamma'_1 \rangle + \langle \gamma'_1 \rightarrow \mathcal{F}'_1 \rangle = 0$.

Consequence 2: Mixed lensing field correlations provide information from more pairs

One can measure both $\xi_{\pm}^{\mathcal{F} \rightarrow \mathcal{G}}$ and $\xi_{\pm}^{\mathcal{G} \rightarrow \mathcal{F}}$ for a given set of galaxy pairs (for instance, selected as in Eq. (3.34) as galaxies $i, j > i$). This is an example of how cross-correlation of different lensing fields offers *twice* the number of available measurements as their autocorrelation counterparts. We can define

$$\xi_{\pm}^{\mathcal{FG}} \equiv \xi_{\pm}^{\mathcal{F} \rightarrow \mathcal{G}} \cup \xi_{\pm}^{\mathcal{G} \rightarrow \mathcal{F}} \quad (3.30)$$

as the combination of both $\mathcal{F} \rightarrow \mathcal{G}$ and $\mathcal{G} \rightarrow \mathcal{F}$ correlation measurements. Here, \cup refers to combining both measurements together while accounting for the algebraic sign of each so as not to cancel to zero. The spin combination for \mathcal{F} and \mathcal{G} is even, so $\xi_{\pm}^{\mathcal{F} \rightarrow \mathcal{G}} = \xi_{\pm}^{\mathcal{G} \rightarrow \mathcal{F}}$. Therefore, for this field combination, \cup is equivalent to addition.

Similarly, one is able to obtain twice the number of galaxy pairs for shear-flexion correlation functions:

$$\xi_{\pm}^{\gamma \mathcal{F}} \equiv \xi_{\pm}^{\gamma \rightarrow \mathcal{F}} \cup \xi_{\pm}^{\mathcal{F} \rightarrow \gamma} \quad (3.31)$$

Here the spin combination is odd and \cup is equivalent to subtraction. The same is true for $\xi_{\pm}^{\mathcal{G} \gamma}$.

3.3 Measuring Cosmic Flexion

3.3.1 Practical Estimators for Cosmic Flexion

Let us consider practical estimators of the correlation functions. For the case of cosmic shear, one estimates the ellipticity¹⁰ of a galaxy – that is, the combination of the effect of shear and an intrinsic ellipticity – rather than just the shear. As we recall from Sec. 1.2.8, observable ellipticity ϵ_i of a galaxy image at angular position ϑ_i is related to the intrinsic ellipticity ϵ_i^s and the shear¹¹ $\gamma(\vartheta_i)$ by [49, 4]

$$\epsilon_i = \epsilon_i^s + \gamma(\vartheta_i) \quad (3.32)$$

¹⁰Ellipticity is given by $\epsilon = (a-b)/(a+b) \times e^{2i\phi}$, where a and b are the semi-major and semi-minor axes, respectively, and ϕ is the position angle.

¹¹This is actually the reduced shear, \mathbf{g} , which is equal to γ in the limit $\kappa \ll 1$.

in the weak lensing regime $\kappa \ll 1$. In addition to an observed ellipticity, each galaxy may be assigned a weight factor w_i which reflects the measurement uncertainty. Noisy objects can be down weighted by assigning small values of w_i to them. We shall assume that the correlation function is to be estimated in bins of some (typically logarithmic) angular width $\Delta\theta$, and we define the function $\Delta_\theta(\phi) = 1$ for angular separations within the bin and zero otherwise. The standard estimators of the cosmic shear two-point correlation functions are given by [106]¹²

$$\hat{\xi}_\pm^{\gamma\gamma}(\theta) = \frac{\sum_{i,j>i} w_i w_j (\epsilon'_{i1}\epsilon'_{j1} \pm \epsilon'_{i2}\epsilon'_{j2}) \Delta_\theta(ij)}{N_p(\theta)} \quad (3.33)$$

where again, 1 and 2 refer to the field components, (ij) is shorthand for $(|\boldsymbol{\vartheta}_i - \boldsymbol{\vartheta}_j|)$, and

$$N_p(\theta) = \sum_{i,j>i} w_i w_j \Delta_\theta(ij), \quad (3.34)$$

is the effective number of galaxy pairs per angular bin (it is equal to the number of galaxy pairs in the case that all weights are unity), and where the rotated components of the observed ellipticity are defined in analogy to the corresponding shear components in Eq. (3.9). Schneider et al. [106] showed that this is an unbiased estimator of the cosmic shear.

Following similar lines, we can create estimators for generalized spin fields. The observable field a_i^o of a galaxy image at angular position $\boldsymbol{\vartheta}_i$ is related to the intrinsic field a_i^s and the lensing field $a(\boldsymbol{\vartheta}_i)$ by

$$a_i^o = a_i^s + a(\boldsymbol{\vartheta}_i) \quad (3.35)$$

and similarly, $b_j^o = b_j^s + b(\boldsymbol{\vartheta}_j)$. An estimator for the correlation functions $\xi_\pm^{ab}(\theta)$ is then

$$\hat{\xi}_\pm^{ab}(\theta) = \frac{\sum_{i,j>i} w_i w_j (a'^o_{i1}b'^o_{j1} \pm a'^o_{i2}b'^o_{j2}) \Delta_\theta(ij)}{N_p(\theta)}, \quad (3.36)$$

where we emphasize that this estimator specifically should be written as $\xi_\pm^{a \rightarrow b}$ in the case where a and b are different spin fields. Now, by showing that the expectation value of this estimator is equal

¹²Here, we differ from Schneider et al. [106] by having our second summation over only $j > i$ to avoid double counting.

to the correlation function, we can prove it is an unbiased estimator of the correlation function. The expectation value of the estimator is obtained by averaging over the intrinsic fields, assumed to be randomly oriented, and an ensemble average of the lensing field. Considering just $\hat{\xi}_+^{ab}$, we find

$$\langle a_{i1}'^o b_{j1}'^o \pm a_{i2}'^o b_{j2}'^o \rangle = \sigma_{ab}^2 \delta_{ij} + \xi_+^{ab}(ij) \quad (3.37)$$

where σ_{ab}^2 is the dispersion of the intrinsic fields, and we have used the fact that terms of the form

$$\langle a_i^{s*} b_j^s \rangle = \sigma_{ab}^2 \delta_{ij} = \sigma_a \sigma_b \delta_{ij}, \quad (3.38)$$

and that terms of the form $\langle a_i^{s*} b_j \rangle = 0$, and, by definition, $\langle a_{i1}' b_{j1}' + a_{i2}' b_{j2}' \rangle = \xi_+^{ab}(ij)$, from Eq. (3.12). We therefore see that

$$\left\langle \hat{\xi}_+^{ab}(\theta) \right\rangle = \xi_+^{ab}(\theta) \quad (3.39)$$

since the term $\sigma_{ab}^2 \delta_{ij} \Delta_\theta(ij)$ vanishes for all $i \neq j$, which is the definition of a galaxy pair. This is similarly the case for $\hat{\xi}_-^{ab}$.

The unbiased estimators for the flexion-flexion correlation functions are therefore

$$\hat{\xi}_\pm^{\mathcal{FF}}(\theta) = \frac{\sum_{i,j>i} w_i w_j (\mathcal{F}_{i1}'^o \mathcal{F}_{j1}'^o \pm \mathcal{F}_{i2}'^o \mathcal{F}_{j2}'^o) \Delta_\theta(ij)}{N_p(\theta)} \quad (3.40)$$

$$\hat{\xi}_\pm^{\mathcal{GG}}(\theta) = \frac{\sum_{i,j>i} w_i w_j (\mathcal{G}_{i1}'^o \mathcal{G}_{j1}'^o \pm \mathcal{G}_{i2}'^o \mathcal{G}_{j2}'^o) \Delta_\theta(ij)}{N_p(\theta)} \quad (3.41)$$

$$\hat{\xi}_\pm^{\mathcal{F} \rightarrow \mathcal{G}}(\theta) = \frac{\sum_{i,j>i} w_i w_j (\mathcal{F}_{i1}'^o \mathcal{G}_{j1}'^o \pm \mathcal{F}_{i2}'^o \mathcal{G}_{j2}'^o) \Delta_\theta(ij)}{N_p(\theta)} \quad (3.42)$$

and the (unbiased) estimators for the shear-flexion correlation functions are given by

$$\hat{\xi}_\pm^{\gamma \rightarrow \mathcal{F}}(\theta) = \frac{\sum_{i,j>i} w_i w_j (\epsilon'_{i1} \mathcal{F}_{j1}'^o \pm \epsilon'_{i2} \mathcal{F}_{j2}'^o) \Delta_\theta(ij)}{N_p(\theta)} \quad (3.43)$$

$$\hat{\xi}_\pm^{\mathcal{G} \rightarrow \gamma}(\theta) = \frac{\sum_{i,j>i} w_i w_j (\mathcal{G}_{i1}'^o \epsilon'_{j1} \pm \mathcal{G}_{i2}'^o \epsilon'_{j2}) \Delta_\theta(ij)}{N_p(\theta)}. \quad (3.44)$$

To this end, we have developed a code capable of computing the flexion and shear correlation

functions, known as F-SHARP (Flexion and SHear ARbitrary Point correlations)¹³. This code takes as input the estimated observed flexion and ellipticity components for a set of galaxies, and implements Eqs. (3.40) - (3.44) above to provide correlation function measurements (see for instance Figs. 3.4 and 3.5 below).

3.3.2 Cosmic Flexion Covariance

In addition to the two cosmic shear correlation functions, we have described the existence of six flexion-flexion and four shear-flexion correlation functions. One may wish to calculate covariance matrices for these estimators. Schneider et al. [106] analytically calculated three different covariance matrices for the cosmic shear correlation functions across two different angular bins θ_x and θ_y : $\text{Cov}(\hat{\xi}_+^{\gamma\gamma}, \theta_x; \hat{\xi}_+^{\gamma\gamma}, \theta_y)$, $\text{Cov}(\hat{\xi}_-^{\gamma\gamma}, \theta_x; \hat{\xi}_-^{\gamma\gamma}, \theta_y)$, and $\text{Cov}(\hat{\xi}_+^{\gamma\gamma}, \theta_x; \hat{\xi}_-^{\gamma\gamma}, \theta_y)$. Following this approach, we can calculate three covariance matrices for each of the ten additional cosmic flexion and shear-flexion estimators, for a total of 30 additional covariance matrices. In addition to this, we could calculate the covariance for two different estimators – for instance, $\text{Cov}(\hat{\xi}_+^{\gamma\gamma}, \theta_x; \hat{\xi}_+^{\gamma\mathcal{F}}, \theta_y)$. All told, twelve cosmic weak lensing estimators allow for $12 + 12(12 - 1)/2 = 78$ possible unique covariance matrices.

Owing to the large number of covariance matrix permutations, we choose to calculate the most generalized versions:

$$\text{Cov}(\hat{\xi}_{\pm}^{ab}, \theta_x; \hat{\xi}_{\pm}^{cd}, \theta_y) \quad \text{and} \quad \text{Cov}(\hat{\xi}_+^{ab}, \theta_x; \hat{\xi}_-^{cd}, \theta_y).$$

These covariances are derived in the following subsection.

Derivation of cosmic flexion covariances

Here we calculate the generalized covariance matrices of two generalized two-point correlation function estimators, $\hat{\xi}_{\pm}^{ab}$ and $\hat{\xi}_{\pm}^{cd}$, across two different angular separations θ_x and θ_y , where a, b, c , and d , are four different spin fields. We will not present a closed-form solution here – rather, we work through the steps necessary to compute individual terms. We follow the analysis of Schneider et al.

¹³<https://github.com/evanjarena/F-SHARP>

[106], generalized to arbitrary estimators.

We begin with the ‘++’ and ‘––’ covariances:

$$\text{Cov} \left(\hat{\xi}_{\pm}^{ab}(\theta_x), \hat{\xi}_{\pm}^{cd}(\theta_y) \right) = \left\langle \left(\hat{\xi}_{\pm}^{ab}(\theta_x) - \xi_{\pm}^{ab}(\theta_x) \right) \left(\hat{\xi}_{\pm}^{cd}(\theta_y) - \xi_{\pm}^{cd}(\theta_y) \right) \right\rangle. \quad (3.45)$$

The first term we must evaluate is

$$\left\langle \hat{\xi}_{\pm}^{ab}(\theta_x) \hat{\xi}_{\pm}^{cd}(\theta_y) \right\rangle = \frac{1}{N_p(\theta_x) N_p(\theta_y)} \sum_{i,j > i} \sum_{k,\ell > k} w_i w_j w_k w_\ell \left\langle (a_{i1}'^o b_{j1}'^o \pm a_{i2}'^o b_{j2}'^o)(c_{i1}'^o d_{j1}'^o \pm c_{i2}'^o d_{j2}'^o) \right\rangle \Delta_{\theta_x}(ij) \Delta_{\theta_y}(k\ell) \quad (3.46)$$

where we have used the definition of the estimators given by Eq. (3.36). Now, it is necessary to work in terms of the unrotated coordinate system. We will demonstrate that we can relate the component lensing two-points $\langle a_{i\alpha} b_{j\beta} \rangle$ to the correlation functions in a simple way, whereas it is not convenient to do so in the rotated formalism. Notice that we can simply invert Eq. (3.7) to obtain (up to a factor of $\text{csign}[(-i)^{s_a}]$, which we take to simply be -1 here for simplicity)

$$\begin{pmatrix} a_1 \\ a_2 \end{pmatrix} = - \begin{pmatrix} \cos s_a \varphi & -\sin s_a \varphi \\ \sin s_a \varphi & \cos s_a \varphi \end{pmatrix} \begin{pmatrix} a'_1 \\ a'_2 \end{pmatrix}. \quad (3.47)$$

Using this transformation, we find that

$$\begin{aligned}
& \langle (a_{i1}^{\prime o} b_{j1}^{\prime o} \pm a_{i2}^{\prime o} b_{j2}^{\prime o})(c_{i1}^{\prime o} d_{j1}^{\prime o} \pm c_{i2}^{\prime o} d_{j2}^{\prime o}) \rangle \\
&= \langle (a_{i1}^o b_{j1}^o \cos(s_a \mp s_b) \varphi_{ij} + a_{i2}^o b_{j1}^o \sin(s_a \mp s_b) \varphi_{ij} \mp a_{i1}^o b_{j2}^o \sin(s_a \mp s_b) \varphi_{ij} \pm a_{i2}^o b_{j2}^o \cos(s_a \mp s_b) \varphi_{ij}) \\
&\quad \times (c_{k1}^o d_{\ell1}^o \cos(s_c \mp s_d) \varphi_{k\ell} + c_{k2}^o d_{\ell1}^o \sin(s_c \mp s_d) \varphi_{k\ell} \mp c_{k1}^o d_{\ell2}^o \sin(s_c \mp s_d) \varphi_{k\ell} \pm c_{k2}^o d_{\ell2}^o \cos(s_c \mp s_d) \varphi_{k\ell}) \rangle \\
&= \langle a_{i1}^o b_{j1}^o c_{k1}^o d_{\ell1}^o \rangle \cos(s_a \mp s_b) \varphi_{ij} \cos(s_c \mp s_d) \varphi_{k\ell} + \langle a_{i1}^o b_{j1}^o c_{k2}^o d_{\ell1}^o \rangle \cos(s_a \mp s_b) \varphi_{ij} \sin(s_c \mp s_d) \varphi_{k\ell} \\
&\quad \mp \langle a_{i1}^o b_{j1}^o c_{k1}^o d_{\ell2}^o \rangle \cos(s_a \mp s_b) \varphi_{ij} \sin(s_c \mp s_d) \varphi_{k\ell} \pm \langle a_{i1}^o b_{j1}^o c_{k2}^o d_{\ell2}^o \rangle \cos(s_a \mp s_b) \varphi_{ij} \cos(s_c \mp s_d) \varphi_{k\ell} \\
&\quad + \langle a_{i2}^o b_{j1}^o c_{k1}^o d_{\ell1}^o \rangle \sin(s_a \mp s_b) \varphi_{ij} \cos(s_c \mp s_d) \varphi_{k\ell} + \langle a_{i2}^o b_{j1}^o c_{k2}^o d_{\ell1}^o \rangle \sin(s_a \mp s_b) \varphi_{ij} \sin(s_c \mp s_d) \varphi_{k\ell} \\
&\quad \mp \langle a_{i2}^o b_{j1}^o c_{k1}^o d_{\ell2}^o \rangle \sin(s_a \mp s_b) \varphi_{ij} \sin(s_c \mp s_d) \varphi_{k\ell} \pm \langle a_{i2}^o b_{j1}^o c_{k2}^o d_{\ell2}^o \rangle \sin(s_a \mp s_b) \varphi_{ij} \cos(s_c \mp s_d) \varphi_{k\ell} \\
&\quad \mp \langle a_{i1}^o b_{j2}^o c_{k1}^o d_{\ell1}^o \rangle \sin(s_a \mp s_b) \varphi_{ij} \cos(s_c \mp s_d) \varphi_{k\ell} \mp \langle a_{i1}^o b_{j2}^o c_{k2}^o d_{\ell1}^o \rangle \sin(s_a \mp s_b) \varphi_{ij} \sin(s_c \mp s_d) \varphi_{k\ell} \\
&\quad + \langle a_{i1}^o b_{j2}^o c_{k1}^o d_{\ell2}^o \rangle \sin(s_a \mp s_b) \varphi_{ij} \sin(s_c \mp s_d) \varphi_{k\ell} - \langle a_{i1}^o b_{j2}^o c_{k2}^o d_{\ell2}^o \rangle \sin(s_a \mp s_b) \varphi_{ij} \cos(s_c \mp s_d) \varphi_{k\ell} \\
&\quad \pm \langle a_{i2}^o b_{j2}^o c_{k1}^o d_{\ell1}^o \rangle \cos(s_a \mp s_b) \varphi_{ij} \cos(s_c \mp s_d) \varphi_{k\ell} \pm \langle a_{i2}^o b_{j2}^o c_{k2}^o d_{\ell1}^o \rangle \cos(s_a \mp s_b) \varphi_{ij} \sin(s_c \mp s_d) \varphi_{k\ell} \\
&\quad - \langle a_{i2}^o b_{j2}^o c_{k1}^o d_{\ell2}^o \rangle \cos(s_a \mp s_b) \varphi_{ij} \sin(s_c \mp s_d) \varphi_{k\ell} + \langle a_{i2}^o b_{j2}^o c_{k2}^o d_{\ell2}^o \rangle \cos(s_a \mp s_b) \varphi_{ij} \cos(s_c \mp s_d) \varphi_{k\ell}.
\end{aligned} \tag{3.48}$$

Next, we need to calculate the four-point correlation functions of the observed fields. We can generalize these sixteen permutations to $\langle a_{i\alpha}^o b_{j\beta}^o c_{k\mu}^o d_{\ell\nu}^o \rangle$, where the Greek letters $\in \{1, 2\}$. Using Eq. (3.35), we see that

$$\langle a_{i\alpha}^o b_{j\beta}^o c_{k\mu}^o d_{\ell\nu}^o \rangle = \langle (a_{i\alpha}^s + a_{i\alpha})(b_{j\beta}^s + b_{j\beta})(c_{k\mu}^s + c_{k\mu})(d_{\ell\nu}^s + d_{\ell\nu}) \rangle. \tag{3.49}$$

Now, using Eq. (3.38) and noting that since there is no preferred direction on average for intrinsic fields, then

$$\langle a_{i\alpha}^s b_{j\beta}^s \rangle = \frac{\sigma_{ab}^2}{2} \delta_{ij} \delta_{\alpha\beta} = \frac{\sigma_a \sigma_b}{2} \delta_{ij} \delta_{\alpha\beta} \tag{3.50}$$

Then, since $\langle a_{i\alpha}^s b_{j\beta}^s c_{k\mu}^s d_{\ell\nu}^s \rangle = \langle a_{i\alpha}^s b_{j\beta}^s \rangle \langle c_{k\mu}^s d_{\ell\nu}^s \rangle = (1/2) \sigma_{ab}^2 \delta_{ij} \delta_{\alpha\beta} \langle c_{k\mu}^s d_{\ell\nu}^s \rangle$, and further noting that

only terms of even power in a^s and a survive, we are left with

$$\begin{aligned} \langle a_{i\alpha}^o b_{j\beta}^o c_{k\mu}^o d_{\ell\nu}^o \rangle &= \langle a_{i\alpha}^s b_{j\beta}^s c_{k\mu}^s d_{\ell\nu}^s \rangle + \frac{\sigma_{ab}^2}{2} \delta_{ij} \delta_{\alpha\beta} \langle c_{k\mu} d_{\ell\nu} \rangle + \frac{\sigma_{bd}^2}{2} \delta_{j\ell} \delta_{\beta\nu} \langle a_{i\alpha} c_{k\mu} \rangle + \frac{\sigma_{bc}^2}{2} \delta_{jk} \delta_{\beta\mu} \langle a_{i\alpha} d_{\ell\nu} \rangle \\ &\quad + \frac{\sigma_{ad}^2}{2} \delta_{i\ell} \delta_{\alpha\nu} \langle b_{j\beta} c_{k\mu} \rangle + \frac{\sigma_{ac}^2}{2} \delta_{ik} \delta_{\alpha\mu} \langle b_{j\beta} d_{\ell\nu} \rangle + \frac{\sigma_{cd}^2}{2} \delta_{k\ell} \delta_{\mu\nu} \langle a_{i\alpha} b_{j\beta} \rangle + \langle a_{i\alpha} b_{j\beta} c_{k\mu} d_{\ell\nu} \rangle \end{aligned} \quad (3.51)$$

Next, let us consider the four-point functions of the intrinsic and the lensing fields. We assume that both are Gaussian, so that the four-point function can be written as a sum over products of two-point functions. Even without the assumption of the intrinsic field being Gaussian, we can note that the four-point function of the intrinsic fields factorizes, since at most two of the indices i, j, k, l are equal. Therefore, the intrinsic four-point function becomes

$$\begin{aligned} \langle a_{i\alpha}^s b_{j\beta}^s c_{k\mu}^s d_{\ell\nu}^s \rangle &= \langle a_{i\alpha}^s b_{j\beta}^s \rangle \langle c_{k\mu}^s d_{\ell\nu}^s \rangle + \langle a_{i\alpha}^s c_{k\mu}^s \rangle \langle b_{j\beta}^s d_{\ell\nu}^s \rangle + \langle a_{i\alpha}^s d_{\ell\nu}^s \rangle \langle b_{j\beta}^s c_{k\mu}^s \rangle \\ &= \frac{\sigma_{ab}^2 \sigma_{cd}^2}{4} (\delta_{ij} \delta_{\alpha\beta} \delta_{k\ell} \delta_{\mu\nu}) + \frac{\sigma_{ac}^2 \sigma_{bd}^2}{4} (\delta_{ik} \delta_{\alpha\mu} \delta_{j\ell} \delta_{\beta\nu}) + \frac{\sigma_{ad}^2 \sigma_{bc}^2}{4} (\delta_{i\ell} \delta_{\alpha\nu} \delta_{jk} \delta_{\beta\mu}). \end{aligned} \quad (3.52)$$

Before analyzing the lensing four-point, we note that some of the terms in the above expressions can be dropped. The summations in Eq. (3.46) require $j > i$ and $\ell > k$, so we can simply drop terms that contain δ_{ij} and/or $\delta_{k\ell}$. Also in the summation, it is possible to have $k = i$, $k > i$, and $k < i$.¹⁴ Therefore, terms where $i = \ell$ and $j = k$ individually survive; however, the requirements $j > i$ and $\ell > k$ require that we can never *simultaneously* have $i = \ell$ and $j = k$, so the product $\delta_{i\ell} \delta_{jk}$ vanishes in the sum. Dropping these terms, and expanding the lensing four-point in the same way as the

¹⁴One may be tempted here to only compute the upper or lower triangle of the covariance matrix, and for example require $k \geq i$ in the summation. While this is reasonable for e.g. the shear-shear covariance matrices, it is not advisable in general. This is because the generalized covariance matrices are **not** symmetric about the diagonal. This can be demonstrated in the case of two angular bins. The covariance matrix elements would be of the form $(ab(\theta_1)cd(\theta_1), ab(\theta_2)cd(\theta_2))$ along the diagonal, and $(ab(\theta_1)cd(\theta_2), ab(\theta_2)cd(\theta_1))$ off the diagonal. These off-diagonal terms are equal only in the case $c = a$ and $d = b$.

intrinsic four-point, we are left with

$$\begin{aligned} \langle a_{i\alpha}^o b_{j\beta}^o c_{k\mu}^o d_{\ell\nu}^o \rangle &= \frac{\sigma_{ac}^2 \sigma_{bd}^2}{4} (\delta_{ik} \delta_{\alpha\mu} \delta_{j\ell} \delta_{\beta\nu}) + \frac{\sigma_{bd}^2}{2} \delta_{j\ell} \delta_{\beta\nu} \langle a_{i\alpha} c_{k\mu} \rangle + \frac{\sigma_{bc}^2}{2} \delta_{jk} \delta_{\beta\mu} \langle a_{i\alpha} d_{\ell\nu} \rangle + \frac{\sigma_{ad}^2}{2} \delta_{i\ell} \delta_{\alpha\nu} \langle b_{j\beta} c_{k\mu} \rangle \\ &\quad + \frac{\sigma_{ac}^2}{2} \delta_{ik} \delta_{\alpha\mu} \langle b_{j\beta} d_{\ell\nu} \rangle + \langle a_{i\alpha} b_{j\beta} \rangle \langle c_{k\mu} d_{\ell\nu} \rangle + \langle a_{i\alpha} c_{k\mu} \rangle \langle b_{j\beta} d_{\ell\nu} \rangle + \langle a_{i\alpha} d_{\ell\mu} \rangle \langle b_{j\beta} c_{k\mu} \rangle. \end{aligned} \quad (3.53)$$

The next step is to express these two-point functions in terms of the correlation functions. Using Eqs. (3.12), (3.13), and (3.47), and noting that terms of the form $\langle a'_{i1} b'_{j2} \rangle$ vanish due to parity in the rotated coordinate system, we find that

$$\begin{aligned} \langle a_{i1} b_{j1} \rangle &= \frac{1}{2} \{ \xi_+^{ab}(ij) \cos [(s_a - s_b)\varphi_{ij}] + \xi_-^{ab}(ij) \cos [(s_a + s_b)\varphi_{ij}] \} \\ \langle a_{i2} b_{j2} \rangle &= \frac{1}{2} \{ \xi_+^{ab}(ij) \cos [(s_a - s_b)\varphi_{ij}] - \xi_-^{ab}(ij) \cos [(s_a + s_b)\varphi_{ij}] \} \\ \langle a_{i1} b_{j2} \rangle &= \frac{1}{2} \{ -\xi_+^{ab}(ij) \sin [(s_a - s_b)\varphi_{ij}] + \xi_-^{ab}(ij) \sin [(s_a + s_b)\varphi_{ij}] \}. \end{aligned} \quad (3.54)$$

The second and third covariance terms we must evaluate are

$$\begin{aligned} \left\langle \hat{\xi}_\pm^{ab}(\theta_x) \hat{\xi}_\pm^{cd}(\theta_y) \right\rangle &= \frac{1}{N_p(\theta_y)} \sum_{k,\ell>k} w_k w_\ell \langle (a'_{i1} b'_{j1} \pm a'_{i2} b'_{j2})(c'_{i1} d'_{j1} \pm c'_{i2} d'_{j2}) \rangle \Delta_{\theta_y}(k\ell) \\ \left\langle \hat{\xi}_\pm^{ab}(\theta_x) \xi_\pm^{cd}(\theta_y) \right\rangle &= \frac{1}{N_p(\theta_x)} \sum_{i,j>i} w_i w_j \langle (a'^o_{i1} b'^o_{j1} \pm a'^o_{i2} b'^o_{j2})(c'_{i1} d'_{j1} \pm c'_{i2} d'_{j2}) \rangle \Delta_{\theta_x}(ij). \end{aligned} \quad (3.55)$$

Consider expanding the expectation value in these terms. They are simply Eq. (3.48) with the replacements $(a^o \rightarrow a, b^o \rightarrow b)$ and $(c^o \rightarrow c, d^o \rightarrow d)$, respectively. For each of these covariance terms, only the lensing four-point functions survive in the generalized terms. This is because we drop terms that are not even in a^s , and we also drop terms where $\ell = k$ and $j = i$, which appear in the second and third covariance terms, respectively. After ignoring these terms, we are left with

$$\langle a_{i\alpha} b_{j\beta} c_{k\mu}^o d_{\ell\nu}^o \rangle = \langle a_{i\alpha}^o b_{j\beta}^o c_{k\mu} d_{\ell\nu} \rangle = \langle a_{i\alpha} b_{j\beta} \rangle \langle c_{k\mu} d_{\ell\nu} \rangle + \langle a_{i\alpha} c_{k\mu} \rangle \langle b_{j\beta} d_{\ell\nu} \rangle + \langle a_{i\alpha} d_{\ell\mu} \rangle \langle b_{j\beta} c_{k\mu} \rangle. \quad (3.56)$$

Finally, the fourth covariance term is

$$\langle \xi_{\pm}^{ab}(\theta_x) \xi_{\pm}^{cd}(\theta_y) \rangle = \langle (a'_{i1} b'_{j1} \pm a'_{i2} b'_{j2}) (c'_{i1} d'_{j1} \pm c'_{i2} d'_{j2}) \rangle. \quad (3.57)$$

Expanding this term gives us Eq. (3.48) with the replacement ($a^o \rightarrow a, b^o \rightarrow b, c^o \rightarrow c, d^o \rightarrow d$).

Again, the only generalized term that survives is the lensing four-point function.

Finally, there also exists the ‘+−’ covariance:

$$\text{Cov} \left(\hat{\xi}_{+}^{ab}, \theta_x; \hat{\xi}_{-}^{cd}, \theta_y \right) = \left\langle \left(\hat{\xi}_{+}^{ab}(\theta_x) - \xi_{+}^{ab}(\theta_x) \right) \left(\hat{\xi}_{-}^{cd}(\theta_y) - \xi_{-}^{cd}(\theta_y) \right) \right\rangle. \quad (3.58)$$

where the first covariance term is

$$\left\langle \hat{\xi}_{\pm}^{ab}(\theta_x) \hat{\xi}_{\pm}^{cd}(\theta_y) \right\rangle = \frac{1}{N_p(\theta_x) N_p(\theta_y)} \sum_{i,j>i} \sum_{k,\ell>k} w_i w_j w_k w_\ell \langle (a'^o_{i1} b'^o_{j1} + a'^o_{i2} b'^o_{j2}) (c'^o_{i1} d'^o_{j1} - c'^o_{i2} d'^o_{j2}) \rangle \Delta_{\theta_x}(ij) \Delta_{\theta_y}(k\ell). \quad (3.59)$$

Using the transformation in Eq. (3.47), we find that

$$\begin{aligned} & \langle (a'^o_{i1} b'^o_{j1} + a'^o_{i2} b'^o_{j2}) (c'^o_{i1} d'^o_{j1} - c'^o_{i2} d'^o_{j2}) \rangle \\ &= \langle (a^o_{i1} b^o_{j1} \cos(s_a - s_b) \varphi_{ij} + a^o_{i2} b^o_{j1} \sin(s_a - s_b) \varphi_{ij} - a^o_{i1} b^o_{j2} \sin(s_a - s_b) \varphi_{ij} + a^o_{i2} b^o_{j2} \cos(s_a - s_b) \varphi_{ij}) \\ & \quad \times (c^o_{k1} d^o_{\ell1} \cos(s_c + s_d) \varphi_{k\ell} + c^o_{k2} d^o_{\ell1} \sin(s_c + s_d) \varphi_{k\ell} + c^o_{k1} d^o_{\ell2} \sin(s_c + s_d) \varphi_{k\ell} - c^o_{k2} d^o_{\ell2} \cos(s_c + s_d) \varphi_{k\ell}) \rangle \end{aligned} \quad (3.60)$$

We note that the remaining calculation follows the same lines as before.

Approximate forms of cosmic flexion covariances

From these covariance matrices, we are able to approximate the autovariance of each estimator – i.e. the diagonal of $\text{Cov} \left(\hat{\xi}_{\pm}^{ab}, \theta; \hat{\xi}_{\pm}^{ab}, \theta \right)$. Under the assumption that the autovariance of the estimators in each bin is dominated by the intrinsic field shape noise, Eq. (3.45) simply becomes

$$\text{Var} \left(\hat{\xi}_{\pm}^{ab}(\theta) \right) \simeq \frac{\sigma_a^2 \sigma_b^2}{2 [N_p(\theta)]^2} \sum_{i,j>i} w_i^2 w_j^2 \Delta_{\theta}(ij) \quad (3.61)$$

where the effective dispersion of the intrinsic field is calculated as

$$\sigma_a^2 = \frac{\sum_i |a_i^o|^2 w_i^2}{\sum_i w_i}. \quad (3.62)$$

Consider the example of the cosmic shear estimators

$$\text{Var}(\hat{\xi}_\pm^{\gamma\gamma}(\theta)) \simeq \frac{\sigma_\epsilon^4}{2[N_p(\theta)]^2} \sum_{i,j>i} w_i^2 w_j^2 \Delta_\theta(ij). \quad (3.63)$$

where the effective dispersion of the intrinsic ellipticity¹⁵

$$\sigma_\epsilon^2 = \frac{\sum_i |\epsilon_i|^2 w_i^2}{\sum_i w_i}. \quad (3.64)$$

In the case of all weights being equal to unity, this expression simplifies to the well known result

$\text{Var}(\hat{\xi}_\pm^{\gamma\gamma}(\theta)) \simeq \sigma_\epsilon^4 / 2N_p(\theta)$ given in e.g. Friedrich et al. [107].

Unlike shear/ellipticity, which is dimensionless, flexion has units of inverse length and is therefore not scale/distance invariant. The combination of a galaxy's size¹⁶, $a = \sqrt{|Q_{11} + Q_{22}|}$ where Q_{ij} are quadrupole image moments, and flexion produces a scale-invariant, dimensionless flexion: $|a\mathcal{F}|$ and $|a\mathcal{G}|$ [42, 50]. We may then define the scatter in intrinsic flexions in the following way:

$$\sigma_{a\mathcal{F}}^2 = \frac{\sum_i |a_i \mathcal{F}_i^o|^2 w_i^2}{\sum_i w_i} \quad (3.65)$$

$$\sigma_{a\mathcal{G}}^2 = \frac{\sum_i |a_i \mathcal{G}_i^o|^2 w_i^2}{\sum_i w_i}. \quad (3.66)$$

¹⁵In cosmic shear studies, it is often standard practice to measure a dispersion **per shear component**; however, we choose not to use this formalism.

¹⁶The size of a galaxy, a , is not to be confused with the generalized lensing field in previous equations.

The autovariance of the flexion-flexion estimators is approximated by

$$\text{Var} \left(\hat{\xi}_{\pm}^{\mathcal{F}\mathcal{F}}(\theta) \right) \simeq \frac{\sigma_{a\mathcal{F}}^4}{2 [N_p(\theta)]^2} \sum_{i,j>i} \frac{w_i^2 w_j^2 \Delta_\theta(ij)}{a_i^2 a_j^2} \quad (3.67)$$

$$\text{Var} \left(\hat{\xi}_{\pm}^{\mathcal{G}\mathcal{G}}(\theta) \right) \simeq \frac{\sigma_{a\mathcal{G}}^4}{2 [N_p(\theta)]^2} \sum_{i,j>i} \frac{w_i^2 w_j^2 \Delta_\theta(ij)}{a_i^2 a_j^2} \quad (3.68)$$

$$\text{Var} \left(\hat{\xi}_{\pm}^{\mathcal{F} \rightarrow \mathcal{G}}(\theta) \right) \simeq \frac{\sigma_{a\mathcal{F}}^2 \sigma_{a\mathcal{G}}^2}{2 [N_p(\theta)]^2} \sum_{i,j>i} \frac{w_i^2 w_j^2 \Delta_\theta(ij)}{a_i^2 a_j^2}, \quad (3.69)$$

and the autovariance of the shear-flexion estimators is

$$\text{Var} \left(\hat{\xi}_{\pm}^{\gamma \rightarrow \mathcal{F}}(\theta) \right) \simeq \frac{\sigma_\epsilon^2 \sigma_{a\mathcal{F}}^2}{2 [N_p(\theta)]^2} \sum_{i,j>i} \frac{w_i^2 w_j^2 \Delta_\theta(ij)}{a_j^2} \quad (3.70)$$

$$\text{Var} \left(\hat{\xi}_{\pm}^{\mathcal{G} \rightarrow \gamma}(\theta) \right) \simeq \frac{\sigma_{a\mathcal{G}}^2 \sigma_\epsilon^2}{2 [N_p(\theta)]^2} \sum_{i,j>i} \frac{w_i^2 w_j^2 \Delta_\theta(ij)}{a_i^2}. \quad (3.71)$$

3.3.3 Testing Cosmic Flexion with a Gaussian Random Field

In order to test both our theoretical assumptions and the estimators for the two-point correlation functions, we make use of a simple toy model. We generate a Gaussian random field for the convergence in Fourier space. We take this to be a delta-function field, which can be used to obtain the lensing potential via the relation given by Eq. (1.159). The shear and flexion relations in Fourier space are given in Sec. 1.2.11. Again, the flexion relations come from BGRT, with a correction for \mathcal{G} that was first presented in AGB.

Using these relations, one can create maps of the lensing fields on some patch of sky by using a Fast Fourier Transform. The patch of sky used in this toy problem is approximately $3' \times 3'$. With random sampling, one can obtain measurements of the correlation functions in angular bins. To do this, F-SHARP makes use of Eqs. (3.40) - (3.44) to compute the estimators of each correlation function. The noise in this toy problem comes from cosmic variance, so we compute errors of the correlation function measurements over multiple random realizations of the field. Given the fact that the convergence power spectrum is a delta function, one easily obtains analytical solutions to Eqs. (3.22) - (3.26) for the various theoretical correlation functions.

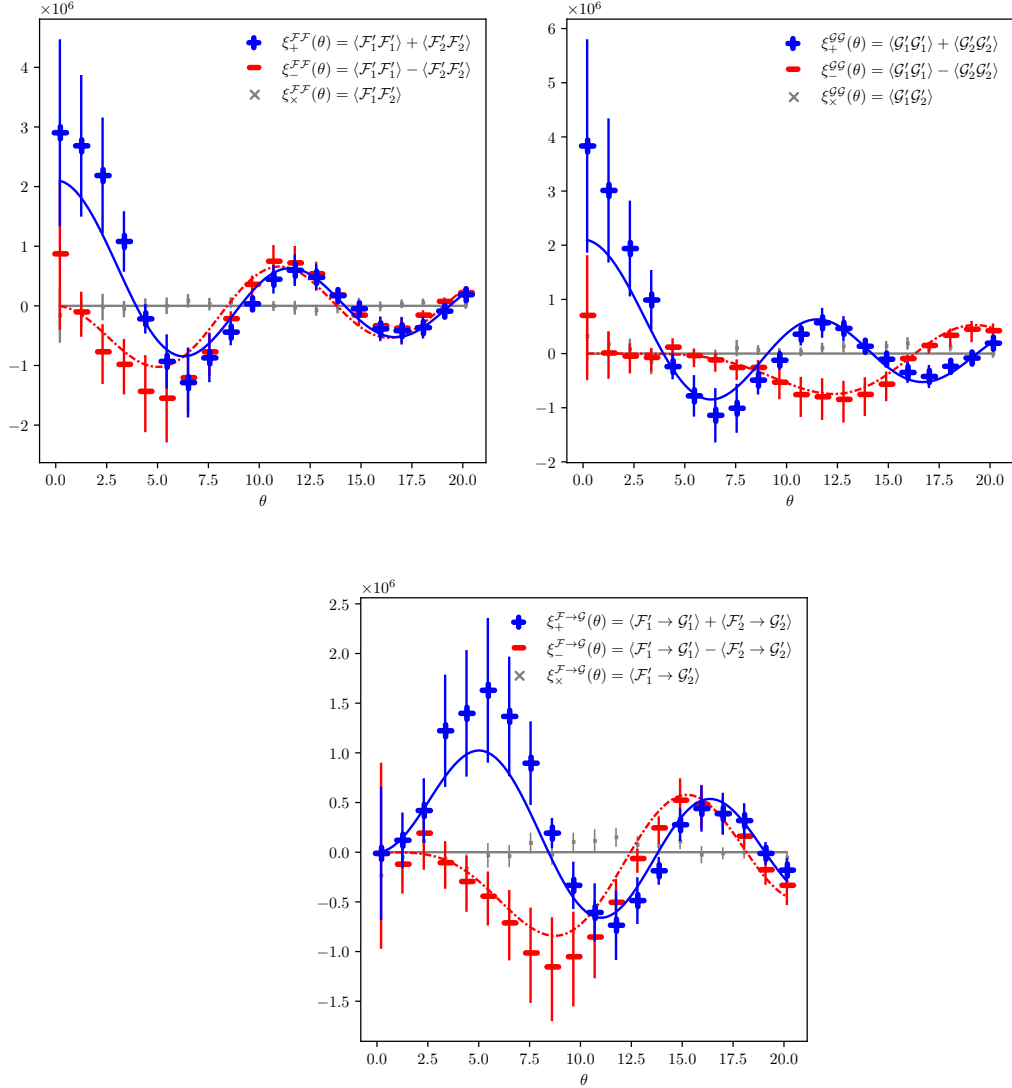


Figure 3.4: Theoretical cosmic flexion-flexion correlation functions $\xi_{\pm}^{\mathcal{F}\mathcal{F}}$, $\xi_{\pm}^{\mathcal{G}\mathcal{G}}$, and $\xi_{\pm}^{\mathcal{F}\rightarrow\mathcal{G}}$ for a delta-function convergence Gaussian random field. The solid (blue) lines are the ‘+’ theoretical correlation functions, and the dash-dotted (red) lines are the ‘-’ correlations. We see that the measurements of the ‘+’ and ‘-’ correlation functions are consistent with the theoretical curves. We also see that the so-called “cross” (‘×’) correlation functions, which vanish due to parity-symmetry, are consistent with zero. Angular separation, θ , has units of arcseconds, and the flexion-flexion correlation functions have units of [radians] $^{-2}$.

Figs. 3.4 and 3.5 show a comparison of the theoretical versus measured two-point correlation functions. These results demonstrate agreement between our theoretical equations for the correlation functions and the estimators of these correlators coded in F-SHARP. Most notably, we point out the fact that our results demonstrate $\xi_{\pm}^{\mathcal{F}\rightarrow\gamma} = -\xi_{\pm}^{\gamma\rightarrow\mathcal{F}}$, as posited in our discussion of the non-

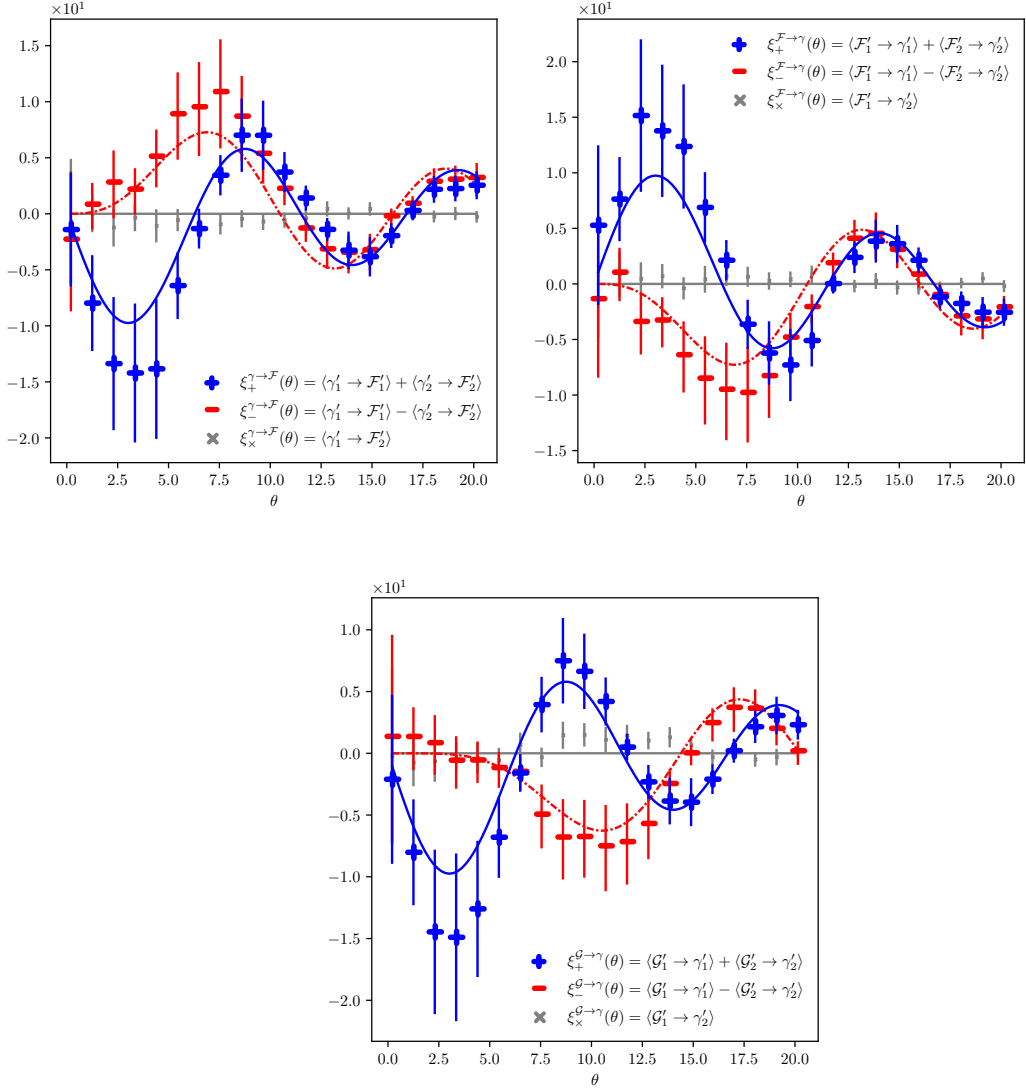


Figure 3.5: Theoretical cosmic shear-flexion correlation functions $\xi_{\pm}^{\gamma \rightarrow F}$, $\xi_{\pm}^{F \rightarrow \gamma}$, and $\xi_{\pm}^{G \rightarrow \gamma}$ for a delta-function convergence Gaussian random field. The solid (blue) lines are the ‘+’ theoretical correlation functions, and the dash-dotted (red) lines are the ‘-’ correlations. We also see that the so-called “cross” (‘x’) correlation functions, which vanish due to parity-symmetry, are consistent with zero. From these plots, we see that $\xi_{\pm}^{F \rightarrow \gamma} = -\xi_{\pm}^{\gamma \rightarrow F}$, which verifies Eqs. (3.27) and (3.28). Angular separation, θ has units of arcseconds, and the shear-flexion correlation functions have units of [radians] $^{-1}$.

commutativity of weak lensing fields with odd spin combinations.

3.4 Cosmic Flexion in Λ CDM for Stage III Lensing Survey

When cosmic flexion was first proposed by BGRT more than a decade ago, there was neither the computational pipeline to compute flexion quickly nor a sufficient dataset for its detection. Now that observations have caught up with theoretical estimates, the time is ripe to measure cosmic flexion, which will give us new insight into cosmic structure on the arcsecond to arcminute scale.

Stage III lensing surveys such as the Dark Energy Survey (DES), the Kilo-Degree Survey (KiDS) and the Hyper Suprime-Cam Subaru Strategic Program (HSC SSP) are ideal candidates for measuring the cosmic flexion signal. As a representative example, in this section we will forecast what could be achieved in measuring flexion correlations with DES.

We first calculate the functional form of the cosmic flexion power spectrum, which is done using **F-SHARP**. **F-SHARP** makes use of the Einstein-Boltzmann code **CLASS** [33] to compute the linear matter power spectrum, which in turn makes use of **halofit** [108] to compute the nonlinear matter power spectrum (see Sec. 1.1.5). This assumes a Planck 18 cosmology [28] using the TT,TE,EE+lowE+lensing constraints. Next, we make use of the DES (Y3) SOMPZ $n(z)$ source distributions for each redshift bin (as described in Secco et al. [109]), which are publicly available,¹⁷ combining these in order to estimate the overall source redshift distribution. **F-SHARP** then makes use of Eqs. (5.36) and (3.4) to calculate the flexion power spectrum; this is shown in Fig. 3.6. Most significantly, this power spectrum peaks around $\ell \simeq 10^4$ or angular scales on the order of an arcsecond. This should be compared to cosmic shear measurements, which typically peak on scales $\sim 100 - 1000$ times larger.

We also calculate the convergence-flexion power spectrum given by Eq. (3.6); as seen in Fig. 3.7, shear-flexion power peaks on scales intermediate to that of flexion-flexion and shear-shear. This cross-power bridges the gap between these two probes; since it is (partly) measurable in the linear regime ($\gtrsim 10$ arcminutes), it offers the possibility of constraining cosmological parameters and allows for systematics checks between cosmic shear and flexion.

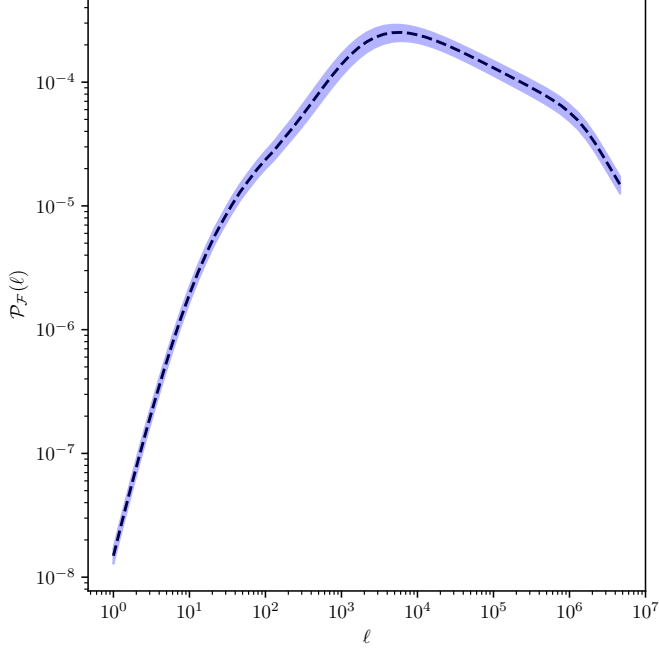


Figure 3.6: The cosmic flexion power spectrum expected for the DES Y3 lensing sample using a Planck 18 cosmology. The shaded region is the response of the power spectrum to varying σ_8 over ten times the TT,TE,EE+lowE+lensing 68% interval. The small width of this region is a consequence of the (very) tight constraints of the current Planck estimates. This does not, however, include variations of modeling approaches to highly nonlinear substructure.

3.4.1 Handling Infinities: Renormalization of Cosmic Flexion

When calculating the theoretical correlation functions from the cosmic flexion power spectrum, one encounters integrals that do not converge. For $\chi \ll \chi_H$, the lensing efficiency scales as $q(\chi) \propto \chi$ (since $a(\chi) \simeq 1$ for $\chi \ll \chi_H$). Asymptotically, the matter power spectrum follows some power law $\mathcal{P}_{\text{NL}}(k = \ell/\chi, \chi) \propto k^{-n'_s}$. Therefore, for low χ and high ℓ , the cosmic flexion power spectrum scales as

$$\mathcal{P}_F(\ell) \propto \ell^{2-n'_s} \quad (\text{asymptotic}). \quad (3.72)$$

If we examine the integrand of the cosmic flexion-flexion two-point correlation functions, they all have the form

$$\frac{d\xi^{\text{flex-flex}}}{d\ell} \propto \ell \mathcal{P}_F(\ell) J_n(\ell\theta). \quad (3.73)$$

¹⁷<https://des.ncsa.illinois.edu/releases/y3a2/Y3key-catalogs>

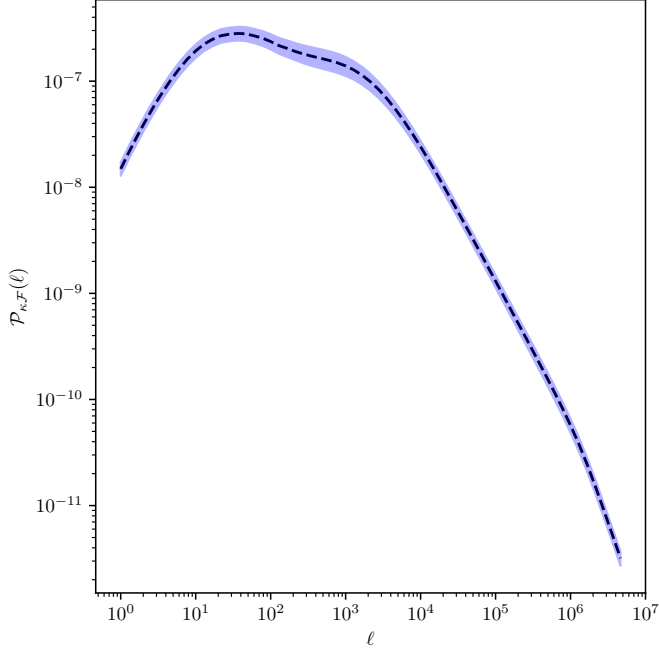


Figure 3.7: The cosmic convergence-flexion power spectrum expected for the DES Y3 using a Planck 18 cosmology. The shaded region is the response of the power spectrum to varying σ_8 over ten times the TT,TE,EE+lowE+lensing 68% interval.

Asymptotically, the Bessel functions of the first kind take the form

$$J_n(x) = \sqrt{\frac{2}{\pi x}} \cos\left(x - (2n + 1)\frac{\pi}{4}\right) + \mathcal{O}\left(\frac{1}{x^{3/2}}\right). \quad (3.74)$$

The integrand then has the asymptotic behavior

$$\frac{d\xi^{\text{flex-flex}}}{d\ell} \propto \ell^{2.5 - n'_s} \cos\left(\ell\theta - (2n + 1)\frac{\pi}{4}\right). \quad (3.75)$$

Therefore, if $n'_s \leq 2.5$, then these integrals do not converge, because the integral takes the form of a runaway cosine envelope. This is indeed the reality we are faced with if one allows the HALOFIT routine to compute P_{NL} out to asymptotically large k (or perform a linear extrapolation to arbitrarily large k). However, in Widrow et al. [110], it is discussed that the matter power spectrum will be proportional to $k^{n_s - 4}$ for arbitrarily large k , where n_s is the scaling of the matter power spectrum at low k : $P_{\text{NL}}(k = \ell/\chi, \chi) \propto k^{n_s}$, where the Planck 18 best fit value for n_s is $\simeq 0.96$ [28].

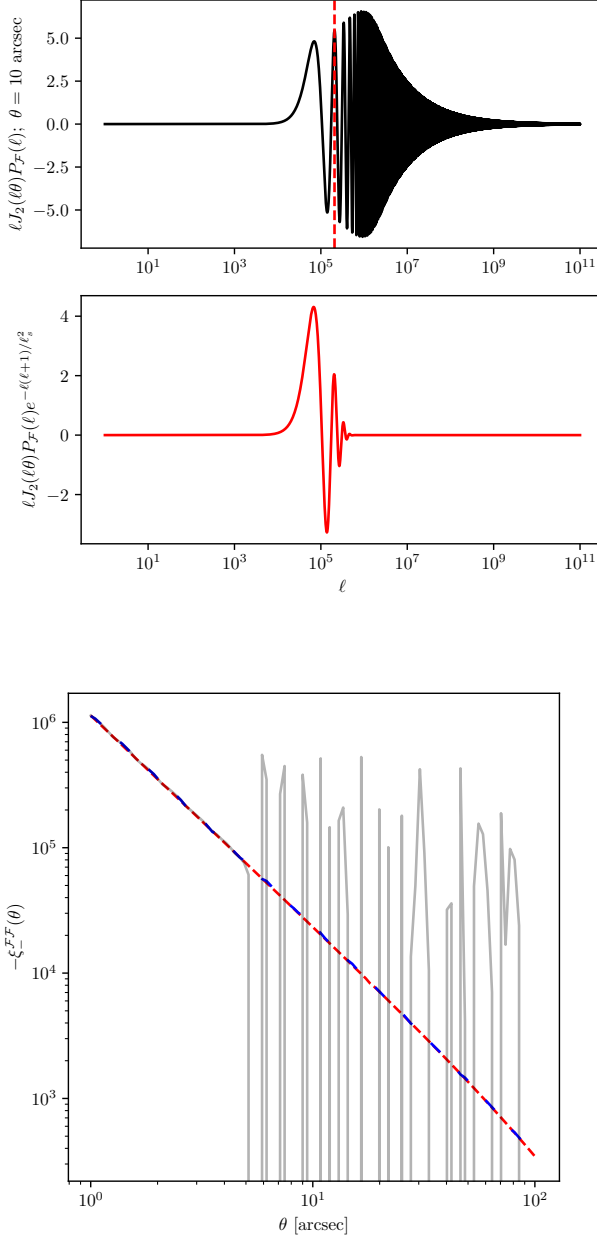


Figure 3.8: In the top panel, we show the integrand of the flexion-flexion correlation function ξ_-^{FF} as a function of ℓ for $\theta = 10$ arcseconds. We see that after the first peak, there is a rapid oscillation of the cosine envelope. This ringing makes numerical integration very computationally expensive. The vertical dashed line is located at the second local maximum, ℓ_s . In the middle panel, we show the renormalized integrand, given by Eq. (3.76). The bottom panel shows the results of integrating the non-renormalized integrand (solid, gray line) and the normalized integrand (tightly dashed, red line). Additionally, we show the result of integration via the double-exponential transform of Eq. (3.77) (loosely dashed, blue line).

We therefore propose the following renormalization: compute the matter power spectrum up to some very large k_{\max} using the small-scale power spectrum generated by `halofit`, and then have the matter power spectrum take the form $k^{n_s - 4}$ for k beyond that computed by `halofit`. This modification of \mathcal{P}_{NL} affects the shape of the convergence power spectrum via Eq. (3.1), which in turn affects the flexion power spectrum via Eq. (3.4). This allows the cosmic flexion integrals of Eqs. (3.22) - (3.24) to converge. We note that, since we are only changing the shape of the power spectrum asymptotically, cosmic shear is very insensitive to this renormalization. For instance, we find that computing $\xi_+^{\gamma\gamma}$ for the non-renormalized and renormalized power spectra are indistinguishable to within one part in 10^7 .

We next encounter another problem with integration, but this time it is numerical. For increasingly large θ , these integrals become very difficult and computationally expensive to integrate due to rapid oscillation of the integrand. Highly oscillatory integrals have been studied extensively in applied mathematics; however, there does not exist a conventional way to numerically handle them [111]. We therefore offer two possible methods that we find to be in agreement with each other at the percent level. First, we offer in this paper a novel technique in which we renormalize the integrals given in Eqs. (3.22) - (3.24). Here, we multiply the integrands by a decaying exponential. These integrands then take the form

$$\frac{d\xi^{\text{flex-flex}}}{d\ell} \propto \ell \mathcal{P}_F(\ell) J_n(\ell\theta) \times e^{-\ell(\ell+1)/\ell_s^2} \quad (3.76)$$

where ℓ_s is taken to be the location of the second maximum of the integrand. An alternative method to a second renormalization is an existing technique: a double-exponential variable transformation based on the zeros of the Bessel function of the first kind [112, 113]. We use the approximation [114]

$$\int_0^\infty dx f(x) J_n(x) \simeq \pi \sum_{k=1}^{\infty} w_{nk} f\left(\frac{\pi\psi(hr_{nk})}{h}\right) J_n\left(\frac{\pi\psi(hr_{nk})}{h}\right) \psi'(hr_{nk}) \quad (3.77)$$

where r_{nk} are the roots of $J_n(x)$ divided by π , $\psi(t) = t \tanh(\frac{1}{2}\pi \sinh t)$ is the double-exponential transform, h is the step size of the integration, and the weights are $w_{nk} = Y_n(\pi r_{nk})/J_{n+1}(\pi r_{nk})$,

where Y_n is the Bessel function of the second kind, order n . For our purposes, we take $f(x) \rightarrow \ell \mathcal{P}_F(\ell)$ and $J_n(x) \rightarrow J_n(\ell\theta)$.

A special technique of either renormalization or the double-exponential transform is not necessary for small θ , where the integrand ringing is negligible. We can therefore test these two approaches by comparing them to the non-renormalized integration at low θ . These results are shown in Fig. 3.8 for $\xi_{-}^{\mathcal{FF}}$. The renormalization integration method is computed using **F-SHARP** and the double-exponential transform integration method is computed using the public library **hankel**¹⁸ (see Murray and Poulin [115]). We see that for small θ , where the integrand ringing is minimal and can be easily integrated numerically, all three methods of integration are in agreement. For large θ , where the non-renormalized numerical integration fails, the renormalization and the double-exponential transform allow for efficient and accurate numerical integration. Again, since both of these techniques agree with each other at the percent level, and are therefore indistinguishable in this context, we can use either.

3.4.2 Forecasts for the Dark Energy Survey

We can preview the expected signal-to-noise of DES flexion correlation functions by measuring flexion estimators for a small sample of galaxies constituting $\simeq 0.5$ square degree patch of sky, taken from the publicly available DES Y3 Shape Catalogue¹⁹ (see Gatti et al. [81]). We retrieve the corresponding galaxy images from the DES Data Management public server.²⁰ The measurement pipeline for this subsample is as follows: first flexion and ellipticity are measured for each individual galaxy using the code **Lenser**²¹ – a fast, open source, minimal-dependency Python tool for estimating flexion and shear from real survey data and realistically simulated images (see Fabritius II et al. [50] for a detailed description). For these forecasts, it is not necessary to measure the correlation functions. Rather, we are interested in measuring the autovariances of the correlation functions using Eqs. (3.67) - (3.71). To do this, we use **F-SHARP** in order to (i) compute the root mean square noise for the various lensing estimators in the subsample of galaxies (which will remain constant across the

¹⁸<https://github.com/steven-murray/hankel>

¹⁹<https://des.ncsa.illinois.edu/releases/y3a2/Y3key-catalogs>

²⁰<https://des.ncsa.illinois.edu>

²¹<https://github.com/DrexelLenser/Lenser>

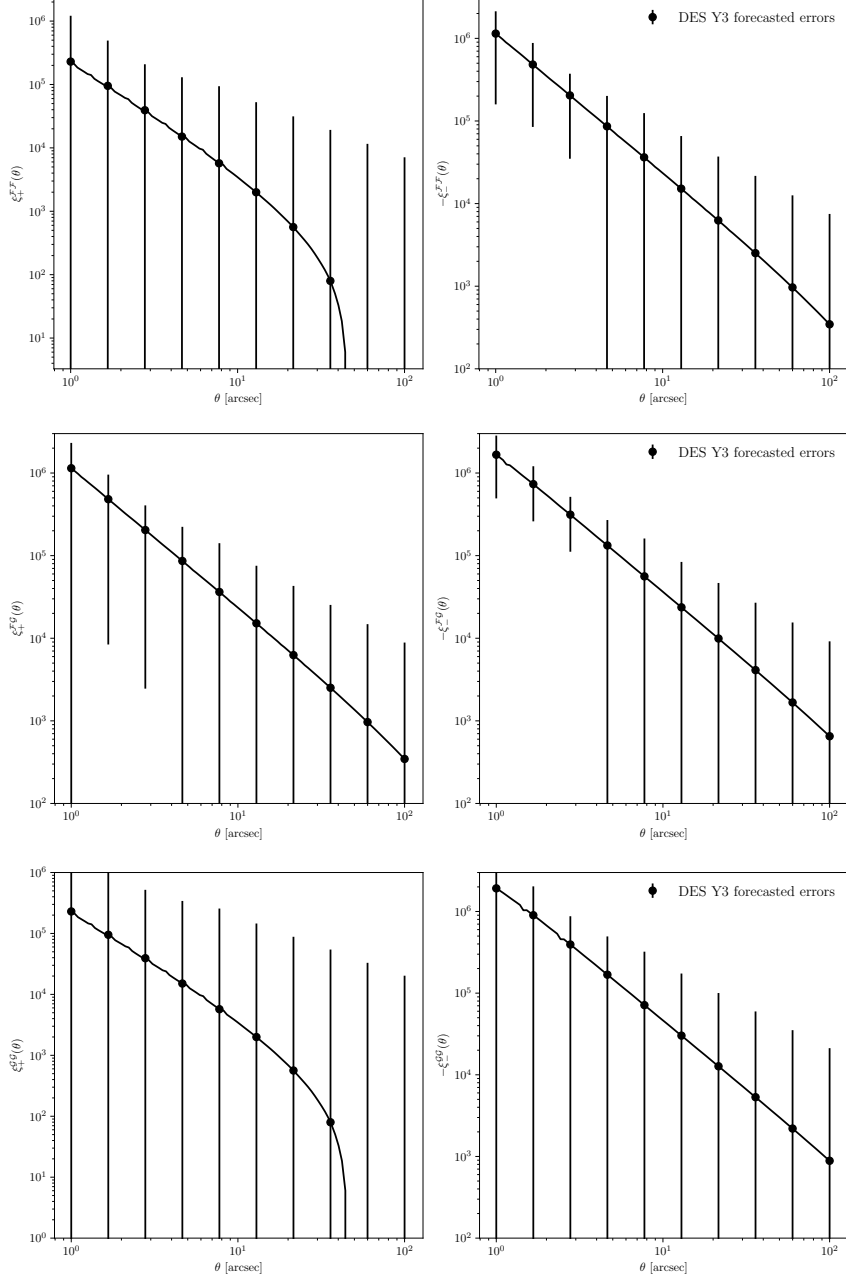


Figure 3.9: The theoretical cosmic flexion \mathcal{F} - \mathcal{F} auto-correlation (top row) and \mathcal{F} - \mathcal{G} cross-correlation functions (bottom row) with forecast errors for DES Y3. Note that the data points are equal to the theoretical values and do not represent a measurement. Here, we anticipate a higher S/N for the \mathcal{F} - \mathcal{G} cross-correlation than the \mathcal{F} - \mathcal{F} auto-correlation. Note that $\xi_{\pm}^{\mathcal{F}\mathcal{G}}$ here represents the combined use of both $\xi_{\pm}^{\mathcal{F}\rightarrow\mathcal{G}}$ and $\xi_{\pm}^{\mathcal{G}\rightarrow\mathcal{F}}$.

entire DES field) using Eqs. (3.64) - (3.66) and (ii) calculate the number of pairs given by Eq. (3.34),

which is scaled to the remaining amount of sky in the survey. These are then used in Eqs. (3.67)

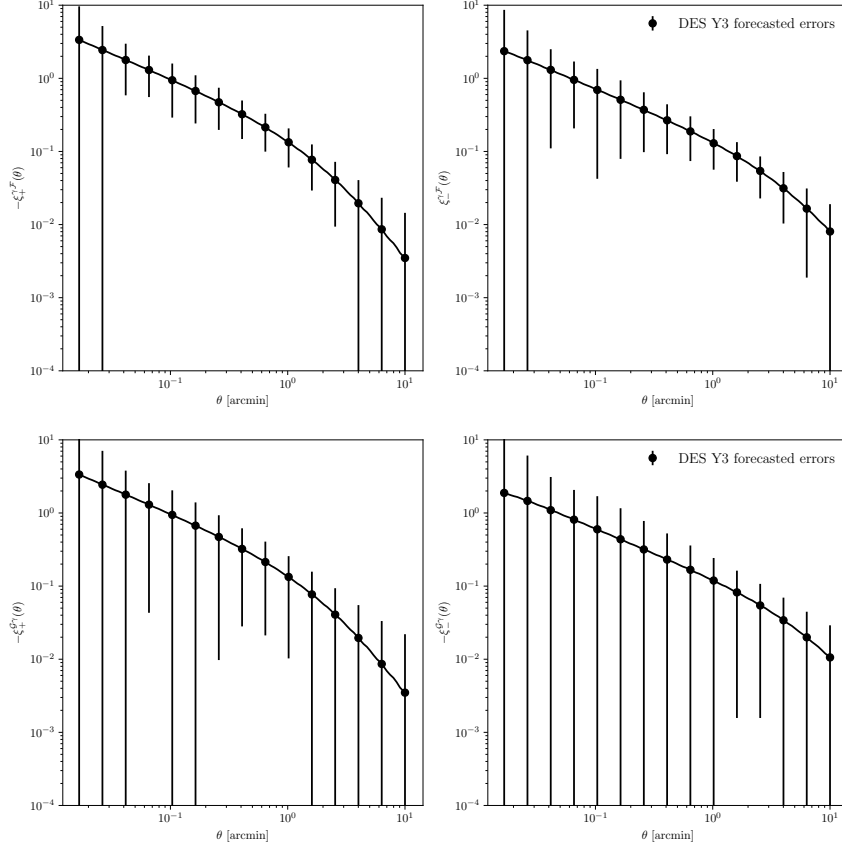


Figure 3.10: The theoretical cosmic shear-flexion $\gamma\text{-}\mathcal{F}$ (top row) and $\mathcal{G}\text{-}\gamma$ (bottom row) cross-correlation functions with forecast errors for DES Y3. Note that the data points are equal to the theoretical values and do not represent a measurement. Here, we anticipate a much higher S/N for shear-flexion than flexion-flexion. Note that $\xi_{\pm}^{\gamma\mathcal{F}}$ here represents the combined use of both $\xi_{\pm}^{\gamma\rightarrow\mathcal{F}}$ and $\xi_{\pm}^{\mathcal{F}\rightarrow\gamma}$ (and similarly for $\xi_{\pm}^{\mathcal{G}\gamma}$).

- (3.71) to calculated predicted errors on the various DES full-survey correlation functions. These forecasts are shown in Figs. 3.9 and 3.10. The cosmic flexion-flexion correlations are just detectable with the full survey. We immediately see why shear-flexion cross-correlation is a very valuable signal to measure – it has a much higher S/N than does flexion-flexion.

Eqs. (3.67) - (3.71) are adequate for calculating errors on the cosmic flexion signals at least in the short term. Typically, cosmic shear studies make use of analytical and/or Gaussian and log-normal simulations to estimate the covariance matrix of the cosmic shear correlation functions. This sub-percent level accuracy of the covariance is necessary in cosmic shear studies that wish to make likelihood analyses that lead to constraints on cosmological parameters. As we do not wish to use the

cosmic flexion results to constrain cosmological parameters, we do not require this sub-percent level accuracy of the covariance. While we have full analytical covariances worked out in Appendix 3.3.2, they have not yet been tested against, and corrected by, N-body simulations as is done with cosmic shear covariances in DES. In addition to the fact that we do not require this level of precision on our errors, there also do not currently exist N-body simulations capable of producing weak-lensing maps at a fine enough resolution to study the small-scale structure probed by cosmic flexion.

3.4.3 Discussion

As we have seen, cosmic flexion peaks at small, nonlinear scales. These scales are typically discarded in weak lensing studies that seek to only use larger scale information to constrain cosmological parameters. However, the fact that cosmic flexion signals peak at these scales put them in a unique position to constrain the amplitude and shape of this small-scale matter power spectrum, which can lead to a better understanding of the physics at the substructure level.

It is interesting to note that shear-flexion cross-correlation is partly measurable in the large-scale, linear regime ($\gtrsim 10$ arcmin). One could undertake a study of how the covariance of the shear-flexion cross correlators at these large scales compare with N-body simulations, as is done with cosmic shear. This could indeed lead to shear-flexion cross-correlation placing constraints on cosmological parameters.

Chapter 4: Flexion in the Dark Energy Survey

In 2020, I joined the Dark Energy Survey as an External Collaborator (EC) with the project proposal “Flexion in the Dark Energy Survey.” The goal of this project was to (i). create a flexion catalogue by using `Lenser` to measure the flexion of all available galaxies in the DES dataset, (ii). with the theoretical work laid out in AGB, take the first-ever measurements of cosmic flexion using the flexion catalogue and my two-point measurement pipeline `F-SHARP`, and (iii). use the flexion catalogue to measure galaxy-galaxy flexion (both \mathcal{F} and \mathcal{G}). In this Chapter, I present the results of science goals (i) and (ii), and leave (iii) for future work.

4.1 The Dark Energy Survey (DES)

The goal of understanding dark energy and measuring the growth and evolution of large-scale structure in our Universe has led to the establishment of many so-called Stage III cosmology surveys. Wide-field weak lensing analyses are integral components of Stage III surveys such as the Dark Energy Survey¹ (DES; [97]), the Kilo-Degree Survey² (KiDS; [98]) and the Hyper Suprime-Cam Subaru Strategic Program³ (HSC SSP; [99]).

In 2019, DES completed six years of observations using the Dark Energy Camera (DECam) mounted on the four-meter Victor M. Blanco Telescope, located at the Cerro Tololo Inter-American Observatory (CITO) in Chile. At the time I began measuring flexion in DES, the most recent dataset available was the first three years of observations (hereafter referred to as Y3). DES key projects using the final dataset, Y6, are still in progress at the time I am writing this thesis. Therefore, the results presented here are flexion measurement in the Y3 dataset.

¹<https://www.darkenergysurvey.org>

²<https://kids.strw.leidenuniv.nl>

³<https://hsc.mtk.nao.ac.jp/ssp>

4.1.1 DES Y3 dataset

The DES Y3 photometric dataset (`Y3 Gold`) consists of the first three years of observations, which covers the full DES footprint of nearly 5000 square degrees of the Southern Sky in the *grizY* bands [116]. Contained in `Y3 Gold` are a total of 388M astronomical objects imaged across all bands. It is important to note that not all of these objects are galaxies that can be used for weak lensing measurement – many objects are stars within our own galaxy, some are unresolved blended objects, etc.

The DES Y3 photometric data consists of $\sim 10,000$ “tiles,” which are $0.73^\circ \times 0.73^\circ$ coadd images. DES makes use of Multi-Epoch Data Structures⁴, hereafter referred to as MEDS files, in order to store the photometric data (see e.g. Jarvis et al. [78] for a description). Each MEDS file represents one DES tile observed in one band, and hence, each MEDS file contains photometric information for $\sim 10,000$ objects. Defined by the coadd image, MEDS files contain images for all available epochs, as well as the coadd, in a particular band. Stored in a MEDS file are postage stamps for every object detected in the coadd image. In addition to the science images (data maps), MEDS files also contain weight maps and segmentation maps for each epoch and for the coadd.

In addition to the data maps, weight maps, and segmentation maps available in the MEDS files, the DES Y3 dataset also has PSF maps available, which are modeled using the PIFF pipeline⁵ [117].

The observations of DES are publicly available in the form of, for example, a cutout service that can generate postage stamps. This was the method I used in AGB to run a forecast for cosmic flexion measurement in DES Y3 (see Sec. 3.4.2). The MEDS and PSF files are, however, not publicly available and are accessible only to DES members. I am only able to get access to these official DES Y3 data products as a DES EC.

4.1.2 DES Y3 results: Shape catalogue, galaxy clustering and weak lensing

One of the major goals of DES is to derive cosmological parameter constraints from the so-called 3×2 -point function – that is, a data-vector comprised of galaxy clustering (the position-position

⁴<https://github.com/esheldon/meds/>

⁵<https://github.com/rmjarvis/Piff>

two-point correlation function of source galaxies), galaxy-galaxy lensing (specifically, galaxy-galaxy shear – see Sec. 1.2.9), and cosmic shear (see Sec. 1.3). This is among the most powerful probes in cosmology and has led to exquisite constraints on cosmology for the low-redshift Universe. These results are summarized in Abbott et al. [40].

In order to measure galaxy-galaxy shear and cosmic shear, it is necessary to have measurements of the observed ellipticity of all source galaxies in the DES Y3 dataset. The official DES data product containing ellipticity measurements for Y3 is the DES Y3 Weak Lensing Shape Catalogue [81]. The DES Y3 Shape Catalogue is derived using the METACALIBRATION [72, 73] pipeline. Ellipticity measurements are made in METACALIBRATION using a multi-band, multi-epoch fit across all available epochs in the r , i , and z bands. After selection cuts associated with Y3 Gold and further selection cuts associated with shape measurement, detailed in Gatti et al. [81], the result is a catalogue of $\sim 100M$ galaxies with successful measurements of ellipticity.

4.2 The DES Y3 Flexion Catalogue

4.2.1 Lenser Catalogue

The starting point for the DES Y3 **Lenser** Catalogue are the DES Y3 MEDS files and PSF files. Like the DES Y3 Shape Catalogue, derived using METACALIBRATION, I make use of information from the r , i , and z bands for the construction of the DES Y3 **Lenser** Catalogue. While the Shape Catalogue makes use of the single-epoch images to do a multi-band, multi-epoch fit for ellipticity measurement, I make use of the coadd r , i , and z images to perform a multi-band (coadd epoch) flexion measurement using **Lenser**.

The DES Y3 **Lenser** Catalogue consists of the **Lenser** best-fit parameter estimates for all objects in the DES Y3 dataset, $\{\theta_0^1, \theta_0^2, n_s, \theta_s, q, \phi, \psi_{111}, \psi_{112}, \psi_{122}, \psi_{222}\}$; the $\chi^2/\text{d.o.f}$ of each fit; the estimated size of each galaxy image, a ; and the central brightness of the galaxy in the r , i , and z bands, $\{I_0\}$. These computations are done using the SCIAMA Supercomputer⁶. The Sciama High Performance Computer cluster is supported by the Institute of Cosmology and Gravitation, SEPNet and the University of Portsmouth in the United Kingdom. Running the DES Y3 dataset through

⁶<http://www.sciamain.icg.port.ac.uk/>

the **Lenser** pipeline takes approximately one million CPU hours.

Lenser is parallelized such that one DES tile is run per SCIAMA core. For each tile, the $\sim 10,000$ objects in that tile are run in series through **Lenser**. In order to parallelize the **Lenser** pipeline, **Lenser** is interfaced with PythonOpenMPI⁷. Each DES tile run through **Lenser** requires reading in MEDS files associated with the r , i , and z bands, which is done using `meds`⁸.

There are known issues with the coadd PSF estimates, which is a major factor in DES using the single-epoch images instead of the coadds for ellipticity measurement. We made the decision to use coadd images in our measurement because they have a higher S/N than the single-epoch images, and we were concerned that it would not be feasible to measure flexion using the **Lenser** pipeline – which relies on image moments first and model fitting second – with the single epoch images. In retrospect, it would be interesting to try to build a DES Y3 **Lenser** Catalogue using the single-epoch images. As is discussed later on, we find that there is likely contamination in some (but not all) of our cosmic flexion measurements owing to PSF mis-estimation. It is unclear at this stage, however, whether this is entirely due to the coadd PSF or whether it is because the PIFF PSF modeling accounts only for ellipticity and not flexion effects.

4.2.2 Object Selection: Flexion Catalogue

The DES Y3 Flexion Catalogue is created from the DES Y3 **Lenser** Catalogue. It consists of ellipticity components, $\{\epsilon_1, \epsilon_2\}$ computed from the **Lenser** q and ϕ estimates via Eq. (2.9) and \mathcal{F} - and \mathcal{G} -flexion components, $\{\mathcal{F}_1, \mathcal{F}_2, \mathcal{G}_1, \mathcal{G}_2\}$ computed from the **Lenser** estimates of ψ_{ijk} via Eqs. (1.121) - (1.124).

There are a number of cuts applied to the **Lenser** catalogue to arrive at the final Flexion Catalogue. The first major cut applied to the DES Y3 **Lenser** Catalogue is to include in the final Flexion Catalogue only objects that pass the selection cuts of the DES Y3 Shape Catalogue. These cuts are fully described in Gatti et al. [81]. To summarize briefly, these cuts are based on survey geometry (objects need to be within the unmasked regions of Y3 Gold); object S/N; object size; objects with the most reliable photometric redshift estimates; objects that are not likely to blend; and objects

⁷<https://github.com/seanlabean/PythonOpenMPI>

⁸<https://github.com/esheldon/meds/>

that are not likely to be binary stars. These cuts ensure a high level of confidence that the remaining objects are galaxies (and not stars or blends) conducive to weak lensing measurement.

Beyond this, additional cuts are made for final selection and are described below:

- Poor **Lenser** fits are excluded by requiring a goodness of fit $\chi^2/\text{d.o.f.} < 5$.
- Objects that **Lenser** best-fit finds to be point sources or nearly point sources are excluded by $n_s < 10$ and $\theta_s > 1e - 10$. These values correspond to the maximum Sérsic index and minimum characteristic size allowed by the parameter bounds in the **Lenser** pipeline.
- Any residual objects with extreme sizes are removed by requiring $0.5 < a < 100$ pixels.
- Cuts are made in flexion in order to remove extreme values: $a|\mathcal{F}| < 0.4$, $a|\mathcal{G}| < 0.8$, $|\mathcal{F}| < 1 \text{ arcsec}^{-1}$, $|\mathcal{G}| < 2 \text{ arcsec}^{-1}$. While ellipticity is bounded by $[-1, 1]$, this is not the case for flexion. An assumption for flexion measurement is that the quantities $a|\mathcal{F}|$ and $a|\mathcal{G}|$ are small with respect to unity – hence, our cuts.
- A final cut removes galaxies that lie in certain regions of the survey area that are problematic in terms of flexion measurement. These areas are defined as those where local mean flexion values are extreme (5σ -outliers). These regions tend to occur near the survey edge as well as areas that are masked out by **Y3 Gold**.

In Fig. 4.1, we show plots of the measured flexion for the DES Y3 Flexion Catalogue. In the left panel of Fig. 4.2, we show histograms of the ellipticity components, as measured by **Lenser**. In the right panel, we show a comparison of the ellipticity measured by **Lenser** in the Y3 Flexion Catalogue compared to the uncalibrated⁹ ellipticities measured by METACALIBRATION in the Y3 Shape Catalogue. As the ellipticity definitions used in these catalogues are different, we compare the two using a quantity that resembles a dot product:

$$\epsilon_{\text{Lenser}} \cdot e_{\text{METACALIBRATION}} = \frac{\epsilon_1 e_1 + \epsilon_2 e_2}{|\epsilon||e|}. \quad (4.1)$$

⁹While METACALIBRATION is a self-calibrating pipeline, this calibration is applied to the shear values after measurement.

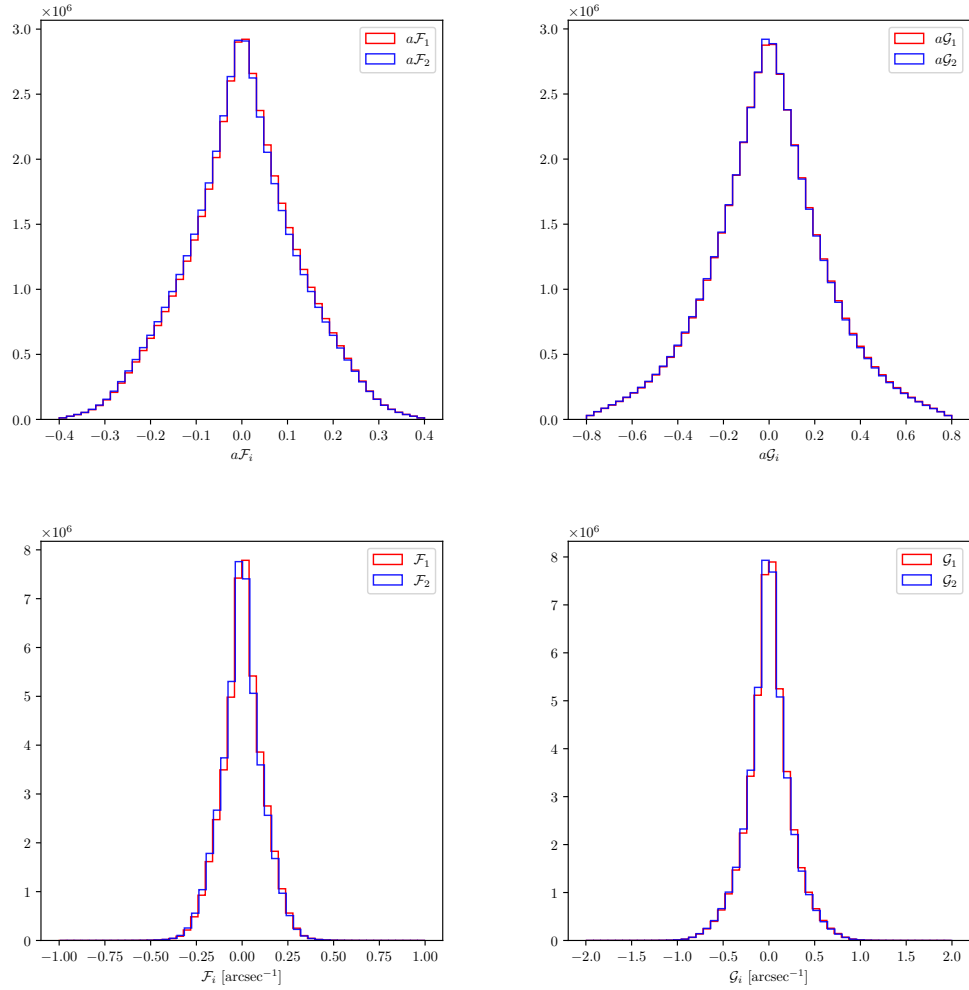


Figure 4.1: Histograms of measured flexion in the DES Y3 Flexion Catalogue.

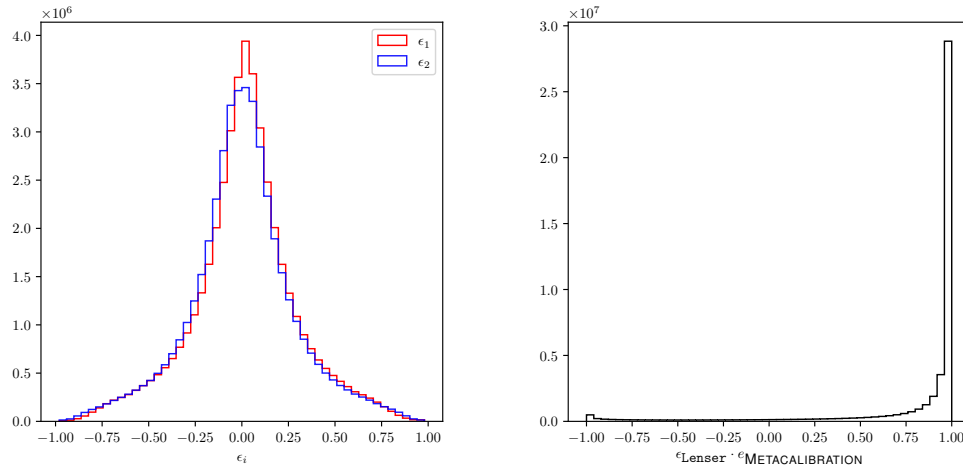


Figure 4.2: *Left:* Histograms of the measured ellipticity in the DES Y3 Flexion Catalogue. *Right:* Comparison of the ellipticity measured in the DES Y3 Flexion Catalogue to ellipticity measurements from the DES Y3 Shape Catalogue.

The “dot product” of these ellipticities is close to unity for the galaxies in the Y3 Flexion Catalogue, with a median value of 0.99, indicating very good agreement between the `Lenser` measurements and the `METACALIBRATION` pipeline.

4.2.3 Systematics in the DES Y3 Flexion Catalogue

Calibration of weak lensing measurement pipelines are a standard component in weak lensing analysis. State-of-the-art shear measurement pipelines such as `METACALIBRATION` are self-calibrating. For measurement pipelines that do not self-calibrate, there is a need to use image simulations as well as the shape catalogue itself to correct for any systematic measurement biases present in the pipeline and/or systematic effects present in the real data. The standard procedure is to quantify a multiplicative and additive bias associated with the $\alpha \in \{1, 2\}$ components of some lensing field a , such that

$$a_\alpha^{\text{obs}} = (1 + m_\alpha)a^{\text{true}} + c_\alpha \quad (4.2)$$

describes the degradation of the true ellipticity or flexion of a galaxy (intrinsic plus lensing) due to systematics [118]. Additive biases can result from, for example, improper PSF modeling or

deconvolution.¹⁰ The idea here is that if the ellipticity and flexion of the PSF is not fully accounted for prior to deconvolution, then some of the PSF shape (ellipticity or flexion) can leak into the measured shape. It is standard procedure in many weak lensing analyses to empirically determine c_α from the shape catalogue, simply by taking $c_\alpha = \langle a_\alpha^o \rangle$, and subtracting it away prior to any science applications.

Using image simulations, one can compare a truth catalogue of, for example, shear values of each galaxy, to an ellipticity value measured by a given pipeline. It is typically found that the additive bias term arising from image simulations is negligible, and that it appears from effects within the real data that are difficult to simulate [119]. The multiplicative bias term, on the other hand, is determined through either self-calibration in the case of METACALIBRATION, or through the image simulations. In the case of shear measurement pipelines, a nonzero multiplicative bias term can arise from blending [120, 121].

We first consider the case of additive bias terms in the ellipticity and flexion measurements in the DES Y3 Flexion Catalogue. In Figs. 4.3 - 4.5, we show `healpix` plots of the flexion and ellipticity fields across the DES Y3 footprint. These plots were created using `healpy` and `skymap`¹¹ with the choice of $N_{\text{side}} = 256$. In Figs. 4.6 - 4.5, we show the flexion and ellipticity sky maps smoothed with a 1° Gaussian beam. For each `healpix` map, this smoothing is done by `healpy.sphtfunc.smoothing(hpxmap, sigma)` where `sigma` is taken to be one degree. This smoothing acts as a high-pass filter for scale. As such, the smoothed sky maps display structure in the flexion and ellipticity fields only for scales larger than one degree. For the cosmic flexion signals, we do not expect to see any coherent signals in any of these lensing fields for scales this large. Therefore, we should expect the smoothed maps to be homogeneous, isotropic, and have means of zero. This is clearly not the case with the signals measured. For all signals, there is a nonzero mean, indicating an additive systematic bias.

As is discussed above, the possible explanations for the origin of the mean additive systematic bias include improper removal of the PSF. This is potentially relevant in the case of the ellipticity,

¹⁰In this formalism, this PSF leakage is folded into the additive bias term, c , though it can also be explicitly included as a separate term.

¹¹<https://github.com/kadrlica/skymap>

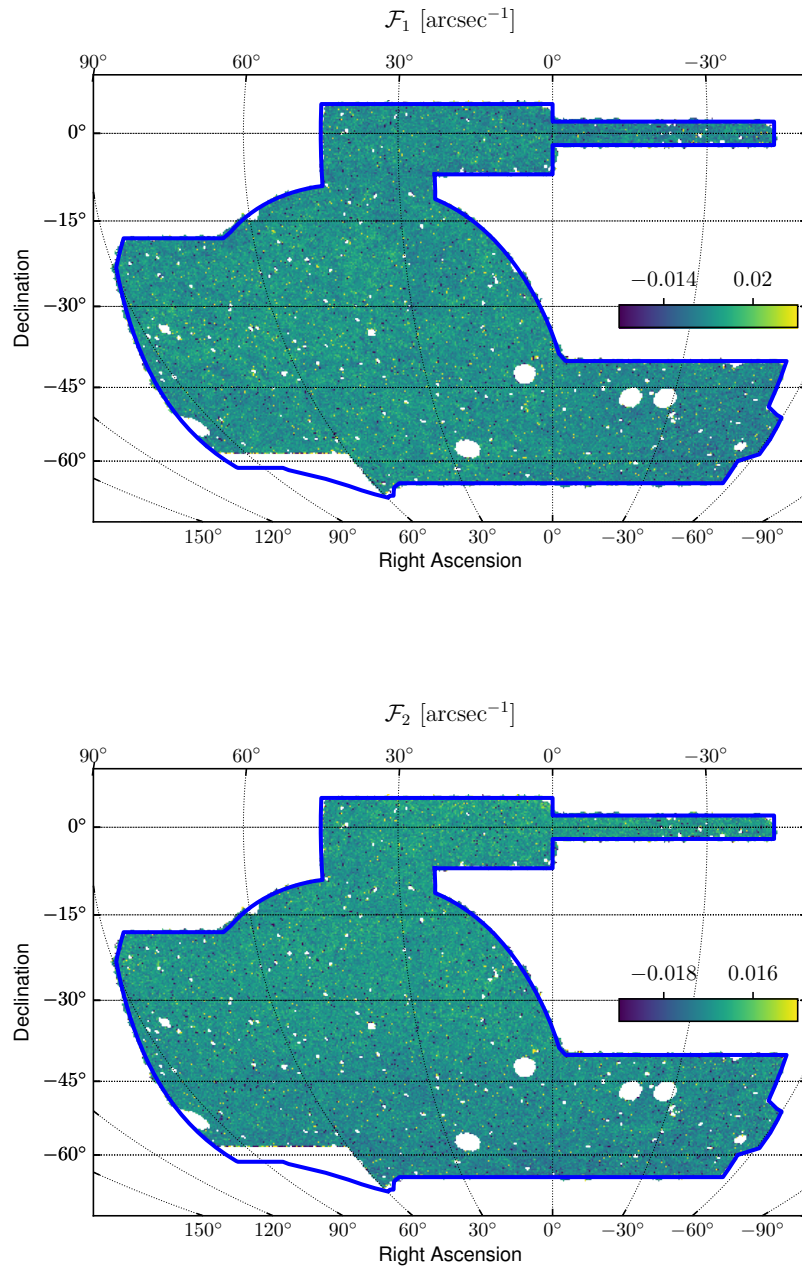


Figure 4.3: \mathcal{F} -flexion of sources in the DES Y3 Flexion Catalogue across the DES Y3 survey footprint.

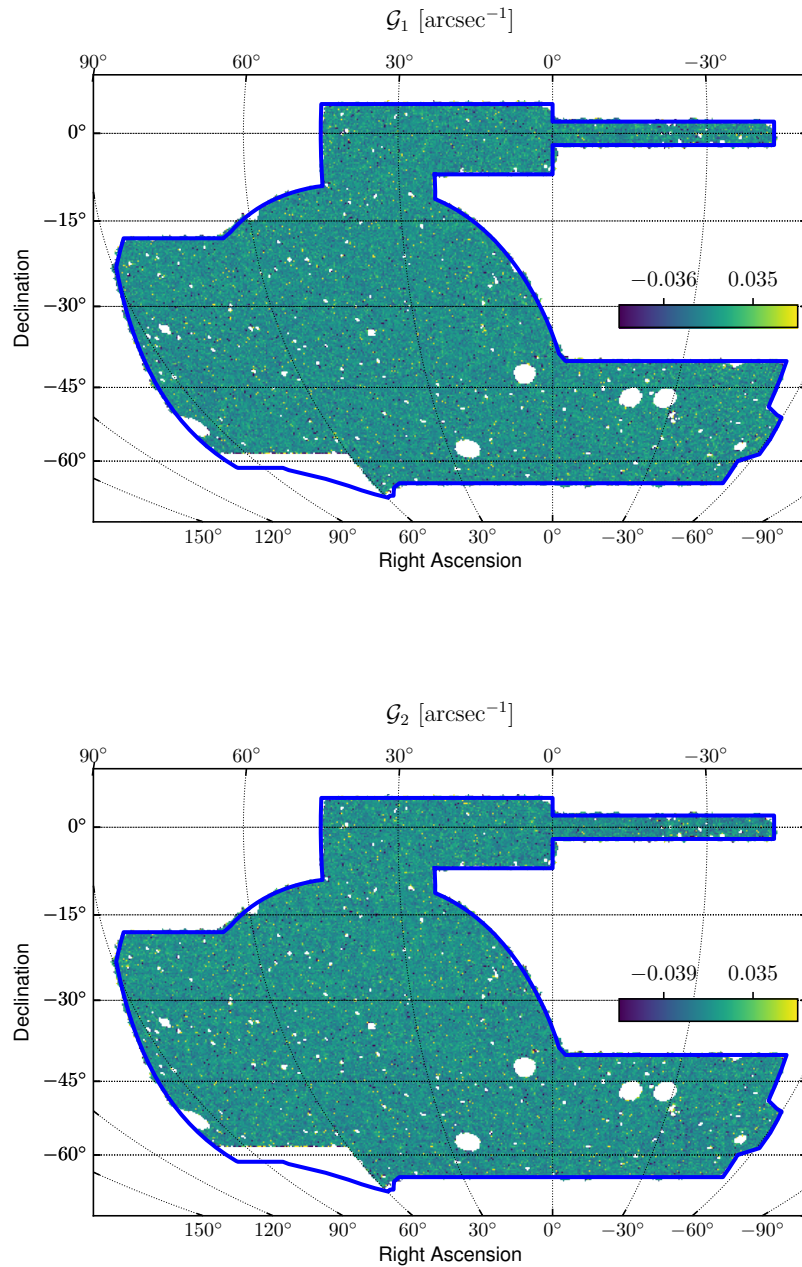


Figure 4.4: \mathcal{G} -flexion of sources in the DES Y3 Flexion Catalogue across the DES Y3 survey footprint.

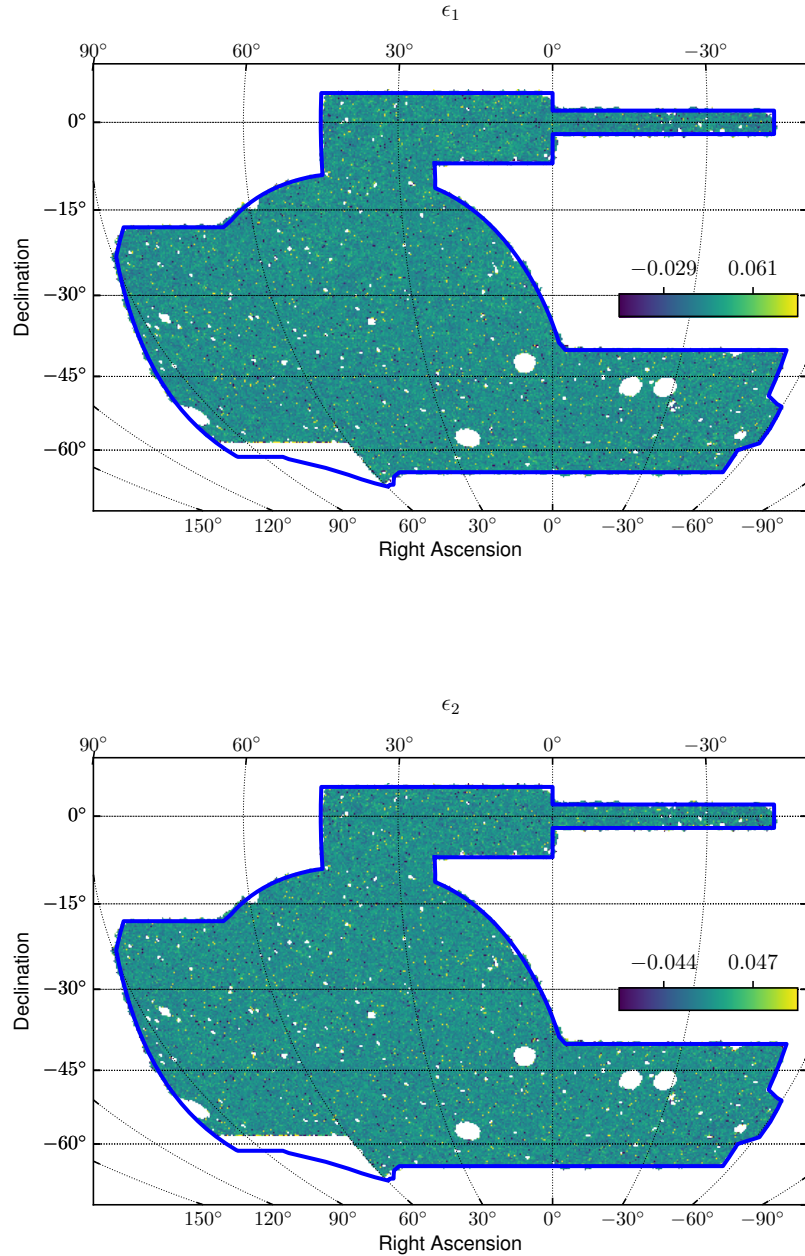


Figure 4.5: Ellipticity of sources in the DES Y3 Flexion Catalogue across the DES Y3 survey footprint.

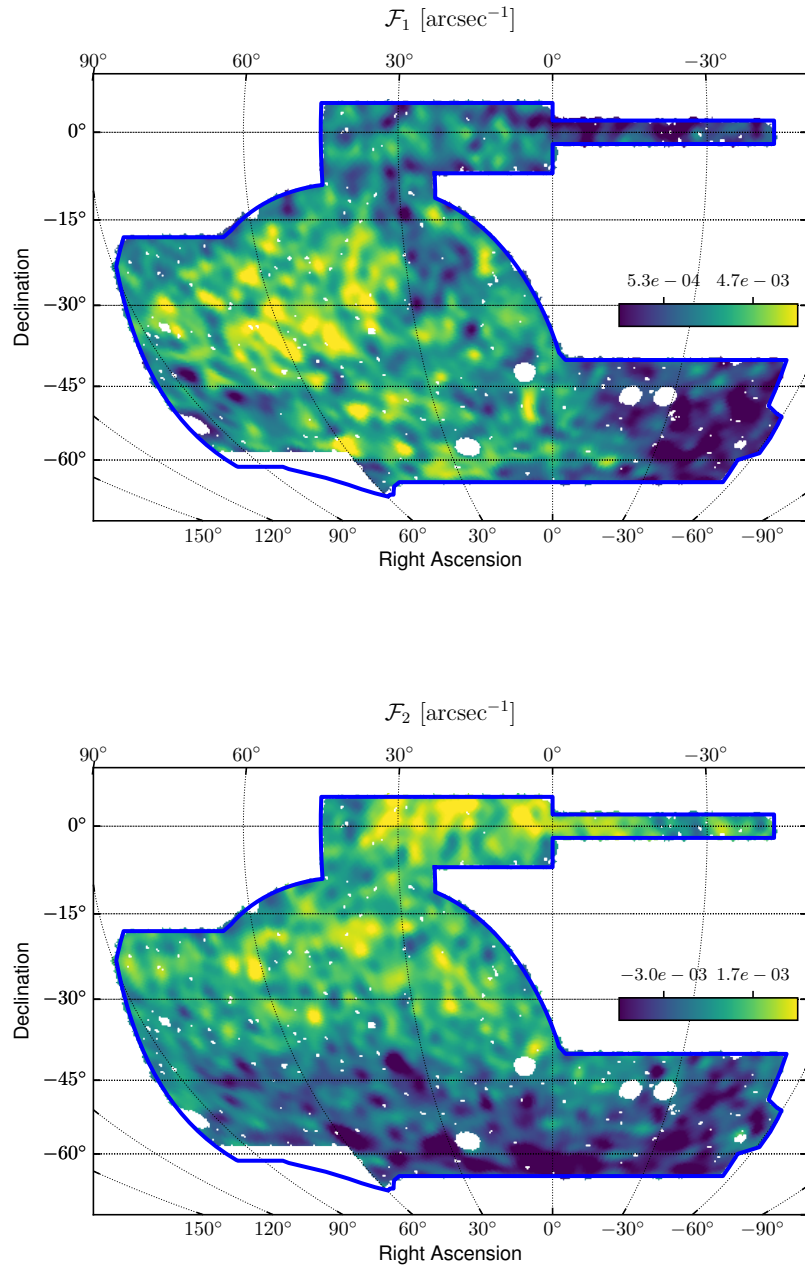


Figure 4.6: DES Y3 \mathcal{F} -flexion maps smoothed with a 1° Gaussian filter.

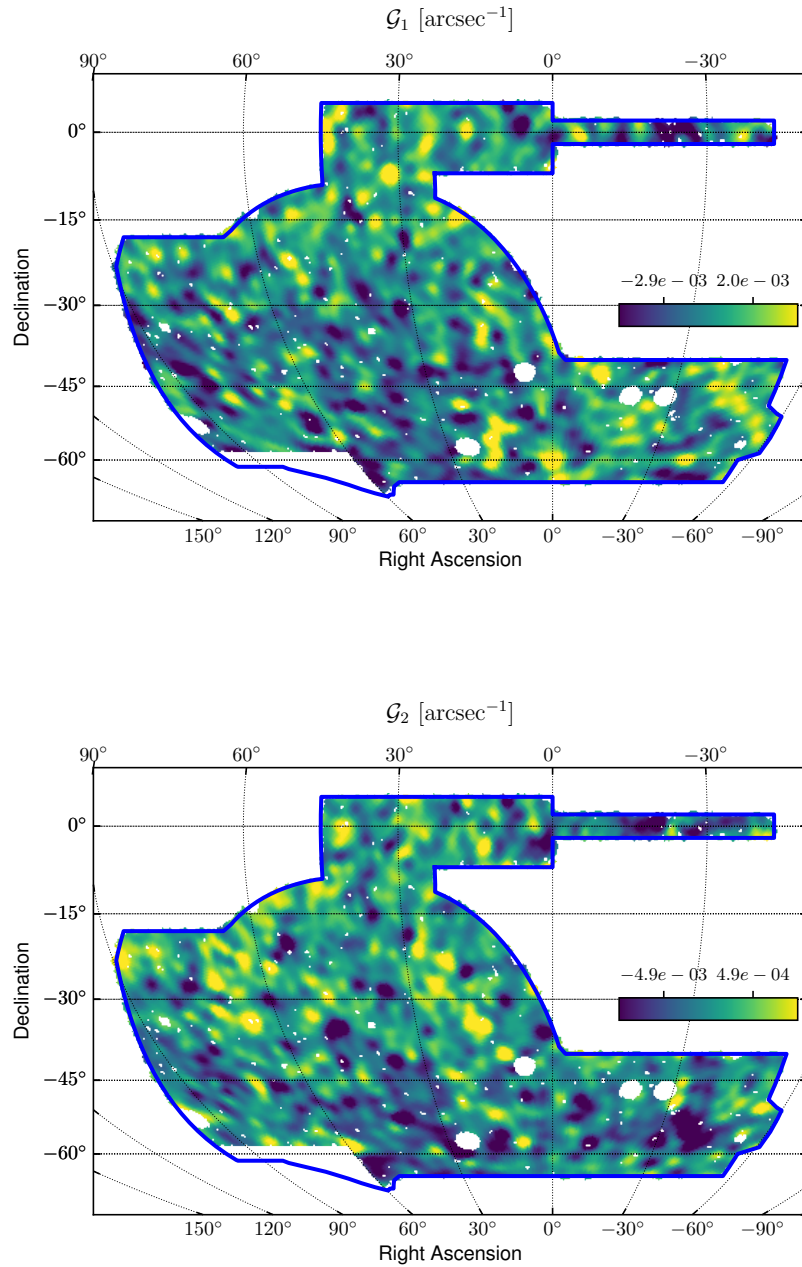


Figure 4.7: DES Y3 \mathcal{G} -flexion maps smoothed with a 1° Gaussian filter.

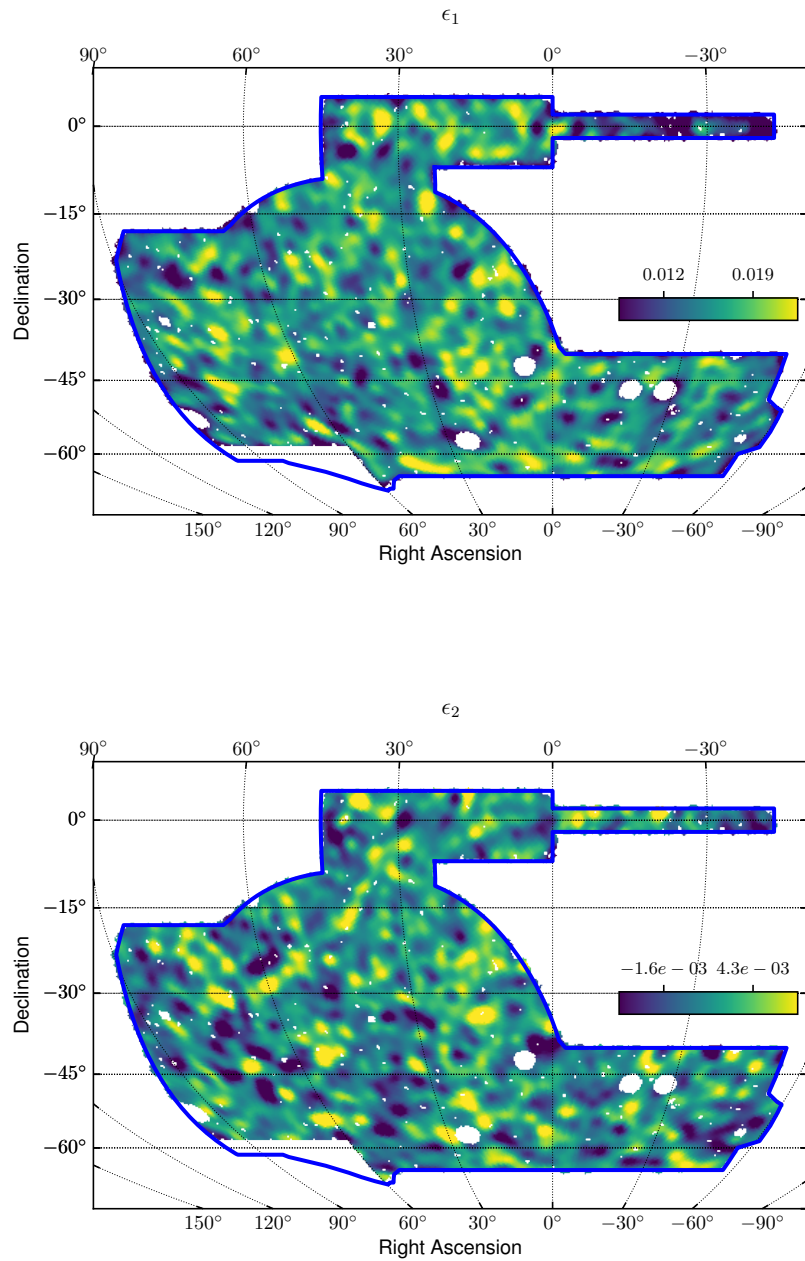


Figure 4.8: DES Y3 ellipticity maps smoothed with a 1° Gaussian filter.

due to the fact that the DES Y3 Flexion Catalogue is built from the coadd images rather than the single-epoch images, where there is less confidence in the PSF modeling. We note that this could be more relevant in the case of the flexion fields given the fact that the PSF models account only for ellipticity and not flexion, as they were built and tested by the DES collaboration in the context of shear measurement exclusively.

In addition to the mean additive systematic bias, we also see that, for some signals, there is an isotropic dependence on the WCS – for example, \mathcal{F}_2 has a strong dependence on Dec, while \mathcal{F}_1 has a noticeable dependence on RA. These coherent signals present in the smoothed maps are far too large to be cosmological in origin. As such, this indicates the presence of a systematic bias in the DES Y3 Flexion Catalogue that varies across the survey footprint. Given the fact that this can be thought of as the average ellipticity and flexion varying across the footprint, we might consider this to be an additive systematic bias that varies across the footprint. The first-order dependence – i.e., the linear dependence as a function of RA and Dec – could perhaps arise from the level of PSF leakage varying across the footprint, owing to some dependence on differential chromatic refraction (DCR). Second-order dependence – i.e., the local variation in the average ellipticity and flexion across the footprint, also evident in the sky maps – could possibly arise from varying survey depth, S/N, the ratio of galaxy size to PSF size, exposure time, brightness, and airmass.

Regardless of the origin of the large-scale systematics, it is important to point out that we are able to remove them from the DES Y3 Flexion Catalogue. For each lensing signal, we simply subtract off the smoothed `healpix` maps from the DES Y3 Flexion Catalogue – i.e., for every galaxy i in the catalogue:

$$\begin{aligned} a_{i1}(\boldsymbol{\vartheta}) &= a_{i1}^{\text{original}}(\boldsymbol{\vartheta}) - a_{i1}^{\text{smoothed}}(\boldsymbol{\vartheta}) \\ a_{i2}(\boldsymbol{\vartheta}) &= a_{i2}^{\text{original}}(\boldsymbol{\vartheta}) - a_{i2}^{\text{smoothed}}(\boldsymbol{\vartheta}) \end{aligned} \quad (4.3)$$

where $a_{\{1,2\}}$ are the components of the lensing field of galaxy i at sky-coordinate $\boldsymbol{\vartheta}$, the “original” superscript denotes the lensing field value in the DES Y3 Flexion Catalogue, and the “smoothed”

superscript refers to the interpolated value of the smoothed `healpix` map at the location of galaxy i . This process removes both large-scale systematic effects: the nonzero means and any isotropic dependence on the WCS. It also acts as a low-pass filter, removing any variation in the mean ellipticity and flexion values on scales larger than the smoothing scale of one degree. This systematics removal is applied to the DES Y3 Flexion Catalogue prior to calculation of the cosmic flexion two-point statistics, described in Sec. 4.3. It is also important to note that any small-scale systematics appearing at the scales relevant for the cosmic flexion measurement are not necessarily removed via this process and may still persist in at least some of the cosmic flexion signals.

I note that a limitation of the `Lenser` pipeline is that it is not self-calibrating, and we currently do not have tools in order to create realistic image simulations of galaxies with realistic flexion. While `Lenser` certainly has the capability of creating simulated images of galaxies with shear and flexion values, we would want an independent pipeline capable of simulating these images to calibrate `Lenser` against. As such, we must admit the possibility that there exists a multiplicative bias systematic in the ellipticity and flexion measurements of the DES Y3 Flexion Catalogue.

As the primary science goal of the DES Y3 Flexion Catalogue is the measurement of the cosmic flexion two-point statistics, we are mainly interested in the systematics relevant to these signals. The impact of any residual systematics on the two-point statistics is discussed in Sec. 4.3.4. We find that, while some of the two-point functions are likely completely contaminated by systematics, this is not the case for all of them.

4.3 The first detection of cosmic flexion using DES

In AGB, the theory of cosmic flexion was introduced, as were a number of estimators and covariances for the various two-point correlation functions (2PCFs). For a review of this, see Chapter 3. The assumption of these estimators is that the two-point functions are well described by a Gaussian likelihood. This is to say that the probability distribution function (PDF) for any angular separation bin, θ_x of any cosmic flexion 2PCF estimator, $\hat{\xi}^{ab}(\theta_x)$, is Gaussian. As will be discussed in more detail below, we ultimately find the cosmic flexion likelihood to be non-Gaussian, in contrast to the cosmic shear Gaussian likelihood.

It is useful to describe the cosmic flexion 2PCFs as statistics of underlying sets. Let \mathbf{L} be the set of all galaxies in the DES Y3 Flexion Catalogue with **Lenser** best-fit parameter values. Here, we are going to choose to weight all galaxies equally ($w = 1$). We introduce the *two-point pair-wise set function* (2PSF):

$$\Xi_{\pm}^{ab}(\theta) \equiv \{(a_{i1}^{t_0} b_{j1}^{t_0} \pm a_{i2}^{t_0} b_{j2}^{t_0}) \Delta_{\theta}(ij) | i \in \mathbf{L}, j > i\} \quad (4.4)$$

such that the estimator of Eq. (3.36), with $w = 1$, is recovered by

$$\hat{\xi}_{\pm}^{ab}(\theta) = \frac{\sum \Xi_{\pm}^{ab}(\theta)}{N_p(\theta)} = \text{mean} [\Xi_{\pm}^{ab}] (\theta) \quad (4.5)$$

The two-point correlation functions described by Eq. (3.36) are the EE-mode signals, as they probe the EE-mode part of the power spectrum (see e.g. Kilbinger [4]). There are also the EB-mode signals, referred to as the “cross” two-point functions in AGB, which vanish due to parity symmetry. The 2PSFs for the EB-mode signals are

$$\begin{aligned} \Xi_{\times 1}^{ab}(\theta) &\equiv \{(a_{i1}^{\prime t_0} b_{j2}^{\prime t_0}) \Delta_{\theta}(ij) | i \in \mathbf{L}, j > i\} \\ \Xi_{\times 2}^{ab}(\theta) &\equiv \{(a_{i2}^{\prime t_0} b_{j1}^{\prime t_0}) \Delta_{\theta}(ij) | i \in \mathbf{L}, j > i\} \end{aligned} \quad (4.6)$$

There are a total of eight flexion-flexion EE-mode signals, eight flexion-flexion EB-mode signals, eight shear-flexion EE-mode signals, and eight shear-flexion EB-mode signals that can be measured from the DES Y3 Flexion Catalogue. It is useful to measure the EB-mode signals, because they should be consistent with the null hypothesis – if they do not, it is indicative of systematics contamination in the data.

4.3.1 F-SHARP: Measuring cosmic flexion 2PCFs

F-SHARP was originally intended as a code to calculate the mean statistics of the cosmic flexion 2PCFs, where it simply calculates the estimators of each 2PCF via Eq. (3.36) and their corresponding autovariances via Eq. (3.61). In concert with this, F-SHARP has modules that allow for parallelization (making use of PythonOpenMPI) by chunking the dataset \mathbf{L} into N_{chunks} of the data

that each get run through **F-SHARP**. This, in turn, allows for **F-SHARP** to use these chunks to get a jackknife estimate of the covariance matrices for each 2PCF.

Since we ultimately find that the cosmic flexion signal is highly non-Gaussian, mean statistics are not sufficient to characterize the 2PCFs. As such, I have incorporated a number of additional capabilities in **F-SHARP**. I describe them below, and assign a name to each sub-pipeline within **F-SHARP** for convenience. All of these sub-pipelines have modules written for both series and parallel computation:

- F^\sharp Major: This is the original **F-SHARP** pipeline, which estimates mean statistics of the 2PCFs.

While we find mean statistics are not suitable to characterize the cosmic flexion 2PCFs, they are suitable for cosmic shear 2PCFs.

- G^b Minor: This sub-pipeline is geared toward simple characterization of the 2PSFs without saving them to disk in their entirety. This sub-pipeline has two components:

1. Calculating a subsample of the 2PSFs and saving them to disk. This subsample can be used in order to estimate the central moment and scatter in the 2PSF distributions, quantified by the median and the median absolute deviation (MAD), respectively, where the MAD is defined as

$$\text{MAD}(x) = \text{median}(|x - \text{median}(x)|). \quad (4.7)$$

2. Creating histograms of the 2PSF distributions. This involves first running the subsample module to estimate the MAD of each 2PSF distribution and defining N_{hist} histogram bins that span across $\pm N_{\text{MAD}}\text{MAD}(\Xi)$, where N_{MAD} is nominally taken to be 10.

- F^\sharp Minor: This sub-pipeline attempts to characterize the 2PCFs using clipped set functions.

The 2PSFs are clipped at $\pm N_{\text{MAD}}\text{MAD}(\Xi)$, which can be centered at zero or at the median of the 2PSF, where the median and MAD of the 2PSFs are calculated using G^b Minor. While we ultimately found this sub-pipeline to be unable to characterize the 2PCFs for cosmic flexion, we leave it here for completeness, as it may have other uses.

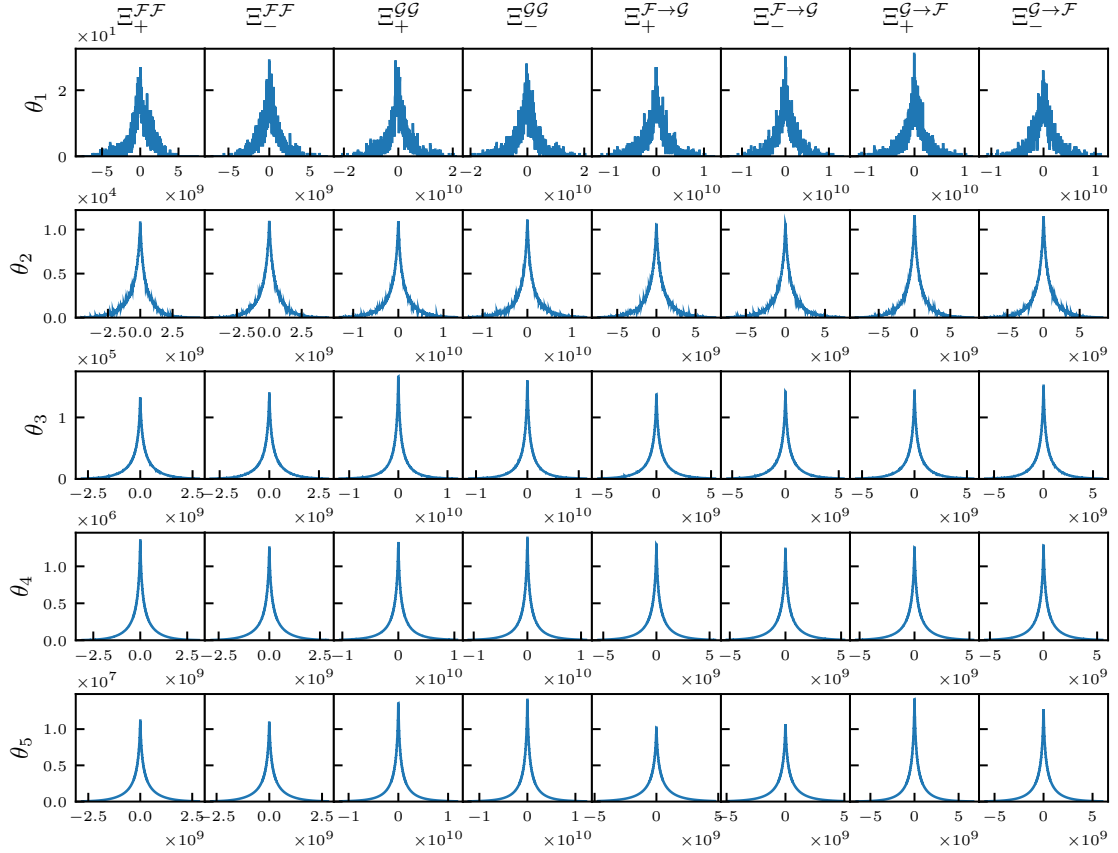


Figure 4.9: Histogram plots of the EE-mode flexion-flexion 2PSFs in five logarithmically spaced angular separation bins centered around the interval 1 to 100 arcseconds. The units on the x -axis are radians $^{-2}$.

- G^b Major: This sub-pipeline saves the entire 2PSFs to disk. This is in concert with additional modules that characterize the 2PCFs by taking median statistics of the 2PSFs. Like $F^\#$ Major, this is also conducive to parallelization and hence jackknifing.

4.3.2 The cosmic flexion 2PSFs

If the cosmic flexion 2PCFs are describable by a Gaussian likelihood, then the distributions of the sets $\Xi_{\pm}^{ab}(\theta)$ will be each by a Gaussian PDF. To characterize the PDFs of the cosmic flexion 2PSFs, I make use of G^b Minor to create histograms of each distribution, where I choose 1000 histogram bins.

For the DES Y3 cosmic flexion analysis, we choose five logarithmically spaced bins for the

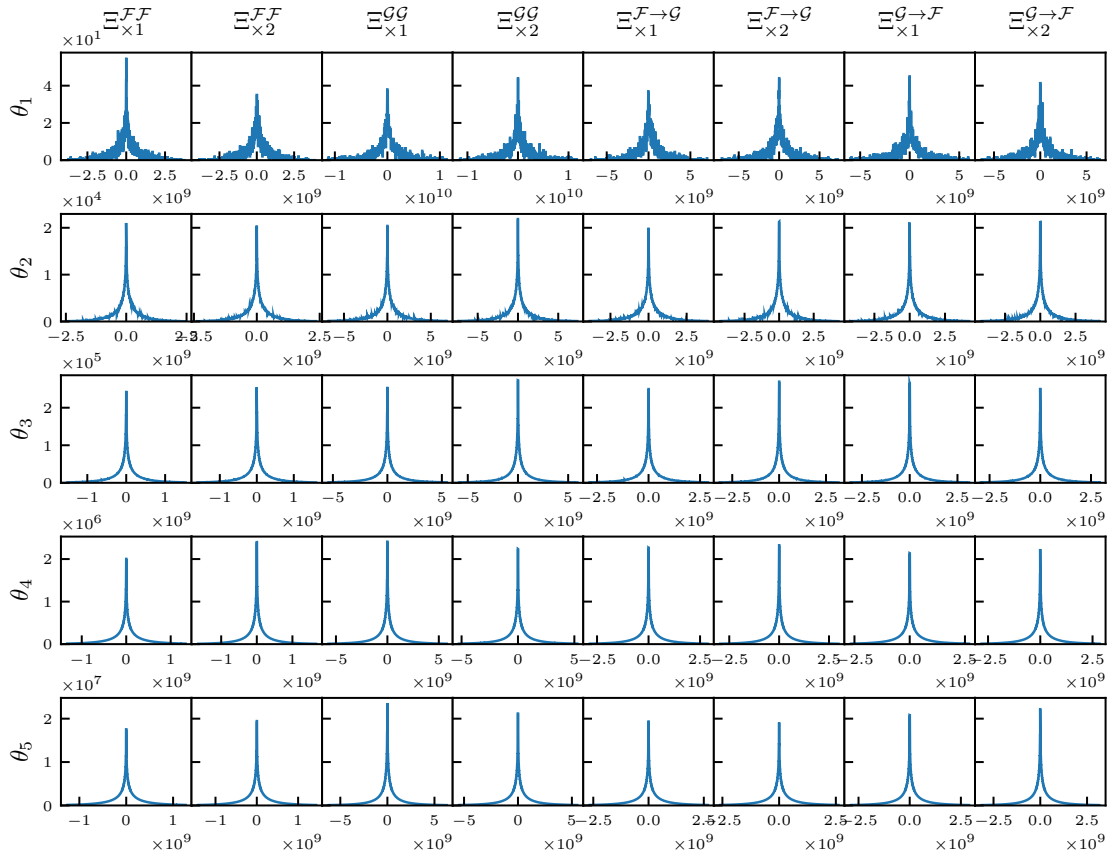


Figure 4.10: Histogram plots of the EB-mode flexion-flexion 2PSFs in five logarithmically spaced angular separation bins centered around the interval 1 to 100 arcseconds. The units on the x -axis are radians $^{-2}$.

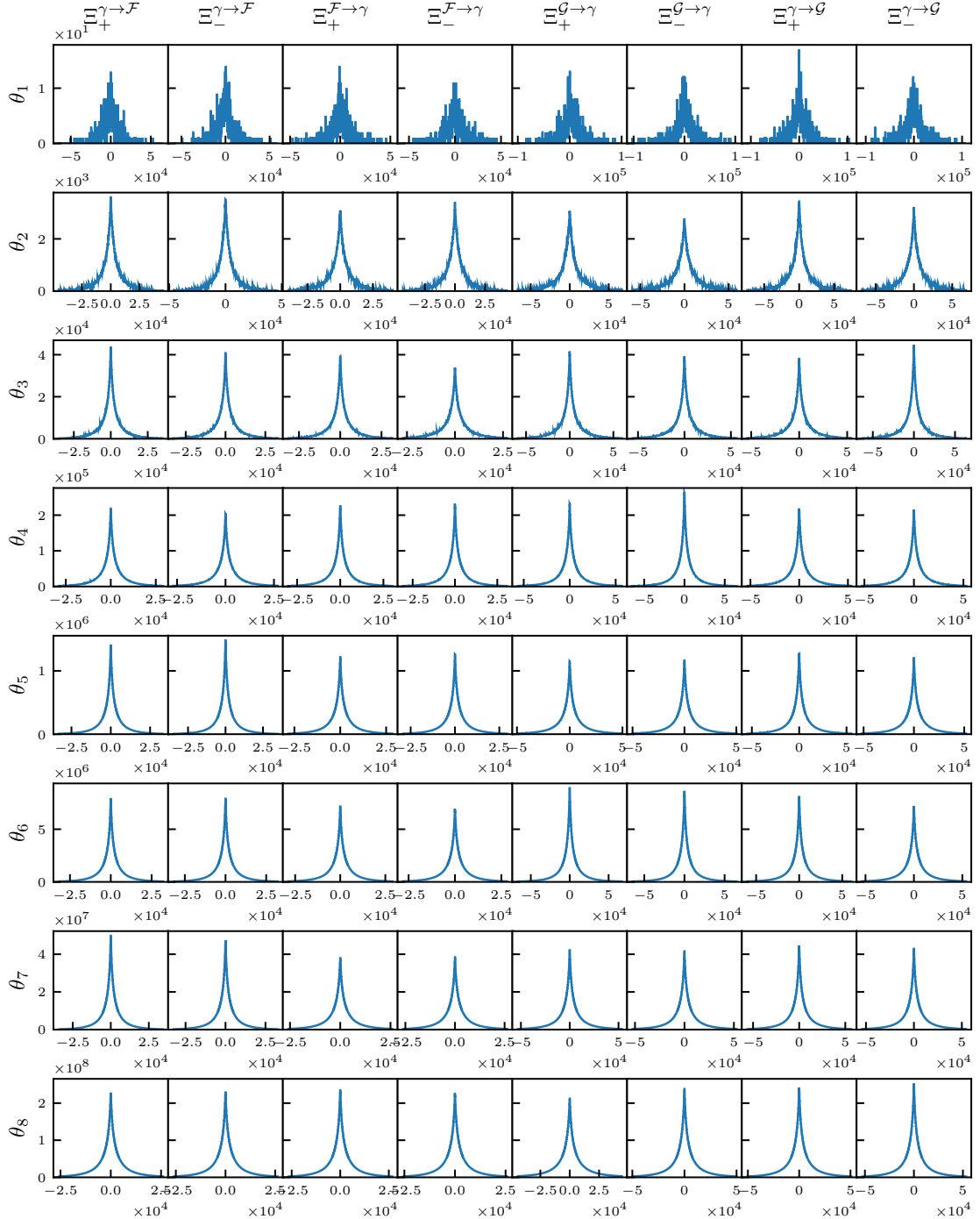


Figure 4.11: Histogram plots of the EE-mode shear-flexion 2PSFs in eight logarithmically spaced angular separation bins centered around the interval 1 arcsecond to 10 arcminutes. The units on the x -axis are radians $^{-1}$.

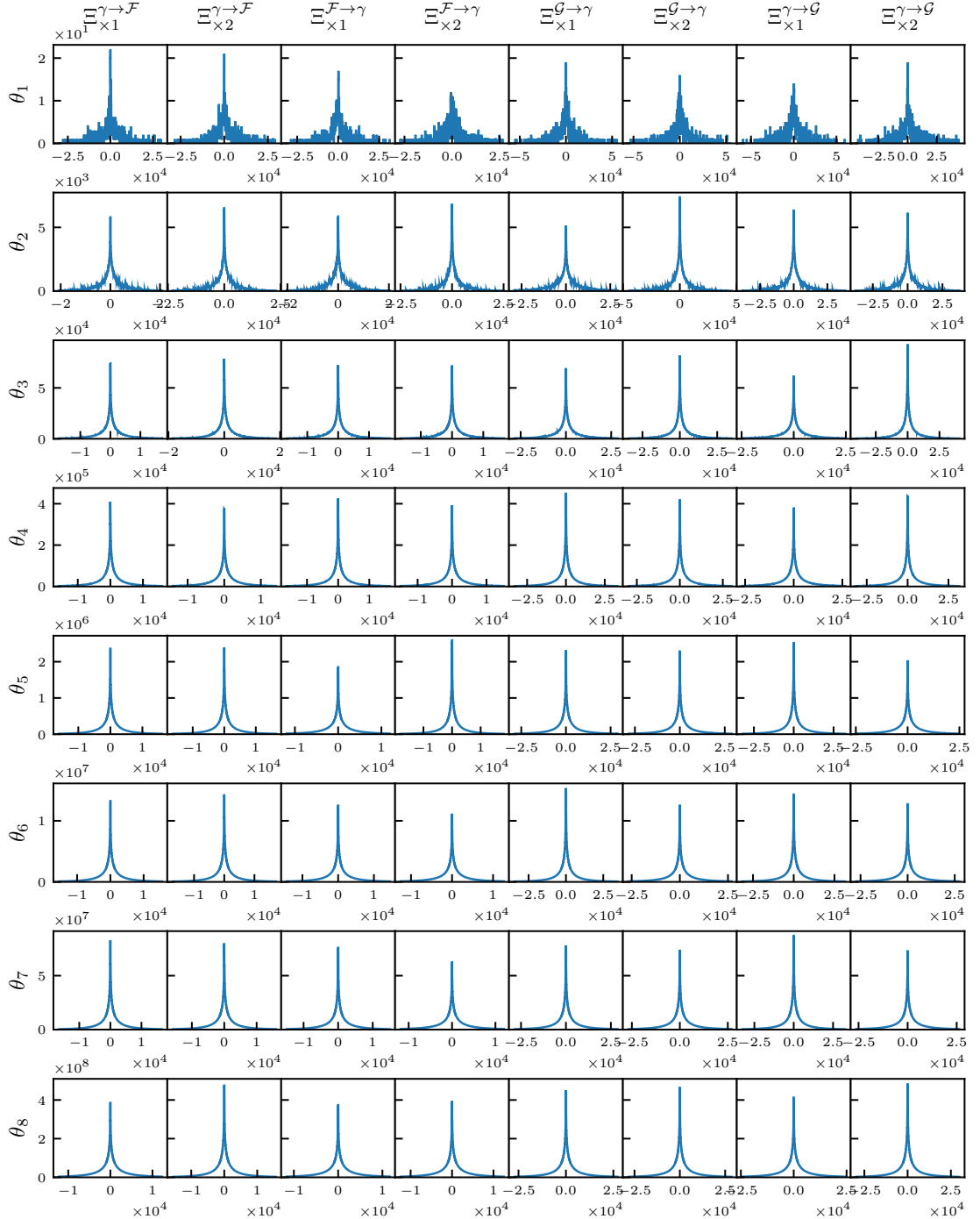


Figure 4.12: Histogram plots of the EB-mode shear-flexion 2PSFs in eight logarithmically spaced angular separation bins centered around the interval 1 arcsecond to 10 arcminutes. The units on the x -axis are radians $^{-1}$.

flexion-flexion correlations, centered around the interval 1 to 100 arcseconds, and eight logarithmically spaced bins for the shear-flexion correlations, centered around the interval 1 arcsecond to 10 arcminutes.

For the cosmic flexion analysis, the DES Y3 Flexion Catalogue, described in Sec. 4.2 is run through the F-SHARP pipeline. Prior to the calculation of the two-point functions, the systematics removal is applied as described in Sec. 4.2.3. I also choose to clip the long tails of the \mathcal{F}_α and \mathcal{G}_α distributions, defined by $\text{median}(X) \pm 5 \times \text{MAD}(X)$, where $X = \{\mathcal{F}_1, \mathcal{F}_2, \mathcal{G}_1, \mathcal{G}_2\}$. These outliers in the flexion distributions lead to extreme outliers in the two-point distributions, and this choice is made to mitigate that effect. It should be noted that the final results are ultimately insensitive to this choice, given the fact that, as is discussed below, we choose to work in terms of median statistics for the two-point functions. This similarly applies to the original flexion cuts I made when creating the DES Y3 Flexion Catalogue.

Figure 4.9 shows histograms of the distributions of each EE-mode flexion-flexion 2PSF for each angular separation bin and Fig. 4.10 shows the flexion-flexion EB-mode 2PSF distributions. Similarly, the 2PSF distributions for the shear-flexion EE and EB modes are shown in Figs. 4.11 and 4.12, respectively. It is evident from visual inspection that none of these distributions are Gaussian. I choose quantify the level of non-Gaussianity in two ways. First, I find that the distributions have very high kurtosis, with median values of about 7.5 for the shear-flexion EE-modes and about 8.0 for the flexion-flexion EE-modes. For reference, a Gaussian distribution has zero kurtosis. Second, I fit each of the 2PSF distributions using a generalized Gaussian PDF:

$$p(\Xi^{ab}) = \frac{c}{2b\Gamma(1/c)} \exp \left[\left(-\frac{|\Xi^{ab} - \mu|}{b} \right)^c \right]. \quad (4.8)$$

The generalized Gaussian PDF recovers a Gaussian PDF in the case $c = 2$, where the maximum likelihood estimator (MLE) of μ is the mean, and the variance is $b^2/2$. This PDF also covers the Laplacian PDF in the case $c = 1$. For a Laplacian, however, the MLE of μ is the median, not the mean. For the flexion-flexion 2PSF PDFs, c ranges from 0.57 to 0.95 for the EE-mode signals and 0.33 to 0.51 for the EB-mode signals. For the shear-flexion 2PSF PDFs, c ranges from 0.60 to 1.15

for the EE-mode signals and 0.28 to 0.54 for the EB-mode signals.

Varanasi and Aazhang [122] found that while the objective function is not strictly differentiable for $c < 1$, and hence one cannot obtain a MLE of μ in that way, computational models show that the median vastly outperforms the sample mean as an estimate of μ for $c \leq 1$.

Intuitively, the mean is a poor estimate of μ for these distributions due to their heavy tails. It is much more likely for outliers in a heavy tail to destroy the estimate of the mean. The median, on the other hand, is unaffected by these outliers.

4.3.3 The cosmic flexion 2PCFs

Owing to the non-Gaussianity of all cosmic flexion 2PSFs, the appropriate estimator for the corresponding 2PCFs is the median:

$$\check{\xi}_{\pm}^{ab}(\theta) = \text{median} [\Xi_{\pm}^{ab}] (\theta) \quad (4.9)$$

$$\check{\xi}_{\{\times 1, \times 2\}}^{ab}(\theta) = \text{median} [\Xi_{\{\times 1, \times 2\}}^{ab}] (\theta). \quad (4.10)$$

where the $\check{\xi}$ notation refers to the median estimator, contrasting it with the mean estimator $\hat{\xi}$.

The non-Gaussianity of the cosmic flexion 2PSF distributions presents a significant computational challenge. For the cosmic shear 2PSFs, which are Gaussian, the 2PCFs are simply characterized by the mean. This is to say that, for each 2PCF, one only needs to keep track of – and hold in RAM – two floats per 2PCF angular separation bin: a running sum of each pair-wise ellipticity product, and a running sum of the number of galaxy pairs in said bin. From a standpoint of RAM, the cosmic shear 2PCF estimator is invariant to the number of total galaxy pairs.

On the other hand, for cosmic flexion, the fact that the MLE of the central moment is the median results in a much more complicated computation for the 2PCFs. Naively, in order to calculate the median estimator of a 2PCF, one needs access to the entire corresponding 2PSF. In Tables 4.1 and 4.2, I show the total number of galaxy pairs for each angular separation bin, for the flexion-flexion and shear-flexion 2PSFs, respectively – say, for example, that in a given angular separation bin there are a billion galaxy pairs, which roughly corresponds to bin 7 for the shear-flexion signals.

Table 4.1: Total number of galaxy pairs in each flexion-flexion angular separation bin, i.e. the length of each 2PSF, for the DES Y3 cosmic flexion analysis.

Flexion-flexion bin	Number of pairs
θ_1	1.11×10^2
θ_2	5.15×10^4
θ_3	5.59×10^5
θ_4	4.89×10^6
θ_5	4.42×10^7

Table 4.2: Total number of galaxy pairs in each shear-flexion angular separation bin – i.e. the length of each 2PSF for the DES Y3 cosmic flexion analysis.

Shear-flexion bin	Number of pairs
θ_1	9.87×10^2
θ_2	3.97×10^5
θ_3	4.31×10^6
θ_4	2.40×10^7
θ_5	1.36×10^8
θ_6	7.93×10^8
θ_7	4.70×10^9
θ_8	2.84×10^{10}

This corresponds to one billion elements in a corresponding 2PSF. When held as an array of floats, this corresponds to 8 GB of RAM. For eight EE-mode signals and eight EB-mode signals there are a total of 16 2PSFs for this angular separation bin, which corresponds to a total of 128 GB of RAM required to hold all 2PSFs in RAM for said bin. For 10 billion galaxy pairs, this requires 1.28 TB of RAM. It is not feasible to simultaneously hold in RAM the 2PSFs for all signals. Therefore, I make use of G^b Major in order to save all 2PSFs to disk on the SCIAMA Supercomputer storage. Then, each bin of each 2PSF is read into RAM one at a time on the high memory partition of SCIAMA, and median statistics are used in order to calculate the estimators of the 2PCFs. With access to the full 2PSF, a number of statistics can be calculated along with the median. Among the statistics I calculate are the 16th and 84th percentiles of each 2PSF bin. In a Gaussian distribution, this defines one standard deviation. We choose as an estimator of the standard error on the median

$$\text{Err}(\xi^{ab}(\theta)) = \frac{|P_{16}[\Xi^{ab}](\theta)| + |P_{84}[\Xi^{ab}](\theta)|}{2\sqrt{N_p(\theta)}} \quad (4.11)$$

where $P_x[\Xi^{ab}]$ denotes the x^{th} percentile of the 2PSF.

4.3.4 Results: Cosmic flexion 2PCF measurements

In Figs. 4.13 and 4.15, I present the first ever measurements of the cosmic flexion-flexion and shear-flexion 2PCFs, respectively, using the DES Y3 Flexion Catalogue. Using the G^\flat Major sub-pipeline in **F-SHARP**, data points of the 2PCFs are calculated using Eq. (4.9) and the errorbars using Eq. (4.11). In Figs 4.14 and 4.16 are the corresponding EB-mode signals.

The angular separation bins for the 2PCFs are the same as those described in Sec. 4.3.2; however, I do not calculate the 2PCFs in the shear-flexion bin 8, centered around 10 arcminutes, owing to RAM constraints, run-time considerations, and the relatively low S/N of the bin. Therefore, we work only with the first seven out of eight angular separation bins for the shear-flexion correlations.

Before drawing any conclusions from the EE-mode cosmic flexion signals, we first consider the possible systematics effects in our two-point measurements. The first systematics check we can look at are the EB-mode signals. Again, these “cross” two-point functions are expected to vanish due to the parity symmetry of the Universe. While a nonzero measurement of these signals could point to new physics, as is discussed in Chapter 6, the primary cause of nonzero measurement is systematics contamination. For both the flexion-flexion and shear-flexion signals, the EB-modes are fully consistent with the null hypothesis, indicating no EB-mode systematic effects.

While there are no EB-mode systematics in the DES Y3 cosmic flexion measurements, this does not exclude the possibility of other systematics being present in the EE-mode signals. Indeed, I find that the flexion-flexion signals $\xi_+^{\mathcal{FF}}$ and $\xi_+^{\mathcal{GG}}$ are very likely completely dominated by systematics. I come to this conclusion based on the fact that these signals have an extraordinarily large tension with both theoretical predictions and the null hypothesis. I attribute the most likely cause of this contamination to PSF leakage at small scales that was not removed by the large-scale systematics removal described in Sec. 4.2. In Appendix D, I demonstrate that the “plus” combination correlations of same spin fields are conducive to contamination from PSF leakage, while this is not the case for all other correlations. Given this fact, I choose to exclude $\xi_+^{\mathcal{FF}}$ and $\xi_+^{\mathcal{GG}}$ from the analysis.

With no other obvious evidence of systematic contamination of the other EE-mode flexion-flexion

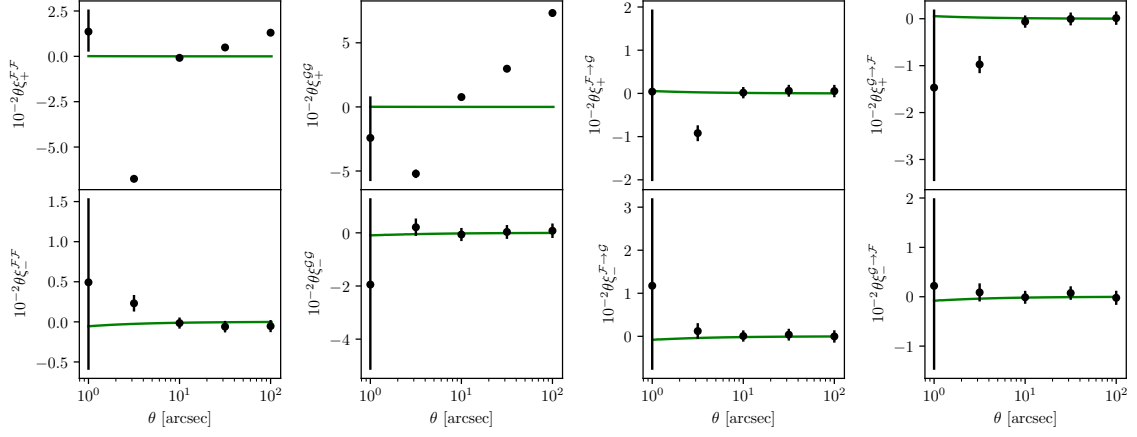


Figure 4.13: Measured DES Y3 flexion-flexion 2PCFs scaled by θ , such that the y -axis has units of radians $^{-1}$. The green line indicates the theoretical predictions from the fiducial cosmology, as described in AGB.

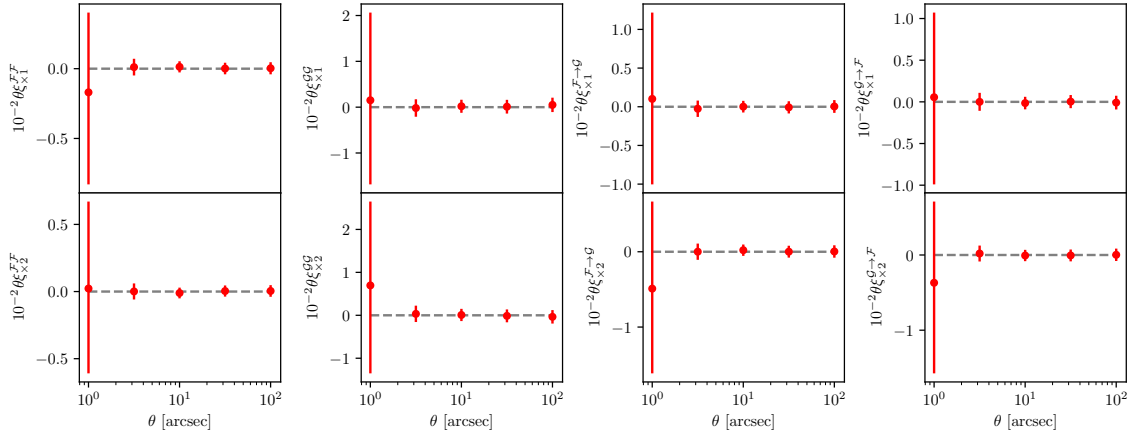


Figure 4.14: Measured DES Y3 EB-mode flexion-flexion 2PCFs scaled by θ , such that the y -axis has units of radians $^{-1}$.

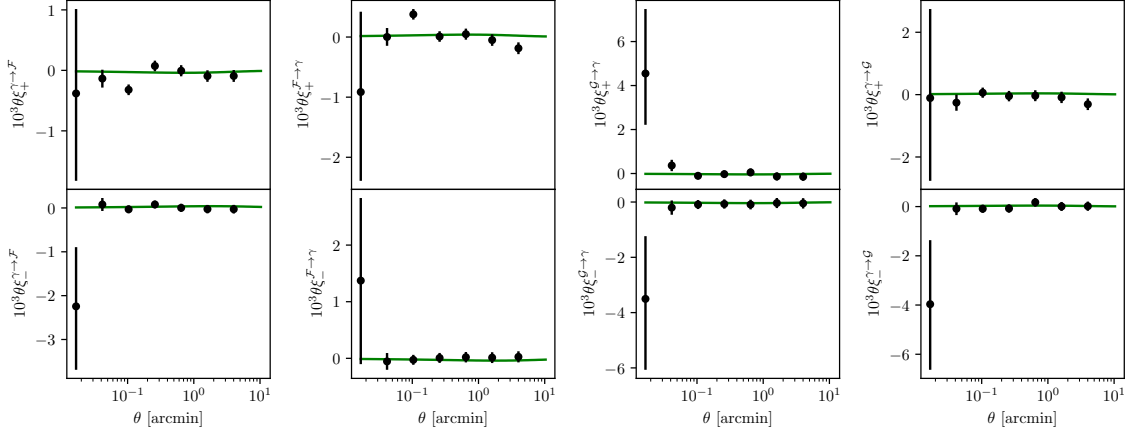


Figure 4.15: Measured DES Y3 shear-flexion 2PCFs scaled by θ , such that the y -axis is dimensionless. The green line indicates the theoretical predictions from the fiducial cosmology, as described in AGB.

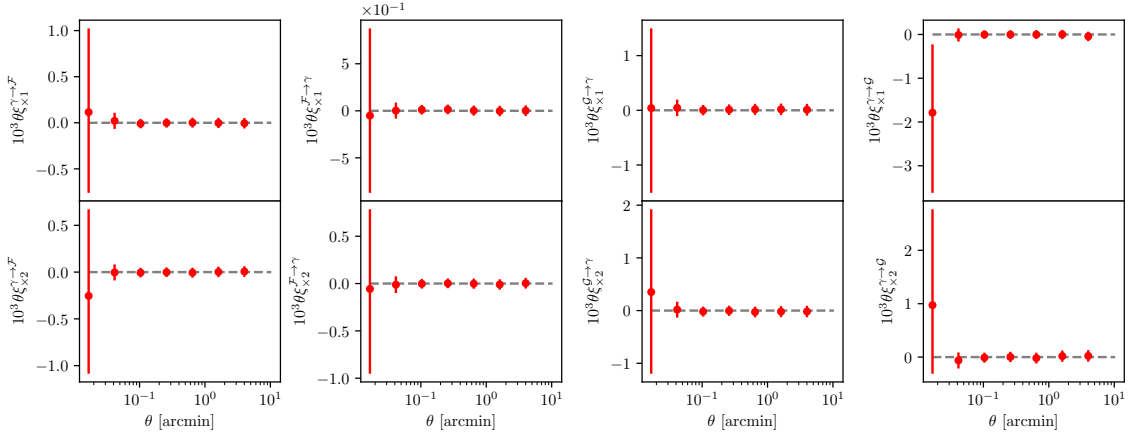


Figure 4.16: Measured DES Y3 EB-mode shear-flexion 2PCFs scaled by θ , such that the y -axis is dimensionless.

or shear-flexion signals, I move on to analyzing the results of these measurements.

We wish to compare the cosmic flexion measurements to the theoretical predictions from AGB. I define a “data vector,” $\check{\xi}$ containing the DES Y3 2PCF measurements. For example, if we were to consider all available 2PCF measurements, the data vector would be

$$\check{\xi} \equiv \{\check{\xi}_{\pm}^{\mathcal{FF}}(\theta), \check{\xi}_{\pm}^{\mathcal{GG}}(\theta), \check{\xi}_{\pm}^{\mathcal{F}\rightarrow\mathcal{G}}(\theta), \check{\xi}_{\pm}^{\mathcal{G}\rightarrow\mathcal{F}}(\theta), \check{\xi}_{\pm}^{\gamma\rightarrow\mathcal{F}}(\theta), \check{\xi}_{\pm}^{\mathcal{F}\rightarrow\gamma}(\theta), \check{\xi}_{\pm}^{\mathcal{G}\rightarrow\gamma}(\theta), \check{\xi}_{\pm}^{\gamma\rightarrow\mathcal{G}}(\theta)\}. \quad (4.12)$$

There is a corresponding theoretical model vector, $\xi_M(\mathbf{p})$, of the 2PCFs computed using the parameters \mathbf{p} of a given model M :

$$\xi_M(\mathbf{p}) \equiv \{\xi_{\pm}^{\mathcal{FF}}(\theta, \mathbf{p}), \xi_{\pm}^{\mathcal{GG}}(\theta, \mathbf{p}), \xi_{\pm}^{\mathcal{F}\rightarrow\mathcal{G}}(\theta, \mathbf{p}), \xi_{\pm}^{\mathcal{G}\rightarrow\mathcal{F}}(\theta, \mathbf{p}), \xi_{\pm}^{\gamma\rightarrow\mathcal{F}}(\theta, \mathbf{p}), \xi_{\pm}^{\mathcal{F}\rightarrow\gamma}(\theta, \mathbf{p}), \xi_{\pm}^{\mathcal{G}\rightarrow\gamma}(\theta, \mathbf{p}), \xi_{\pm}^{\gamma\rightarrow\mathcal{G}}(\theta, \mathbf{p})\}. \quad (4.13)$$

We assume that, once we have estimated the 2PCFs using median statistics, that there exists a Gaussian-type likelihood

$$\mathcal{L}(\check{\xi}|\mathbf{p}, M) \propto \exp \left[-\frac{1}{2} (\check{\xi} - \xi_M(\mathbf{p}))^\top \mathbf{C}_m^{-1} (\check{\xi} - \xi_M(\mathbf{p})) \right] \quad (4.14)$$

where we introduce \mathbf{C}_m as the median error matrix.

Rather than adopt a model whereby we fit cosmological parameters, I choose to adopt a fixed fiducial model, consisting of the theoretical predictions from AGB using the fiducial cosmology, and parameterize the theoretical model vector with one single parameter: an overall normalization factor \mathfrak{N} . Therefore, we have:

$$\xi_M(\mathbf{p}) = \mathfrak{N}\xi \quad (4.15)$$

where ξ is the fiducial theory predictions. With this parameterization, we can define a best-fit chisquared from the log-likelihood:

$$\chi^2 = -2 \ln \mathcal{L} = (\check{\xi} - \mathfrak{N}\xi)^\top \mathbf{C}_m^{-1} (\check{\xi} - \mathfrak{N}\xi) \quad (4.16)$$

By setting $\frac{\partial \chi^2}{\partial \mathfrak{N}} = 0$, we find that the value of \mathfrak{N} that minimizes the chisquared is given by

$$\mathfrak{N} = \frac{\boldsymbol{\xi}^T \mathbf{C}_m^{-1} \hat{\boldsymbol{\xi}} + \hat{\boldsymbol{\xi}}^T \mathbf{C}_m^{-1} \boldsymbol{\xi}}{2 \boldsymbol{\xi}^T \mathbf{C}_m^{-1} \boldsymbol{\xi}} \quad (4.17)$$

Taking the case of a diagonal-only median error matrix, such that the diagonal is the square of error on the median for each element in the data vector, as given by Eq. (4.11), the chisquared takes the familiar form

$$\chi^2 = \sum_i \frac{(\check{\xi}_i - \mathfrak{N} \xi_i)^2}{\text{Err}^2(\check{\xi}_i)}. \quad (4.18)$$

and the corresponding value of \mathfrak{N} that minimizes this chisquared is given by

$$\mathfrak{N} = \frac{\sum_i \xi_i \check{\xi}_i / \text{Err}^2(\check{\xi}_i)}{\sum_i \xi_i^2 / \text{Err}^2(\check{\xi}_i)} \quad (4.19)$$

In order to get an estimate of \mathfrak{N} and its uncertainty, I utilize $N_{jk} = 100$ jackknife patches that are created from the chunks of the DES Y3 Flexion Catalogue used for parallelization. The jackknife estimate of the average value of \mathfrak{N} is given by

$$\langle \mathfrak{N} \rangle = \frac{1}{N_{jk}} \sum_{i=1}^{N_{jk}} \mathfrak{N}_{(i)} \quad (4.20)$$

and the uncertainty on this estimate is

$$\widehat{\text{Var}}(\langle \mathfrak{N} \rangle) = \frac{N_{jk} - 1}{N_{jk}} \sum_{i=1}^{N_{jk}} (\mathfrak{N}_{(i)} - \langle \mathfrak{N} \rangle)^2 \quad (4.21)$$

where (i) denotes the removal of patch i from the summation.

In Table 4.3, I present the results for constraints on \mathfrak{N} from the DES Y3 cosmic flexion 2PCFs. Owing to the fact that the flexion-flexion and shear-flexion signals are subject to different systematic effects, and we have different levels of confidence regarding contamination of each, we do not make use of one single data vector encompassing every 2PCF. I consider three different data vectors

comprising various combinations of the shear-flexion signals:

$$\check{\boldsymbol{\xi}}^{\text{shear-flexion}} = \{\check{\xi}_{\pm}^{\gamma \rightarrow \mathcal{F}}(\theta), \check{\xi}_{\pm}^{\mathcal{F} \rightarrow \gamma}(\theta), \check{\xi}_{\pm}^{\mathcal{G} \rightarrow \gamma}(\theta), \check{\xi}_{\pm}^{\gamma \rightarrow \mathcal{G}}(\theta)\} \quad (4.22)$$

$$\check{\boldsymbol{\xi}}^{\text{shear-}\mathcal{F}} = \{\check{\xi}_{\pm}^{\gamma \rightarrow \mathcal{F}}(\theta), \check{\xi}_{\pm}^{\mathcal{F} \rightarrow \gamma}(\theta)\} \quad (4.23)$$

$$\check{\boldsymbol{\xi}}^{\text{shear-}\mathcal{G}} = \{\check{\xi}_{\pm}^{\mathcal{G} \rightarrow \gamma}(\theta), \check{\xi}_{\pm}^{\gamma \rightarrow \mathcal{G}}(\theta)\} \quad (4.24)$$

and a single flexion-flexion data vector which excludes $\xi_{+}^{\mathcal{FF}}$ and $\xi_{+}^{\mathcal{GG}}$ outright, owing to the obvious systematics contamination:

$$\hat{\boldsymbol{\xi}}^{\text{flexion-flexion}} = \{\check{\xi}_{-}^{\mathcal{FF}}(\theta), \check{\xi}_{-}^{\mathcal{GG}}(\theta), \check{\xi}_{\pm}^{\mathcal{F} \rightarrow \mathcal{G}}(\theta), \check{\xi}_{\pm}^{\mathcal{G} \rightarrow \mathcal{F}}(\theta)\} \quad (4.25)$$

I find that all three shear-flexion data vectors are consistent with theoretical predictions (i.e. $\mathfrak{N} = 1$) to within $\sim 1\sigma$. We can quantify the overall signal to noise (S/N) of the data vectors by

$$\text{S/N} = \frac{\langle \mathfrak{N} \rangle}{\sqrt{\text{Var}(\langle \mathfrak{N} \rangle)}} \quad (4.26)$$

which is equivalent to the statement that a data vector rejects the null hypothesis (i.e. $\mathfrak{N} = 0$) to $X\sigma$, where $X = \text{S/N}$. We define a data vector to *significantly* reject the null hypothesis if $\text{S/N} > 2.5$, which corresponds to a *p*-value of $p \lesssim 0.01$. The combined shear- \mathcal{F} - \mathcal{G} data vector rejects the null hypothesis to 2.8σ , and the shear- \mathcal{F} data vector to 3.1σ . Due to the fact that the shear- \mathcal{G} data vector is noisier than shear- \mathcal{F} , it is consistent with both the null hypothesis and with theoretical predictions.

For practical purposes, we consider a detection to occur when a data vector is consistent with theoretical predictions and when it significantly rejects the null hypothesis. Therefore, we report the first ever detection of cosmic flexion in the form of the shear-flexion 2PCFs.

As for the flexion-flexion data vector, there is significant disagreement with theoretical predictions. Given the negative sign on \mathfrak{N} , this disagreement is likely attributable to systematic effects. For the moment, I remain agnostic about the source of these systematics. It is interesting that

Table 4.3: Single parameter constraints on theoretical predictions from DES Y3 cosmic flexion measurements

Data vector	Constraints on \mathfrak{N}
Shear-flexion	0.81 ± 0.29
Shear- \mathcal{F}	0.96 ± 0.31
Shear- \mathcal{G}	0.31 ± 0.64
Flexion-Flexion	-7.17 ± 1.28

these effects appear only in the flexion-flexion and not the shear-flexion signals. It is possible that these systematics vanish for the odd-spin combinations of the shear-flexion signals and not the even-spin combinations of the flexion-flexion signals. As such, I do not claim a detection of the cosmic flexion-flexion signal.

Finally, it is interesting to note that these results confirm the non-commutativity prediction of AGB for odd-spin combinations (see Sec. 3.2.4), where e.g. $\xi_+^{\mathcal{F} \rightarrow \gamma} = -\xi_+^{\gamma \rightarrow \mathcal{F}}$. Indeed, I find that the combination $\xi_+^{\mathcal{F} \rightarrow \gamma}(\theta) + \xi_+^{\gamma \rightarrow \mathcal{F}}(\theta)$ is consistent with the null hypothesis. On the other hand, the combination with the proper sign does improve the overall detection of the $\xi_+^{\gamma \rightarrow \mathcal{F}}$ signal. This does not change the results in Table 4.3, however, since combining the constraining power of the signals is equivalent to keeping both signals separate in a data vector.

4.3.5 Discussion

It is important to stress that we recognize the limitations in this measurement at this time. This work represents the first-ever attempt at measuring any cosmic flexion signal in data. In order to be confident that measurement of the cosmic flexion signals are arising from cosmological effects, and in order to use these measurements to constrain the small-scale matter power spectrum, future work needs to include careful analysis of a number of different effects. First, there is the need for realistic image simulations of galaxies with flexion in order to calibrate the **Lenser** pipeline against multiplicative bias, or, **Lenser** needs to be improved by making it a self-calibrating pipeline. Second, work needs to be done to study the interplay between flexion and the PSF modeling of the survey. Again, we recognize, from the perspective of an accurate PSF model, that this analysis could be potentially improved by using the single-epoch images rather than the coadds, but it is also unclear

that, at this stage, the single-epoch PSFs would be able to accurately model the effects of flexion. Generally, a more careful analysis of both the PSF and the other systematics represent a significant amount of interesting work in their own right, and we need to leave it to future studies.

Chapter 5: Flexion in various spacetimes: Exotic lenses and modified gravity

5.1 Introduction

In weak lensing, there exist a variety of simple lens models that make the assumption of a circularly symmetric profile. These include the Schwarzschild lens (see Sec. 1.2.1 and Bartelmann and Schneider [41]), the singular isothermal sphere (SIS; see Sec. 1.2.9 and Binney and Tremaine [37]), and the Navarro-Frenk-White (NFW) density profile (see Sec. 1.2.9), to name a few. Recently, exotic lens models have been discussed in which the lens can repulse rather than attract light, by having, for example, negative mass. These models have been inspired by modified gravity theories as well as individual exotic objects such as the Ellis wormhole, which is a particular example of the Morris-Thorne traversable wormhole class [123, 124, 125]. In Kitamura et al. [126], a family of exotic lens models is constructed by considering an exotic spacetime metric that is static and circularly symmetric, can describe both positive and negative masses, and depends on the inverse distance to the power of n (e.g. $n = 1$ for Schwarzschild metric, $n = 2$ for Ellis wormhole). Then, in Izumi et al. [127], the gravitational shear is worked out for these exotic lenses, and it is shown that the shear can exhibit behavior that suggests a positive mass lens in the presence of an exotic lens.

In cosmology, studies of the CMB have found that observations agree with the standard cosmological model (Λ CDM) to remarkable accuracy [82, 24, 25, 28]. As we look at more recent parts of cosmic history, using tools such as weak lensing, Λ CDM still appears to be the law of the land. Subtle discrepancies are found, however, between these low-redshift observations and the high-redshift measurements of the CMB [83, 28, 84, 85]. These discrepancies could indicate that Λ CDM might not be sufficient to connect all parts of the cosmic history [86]. It is therefore necessary to have multiple cosmological probes that complement each other in order to get the full picture of cosmology across all length scales and cosmic times. To this end, the effort to explain the origin of cosmic acceleration has uncovered a vast zoo of dark energy and modified gravity models. These

can be broadly classified according to how they modify general relativity (GR) or replace the cosmological constant, Λ – for example, by adding new scalar, vector or tensor fields (e.g. the broad class of Horndeski models [87, 88]); adding extra spatial dimensions; introducing higher-derivative or nonlocal operators in the action; or introducing exotic mechanisms for mediating gravitational interactions [128, 129, 130, 131, 132, 133]. A systematic study of these models suggests a number of new gravitational phenomena that can arise if there are any deviations from the standard cosmological model. These include the possibility of time- and scale-dependent variations in the gravitational constant, leading to modifications to the growth rate of large-scale structure and gravitational lensing [134, 135, 136, 137, 138]. These deviations from how gravitational lensing behaves in GR can be studied in the context of strong lensing (see Collett et al. [139]) and with cosmic shear by employing both parametric and nonparametric approaches [140, 141, 142, 143, 144, 145, 146, 147, 148, 149, 150].

The goal of this Chapter is to consider how weak gravitational flexion behaves in the context of two different types of spacetime metrics. In Sec. 5.2 and 5.3, we consider flexion in the presence of a family of exotic lenses, and in Sec. 5.4 we consider how cosmic flexion behaves in a parametrized modified gravity model. We conclude in Sec. 5.5.

5.2 Gravitational lensing in single-lens metrics

5.2.1 The Schwarzschild metric

Discussions of gravitational lensing typically begin by considering the simple case of light deflection by a point mass M . We start with the Schwarzschild metric of Eq. (1.74), where we are using units $c = G = 1$, and hence $R_s = 2M$ is the Schwarzschild radius. In the weak-field (i.e. far-field) limit $r \gg R_s$, the line element of the metric ($ds^2 = g_{\mu\nu}dx^\mu dx^\nu$) simply becomes

$$ds^2 \simeq - \left(1 - \frac{R_s}{r}\right) dt^2 + \left(1 + \frac{R_s}{r}\right) dr^2 + r^2 d\Omega^2, \quad (5.1)$$

where $d\Omega^2 \equiv d\theta^2 + \sin^2 \theta d\phi^2$. Since this spacetime is spherically symmetric, we can consider only the equatorial plane $\theta = \pi/2$ without loss of generality, and the deflection angle of light is simply

[151]

$$\hat{\alpha} = \frac{2R_s}{b} \int_0^{\pi/2} d\phi \cos \phi = \frac{2R_s}{b} \quad (5.2)$$

where b is the impact parameter.

In the thin lens approximation, the lensing equation describes the coordinate mapping from the foreground (angular position of the image relative to the lens), $\boldsymbol{\theta}^1$, to background (angular position of the source), $\boldsymbol{\beta}$, positions via (see Sec. 1.2.2)

$$\boldsymbol{\beta} = \frac{\mathbf{b}}{D_d} - \frac{D_{ds}}{D_s} \hat{\alpha}(\mathbf{b}) \equiv \boldsymbol{\theta} - \boldsymbol{\alpha}(\boldsymbol{\theta}), \quad (5.3)$$

where D_d , D_s , and D_{ds} are the observer-lens, observer-source, and lens-source distances, respectively, $\boldsymbol{\theta} \equiv \mathbf{b}/D_d$, and the reduced deflection angle is defined as $\boldsymbol{\alpha} = \hat{\alpha} D_{ds}/D_s$.

5.2.2 Exotic spacetime metric

Consider an exotic spacetime metric, as first given by Kitamura et al. [126]:

$$ds^2 = - \left(1 - \frac{\varepsilon_1}{r^n}\right) dt^2 + \left(1 + \frac{\varepsilon_2}{r^n}\right) dr^2 + r^2 d\Omega^2 + \mathcal{O}(\varepsilon_1^2, \varepsilon_2^2, \varepsilon_1, \varepsilon_2). \quad (5.4)$$

This generalizes the metric such that (i) the spacetime can depend on the inverse distance to the power of n in the weak-field, and (ii) small ‘‘book-keeping’’ parameters ε_1 and ε_2 are introduced. Notice that for $n = 1$ with negative ε_1 and ε_2 , we recover the linearized Schwarzschild metric with a negative Schwarzschild radius and hence negative mass.

With this exotic metric, the deflection angle given in Eq. (5.2) becomes [127]

$$\hat{\alpha} = \frac{\varepsilon}{b^n} \int_0^{\pi/2} d\phi \cos^n \phi + \mathcal{O}(\varepsilon^2) \equiv \frac{\bar{\varepsilon}}{b^n} \quad (5.5)$$

where we have defined $\varepsilon \equiv n\varepsilon_1 + \varepsilon_2$, and absorbed the positive-definite integral into ε such that the sign of $\bar{\varepsilon}$ is the same as ε . As Izumi et al. [127] points out, this deflection angle recovers the Schwarzschild ($n = 1$) and Ellis wormhole ($n = 2$) cases. We further point out that the SIS ($n = 0$)

¹Not to be confused with the coordinate θ in the Schwarzschild metric

case is also recovered.

From here, one can obtain an expression for the convergence (in its interpretation as a dimensionless surface mass density). From Eq. (1.117), we know that $\kappa = \partial^* \boldsymbol{\alpha}/2$. Using this, Eq. (5.5), and the definitions of $\boldsymbol{\alpha}$ and $\boldsymbol{\theta}$ given in Eq. (5.3), we find that²

$$\kappa(b) = \frac{D_{\text{ds}} D_{\text{d}}}{D_{\text{s}}} \frac{\bar{\varepsilon}(1-n)}{2} \frac{1}{b^{n+1}}. \quad (5.6)$$

By Eq. (5.5), we see that there exists gravitational attraction on light rays for $\varepsilon > 0$ and repulsion for $\varepsilon < 0$. From Eq. (5.6), we note that for $\varepsilon > 0$ and $n > 1$ or for $\varepsilon < 0$ and $n < 1$, the convergence is negative. In this context, negative convergence requires that matter (and energy) be exotic.

For $\varepsilon > 0$, there exists a positive root corresponding to the Einstein ring, $\beta = 0$. For $\varepsilon < 0$, on the other hand, there does not exist a positive root corresponding to $\beta = 0$. This means that there is no Einstein ring for this case, which is to be expected since this case corresponds to light repulsion. We can still define a typical angular size for this lens, though, as the “Einstein radius.” In either case, the Einstein radius is defined generally as [127]

$$\theta_E \equiv \left(\frac{|\bar{\varepsilon}| D_{\text{ds}}}{D_{\text{s}} D_d^n} \right)^{1/(n+1)}. \quad (5.7)$$

5.3 Flexion in exotic spacetime metrics

5.3.1 Weak lensing in exotic spacetimes

Let us restrict ourselves to $\boldsymbol{\theta}/\theta_E > 0$ (the other image solution occurring for $\boldsymbol{\theta}/\theta_E < 0$ for $\varepsilon > 0$). Recognizing that $\bar{\varepsilon} = \text{sgn}(\varepsilon)|\bar{\varepsilon}|$, where $\text{sgn}(x)$ is the signum function, and using Eq. (5.7), we can then write Eq. (5.3) as

$$\boldsymbol{\beta} = \boldsymbol{\theta} - \text{sgn}(\varepsilon) \theta_E^{n+1} \frac{\boldsymbol{\theta}}{\theta^{n+1}}. \quad (5.8)$$

From here, we can compute the distortion matrix $\mathcal{A}_{ij} \equiv \partial \beta_i / \partial \theta_j$ (see Eq. 1.99). The elements of

²Note that this expression includes a coefficient $D_{\text{ds}} D_{\text{d}} / D_{\text{s}}$ not present in Kitamura et al. [126], Izumi et al. [127]. This coefficient, with dimensionality r (i.e. distance), is necessary so that convergence is dimensionless: $\bar{\varepsilon}$ has dimensionality r^n (see Eq. 5.4) and impact parameter has dimensionality r .

this matrix are

$$\begin{aligned}\mathcal{A}_{11} &= 1 - \text{sgn}(\varepsilon) \frac{\theta_E^{n+1}}{\theta^{n+1}} + \text{sgn}(\varepsilon)(n+1)\theta_E^{n+1} \frac{\theta_1\theta_1}{\theta^{n+3}} \\ \mathcal{A}_{12} &= \text{sgn}(\varepsilon)(n+1)\theta_E^{n+1} \frac{\theta_1\theta_2}{\theta^{n+3}} \\ \mathcal{A}_{21} &= \text{sgn}(\varepsilon)(n+1)\theta_E^{n+1} \frac{\theta_1\theta_2}{\theta^{n+3}} \\ \mathcal{A}_{22} &= 1 - \text{sgn}(\varepsilon) \frac{\theta_E^{n+1}}{\theta^{n+1}} + \text{sgn}(\varepsilon)(n+1)\theta_E^{n+1} \frac{\theta_2\theta_2}{\theta^{n+3}}.\end{aligned}\tag{5.9}$$

Izumi et al. [127] were able to obtain the convergence and shear in the case $\theta_i = (\theta, 0)$ and $\beta_i = (\beta, 0)$.

In this work, we will obtain general expressions for the convergence and both components of the shear. We do this by working in terms of the second derivatives of the lensing potential. The distortion matrix can be written as

$$\mathcal{A}_{ij} = \beta_{i,j} = \delta_{ij} - \psi_{,ij} = \begin{pmatrix} 1 - \kappa - \gamma_1 & -\gamma_2 \\ -\gamma_2 & 1 - \kappa + \gamma_1 \end{pmatrix} = \begin{pmatrix} 1 - \psi_{,11} & -\psi_{,12} \\ -\psi_{,12} & 1 - \psi_{,22} \end{pmatrix}.\tag{5.10}$$

(see Eq. 1.100 and 1.103). Using this with Eq. (5.9), we see that

$$\begin{aligned}\psi_{,11} &= \text{sgn}(\varepsilon) \frac{\theta_E^{n+1}}{\theta^{n+1}} - \text{sgn}(\varepsilon)(n+1)\theta_E^{n+1} \frac{\theta_1^2}{\theta^{n+3}} \\ \psi_{,12} &= -\text{sgn}(\varepsilon)(n+1)\theta_E^{n+1} \frac{\theta_1\theta_2}{\theta^{n+3}} \\ \psi_{,22} &= \text{sgn}(\varepsilon) \frac{\theta_E^{n+1}}{\theta^{n+1}} - \text{sgn}(\varepsilon)(n+1)\theta_E^{n+1} \frac{\theta_2^2}{\theta^{n+3}}.\end{aligned}\tag{5.11}$$

The convergence is therefore given by

$$\begin{aligned}\kappa &= \frac{1}{2}(\psi_{,11} + \psi_{,22}) \\ &= \text{sgn}(\varepsilon) \frac{(1-n)}{2} \frac{\theta_E^{n+1}}{\theta^{n+1}}\end{aligned}\tag{5.12}$$

and the components of the shear are

$$\begin{aligned}\gamma_1 &= \frac{1}{2}(\psi_{,11} - \psi_{,22}) \\ &= -\text{sgn}(\varepsilon) \frac{(1+n)}{2} \frac{\theta_E^{n+1}}{\theta^{n+3}} (\theta_1^2 - \theta_2^2)\end{aligned}\quad (5.13)$$

$$\begin{aligned}\gamma_2 &= \psi_{,12} \\ &= -\text{sgn}(\varepsilon)(1+n) \frac{\theta_E^{n+1} \theta_1 \theta_2}{\theta^{n+3}}.\end{aligned}\quad (5.14)$$

The total shear is therefore³

$$\gamma = -\text{sgn}(\varepsilon) \frac{(1+n)}{2} \frac{\theta_E^{n+1}}{\theta^{n+1}} e^{2i\phi}. \quad (5.15)$$

Now, the flexion fields can be obtained either by differentiating the convergence and shear directly, or by first obtaining the third derivatives of the lensing potential. We choose to do the latter for completeness. From Eq. (5.11), we obtain

$$\begin{aligned}\psi_{,111} &= -\text{sgn}(\varepsilon)3(1+n)\theta_E^{n+1} \frac{\theta_1}{\theta^{n+3}} + \text{sgn}(\varepsilon)(1+n)(3+n)\theta_E^{n+1} \frac{\theta_1^3}{\theta^{n+5}} \\ \psi_{,112} &= -\text{sgn}(\varepsilon)(1+n)\theta_E^{n+1} \frac{\theta_2}{\theta^{n+3}} + \text{sgn}(\varepsilon)(1+n)(3+n)\theta_E^{n+1} \frac{\theta_1^2 \theta_2}{\theta^{n+5}} \\ \psi_{,122} &= -\text{sgn}(\varepsilon)(1+n)\theta_E^{n+1} \frac{\theta_1}{\theta^{n+3}} + \text{sgn}(\varepsilon)(1+n)(3+n)\theta_E^{n+1} \frac{\theta_1 \theta_2^2}{\theta^{n+5}} \\ \psi_{,222} &= -\text{sgn}(\varepsilon)3(1+n)\theta_E^{n+1} \frac{\theta_2}{\theta^{n+3}} + \text{sgn}(\varepsilon)(1+n)(3+n)\theta_E^{n+1} \frac{\theta_2^3}{\theta^{n+5}}.\end{aligned}\quad (5.16)$$

From this, the components of the \mathcal{F} -flexion are given by

$$\begin{aligned}\mathcal{F}_1 &= \frac{1}{2}(\psi_{,111} + \psi_{,122}) \\ &= -\text{sgn}(\varepsilon) \frac{(1-n^2)}{2} \theta_E^{n+1} \frac{\theta_1}{\theta^{n+3}}\end{aligned}\quad (5.17)$$

$$\begin{aligned}\mathcal{F}_2 &= \frac{1}{2}(\psi_{,112} + \psi_{,222}) \\ &= -\text{sgn}(\varepsilon) \frac{(1-n^2)}{2} \theta_E^{n+1} \frac{\theta_2}{\theta^{n+3}}\end{aligned}\quad (5.18)$$

³Where ϕ in the $e^{2i\phi}$ term of the shear is the polar angle of the lens-plane position vector $\boldsymbol{\theta}$, not to be confused with the coordinate ϕ is the Schwarzschild metric.

such that the total \mathcal{F} -flexion is

$$\mathcal{F} = -\text{sgn}(\varepsilon) \frac{(1-n^2)}{2} \frac{\theta_E^{n+1}}{\theta^{n+2}} e^{i\phi}, \quad (5.19)$$

and the components of the \mathcal{G} -flexion are given by

$$\begin{aligned} \mathcal{G}_1 &= \frac{1}{2} (\psi_{,111} - 3\psi_{,122}) \\ &= \text{sgn}(\varepsilon) \frac{(1+n)(3+n)}{2} \theta_E^{n+1} \frac{\theta_1^3 - 3\theta_1\theta_2^2}{\theta^{n+5}} \end{aligned} \quad (5.20)$$

$$\begin{aligned} \mathcal{G}_2 &= \frac{1}{2} (3\psi_{,112} - \psi_{,222}) \\ &= \text{sgn}(\varepsilon) \frac{(1+n)(3+n)}{2} \theta_E^{n+1} \frac{3\theta_1^2\theta_2 - \theta_2^3}{\theta^{n+5}} \end{aligned} \quad (5.21)$$

such that the total \mathcal{G} -flexion is

$$\mathcal{G} = \text{sgn}(\varepsilon) \frac{(1+n)(3+n)}{2} \frac{\theta_E^{n+1}}{\theta^{n+2}} e^{3i\phi}. \quad (5.22)$$

As pointed out by Izumi et al. [127], the expression for convergence given by Eq. (5.12) is consistent with the Schwarzschild lens for $\varepsilon > 0$ and $n = 1$. We point out that this is also true of the shear, given by Eq. (5.15), and the flexions, given by Eqs. (5.19) and (5.22). Additionally, we note that all four lensing fields recover the SIS lens for $\varepsilon > 0$ and $n = 0$. One will also immediately notice that the lensing fields in the $\varepsilon < 0$ case are the negatives of the $\varepsilon > 0$ case.

5.3.2 Discussion of shear and flexion behavior

Lensing field signatures from ordinary matter

Let us first discuss the behavior of convergence, shear, and flexion in nonexotic, typical weak lensing situations. As an illustrative example, consider the SIS lens ($\varepsilon > 0$ and $n = 0$). This type of lens corresponds to an ordinary, positive mass, for which $\kappa > 0$. We can study the behavior of the shear and flexion lensing fields by considering the simple example of a source (background) galaxy located at polar angle $\phi = 0$ around the lens. Then, the direction of the field is encoded in the sign of the lensing field amplitude. Around such a lens, there exists “tangential” alignment of galaxy

ellipticities, such that the shear given by Eq. (5.15) $\gamma < 0$ (again, for $\phi = 0$). \mathcal{F} -flexion, which has the spin properties of a vector, points radially toward the lens, such that $\mathcal{F} < 0$ in Eq. (5.19). \mathcal{G} -flexion oscillates around the lens as a spin-3 quantity; however, its behavior could also be described as a type of radial alignment, but where $\mathcal{G} > 0$ in Eq. (5.22).

This is the behavior of lensing fields in the presence of some ordinary positive mass, and therefore it also describes the picture of galaxy-galaxy lensing. Furthermore, this lensing signature is also found in lensing by cosmological large-scale structure. In cosmology, there exists matter density perturbations relative to some mean density in the Universe. There are regions of mass overdensity (a mass peak) and regions of mass underdensity (a mass trough). The mass overdensity can be modeled as, for example, an SIS lens. In the presence of a mass overdensity, there is tangential shear alignment and radial flexion alignment of background galaxies. Lensing fields display the opposite behavior when a mass underdensity is a lens: there is tangential anti-alignment⁴ of shear: $\gamma > 0$ (again, for $\phi = 0$) and anti-radial alignment for flexion: $\mathcal{F} > 0$ and $\mathcal{G} < 0$.

This is all to say that, when we simultaneously observe tangential alignment of shear and radial alignment of flexion, we expect there to be a mass peak (e.g. a positive mass lens or some local mass overdensity) and when anti-tangential alignment of shear and anti-radial alignment of flexion is observed, we expect the lens to be some local mass underdensity.

Lensing field signatures from exotic matter

Let us now turn our attention to weak lensing in the exotic spacetime metric. Figure 5.1 shows the magnitude and algebraic sign of the amplitudes of the various lensing fields for the $\varepsilon > 0$ and $\varepsilon < 0$ cases, respectively.

First, we consider the $\varepsilon > 0$ case, where we know from the deflection angle in Eq. (5.5) that there exists a gravitational attraction on light rays from the lens. If and only if $n > -1$, tangential alignment of shear exists. Interestingly, for $\varepsilon > 0$ and $n > 1$, the convergence is negative, despite there being a tangential shear. As discussed earlier, this negative convergence corresponds to exotic matter (and energy). This was pointed out in Izumi et al. [127]; however, in this work, we have

⁴Tangential anti-alignment is referred to as “cross”-alignment in the literature

additional information from the flexion fields. Here, radial alignment of \mathcal{F} -flexion only exists for $\varepsilon > 0$ and $-1 < n < 1$. For $n > 1$, there is an anti-radial \mathcal{F} -flexion alignment despite the fact that there is a tangential alignment of shear. \mathcal{G} -flexion, on the other hand, is radially aligned for $n > -1$. This is all to say that there is a stark difference in the behavior of the lensing fields for $n > 1$. Whereas shear and \mathcal{G} -flexion would indicate the presence of a mass-overdense lens that pulls on light rays, the convergence and \mathcal{F} -flexion behave as if there is a mass-underdense lens. This is a consequence of the fact that \mathcal{F} -flexion is the derivative of convergence and \mathcal{G} -flexion is the derivative of shear. Therefore, \mathcal{F} -flexion responds locally to convergence, and \mathcal{G} -flexion responds nonlocally to the shear.

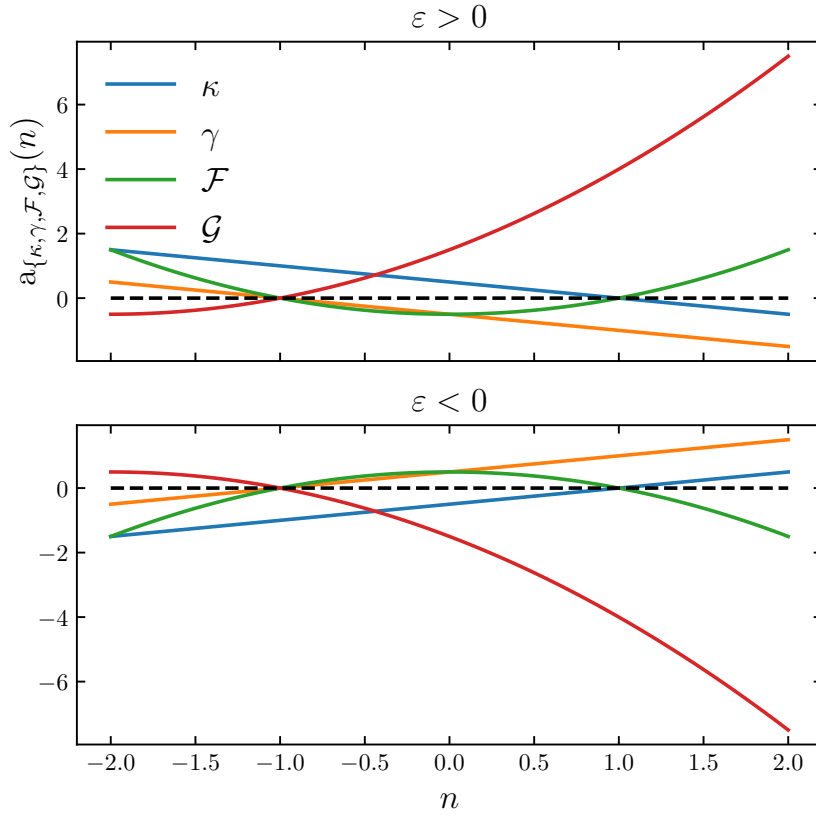


Figure 5.1: Here we plot the amplitudes as a function of n for convergence, shear, \mathcal{F} -flexion, and \mathcal{G} -flexion for the cases $\varepsilon > 0$ (top) and $\varepsilon < 0$ (bottom). The signs of each amplitude for shear and flexion indicate alignment around a lens (for $\phi = 0$), whereas the sign on the amplitude for convergence indicates positive or negative convergence. Here we see how the \mathcal{F} -flexion is coupled to the convergence and the \mathcal{G} -flexion to the shear for $n > 1$. Specifically, we note that the \mathcal{F} -flexion behaves opposite to that of the shear in the presence of an $n > 1$ lens.

Next, we consider the $\varepsilon < 0$ case, in which there exists a gravitational repulsion on light rays from the lens. Here, we observe precisely the opposite behavior as in the $\varepsilon > 0$ case. For $n > 1$, the convergence and \mathcal{F} -flexion behave as if there is a mass-overdense lens, whereas the shear and \mathcal{G} -flexion act as if there is a mass-underdense lens.

In Fig. 5.2, we show a cartoon of the behavior of shear and \mathcal{F} -flexion for three different cases. In each case, there are two source galaxies on opposite sides of a lens (one at $\phi = 0$ and the other at $\phi = \pi$ radians). The top panel recovers the typical case of lensing by a nonexotic object such as, for example, the SIS lens. In the middle case, we see the shear and \mathcal{F} -flexion responding to a negative convergence with $\varepsilon < 0$ and $-1 < n < 1$. In this formalism, this is considered an exotic lens. In the context of cosmology; however, this could be interpreted as the lensing fields responding to a local mass underdensity, such as a cosmic void [127]. Finally, the case on the bottom recovers that of an Ellis-wormhole type metric. Here, there is a negative convergence for the exotic object. As discussed earlier, while the shear is tangentially aligned, behaving as if there is an overdense lens, the flexion behaves as if there is an underdense lens, responding to the convergence.

We can also remark on the behavior of the lensing fields in the presence of a negative-mass compact object. A compact object can be described by the Schwarzschild metric ($n = 1$). For the case of a positive mass ($\varepsilon > 0$), shear is tangentially aligned, \mathcal{G} -flexion is radially aligned, but the convergence and \mathcal{F} -flexion, interestingly, both vanish. Flexion can add additional information when looking for negative-mass compact objects ($\varepsilon < 0$): one would expect the following lensing signature: tangential anti-alignment of shear, radial anti-alignment of \mathcal{G} -flexion, and $\mathcal{F} = 0$.

Flexion to the rescue

In the work presented in Izumi et al. [127], it is difficult to distinguish between various exotic lenses. Since convergence is not a directly observable quantity, one is relying entirely on shear. For example, two vastly different lenses – a lens with a positive convergence versus one with a negative convergence – are both capable of exhibiting identical directional behavior for shear. This can only be disambiguated by examining the relative strengths of the shear signals; however, this method could be difficult for, e.g. an $n \rightarrow 1^-$ negative convergence versus an $n \rightarrow 1^+$ positive convergence.

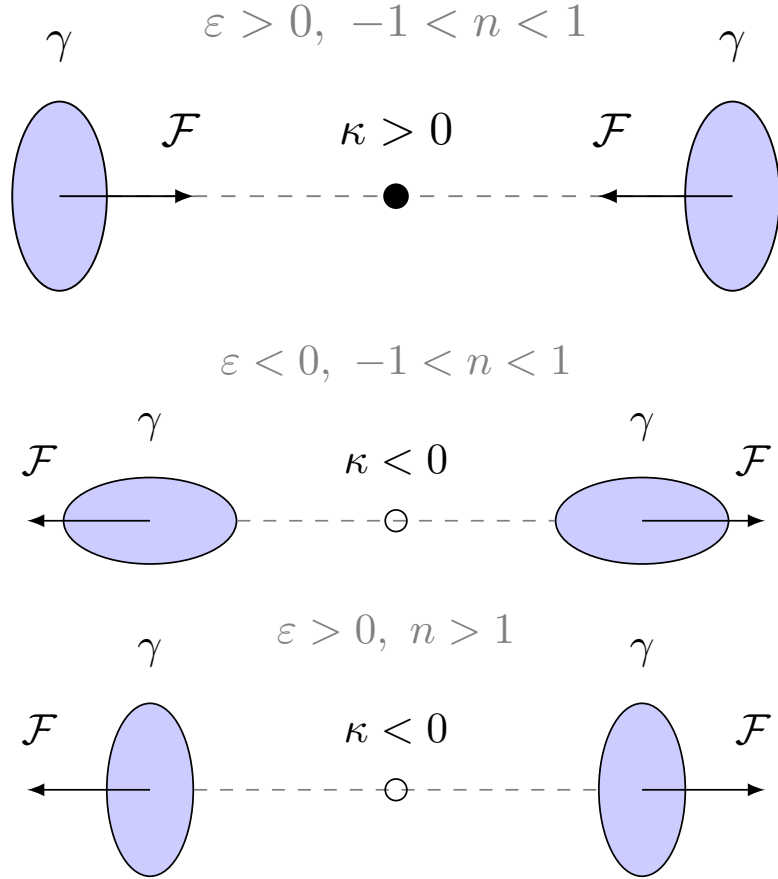


Figure 5.2: The behavior of shear and \mathcal{F} -flexion for two source (background) galaxies on opposite sides ($\phi = 0$ and $\phi = \pi$ radians) of three different lenses. *Top:* a typical scenario of lensing by a nonexotic mass defined by $\varepsilon > 0$ and $-1 < n < 1$ (we exclude the $n = 1$ Schwarzschild case where convergence and \mathcal{F} -flexion vanish). The shear has a tangential alignment around the lens and the \mathcal{F} -flexion points radially toward the lens (radial alignment). *Middle:* lensing by some exotic object ($\kappa < 0$) defined by $\varepsilon < 0$ and $-1 < n < 1$. Here, shear has tangential anti-alignment and \mathcal{F} -flexion points radially outward (radial anti-alignment). *Bottom:* lensing by some exotic object ($\kappa < 0$) defined by $\varepsilon > 0$ and $n > 1$. Here, shear has tangential alignment and \mathcal{F} -flexion points radially outward.

There is also another difficulty with relying only on shear, which comes from the fact that, unlike in e.g. galaxy-galaxy lensing, exotic lenses such as the Ellis wormhole may be completely invisible. This means that the lens position is unknown. Shear responds rather weakly to substructure, so using tangential alignment in order to locate the position of a lens, while possible, may not be ideal.

Both of these problems can be ameliorated with the addition of flexion. \mathcal{F} -flexion in particular is locally connected to the convergence, such that its directional information can distinguish between negative and positive convergences that cause identical shear directional patterns. Additionally, \mathcal{F} -flexion responds strongly to substructure, and so it could be more easily used to identify an unknown lens position. \mathcal{G} -flexion could be useful as a systematics check between shear and \mathcal{F} -flexion. While it is complementary to \mathcal{F} -flexion in terms of strength, it should follow the directional behavior of the shear.

In Izumi et al. [127], it can also prove difficult to distinguish between ordinary and exotic lenses. The Ellis wormhole ($\varepsilon > 0$ and $n = 2$) is an illustrative example of this. If relying on directional information alone, the Ellis wormhole creates a tangentially aligned shear pattern that resembles that of a typical nonexotic positive-mass lens. When we add flexion, however, the Ellis wormhole produces a unique lensing signature: tangential alignment of shear, anti-radial alignment of \mathcal{F} -flexion, and radial alignment of \mathcal{G} -flexion. To the best of our knowledge, only an exotic lens is capable of producing this type of lensing signature. Therefore, when combined with shear, flexion can be used to uniquely associate particular lensing signatures to exotic objects.

5.4 Cosmic flexion in modified gravity

In the standard Λ CDM model of cosmology, the field equations of GR describe the relationship between spacetime geometry and the matter-energy content of the Universe governed by gravity. The Friedmann–Lemaître–Robertson–Walker (FLRW) metric describes a homogeneous and isotropic Universe. To quantify gravitational lensing in a cosmological context, however, it is necessary to consider scalar perturbations in the FLRW metric. In the conformal Newtonian gauge, the line

element of such a metric is given by [30]

$$ds^2 = a^2(\tau) \left[\left(1 + \frac{2\Psi}{c^2} \right) c^2 d\tau^2 - \left(1 - \frac{2\Phi}{c^2} \right) dl^2 \right] \quad (5.23)$$

where τ is the conformal time, a is the scale factor, and $dl^2 = d\chi^2 + f_K^2(\chi)d\Omega^2$, where $f_K(\chi)$ is the comoving angular distance, which is simply equal to χ for a flat Universe, in which case $dl^2 = \delta_{ij}dx^i dx^j$. The two Bardeen potentials, $\Psi(\boldsymbol{x}, \tau)$ and $\Phi(\boldsymbol{x}, \tau)$ are considered to describe weak fields, $\Psi, \Phi \ll c^2$. In GR, the two Bardeen potentials are equal to each other:

$$\Phi_N = \Phi = \Psi, \quad (5.24)$$

where Φ_N is the Newtonian gravitational potential defined via the Poisson equation. In modified gravity, these potentials need not be equivalent.

The local deflection of light rays – propagating along null geodesics – relative to unperturbed ones, depends on the light travel time obtained from the metric:

$$\frac{d\tau}{dl} \approx \frac{1}{c} \left[1 - \frac{1}{c^2} (\Phi + \Psi) \right]. \quad (5.25)$$

Using this to obtain the deflection $d\alpha$, integrating over comoving distance, and using the lens equation, one obtains the cosmological effective convergence (obtained for GR in Sec. 1.3),

$$\kappa_{\text{eff}}(\boldsymbol{\theta}, \chi) = \frac{1}{2c^2} \int_0^\chi d\chi' \frac{f_K(\chi - \chi') f_K(\chi')}{f_K(\chi)} \nabla^2 [\Psi + \Phi](f_K(\chi') \boldsymbol{\theta}, \chi') \quad (5.26)$$

where $\boldsymbol{\theta}$ is the angular position on the sky, χ is the comoving distance (along the line of sight), and the Laplacian is given by $\nabla^2 = \partial^2/\partial x_i \partial x_i + \partial^2/\partial \chi^2$, where summation over i is implied, and x are physical distances perpendicular to the line of sight.

In GR, the linearized Einstein equations relate the metric perturbations (the Bardeen potentials) to the perturbations of the cosmological fluid. These include the matter density contrast $\delta \equiv \delta\rho/\bar{\rho}$, the pressure perturbation δp , the divergence of the fluid velocity θ , and the stress or anisotropic

pressure σ . Computing the Einstein equations is most easily done in Fourier space, where we exchange spatial derivatives with powers of $i\mathbf{k}$, where k is the comoving wavenumber. A combination of the $0 - 0$ and $0 - i$ equations yields the generalized Poisson equation (see Sec. 1.1.5):

$$-k^2\tilde{\Phi} = 4\pi G a^2 \bar{\rho} \tilde{\Delta} = \frac{3}{2} \Omega_{m,0} H_0^2 a^{-1} \tilde{\Delta} \quad (5.27)$$

where H_0 is the Hubble constant, $\Omega_{m,0}$ is the matter density parameter at present epoch,

$$\tilde{\Delta}(\mathbf{k}, a) = \tilde{\delta}(\mathbf{k}, a) + \frac{3H(a)(1+w)\theta}{k^2} \quad (5.28)$$

is the comoving density perturbation, $H(a)$ is the Hubble parameter, $w = \bar{p}/\bar{\rho}$ is the equation of state parameter, and the second equality in Eq. (5.27) is written for matter only. We can parametrize deviations from GR through use of the mass-screening phenomenological post-GR function $\tilde{Q}(\mathbf{k}, a)$, replacing Newton's gravitational constant by an effective function

$$G_{\text{eff}} = G\tilde{Q} \implies -k^2\tilde{\Phi} = 4\pi G\tilde{Q}a^2\bar{\rho}\tilde{\Delta}. \quad (5.29)$$

From the $i - j$ Einstein equation, one obtains

$$k^2(\tilde{\Phi} - \tilde{\Psi}) = 12\pi G a^2 \bar{\rho}(1+w)\sigma. \quad (5.30)$$

Here, we can pursue a further deviation from GR which quantifies the difference in the Bardeen potentials, $\Psi - \Phi$, through use of the gravitational slip phenomenological post-GR function, $\tilde{\eta}(\mathbf{k}, a)$:

$$\tilde{\Psi} = (1 + \tilde{\eta})\tilde{\Phi} \implies k^2(\tilde{\Phi} - \tilde{\Psi}) = 4\pi G\tilde{Q}\tilde{\eta}a^2\bar{\rho}\tilde{\Delta}. \quad (5.31)$$

From this, we obtain

$$-k^2(\tilde{\Phi} + \tilde{\Psi}) = 8\pi G \tilde{Q} \left(1 + \frac{\tilde{\eta}}{2}\right) a^2 \bar{\rho} \tilde{\Delta} = 8\pi G \tilde{\Sigma} a^2 \bar{\rho} \tilde{\Delta} \quad (5.32)$$

$$-k^2 \tilde{\Psi} = 4\pi G Q (1 + \tilde{\eta}) a^2 \bar{\rho} \tilde{\Delta} = 4\pi G \tilde{\Gamma} a^2 \bar{\rho} \tilde{\Delta} \quad (5.33)$$

where we have defined $\tilde{\Sigma}(\mathbf{k}, a) = \tilde{Q}(\mathbf{k}, a)(1 + \tilde{\eta}(\mathbf{k}, a)/2)$ and $\tilde{\Gamma}(\mathbf{k}, a) = \tilde{Q}(\mathbf{k}, a)(1 + \tilde{\eta}(\mathbf{k}, a))$. These two derived post-GR functions are commonly used in cosmic shear studies. In general, these functions can depend on both cosmic time and scale [149].

5.4.1 Case 1: Scale-independent post-GR functions

The two derived post-GR functions have been taken to be scale-independent for various cosmic shear studies (see e.g. Tereno et al. [149]). In this case, we have the following simplification for Eq. (5.32):

$$-k^2 [\tilde{\Phi} + \tilde{\Psi}] (\mathbf{k}, a) = 3\Omega_{m,0} H_0^2 a^{-1} \Sigma(a) \tilde{\Delta}(\mathbf{k}, a). \quad (5.34)$$

Taking the Fourier transform of this, the cosmological effective convergence can be written [149]

$$\kappa_{\text{eff}}(\boldsymbol{\theta}, \chi) = \frac{3}{2} \Omega_{m,0} \left(\frac{H_0}{c}\right)^2 \int_0^\chi d\chi' \frac{f_K(\chi - \chi') f_K(\chi')}{f_K(\chi) a(\chi')} \Sigma(a(\chi')) \Delta(f_K(\chi') \boldsymbol{\theta}, \chi'). \quad (5.35)$$

This gives the effective convergence for a fixed source redshift corresponding to a comoving distance χ . When the sources are distributed in comoving distance, the cosmological effective convergence needs to be averaged over the (normalized) source distribution $n(\chi)$. This is to say that $\kappa_{\text{eff}}(\boldsymbol{\theta}) = \int_0^{\chi_H} d\chi n(\chi) \kappa_{\text{eff}}(\boldsymbol{\theta}, \chi)$, where χ_H is the horizon distance obtained for infinite redshift. By introducing the lensing efficiency function,

$$q(\chi) = \frac{3}{2} \Omega_{m,0} \left(\frac{H_0}{c}\right)^2 \frac{f_K(\chi)}{a(\chi)} \int_\chi^{\chi_H} d\chi' n(\chi') \frac{f_K(\chi' - \chi)}{f_K(\chi')}, \quad (5.36)$$

and rearranging integration limits, we obtain

$$\kappa_{\text{eff}}(\boldsymbol{\theta}) = \int_0^{\chi_H} d\chi q(\chi) \Sigma(a(\chi)) \Delta(f_K(\chi) \boldsymbol{\theta}, \chi). \quad (5.37)$$

We recall from Eq. (1.192), Limber's equation/approximation states that for two quantities, g_a and g_b of the $g_a = \int_0^{\chi_H} d\chi h_a(\chi) X(f_K(\chi) \boldsymbol{\theta}, \chi)$ where X is some field, e.g. the density contrast, the cross-power spectrum of g_a and g_b is [41, 59, 60]

$$\mathcal{P}_{ab}(\ell) = \int_0^{\chi_H} d\chi \frac{h_a(\chi) h_b(\chi)}{f_K^2(\chi)} \mathcal{P}_X \left(k = \frac{\ell + 1/2}{f_K(\chi)}, \chi \right). \quad (5.38)$$

where ℓ is the angular wavenumber. If one sets $h_a = h_b = q(\chi) \Sigma(a(\chi))$, we obtain the convergence power spectrum

$$\mathcal{P}_\kappa(\ell) = \int_0^{\chi_H} d\chi \frac{q^2(\chi) \Sigma^2(a(\chi))}{f_K^2(\chi)} \mathcal{P}_\Delta^{\text{MG}} \left(k = \frac{\ell + 1/2}{f_K(\chi)}, \chi \right) \quad (5.39)$$

where $\mathcal{P}_\Delta^{\text{MG}}(k, z) \neq \mathcal{P}_\Delta^{\text{GR}}(k, z)$ is the (nonlinear) matter power spectrum in modified gravity. It is clear that deviations to GR modify the cosmic shear power spectrum amplitude via $\Sigma(a)$. They further impact the power spectrum, though, via a modification of the matter power spectrum. This is because the evolution of the density contrast is modified via Eq. (5.27), leading to a different cosmic evolution than in GR [145].

Next, we wish to obtain the cosmic flexion power spectrum (this process was detailed in Sec. 1.3 for the case of GR). Making use of the definition of flexion given by Eq (1.119), i.e.

$$\mathcal{F}_i = \partial_i \kappa = \frac{\partial}{\partial \theta_i} \kappa = f_K(\chi) \frac{\partial}{\partial x_i} \kappa, \quad (5.40)$$

the cosmological effective flexion can be written as

$$\mathcal{F}_{\text{eff}}(\boldsymbol{\theta}, \chi) = \frac{3}{2} \Omega_{m,0} \left(\frac{H_0}{c} \right)^2 \int_0^\chi d\chi' \frac{f_K(\chi - \chi') f_K(\chi')}{f_K(\chi) a(\chi')} \Sigma(a(\chi')) f_K(\chi') \Delta'(f_K(\chi') \boldsymbol{\theta}, \chi') \quad (5.41)$$

where Δ' is the transverse gradient of the density contrast. Following the same process as was done

for the cosmological effective convergence, we therefore obtain $\mathcal{F}_{\text{eff}}(\boldsymbol{\theta}) = \int_0^{\chi_H} d\chi q(\chi) \Delta'(f_K(\chi)\boldsymbol{\theta}, \chi)$.

This time, we set $h_a = h_b = f_K(\chi)q(\chi)\Sigma(a(\chi))$ and obtain, via Limber's equation,

$$\begin{aligned}\mathcal{P}_{\mathcal{F}}(\ell) &= \int_0^{\chi_H} d\chi q^2(\chi) \Sigma^2(a(\chi)) \mathcal{P}_{\Delta'}^{\text{MG}} \left(k = \frac{\ell + 1/2}{f_K(\chi)}, \chi \right) \\ &= \ell^2 \mathcal{P}_\kappa(\ell)\end{aligned}\quad (5.42)$$

where we have noted that $|X'|^2 = |X|^2 k_i k^i$ and hence (taking $k = (\ell + 1/2)/f_K(\chi) \approx \ell/f_K(\chi)$) [43]

$$\mathcal{P}_{X'} \left(\frac{\ell}{f_K(\chi), \chi} \right) = \mathcal{P}_X \left(\frac{\ell}{f_K(\chi), \chi} \right) \frac{\ell^2}{f_K^2(\chi)}. \quad (5.43)$$

In addition to the cosmic flexion power spectrum, we can also obtain the convergence-flexion cross-spectrum (as was done in Sec. 1.3 for the case of GR). We again use Limber's equation, but this time we work in terms of $\mathcal{P}_\Delta^{\text{MG}}$ rather than $\mathcal{P}_{\Delta'}^{\text{MG}}$. We set $h_\kappa = q(\chi)\Sigma(a(\chi))$ and $h_{\mathcal{F}} = q(\chi)\Sigma(a(\chi))\ell$ to obtain

$$\mathcal{P}_{\kappa\mathcal{F}}(\ell) = \ell \mathcal{P}_\kappa(\ell). \quad (5.44)$$

We note that, owing to the fact that shear and convergence statistics are the same, i.e. $\mathcal{P}_\gamma(\ell) = \mathcal{P}_\kappa(\ell)$ [4], so too (because of the relations in Eq. 1.120) are the \mathcal{F} - and \mathcal{G} -flexion power spectra,

$$\mathcal{P}_{\mathcal{G}}(\ell) = \mathcal{P}_{\mathcal{F}}(\ell), \quad (5.45)$$

and similarly,

$$\mathcal{P}_{\kappa\mathcal{G}}(\ell) = \mathcal{P}_{\kappa\mathcal{F}}(\ell). \quad (5.46)$$

5.4.2 Case 2: Scale-dependent post-GR functions

In general the two derived post-GR functions are functions of scale. In Fourier space,

$$-k^2 \left[\tilde{\Phi} + \tilde{\Psi} \right] (\mathbf{k}, a) = 3\Omega_{m,0} H_0^2 a^{-1} \tilde{\Sigma}(\mathbf{k}, a) \tilde{\Delta}(\mathbf{k}, a). \quad (5.47)$$

We define the following quantity:

$$\tilde{\Delta}_\Sigma(\mathbf{k}, a) \equiv \tilde{\Sigma}(\mathbf{k}, a)\tilde{\Delta}(\mathbf{k}, a), \quad (5.48)$$

and obtain the cosmological effective convergence

$$\kappa_{\text{eff}}(\boldsymbol{\theta}, \chi) = \frac{3}{2}\Omega_{m,0} \left(\frac{H_0}{c}\right)^2 \int_0^\chi d\chi' \frac{f_K(\chi - \chi')f_K(\chi')}{f_K(\chi)a(\chi')} \Delta_\Sigma(f_K(\chi')\boldsymbol{\theta}, \chi'). \quad (5.49)$$

Again using Limber's equation, we obtain the convergence power spectrum

$$\mathcal{P}_\kappa(\ell) = \int_0^{\chi_H} d\chi \frac{q^2(\chi)}{f_K^2(\chi)} \mathcal{P}_{\Delta_\Sigma}^{\text{MG}} \left(k = \frac{\ell + 1/2}{f_K(\chi)}, \chi \right), \quad (5.50)$$

where $\mathcal{P}_{\Delta_\Sigma}^{\text{MG}}(k, z)$ is defined in Fourier space via Eq. (5.48). Following the same steps as before, the cosmological effective convergence is given by

$$\mathcal{F}_{\text{eff}}(\boldsymbol{\theta}, \chi) = \frac{3}{2}\Omega_{m,0} \left(\frac{H_0}{c}\right)^2 \int_0^\chi d\chi' \frac{f_K(\chi - \chi')f_K(\chi')}{f_K(\chi)a(\chi')} f_K(\chi') \Delta'_\Sigma(f_K(\chi')\boldsymbol{\theta}, \chi'). \quad (5.51)$$

We immediately note that the cosmological effective convergence depends on the transverse gradient of Δ_Σ , and therefore it is a probe of the derivative of the derived post-GR function Σ . This positions flexion as a unique probe of modified gravity, allowing the measurement of Σ' alongside Σ .

Finally, we find that $\mathcal{P}_F(\ell) = \mathcal{P}_G(\ell) = \ell^2 \mathcal{P}_\kappa(\ell)$ and $\mathcal{P}_{\kappa F}(\ell) = \mathcal{P}_{\kappa G}(\ell) = \ell \mathcal{P}_\kappa(\ell)$, as before. Cosmic shear-shear, flexion-flexion, and shear-flexion correlations probe different scales (see AGB for a detailed discussion). While cosmic shear has a broad window function for power at the scale of arcminutes, cosmic flexion peaks at the arcsecond scale, with shear-flexion peaking intermediate to these two signals. With the use of cosmic flexion in addition to cosmic shear, there exists the opportunity to probe the behavior of modified gravity across a wide range of cosmic scales and times.

5.5 Conclusions

In this Chapter we have considered the weak gravitational flexion that is induced by exotic lenses, such as the Ellis wormhole, through use of an exotic spacetime metric. We have also reported a more generalized expression for the weak gravitational shear. We show that the analytic equations for convergence, shear, and the flexions in this exotic spacetime recover familiar nonexotic lenses such as the Schwarzschild lens and the SIS lens. We find that flexion can provide valuable information about exotic lenses when used in addition to shear. In particular, the directional information from \mathcal{F} -flexion can be used to distinguish between positive and negative convergences, and can provide unique lensing signatures for objects such as the Ellis wormhole, whereas the directional information from shear alone cannot.

We also consider cosmic flexion in the context of modified gravity. We find that the cosmological effective flexion depends on the transverse spatial derivative of the derived phenomenological post-GR function Σ , positioning flexion as a unique probe of parametric modified gravity. Additionally, we are able to construct cosmic flexion-flexion and shear-flexion power spectra, which probe different scales than cosmic shear, allowing for further exploration of deviations from GR, particularly in the case of scale-dependent post-GR functions.

Chapter 6: Future Prospects

In this thesis, I have developed a full theoretical formalism for cosmic flexion in Fourier and configuration space, discovered novel flexion-flexion and shear-flexion two-point correlation functions, and discovered the non-commutativity of odd-spin combinations of weak lensing fields. I also measured, for the first time, cosmic flexion using the first three years (Y3) of Dark Energy Survey (DES) observations where I detected a cosmic shear-flexion signal to $\sim 3\sigma$, and uncovered the non-Gaussianity of the cosmic flexion signals. This work has also led to the development of two flexion-based computational tools: a novel tool for flexion measurement, `Lenser`, which is the first such open-source Python code, as well as the first (and only) multi-band, multi-epoch flexion measurement pipeline; and an open-source flexion and shear two-point measurement pipeline, `F-SHARP`. This thesis also includes an investigation of flexion in the context of exotic single-lens metrics as well as cosmic flexion in modified gravity.

This thesis represents significant progress toward cosmic flexion becoming a useful probe of cosmology and the small-scale matter power spectrum. In the following sections, I share my thoughts about what work can be done to improve cosmic flexion measurement and modeling going forward, what cosmic flexion will look like in the upcoming era of Stage IV cosmology surveys, other flexion signals that I believe will be interesting to develop and measure, and the landscape of physics that can possibly be probed by cosmic flexion.

6.1 Future work for flexion in Stage III cosmology surveys

6.1.1 Systematics

For current Stage III cosmology surveys such as DES, there are a number of improvements that can be made to cosmic flexion measurement. As is outlined in Secs. 4.3.4 and 4.3.5, more work needs to be done on a careful understanding of the systematics related to ground-based flexion measurement in DES and how they propagate into the cosmic flexion two-point functions. In terms of additive

systematic effects, this should include studying the effects of flexion on the PSF modeling. This may also include a comparison of multi-epoch versus coadd flexion measurement using `Lenser`. I also think there is a need to develop flexion-based statistics to quantify an acceptable level of PSF leakage, similar to the ρ -statistics used for shear measurement [152, 78]. In terms of multiplicative bias, it will be necessary moving forward to either create simulations of galaxies with realistic flexion values to calibrate the `Lenser` pipeline, or, given that `Lenser` is forward-modeling, create a self-calibrating version of `Lenser` similar to the METACALIBRATION pipeline. It is important to note that this calibration may not account for all effects at small-scales, as is the case with METACALIBRATION, and it may be necessary to study potential causes of multiplicative bias, such as blending, independently.

6.1.2 Computation of 2PCFs

The unexpected realization that median statistics are necessary for 2PCF computation introduces another significant challenge that will need to be addressed by future analyses: efficient computation of the median and error on the median. The DES Y3 cosmic flexion 2PSFs currently test the limits on what is reasonably possible with disk space and RAM constraints on a supercomputer. As far as estimating the median of the 2PSFs, I can imagine computing the median through an iterative process, where with multiple iterations of the `F-SHARP` pipeline, you narrow in on the median of each 2PSF. First, you would find a reasonable range around the median similar to the process in `Gb Minor`, restrict the next run of `F-SHARP` to that range, and repeat until you find the true median. Here, you trade an increased run-time for not saving the entire 2PSFs to disk, nor holding them in their entirety in RAM. There is one additional complication here, which is that it may be difficult to estimate the true median across multiple parallelization chunks. As for the errors, rather than trying to directly calculate the error on the median from each 2PSF, one could simply compute jackknife estimate of the median error matrix. This could be done by applying the iterative median estimation to N_{jk} jackknife chunks of the dataset. This leaves us with N_{jk} estimates of the median

of each 2PSF, $\check{\xi}_{\pm}^{ab}$. Then, one could calculate a co-median matrix [153]

$$\text{COM}(\check{\xi}_{\pm}^{ab}(\theta_x), \check{\xi}_{\pm}^{ab}(\theta_y)) \equiv \text{med} \left(\check{\xi}_{\pm}^{ab}(\theta_x) - \text{med}(\check{\xi}_{\pm}^{ab}(\theta_x)) \right) \left(\check{\xi}_{\pm}^{ab}(\theta_y) - \text{med}(\check{\xi}_{\pm}^{ab}(\theta_y)) \right). \quad (6.1)$$

There would need to be an investigation into the proper normalization factor for this matrix. There are two normalizations: one coming from the jackknife; the other requiring that the square root of the diagonal of this matrix is equivalent to the error on the median, as is discussed in Sec. 4.3.3. This can be done by comparing the diagonal to the estimate of the error on the median I use in the DES Y3 cosmic flexion analysis, defined by the 16th and 84th percentiles of the 2PSFs (see Eq. 4.11), and/or by calculating the error on the median based on the best-fit PDF of each 2PSF, $p(\Xi)$, given by [154]

$$\text{Err}(\check{\xi}^{ab}(\theta)) = \frac{1}{\sqrt{4N_p(\theta)p^2(\Xi_{\text{med}})}} \quad (6.2)$$

g where $p(\Xi_{\text{med}})$ is the value of the PDF at the median.

6.1.3 Theoretical work

I note that there also needs to be more progress on the theoretical front. Crucial to a robust understanding of the cosmic flexion signal will be the use of both N-body and hydrodynamical simulations. Typically, N-body simulations do not have the resolution required to study the small scales probed by cosmic flexion. There has been some progress made on this front by Lopez-Arenillas et al. [155], in which a full-sky formalism for flexion was worked out, and an N-body simulation was used at a resolution of 0.4294 arcminutes in order to compare the large-scale parts of the flexion power spectra to theoretical predictions. I am interested in continuing this work in the future, with Dr. Enrique Gaztanaga, in order to simulate the cosmic flexion signal in real space, injecting realistic DES Y3 noise, and comparing the theoretical predictions of the 2PCFs from AGB to those measured in the simulations. It will also be necessary to model the effect of baryonic feedback on the cosmic flexion signals through hydrodynamical simulations. Constraints from cosmic flexion could allow us to place limits on various models of poorly understood baryonic effects at these small, nonlinear scales [156].

I believe it is also necessary to get a better understanding of the intrinsic alignment of flexion, and how that influences that flexion-flexion and shear-flexion two-point correlation functions. This could potentially be studied with the existing DES Y3 Flexion Catalogue by analyzing those nearby pairs of galaxies at the same redshift.

6.1.4 Other signals to measure

In addition to the cosmic flexion measurements, the DES Y3 Flexion Catalogue can also be used to undertake the largest-ever study of galaxy-galaxy flexion (both \mathcal{F} and \mathcal{G}), which is also a probe of small scales. This work is currently in progress.

6.1.5 Other datasets and surveys

I would like to repeat this analysis for the DES Y6 data, the final data product from DES. Here, I anticipate a higher S/N detection of cosmic flexion and galaxy-galaxy flexion, owing to the fact that Y6 has the same footprint as Y3, but with more objects, which leads to a higher number density of source galaxies. Higher number density is particularly beneficial for cosmic flexion, as its signal increases with decreasing galaxy separation.

I believe it could be interesting to measure cosmic flexion and galaxy-galaxy flexion in the Hyper Suprime-Cam (HSC) survey, another Stage III cosmology survey [157]. Given the higher number density of sources in HSC compared to DES, we might expect to achieve a larger S/N detection for cosmic flexion at small scales. Being able to compare measurements of cosmic flexion and galaxy-galaxy flexion across different surveys would also be critical to understanding these signals.

6.1.6 Constraints on cosmology

If we can get the systematics of the cosmic flexion signals fully under control, I am interested in exploring what optimized constraints on the small-scale matter power spectrum can be obtained from DES (particularly Y6) and/or HSC cosmic flexion and galaxy-galaxy flexion measurements when combined the DES/HSC 3×2 point function (galaxy clustering, galaxy-galaxy shear, and cosmic shear). As it currently stands in weak lensing cosmological analyses, information from small, nonlinear scales are typically not used in order to constrain cosmology. In the DES Y3 3×2 point

data vector, for example, scale cuts are made to exclude any scales where there is significant modeling uncertainty due to baryonic effects on the small-scale matter power spectrum. Due to this, a very significant amount of constraining power is lost. This is precisely the issue which cosmic flexion (and galaxy-galaxy flexion) can address. Cosmic flexion signals peak at the very scales that are thrown away by DES. As such, cosmic flexion is in a unique position to constrain the amplitude and shape of this small-scale matter power spectrum. Cosmic flexion, therefore, can potentially place constraints on baryonic feedback models. These constraints can lead to a smaller modeling uncertainty, which can, in turn, allow for less aggressive scale cuts in the standard 3×2 point analysis, leading to tighter constraints on cosmological parameters.

6.2 The upcoming era of Stage IV cosmology surveys

I would like to consider cosmic flexion and galaxy-galaxy flexion in the context of upcoming Stage IV experiments such as the Vera C. Rubin Observatory Legacy Survey of Space and Time (LSST), Euclid, and the Nancy Grace Roman Telescope (*Roman*). Stage IV surveys offer enormous benefits to weak lensing. They will all offer a higher number density of source galaxies as compared to Stage III surveys such as DES and HSC, and LSST and Euclid also offer more sky coverage, which will lead to even stronger constraints from cosmological weak lensing signals. The benefits from Stage IV surveys, though, also come with challenges. The tighter constraints on signals such as cosmic shear, the more carefully we need to understand the behavior of shear and systematics of the instruments at the sub-percent level. This translates into even more aggressive scale cuts on the 3×2 point data vector if constraints on the small-scale matter power spectrum as well as modeling uncertainty are not improved. This is, again, where cosmic flexion and galaxy-galaxy flexion can play a role.

6.2.1 New physics

When I first has the idea of this Ph.D. thesis, my main motivation for studying cosmic flexion was my belief that it could be an interesting probe of modified gravity. Indeed, there may exist modified gravity models that deviate from General Relativity+ Λ on small scales that cannot be detected by cosmic shear or other large-scale cosmological probes. This idea is explored in detail in Chapter

5. With the constraining power from cosmic flexion in Stage IV surveys, it may be possible to discriminate between some of these modified gravity models. It should be noted that the effects of some of these models may be degenerate with different baryonic feedback models if they both alter the growth of structure in the same way.

As for other new physics, it has been proposed that cosmic flexion could place constraints on primordial non-Gaussianity using Stage IV surveys [158] and recently, it was suggested that cosmic flexion could probe vector and tensor modes in the late Universe, including cosmic strings on small scales [159].

6.2.2 Higher-order flexion signals

I am also interested in what additional statistics may be interesting/detectable in future surveys. On the theoretical front, there are still many signals that could be formalized. I believe that both galaxy-shear-flexion and galaxy-flexion-flexion signals exist, as do a (very large) family of three-point cosmic flexion signals. It could potentially be interesting to work these out, expanding using the framework of three-point cosmic shear as well as the two-point cosmic flexion family, as these may be measurable in Stage IV surveys.

Bibliography

- [1] Scott Dodelson and Fabian Schmidt. *Modern Cosmology*. 2020. doi: 10.1016/C2017-0-01943-2.
- [2] Katrin Heitmann, Earl Lawrence, Juliana Kwan, Salman Habib, and David Higdon. The Coyote Universe Extended: Precision Emulation of the Matter Power Spectrum. *Astrophys. J.*, 780:111, 2014. doi: 10.1088/0004-637X/780/1/111.
- [3] Joseph M Fabritius II. *Flexion based measures in galaxy clusters*. PhD thesis, Drexel University, 2021.
- [4] Martin Kilbinger. Cosmology with cosmic shear observations: a review. *Rept. Prog. Phys.*, 78:086901, 2015. doi: 10.1088/0034-4885/78/8/086901.
- [5] Marios Karouzos. Cosmic shear to the rescue. *Nature Astronomy*, 4(3):216–216, Mar 2020. ISSN 2397-3366. doi: 10.1038/s41550-020-1044-0. URL <https://doi.org/10.1038/s41550-020-1044-0>.
- [6] A. et al Koekemoer. CANDELS: THE COSMIC ASSEMBLY NEAR-INFRARED DEEP EXTRAGALACTIC LEGACY SURVEY—THE HUBBLE SPACE TELESCOPE OBSERVATIONS, IMAGING DATA PRODUCTS, AND MOSAICS. *The Astrophysical Journal Supplement Series*, 197(2):36, dec 2011. doi: 10.1088/0067-0049/197/2/36. URL <https://doi.org/10.1088/0067-0049/197/2/36>.
- [7] Albert Einstein. Zur Allgemeinen Relativitätstheorie. *Sitzungsber. Preuss. Akad. Wiss. Berlin (Math. Phys.)*, 1915:778–786, 1915. [Addendum: Sitzungsber.Preuss.Akad.Wiss.Berlin (Math.Phys.) 1915, 799–801 (1915)].
- [8] Albert Einstein. The foundation of the general theory of relativity. *Annalen Phys.*, 49(7):769–822, 1916. doi: 10.1002/andp.19163540702.
- [9] Isaac Newton. *Philosophiae Naturalis Principia Mathematica*. England, 1687.
- [10] Karl Schwarzschild. Über das Gravitationsfeld eines Massenpunktes nach der Einsteinschen Theorie. *Sitzungsberichte der Königlich Preußischen Akademie der Wissenschaften (Berlin)*, pages 189–196, January 1916.
- [11] C. W. Misner, K. S. Thorne, and J. A. Wheeler. *Gravitation*. 1973.
- [12] H. P. Robertson. Kinematics and World-Structure. *Astrophys. J.*, 82:284–301, 1935. doi: 10.1086/143681.
- [13] A. G. Walker. On Milne’s Theory of World-Structure. *Proceedings of the London Mathematical Society*, 42:90–127, January 1937. doi: 10.1112/plms/s2-42.1.90.
- [14] A. Friedmann. Über die Krümmung des Raumes. *Zeitschrift fur Physik*, 10:377–386, January 1922. doi: 10.1007/BF01332580.
- [15] G. Lemaître. A homogeneous universe of constant mass and increasing radius accounting for the radial velocity of extra-galactic nebulae. *MNRAS*, 91:483–490, March 1931. doi: 10.1093/mnras/91.5.483.
- [16] F. Zwicky. Die Rotverschiebung von extragalaktischen Nebeln. *Helv. Phys. Acta*, 6:110–127, 1933. doi: 10.1007/s10714-008-0707-4.

- [17] T. S. van Albada, J. N. Bahcall, K. Begeman, and R. Sancisi. Distribution of dark matter in the spiral galaxy NGC 3198. *ApJ*, 295:305–313, August 1985. doi: 10.1086/163375.
- [18] T. S. van Albada and R. Sancisi. Dark Matter in Spiral Galaxies. *Philosophical Transactions of the Royal Society of London Series A*, 320(1556):447–464, December 1986. doi: 10.1098/rsta.1986.0128.
- [19] E. Noordermeer, J. M. van der Hulst, R. Sancisi, R. S. Swaters, and T. S. van Albada. The mass distribution in early-type disc galaxies: declining rotation curves and correlations with optical properties. *MNRAS*, 376(4):1513–1546, April 2007. doi: 10.1111/j.1365-2966.2007.11533.x.
- [20] P. Salucci, A. Lapi, C. Tonini, G. Gentile, I. Yegorova, and U. Klein. The universal rotation curve of spiral galaxies - II. The dark matter distribution out to the virial radius. *MNRAS*, 378(1):41–47, June 2007. doi: 10.1111/j.1365-2966.2007.11696.x.
- [21] Douglas Clowe, Maruša Bradač, Anthony H. Gonzalez, Maxim Markevitch, Scott W. Randall, Christine Jones, and Dennis Zaritsky. A Direct Empirical Proof of the Existence of Dark Matter. *ApJ*, 648(2):L109–L113, September 2006. doi: 10.1086/508162.
- [22] Maruša Bradač, Douglas Clowe, Anthony H. Gonzalez, Phil Marshall, William Forman, Christine Jones, Maxim Markevitch, Scott Randall, Tim Schrabback, and Dennis Zaritsky. Strong and Weak Lensing United. III. Measuring the Mass Distribution of the Merging Galaxy Cluster 1ES 0657-558. *ApJ*, 652(2):937–947, December 2006. doi: 10.1086/508601.
- [23] A. A. Penzias and R. W. Wilson. A Measurement of Excess Antenna Temperature at 4080 Mc/s. *ApJ*, 142:419–421, July 1965. doi: 10.1086/148307.
- [24] Adam G. Riess et al. Observational evidence from supernovae for an accelerating universe and a cosmological constant. *Astron. J.*, 116:1009–1038, 1998. doi: 10.1086/300499.
- [25] S. Perlmutter et al. Measurements of Ω and Λ from 42 high redshift supernovae. *Astrophys. J.*, 517:565–586, 1999. doi: 10.1086/307221.
- [26] T. M. C. Abbott, M. Aguena, A. Alarcon, O. Alves, A. Amon, F. Andrade-Oliveira, J. Annis, S. Avila, D. Bacon, E. Baxter, K. Bechtol, M. R. Becker, G. M. Bernstein, S. Birrer, J. Blazek, S. Bocquet, A. Brando-Souza, S. L. Bridle, D. Brooks, D. L. Burke, H. Camacho, A. Campos, A. Carnero Rosell, M. Carrasco Kind, J. Carretero, F. J. Castander, R. Cawthon, C. Chang, A. Chen, R. Chen, A. Choi, C. Conselice, J. Cordero, M. Costanzi, M. Crocce, L. N. da Costa, M. E. S. Pereira, C. Davis, T. M. Davis, J. DeRose, S. Desai, E. Di Valentino, H. T. Diehl, S. Dodelson, P. Doel, C. Doux, A. Drlica-Wagner, K. Eckert, T. F. Eifler, F. Elsner, J. Elvin-Poole, S. Everett, X. Fang, A. Farahi, I. Ferrero, A. Ferté, B. Flaugher, P. Fosalba, D. Friedel, O. Friedrich, J. Frieman, J. García-Bellido, M. Gatti, L. Giani, T. Giannantonio, G. Giannini, D. Gruen, R. A. Gruendl, J. Gschwend, G. Gutierrez, N. Hamaus, I. Harrison, W. G. Hartley, K. Herner, S. R. Hinton, D. L. Hollowood, K. Honscheid, H. Huang, E. M. Huff, D. Huterer, B. Jain, D. J. James, M. Jarvis, N. Jeffrey, T. Jeltema, A. Kovacs, E. Krause, K. Kuehn, N. Kuropatkin, O. Lahav, S. Lee, P. F. Leget, P. Lemos, C. D. Leonard, A. R. Liddle, M. Lima, H. Lin, N. MacCrann, J. L. Marshall, J. McCullough, J. Mena-Fernández, F. Menanteau, R. Miquel, V. Miranda, J. J. Mohr, J. Muir, J. Myles, S. Nadathur, A. Navarro-Alsina, R. C. Nichol, R. L. C. Ogando, Y. Omori, A. Palmese, S. Pandey, Y. Park, M. Paterno, F. Paz-Chinchón, W. J. Percival, A. Pieres, A. A. Plazas Malagón, A. Porredon, J. Prat, M. Raveri, M. Rodriguez-Monroy, P. Rogozenski, R. P. Rollins, A. K. Romer, A. Roodman, R. Rosenfeld, A. J. Ross, E. S. Rykoff, S. Samuroff, C. Sánchez, E. Sanchez, J. Sanchez, D. Sanchez Cid, V. Scarpine, D. Scolnic, L. F. Secco, I. Sevilla-Noarbe, E. Sheldon, T. Shin, M. Smith, M. Soares-Santos, E. Suchyta, M. Tabbutt, G. Tarle, D. Thomas, C. To, A. Troja, M. A. Troxel, I. Tutusaus, T. N. Varga, M. Vincenzi, A. R. Walker, N. Weaverdyck, R. H. Wechsler, J. Weller, B. Yanny, B. Yin, Y. Zhang, J. Zuntz, and DES Collaboration. Dark Energy Survey Year 3 results: Constraints on extensions to Λ CDM with weak lensing and

- galaxy clustering. *Phys. Rev. D*, 107(8):083504, April 2023. doi: 10.1103/PhysRevD.107.083504.
- [27] Edwin Hubble. A relation between distance and radial velocity among extra-galactic nebulae. *Proc. Nat. Acad. Sci.*, 15:168–173, 1929. doi: 10.1073/pnas.15.3.168.
 - [28] N. Aghanim et al. Planck 2018 results. VI. Cosmological parameters. *Astron. Astrophys.*, 641: A6, 2020. doi: 10.1051/0004-6361/201833910. [Erratum: *Astron. Astrophys.* 652, C4 (2021)].
 - [29] Alan H. Guth. The Inflationary Universe: A Possible Solution to the Horizon and Flatness Problems. *Phys. Rev. D*, 23:347–356, 1981. doi: 10.1103/PhysRevD.23.347.
 - [30] Chung-Pei Ma and Edmund Bertschinger. Cosmological Perturbation Theory in the Synchronous and Conformal Newtonian Gauges. *ApJ*, 455:7, December 1995. doi: 10.1086/176550.
 - [31] James M. Bardeen. Gauge Invariant Cosmological Perturbations. *Phys. Rev. D*, 22:1882–1905, 1980. doi: 10.1103/PhysRevD.22.1882.
 - [32] Antony Lewis, Anthony Challinor, and Anthony Lasenby. Efficient computation of CMB anisotropies in closed FRW models. *Astrophys. J.*, 538:473–476, 2000. doi: 10.1086/309179.
 - [33] Diego Blas, Julien Lesgourgues, and Thomas Tram. The cosmic linear anisotropy solving system (class). part ii: Approximation schemes. *Journal of Cosmology and Astroparticle Physics*, 2011(07):034–034, Jul 2011. ISSN 1475-7516. doi: 10.1088/1475-7516/2011/07/034. URL <http://dx.doi.org/10.1088/1475-7516/2011/07/034>.
 - [34] Julio F. Navarro, Carlos S. Frenk, and Simon D. M. White. Simulations of x-ray clusters. *Mon. Not. Roy. Astron. Soc.*, 275:720–740, 1995. doi: 10.1093/mnras/275.3.720.
 - [35] Julio F. Navarro, Carlos S. Frenk, and Simon D. M. White. The Structure of cold dark matter halos. *Astrophys. J.*, 462:563–575, 1996. doi: 10.1086/177173.
 - [36] Julio F. Navarro, Carlos S. Frenk, and Simon D. M. White. A Universal density profile from hierarchical clustering. *Astrophys. J.*, 490:493–508, 1997. doi: 10.1086/304888.
 - [37] James Binney and Scott Tremaine. *Galactic dynamics*. 1987.
 - [38] Amandine M. C. Le Brun, Ian G. McCarthy, Joop Schaye, and Trevor J. Ponman. Towards a realistic population of simulated galaxy groups and clusters. *Mon. Not. Roy. Astron. Soc.*, 441(2):1270–1290, 2014. doi: 10.1093/mnras/stu608.
 - [39] Giovanni Aricò, Raul E. Angulo, Sergio Contreras, Lurdes Ondaro-Mallea, Marcos Pellejero-Ibañez, and Matteo Zennaro. The BACCO simulation project: a baryonification emulator with neural networks. *Mon. Not. Roy. Astron. Soc.*, 506(3):4070–4082, 2021. doi: 10.1093/mnras/stab1911.
 - [40] T. M. C. Abbott, M. Aguena, A. Alarcon, S. Allam, O. Alves, A. Amon, F. Andrade-Oliveira, J. Annis, S. Avila, D. Bacon, E. Baxter, K. Bechtol, M. R. Becker, G. M. Bernstein, S. Bhargava, S. Birrer, J. Blazek, A. Brandao-Souza, S. L. Bridle, D. Brooks, E. Buckley-Geer, D. L. Burke, H. Camacho, A. Campos, A. Carnero Rosell, M. Carrasco Kind, J. Carretero, F. J. Castander, R. Cawthon, C. Chang, A. Chen, R. Chen, A. Choi, C. Conselice, J. Cordero, M. Costanzi, M. Crocce, L. N. da Costa, M. E. da Silva Pereira, C. Davis, T. M. Davis, J. De Vicente, J. DeRose, S. Desai, E. Di Valentino, H. T. Diehl, J. P. Dietrich, S. Dodelson, P. Doel, C. Doux, A. Drlica-Wagner, K. Eckert, T. F. Eifler, F. Elsner, J. Elvin-Poole, S. Everett, A. E. Evrard, X. Fang, A. Farahi, E. Fernandez, I. Ferrero, A. Ferté, P. Fosalba, O. Friedrich, J. Frieman, J. García-Bellido, M. Gatti, E. Gaztanaga, D. W. Gerdes, T. Giannantonio, G. Giannini, D. Gruen, R. A. Gruendl, J. Gschwend, G. Gutierrez, I. Harrison, W. G. Hartley, K. Herner, S. R. Hinton, D. L. Hollowood, K. Honscheid, B. Hoyle, E. M. Huff, D. Huterer, B. Jain, D. J. James, M. Jarvis, N. Jeffrey, T. Jeltema, A. Kovacs,

- E. Krause, R. Kron, K. Kuehn, N. Kuropatkin, O. Lahav, P. F. Leget, P. Lemos, A. R. Liddle, C. Lidman, M. Lima, H. Lin, N. MacCrann, M. A. G. Maia, J. L. Marshall, P. Martini, J. McCullough, P. Melchior, J. Mena-Fernández, F. Menanteau, R. Miquel, J. J. Mohr, R. Morgan, J. Muir, J. Myles, S. Nadathur, A. Navarro-Alsina, R. C. Nichol, R. L. C. Ogando, Y. Omori, A. Palmese, S. Pandey, Y. Park, F. Paz-Chinchón, D. Petracick, A. Pieres, A. A. Plazas Malagón, A. Porredon, J. Prat, M. Raveri, M. Rodriguez-Monroy, R. P. Rollins, A. K. Romer, A. Roodman, R. Rosenfeld, A. J. Ross, E. S. Rykoff, S. Samuroff, C. Sánchez, E. Sanchez, J. Sanchez, D. Sanchez Cid, V. Scarpine, M. Schubnell, D. Scolnic, L. F. Secco, S. Serrano, I. Sevilla-Noarbe, E. Sheldon, T. Shin, M. Smith, M. Soares-Santos, E. Suchyta, M. E. C. Swanson, M. Tabbutt, G. Tarle, D. Thomas, C. To, A. Troja, M. A. Troxel, D. L. Tucker, I. Tutusaus, T. N. Varga, A. R. Walker, N. Weaverdyck, R. Wechsler, J. Weller, B. Yanny, B. Yin, Y. Zhang, J. Zuntz, and DES Collaboration. Dark Energy Survey Year 3 results: Cosmological constraints from galaxy clustering and weak lensing. *Phys. Rev. D*, 105(2):023520, January 2022. doi: 10.1103/PhysRevD.105.023520.
- [41] Matthias Bartelmann and Peter Schneider. Weak gravitational lensing. *Phys. Rept.*, 340: 291–472, 2001. doi: 10.1016/S0370-1573(00)00082-X.
 - [42] David M. Goldberg and David J. Bacon. Galaxy-galaxy flexion: Weak lensing to second order. *Astrophys. J.*, 619:741–748, 2005. doi: 10.1086/426782.
 - [43] David J. Bacon, D. M. Goldberg, B. T. P. Rowe, and A. N. Taylor. Weak gravitational flexion. *Mon. Not. Roy. Astron. Soc.*, 365:414–428, 2006. doi: 10.1111/j.1365-2966.2005.09624.x.
 - [44] Yuki Okura, Keiichi Umetsu, and Toshifumi Futamase. A Method for Weak Lensing Flexion Analysis by the HOLICs Moment Approach. *Astrophys. J.*, 680:1, 2008. doi: 10.1086/587676.
 - [45] Peter Schneider and Xinzong Er. Weak lensing goes bananas: What flexion really measures. *Astron. Astrophys.*, 485:363–376, 2008. doi: 10.1051/0004-6361:20078631.
 - [46] Nick Kaiser. Nonlinear Cluster Lens Reconstruction. *ApJ*, 439:L1, January 1995. doi: 10.1086/187730.
 - [47] Patricia G. Castro, A. F. Heavens, and T. D. Kitching. Weak lensing analysis in three dimensions. *Phys. Rev. D*, 72:023516, 2005. doi: 10.1103/PhysRevD.72.023516.
 - [48] Peter Schneider and Carolin Seitz. Steps towards nonlinear cluster inversion through gravitational distortions. I. Basic considerations and circular clusters. *A&A*, 294:411–431, February 1995. doi: 10.48550/arXiv.astro-ph/9407032.
 - [49] Carolin Seitz and Peter Schneider. Steps towards nonlinear cluster inversion through gravitational distortions. 3. Including a redshift distribution of the sources. *Astron. Astrophys.*, 318: 687, 1997.
 - [50] Joseph M Fabritius II, Evan J Arena, and David M Goldberg. Shape, colour, and distance in weak gravitational flexion. *Monthly Notices of the Royal Astronomical Society*, 501(3): 4103–4109, Dec 2020. ISSN 1365-2966. doi: 10.1093/mnras/staa3928. URL <http://dx.doi.org/10.1093/mnras/staa3928>.
 - [51] M. Bartelmann. Arcs from a universal dark-matter halo profile. *A&A*, 313:697–702, September 1996. doi: 10.48550/arXiv.astro-ph/9602053.
 - [52] Candace Oaxaca Wright and Tereasa G. Brainerd. Gravitational Lensing by NFW Halos. *ApJ*, 534(1):34–40, May 2000. doi: 10.1086/308744.
 - [53] Malin Velander, Konrad Kuijken, and Tim Schrabback. Probing galaxy dark matter haloes in COSMOS with weak lensing flexion. *MNRAS*, 412(4):2665–2677, April 2011. doi: 10.1111/j.1365-2966.2010.18085.x.

- [54] Adrienne Leonard, David M. Goldberg, Jason L. Haaga, and Richard Massey. Gravitational Shear, Flexion, and Strong Lensing in Abell 1689. *ApJ*, 666(1):51–63, September 2007. doi: 10.1086/520109.
- [55] Benjamin Cain, Paul L. Schechter, and M.W. Bautz. MEASURING GRAVITATIONAL LENSING FLEXION IN a1689 USING AN ANALYTIC IMAGE MODEL. *The Astrophysical Journal*, 736(1):43, jul 2011. doi: 10.1088/0004-637X/736/1/43.
- [56] Justin P. Bird and David M. Goldberg. Flexion in Abell 2744. *Mon. Not. Roy. Astron. Soc.*, 476(1):1198–1212, 2018. doi: 10.1093/mnras/sty300.
- [57] Nick Kaiser and Gordon Squires. Mapping the Dark Matter with Weak Gravitational Lensing. *ApJ*, 404:441, February 1993. doi: 10.1086/172297.
- [58] Nick Kaiser, Gordon Squires, and Thomas J. Broadhurst. A Method for weak lensing observations. *Astrophys. J.*, 449:460–475, 1995. doi: 10.1086/176071.
- [59] D. Nelson Limber. The Analysis of Counts of the Extragalactic Nebulae in Terms of a Fluctuating Density Field. *ApJ*, 117:134, January 1953. doi: 10.1086/145672.
- [60] Marilena LoVerde and Niayesh Afshordi. Extended Limber Approximation. *Phys. Rev. D*, 78: 123506, 2008. doi: 10.1103/PhysRevD.78.123506.
- [61] Gary M. Bernstein and Robert Armstrong. Bayesian lensing shear measurement. *MNRAS*, 438(2):1880–1893, February 2014. doi: 10.1093/mnras/stt2326.
- [62] Michael D. Schneider, David W. Hogg, Philip J. Marshall, William A. Dawson, Joshua Meyers, Deborah J. Bard, and Dustin Lang. Hierarchical Probabilistic Inference of Cosmic Shear. *ApJ*, 807(1):87, July 2015. doi: 10.1088/0004-637X/807/1/87.
- [63] G. M. Bernstein and M. Jarvis. Shapes and Shears, Stars and Smears: Optimal Measurements for Weak Lensing. *AJ*, 123(2):583–618, February 2002. doi: 10.1086/338085.
- [64] Reiko Nakajima and Gary Bernstein. Shear Recovery Accuracy in Weak-Lensing Analysis with the Elliptical Gauss-Laguerre Method. *AJ*, 133(4):1763–1779, April 2007. doi: 10.1086/511957.
- [65] Konrad Kuijken. Weak weak lensing: correcting weak shear measurements accurately for PSF anisotropy. *A&A*, 352:355–362, December 1999. doi: 10.48550/arXiv.astro-ph/9904418.
- [66] John Irwin, Marina Shmakova, and Jay Anderson. Lensing Signals in the Hubble Ultra Deep Field Using All Second-Order Shape Deformations. *ApJ*, 671(2):1182–1195, December 2007. doi: 10.1086/522819.
- [67] K. Kuijken. Shears from shapelets. *A&A*, 456(3):827–838, September 2006. doi: 10.1051/0004-6361:20054794.
- [68] L. Miller, T. D. Kitching, C. Heymans, A. F. Heavens, and L. van Waerbeke. Bayesian galaxy shape measurement for weak lensing surveys - I. Methodology and a fast-fitting algorithm. *MNRAS*, 382(1):315–324, November 2007. doi: 10.1111/j.1365-2966.2007.12363.x.
- [69] Alexandre Refregier. Weak Gravitational Lensing by Large-Scale Structure. *ARA&A*, 41: 645–668, January 2003. doi: 10.1146/annurev.astro.41.111302.102207.
- [70] Alexandre Refregier and David Bacon. Shapelets - II. A method for weak lensing measurements. *MNRAS*, 338(1):48–56, January 2003. doi: 10.1046/j.1365-8711.2003.05902.x.
- [71] Richard Massey and Alexandre Refregier. Polar shapelets. *MNRAS*, 363(1):197–210, October 2005. doi: 10.1111/j.1365-2966.2005.09453.x.

- [72] Eric Huff and Rachel Mandelbaum. Metacalibration: Direct Self-Calibration of Biases in Shear Measurement. *arXiv e-prints*, art. arXiv:1702.02600, February 2017. doi: 10.48550/arXiv.1702.02600.
- [73] Erin S. Sheldon and Eric M. Huff. Practical Weak-lensing Shear Measurement with Metacalibration. *ApJ*, 841(1):24, May 2017. doi: 10.3847/1538-4357/aa704b.
- [74] David M. Goldberg and Adrienne Leonard. Measuring Flexion. *Astrophys. J.*, 660:1003–1015, 2007. doi: 10.1086/513137.
- [75] Richard Massey, Barnaby Rowe, Alexandre Refregier, David J. Bacon, and Joel Berge. Weak gravitational shear and flexion with polar shapelets. *Mon. Not. Roy. Astron. Soc.*, 380:229, 2007. doi: 10.1111/j.1365-2966.2007.12072.x.
- [76] Sérsic, J. L. Influence of the atmospheric and instrumental dispersion on the brightness distribution in a galaxy. *Boletin de la Asociacion Argentina de Astronomia La Plata Argentina*, 6:41–43, feb 1963.
- [77] Alister W. Graham and Simon P. Driver. A Concise Reference to (Projected) Sérsic $R^{1/n}$ Quantities, Including Concentration, Profile Slopes, Petrosian Indices, and Kron Magnitudes. *PASA*, 22(2):118–127, January 2005. doi: 10.1071/AS05001.
- [78] M. Jarvis, E. Sheldon, J. Zuntz, T. Kacprzak, S. L. Bridle, A. Amara, R. Armstrong, M. R. Becker, G. M. Bernstein, C. Bonnett, C. Chang, R. Das, J. P. Dietrich, A. Drlica-Wagner, T. F. Eifler, C. Gangkofner, D. Gruen, M. Hirsch, E. M. Huff, B. Jain, S. Kent, D. Kirk, N. MacCrann, P. Melchior, A. A. Plazas, A. Refregier, B. Rowe, E. S. Rykoff, S. Samuroff, C. Sánchez, E. Suchyta, M. A. Troxel, V. Vikram, T. Abbott, F. B. Abdalla, S. Allam, J. Annis, A. Benoit-Lévy, E. Bertin, D. Brooks, E. Buckley-Geer, D. L. Burke, D. Capozzi, A. Carnero Rosell, M. Carrasco Kind, J. Carretero, F. J. Castander, J. Clampitt, M. Crocce, C. E. Cunha, C. B. D’Andrea, L. N. da Costa, D. L. DePoy, S. Desai, H. T. Diehl, P. Doel, A. Fausti Neto, B. Flaugher, P. Fosalba, J. Frieman, E. Gaztanaga, D. W. Gerdes, R. A. Gruendl, G. Gutierrez, K. Honscheid, D. J. James, K. Kuehn, N. Kuropatkin, O. Lahav, T. S. Li, M. Lima, M. March, P. Martini, R. Miquel, J. J. Mohr, E. Neilsen, B. Nord, R. Ogando, K. Reil, A. K. Romer, A. Roodman, M. Sako, E. Sanchez, V. Scarpine, M. Schubnell, I. Sevilla-Noarbe, R. C. Smith, M. Soares-Santos, F. Sobreira, M. E. C. Swanson, G. Tarle, J. Thaler, D. Thomas, A. R. Walker, and R. H. Wechsler. The DES Science Verification weak lensing shear catalogues. *MNRAS*, 460(2):2245–2281, August 2016. doi: 10.1093/mnras/stw990.
- [79] Peter Schneider. Detection of (dark) matter concentrations via weak gravitational lensing. *MNRAS*, 283(3):837–853, December 1996. doi: 10.1093/mnras/283.3.837.
- [80] Joseph M. Fabritius and David M. Goldberg. A new estimate of galaxy mass-to-light ratios from flexion lensing statistics. *MNRAS*, 515(4):6191–6197, October 2022. doi: 10.1093/mnras/stac2158.
- [81] M. Gatti et al. Dark energy survey year 3 results: weak lensing shape catalogue. *Mon. Not. Roy. Astron. Soc.*, 504(3):4312–4336, 2021. doi: 10.1093/mnras/stab918.
- [82] George R. Blumenthal, S. M. Faber, Joel R. Primack, and Martin J. Rees. Formation of Galaxies and Large Scale Structure with Cold Dark Matter. *Nature*, 311:517–525, 1984. doi: 10.1038/311517a0.
- [83] T. M. C. Abbott et al. Dark Energy Survey Year 3 results: Cosmological constraints from galaxy clustering and weak lensing. *Phys. Rev. D*, 105(2):023520, 2022. doi: 10.1103/PhysRevD.105.023520.
- [84] Adam G. Riess, Stefano Casertano, Wenlong Yuan, J. Bradley Bowers, Lucas Macri, Joel C. Zinn, and Dan Scolnic. Cosmic Distances Calibrated to 1% Precision with Gaia EDR3 Parallaxes and Hubble Space Telescope Photometry of 75 Milky Way Cepheids Confirm Tension with Λ CDM. *Astrophys. J. Lett.*, 908(1):L6, 2021. doi: 10.3847/2041-8213/abdbaf.

- [85] Caroline D. Huang et al. Hubble space telescope observations of mira variables in the sn ia host ngc 1559: An alternative candle to measure the hubble constant. *The Astrophysical Journal*, 889(1):5, Jan 2020. ISSN 1538-4357. doi: 10.3847/1538-4357/ab5dbd. URL <http://dx.doi.org/10.3847/1538-4357/ab5dbd>.
- [86] Noemi Frusciante and Louis Perenon. Effective field theory of dark energy: A review. *Phys. Rept.*, 857:1–63, 2020. doi: 10.1016/j.physrep.2020.02.004.
- [87] Jolyon Bloomfield, Éanna É. Flanagan, Minjoon Park, and Scott Watson. Dark energy or modified gravity? An effective field theory approach. *J. Cosmology Astropart. Phys.*, 2013(8):010, August 2013. doi: 10.1088/1475-7516/2013/08/010.
- [88] Emilio Bellini and Ignacy Sawicki. Maximal freedom at minimum cost: linear large-scale structure in general modifications of gravity. *J. Cosmology Astropart. Phys.*, 2014(7):050, July 2014. doi: 10.1088/1475-7516/2014/07/050.
- [89] G. Soucail, B. Fort, Y. Mellier, and J. P. Picat. A blue ring-like structure in the center of the A 370 cluster of galaxies. *A&A*, 172:L14–L16, January 1987.
- [90] J. A. Tyson, F. Valdes, and R. A. Wenk. Detection of Systematic Gravitational Lens Galaxy Image Alignments: Mapping Dark Matter in Galaxy Clusters. *ApJ*, 349:L1, January 1990. doi: 10.1086/185636.
- [91] Tereasa G. Brainerd, Roger D. Blandford, and Ian Smail. Measuring galaxy masses using galaxy - galaxy gravitational lensing. *Astrophys. J.*, 466:623, 1996. doi: 10.1086/177537.
- [92] Philippe Fischer et al. Weak lensing with SDSS commissioning data: The Galaxy mass correlation function to $1h^{-1}$ Mpc. *Astron. J.*, 120:1198–1208, 2000. doi: 10.1086/301540.
- [93] David J. Bacon, Alexandre R. Refregier, and Richard S. Ellis. Detection of weak gravitational lensing by large-scale structure. *Mon. Not. Roy. Astron. Soc.*, 318:625, 2000. doi: 10.1046/j.1365-8711.2000.03851.x.
- [94] Nick Kaiser, Gillian Wilson, and Gerard A. Luppino. Large-Scale Cosmic Shear Measurements. *arXiv e-prints*, art. astro-ph/0003338, March 2000.
- [95] Ludovic van Waerbeke et al. Detection of correlated galaxy ellipticities on CFHT data: First evidence for gravitational lensing by large scale structures. *Astron. Astrophys.*, 358:30–44, 2000.
- [96] David M. Wittman, J. Anthony Tyson, David Kirkman, Ian Dell’Antonio, and Gary Bernstein. Detection of weak gravitational lensing distortions of distant galaxies by cosmic dark matter at large scales. *Nature*, 405:143–149, 2000. doi: 10.1038/35012001.
- [97] T. Abbott et al. The Dark Energy Survey: more than dark energy – an overview. *Mon. Not. Roy. Astron. Soc.*, 460(2):1270–1299, 2016. doi: 10.1093/mnras/stw641.
- [98] Konrad Kuijken et al. Gravitational Lensing Analysis of the Kilo Degree Survey. *Mon. Not. Roy. Astron. Soc.*, 454(4):3500–3532, 2015. doi: 10.1093/mnras/stv2140.
- [99] Hiroaki Aihara et al. The hyper suprime-cam ssp survey: Overview and survey design. *Publications of the Astronomical Society of Japan*, 70:S4, January 2018. doi: 10.1093/pasj/psx066.
- [100] Paul A Abell et al. LSST Science Book, Version 2.0. *arXiv e-prints*, art. arXiv:0912.0201, December 2009.
- [101] A. Refregier et al. Euclid Imaging Consortium Science Book. *arXiv e-prints*, art. arXiv:1001.0061, January 2010.

- [102] D. Spergel et al. Wide-Field InfrarRed Survey Telescope-Astrophysics Focused Telescope Assets WFIRST-AFTA 2015 Report. *arXiv e-prints*, art. arXiv:1503.03757, March 2015.
- [103] Nora Elisa Chisari, David Alonso, Elisabeth Krause, C. Danielle Leonard, Philip Bull, Jérémie Neveu, Antonio Villarreal, Sukhdeep Singh, Thomas McClintock, John Ellison, and et al. Core cosmology library: Precision cosmological predictions for lsst. *The Astrophysical Journal Supplement Series*, 242(1):2, May 2019. ISSN 1538-4365. doi: 10.3847/1538-4365/ab1658. URL <http://dx.doi.org/10.3847/1538-4365/ab1658>.
- [104] Kin-Wang Ng and Guo-Chin Liu. Correlation functions of CMB anisotropy and polarization. *Int. J. Mod. Phys. D*, 8:61–83, 1999. doi: 10.1142/S0218271899000079.
- [105] Gayoung Chon, Anthony Challinor, Simon Prunet, Eric Hivon, and Istvan Szapudi. Fast estimation of polarization power spectra using correlation functions. *Mon. Not. Roy. Astron. Soc.*, 350:914, 2004. doi: 10.1111/j.1365-2966.2004.07737.x.
- [106] Peter Schneider, Ludovic van Waerbeke, Martin Kilbinger, and Yannick Mellier. Analysis of two-point statistics of cosmic shear: I. estimators and covariances. *Astron. Astrophys.*, 396: 1–20, 2002. doi: 10.1051/0004-6361:20021341.
- [107] O. Friedrich et al. Dark Energy Survey year 3 results: covariance modelling and its impact on parameter estimation and quality of fit. *Mon. Not. Roy. Astron. Soc.*, 508(3):3125–3165, 2021. doi: 10.1093/mnras/stab2384.
- [108] R. E. Smith, J. A. Peacock, A. Jenkins, S. D. M. White, C. S. Frenk, F. R. Pearce, P. A. Thomas, G. Efstathiou, and H. M. P. Couchman. Stable clustering, the halo model and non-linear cosmological power spectra. *Monthly Notices of the Royal Astronomical Society*, 341(4):1311–1332, Jun 2003. ISSN 1365-2966. doi: 10.1046/j.1365-8711.2003.06503.x. URL <http://dx.doi.org/10.1046/j.1365-8711.2003.06503.x>.
- [109] L. F. Secco et al. Dark Energy Survey Year 3 results: Cosmology from cosmic shear and robustness to modeling uncertainty. *Phys. Rev. D*, 105(2):023515, 2022. doi: 10.1103/PhysRevD.105.023515.
- [110] Lawrence M. Widrow, Pascal J. Elahi, Robert J. Thacker, Mark Richardson, and Evan Scannapieco. Power spectrum for the small-scale universe. *Monthly Notices of the Royal Astronomical Society*, 397(3):1275–1285, Aug 2009. ISSN 1365-2966. doi: 10.1111/j.1365-2966.2009.15075.x. URL <http://dx.doi.org/10.1111/j.1365-2966.2009.15075.x>.
- [111] D. Huybrechs and S. Olver. *Highly oscillatory quadrature*, page 25–50. London Mathematical Society Lecture Note Series. Cambridge University Press, 2009. doi: 10.1017/CBO9781139107136.003.
- [112] Takuya Ooura and Masatake Mori. A robust double exponential formula for Fourier-type integrals. *Journal of Computational and Applied Mathematics*, 112(1):229–241, 1999. doi: 10.1016/S0377-0427(99)00223-X.
- [113] Hidenori Ogata. A Numerical Integration Formula Based on the Bessel Functions. *Publ RIMS Kyoto Univ*, 41:949–970, 2005. doi: 10.2977/prims/1145474602.
- [114] István Szapudi, Jun Pan, Simon Prunet, and Tamás Budavári. Fast Edge Corrected Measurement of the Two-Point Correlation Function and the Power Spectrum. *Arxiv E-Prints*, pages 4–4, May 2005. doi: 10.1086/496971.
- [115] Steven G. Murray and Francis J. Poulin. hankel: A python library for performing simple and accurate hankel transformations. *Journal of Open Source Software*, 4(37):1397, 2019. doi: 10.21105/joss.01397. URL <https://doi.org/10.21105/joss.01397>.

- [116] I. Sevilla-Noarbe, K. Bechtol, M. Carrasco Kind, A. Carnero Rosell, M. R. Becker, A. Drlica-Wagner, R. A. Gruendl, E. S. Rykoff, E. Sheldon, B. Yanny, A. Alarcon, S. Allam, A. Amon, A. Benoit-Lévy, G. M. Bernstein, E. Bertin, D. L. Burke, J. Carretero, A. Choi, H. T. Diehl, S. Everett, B. Flaugher, E. Gaztanaga, J. Gschwend, I. Harrison, W. G. Hartley, B. Hoyle, M. Jarvis, M. D. Johnson, R. Kessler, R. Kron, N. Kuropatkin, B. Leistedt, T. S. Li, F. Menanteau, E. Morganson, R. L. C. Ogando, A. Palmese, F. Paz-Chinchón, A. Pieres, C. Pond, M. Rodriguez-Monroy, J. Allyn Smith, K. M. Stringer, M. A. Troxel, D. L. Tucker, J. de Vicente, W. Wester, Y. Zhang, T. M. C. Abbott, M. Aguena, J. Annis, S. Avila, S. Bhargava, S. L. Bridle, D. Brooks, D. Brout, F. J. Castander, R. Cawthon, C. Chang, C. Conselice, M. Costanzi, M. Crocce, L. N. da Costa, M. E. S. Pereira, T. M. Davis, S. Desai, J. P. Dietrich, P. Doel, K. Eckert, A. E. Evrard, I. Ferrero, P. Fosalba, J. García-Bellido, D. W. Gerdes, T. Giannantonio, D. Gruen, G. Gutierrez, S. R. Hinton, D. L. Hollowood, K. Honscheid, E. M. Huff, D. Huterer, D. J. James, T. Jeltema, K. Kuehn, O. Lahav, C. Lidman, M. Lima, H. Lin, M. A. G. Maia, J. L. Marshall, P. Martini, P. Melchior, R. Miquel, J. J. Mohr, R. Morgan, E. Neilsen, A. A. Plazas, A. K. Romer, A. Roodman, E. Sanchez, V. Scarpine, M. Schubnell, S. Serrano, M. Smith, E. Suchyta, G. Tarle, D. Thomas, C. To, T. N. Varga, R. H. Wechsler, J. Weller, R. D. Wilkinson, and DES Collaboration. Dark Energy Survey Year 3 Results: Photometric Data Set for Cosmology. *ApJS*, 254(2):24, June 2021. doi: 10.3847/1538-4365/abeb66.
- [117] M. Jarvis, G. M. Bernstein, A. Amon, C. Davis, P. F. Léget, K. Bechtol, I. Harrison, M. Gatti, A. Roodman, C. Chang, R. Chen, A. Choi, S. Desai, A. Drlica-Wagner, D. Gruen, R. A. Gruendl, A. Hernandez, N. MacCrann, J. Meyers, A. Navarro-Alsina, S. Pandey, A. A. Plazas, L. F. Secco, E. Sheldon, M. A. Troxel, S. Vorperian, K. Wei, J. Zuntz, T. M. C. Abbott, M. Aguena, S. Allam, S. Avila, S. Bhargava, S. L. Bridle, D. Brooks, A. Carnero Rosell, M. Carrasco Kind, J. Carretero, M. Costanzi, L. N. da Costa, J. De Vicente, H. T. Diehl, P. Doel, S. Everett, B. Flaugher, P. Fosalba, J. Frieman, J. García-Bellido, E. Gaztanaga, D. W. Gerdes, G. Gutierrez, S. R. Hinton, D. L. Hollowood, K. Honscheid, D. J. James, S. Kent, K. Kuehn, N. Kuropatkin, O. Lahav, M. A. G. Maia, M. March, J. L. Marshall, P. Melchior, F. Menanteau, R. Miquel, R. L. C. Ogando, F. Paz-Chinchón, E. S. Rykoff, E. Sanchez, V. Scarpine, M. Schubnell, S. Serrano, I. Sevilla-Noarbe, M. Smith, E. Suchyta, M. E. C. Swanson, G. Tarle, T. N. Varga, A. R. Walker, W. Wester, R. D. Wilkinson, and DES Collaboration. Dark Energy Survey year 3 results: point spread function modelling. *MNRAS*, 501(1):1282–1299, February 2021. doi: 10.1093/mnras/staa3679.
- [118] Catherine Heymans, Ludovic Van Waerbeke, David Bacon, Joel Berge, Gary Bernstein, Emmanuel Bertin, Sarah Bridle, Michael L. Brown, Douglas Clowe, Håkon Dahle, Thomas Erben, Meghan Gray, Marco Hettmanseder, Henk Hoekstra, Patrick Hudelot, Mike Jarvis, Konrad Kuijken, Vera Margoniner, Richard Massey, Yannick Mellier, Reiko Nakajima, Alexandre Refregier, Jason Rhodes, Tim Schrabback, and David Wittman. The Shear Testing Programme - I. Weak lensing analysis of simulated ground-based observations. *MNRAS*, 368(3):1323–1339, May 2006. doi: 10.1111/j.1365-2966.2006.10198.x.
- [119] Catherine Heymans, Ludovic Van Waerbeke, Lance Miller, Thomas Erben, Hendrik Hildebrandt, Henk Hoekstra, Thomas D. Kitching, Yannick Mellier, Patrick Simon, Christopher Bonnett, Jean Coupon, Liping Fu, Joachim Harnois Déraps, Michael J. Hudson, Martin Kilbinger, Koenraad Kuijken, Barnaby Rowe, Tim Schrabback, Elisabetta Sembolini, Edo van Uitert, Sanaz Vafaei, and Malin Velander. CFHTLenS: the Canada-France-Hawaii Telescope Lensing Survey. *MNRAS*, 427(1):146–166, November 2012. doi: 10.1111/j.1365-2966.2012.21952.x.
- [120] Erin S. Sheldon, Matthew R. Becker, Niall MacCrann, and Michael Jarvis. Mitigating Shear-dependent Object Detection Biases with Metacalibration. *ApJ*, 902(2):138, October 2020. doi: 10.3847/1538-4357/abb595.
- [121] N. MacCrann, M. R. Becker, J. McCullough, A. Amon, D. Gruen, M. Jarvis, A. Choi, M. A.

- Troxel, E. Sheldon, B. Yanny, K. Herner, S. Dodelson, J. Zuntz, K. Eckert, R. P. Rollins, T. N. Varga, G. M. Bernstein, R. A. Gruendl, I. Harrison, W. G. Hartley, I. Sevilla-Noarbe, A. Pieres, S. L. Bridle, J. Myles, A. Alarcon, S. Everett, C. Sánchez, E. M. Huff, F. Tarsitano, M. Gatti, L. F. Secco, T. M. C. Abbott, M. Aguena, S. Allam, J. Annis, D. Bacon, E. Bertin, D. Brooks, D. L. Burke, A. Carnero Rosell, M. Carrasco Kind, J. Carretero, M. Costanzi, M. Crocce, M. E. S. Pereira, J. De Vicente, S. Desai, H. T. Diehl, J. P. Dietrich, P. Doel, T. F. Eifler, I. Ferrero, A. Ferté, B. Flaugher, P. Fosalba, J. Frieman, J. García-Bellido, E. Gaztanaga, D. W. Gerdes, T. Giannantonio, J. Gschwend, G. Gutierrez, S. R. Hinton, D. L. Hollowood, K. Honscheid, D. J. James, O. Lahav, M. Lima, M. A. G. Maia, M. March, J. L. Marshall, P. Martini, P. Melchior, F. Menanteau, R. Miquel, J. J. Mohr, R. Morgan, J. Muir, R. L. C. Ogando, A. Palmese, F. Paz-Chinchón, A. A. Plazas, M. Rodriguez-Monroy, A. Roodman, S. Samuroff, E. Sanchez, V. Scarpine, S. Serrano, M. Smith, M. Soares-Santos, E. Suchyta, M. E. C. Swanson, G. Tarle, D. Thomas, C. To, R. D. Wilkinson, R. D. Wilkinson, and DES Collaboration. Dark Energy Survey Y3 results: blending shear and redshift biases in image simulations. *MNRAS*, 509(3):3371–3394, January 2022. doi: 10.1093/mnras/stab2870.
- [122] Mahesh K. Varanasi and Behnaam Aazhang. Parametric generalized Gaussian density estimation. *Acoustical Society of America Journal*, 86(4):1404–1415, October 1989. doi: 10.1121/1.398700.
 - [123] H. G. Ellis. Ether flow through a drainhole - a particle model in general relativity. *J. Math. Phys.*, 14:104–118, 1973. doi: 10.1063/1.1666161.
 - [124] M. S. Morris and K. S. Thorne. Wormholes in space-time and their use for interstellar travel: A tool for teaching general relativity. *Am. J. Phys.*, 56:395–412, 1988. doi: 10.1119/1.15620.
 - [125] M. S. Morris, K. S. Thorne, and U. Yurtsever. Wormholes, Time Machines, and the Weak Energy Condition. *Phys. Rev. Lett.*, 61:1446–1449, 1988. doi: 10.1103/PhysRevLett.61.1446.
 - [126] Takao Kitamura, Koki Nakajima, and Hideki Asada. Demagnifying gravitational lenses toward hunting a clue of exotic matter and energy. *Phys. Rev. D*, 87(2):027501, 2013. doi: 10.1103/PhysRevD.87.027501.
 - [127] Koji Izumi, Chisaki Hagiwara, Koki Nakajima, Takao Kitamura, and Hideki Asada. Gravitational lensing shear by an exotic lens object with negative convergence or negative mass. *Phys. Rev. D*, 88:024049, 2013. doi: 10.1103/PhysRevD.88.024049.
 - [128] B. Jain and J. Khoury. Cosmological Tests of Gravity. *Ann. Phys.*, 325:1479, July 2010. doi: 10.1016/j.aop.2010.04.002.
 - [129] Timothy Clifton, Pedro G. Ferreira, Antonio Padilla, and Constantinos Skordis. Modified Gravity and Cosmology. *Phys. Rept.*, 513:1, 2012. doi: 10.1016/j.physrep.2012.01.001.
 - [130] D. H. Weinberg, M. J. Mortonson, D. J. Eisenstein, C. Hirata, A. G. Riess, and E. Rozo. Observational Probes of Cosmic Acceleration. *Phys. Rep.*, 530:87, September 2013. doi: 10.1016/j.physrep.2013.05.001.
 - [131] A. Joyce, B. Jain, J. Khoury, and M. Trodden. Beyond the cosmological standard model. *Phys. Rep.*, 568:1, March 2015. doi: 10.1016/j.physrep.2014.12.002.
 - [132] A. Joyce, L. Lombriser, and F. Schmidt. Dark Energy Versus Modified Gravity. *Annu. Rev. Nucl. Part. S.*, 66:95, October 2016. doi: 10.1146/annurev-nucl-102115-044553.
 - [133] Luca Amendola et al. Cosmology and fundamental physics with the Euclid satellite. *Living Rev. Rel.*, 21(1):2, 2018. doi: 10.1007/s41114-017-0010-3.
 - [134] L. Amendola et al. Cosmology and Fundamental Physics with the Euclid Satellite. *Living Rev. Rel.*, 16:6, September 2013. doi: 10.12942/lrr-2013-6.

- [135] Bhuvnesh Jain et al. Novel Probes of Gravity and Dark Energy. *arXiv e-prints*, art. arXiv:1309.5389, September 2013.
- [136] L. Amendola, M. Kunz, M. Motta, I. D. Saltas, and I. Sawicki. Observables and unobservables in dark energy cosmologies. *Phys. Rev. D*, 87(2):023501, January 2013. doi: 10.1103/PhysRevD.87.023501.
- [137] T. Baker, P. G. Ferreira, C. D. Leonard, and M. Motta. New Gravitational Scales in Cosmological Surveys. *Phys. Rev. D*, 90(12):124030, December 2014. doi: 10.1103/PhysRevD.90.124030.
- [138] C. D. Leonard, T. Baker, and P. G. Ferreira. Exploring degeneracies in modified gravity with weak lensing. *Phys. Rev. D*, 91(8):083504, April 2015. doi: 10.1103/PhysRevD.91.083504.
- [139] Thomas E. Collett, Lindsay J. Oldham, Russell J. Smith, Matthew W. Auger, Kyle B. Westfall, David Bacon, Robert C. Nichol, Karen L. Masters, Kazuya Koyama, and Remco van den Bosch. A precise extragalactic test of General Relativity. *Science*, 360:1342, 2018. doi: 10.1126/science.aao2469.
- [140] Jean-Philippe Uzan and Francis Bernardeau. Lensing at cosmological scales: A test of higher dimensional gravity. *Phys. Rev. D*, 64(8):083004, October 2001. doi: 10.1103/PhysRevD.64.083004.
- [141] Lloyd Knox, Yong-Seon Song, and J. Anthony Tyson. Distance-redshift and growth-redshift relations as two windows on acceleration and gravitation: Dark energy or new gravity? *Phys. Rev. D*, 74(2):023512, July 2006. doi: 10.1103/PhysRevD.74.023512.
- [142] O. Doré, M. Martig, Y. Mellier, M. Kilbinger, J. Benjamin, L. Fu, H. Hoekstra, M. Schultheis, E. Sembolini, and I. Tereno. Testing Gravity with the CFHTLS-Wide Cosmic Shear Survey and SDSS LRGs. *arXiv e-prints*, art. arXiv:0712.1599, December 2007.
- [143] Luca Amendola, Martin Kunz, and Domenico Sapone. Measuring the dark side (with weak lensing). *J. Cosmology Astropart. Phys.*, 2008(4):013, April 2008. doi: 10.1088/1475-7516/2008/04/013.
- [144] Shaun A. Thomas, Filipe B. Abdalla, and Jochen Weller. Constraining modified gravity and growth with weak lensing. *MNRAS*, 395(1):197–209, May 2009. doi: 10.1111/j.1365-2966.2009.14568.x.
- [145] Scott F. Daniel, Robert R. Caldwell, Asantha Cooray, Paolo Serra, and Alessandro Melchiorri. Multiparameter investigation of gravitational slip. *Phys. Rev. D*, 80(2):023532, July 2009. doi: 10.1103/PhysRevD.80.023532.
- [146] Rachel Bean and Matipon Tangmatitham. Current constraints on the cosmic growth history. *Phys. Rev. D*, 81(8):083534, April 2010. doi: 10.1103/PhysRevD.81.083534.
- [147] Gong-Bo Zhao, Tommaso Giannantonio, Levon Pogosian, Alessandra Silvestri, David J. Bacon, Kazuya Koyama, Robert C. Nichol, and Yong-Seon Song. Probing modifications of general relativity using current cosmological observations. *Phys. Rev. D*, 81(10):103510, May 2010. doi: 10.1103/PhysRevD.81.103510.
- [148] Scott F. Daniel and Eric V. Linder. Confronting general relativity with further cosmological data. *Phys. Rev. D*, 82(10):103523, November 2010. doi: 10.1103/PhysRevD.82.103523.
- [149] I. Tereno, E. Sembolini, and T. Schrabbach. COSMOS weak-lensing constraints on modified gravity. *A&A*, 530:A68, June 2011. doi: 10.1051/0004-6361/201016273.
- [150] J. Harnois-Déraps, D. Munshi, P. Valageas, L. van Waerbeke, P. Brax, P. Coles, and L. Rizzo. Testing modified gravity with cosmic shear. *MNRAS*, 454(3):2722–2735, December 2015. doi: 10.1093/mnras/stv2120.

- [151] Peter Schneider, Jürgen Ehlers, and Emilio E. Falco. *Gravitational Lenses*. 1992. doi: 10.1007/978-3-662-03758-4.
- [152] Barnaby Rowe. Improving PSF modelling for weak gravitational lensing using new methods in model selection. *MNRAS*, 404(1):350–366, May 2010. doi: 10.1111/j.1365-2966.2010.16277.x.
- [153] Michael Falk. On mad and comedians. *Annals of the Institute of Statistical Mathematics*, 49(4):615–644, Dec 1997. ISSN 1572-9052. doi: 10.1023/A:1003258024248. URL <https://doi.org/10.1023/A:1003258024248>.
- [154] R. H. Lupton. *Statistics in theory and practice*. Princeton University Press, 1993.
- [155] Carlos Lopez-Arenillas, Enrique Gaztanaga, and Pablo Fosalba. Phd thesis: Weak lensing analysis of an all-sky simulation. *Preprints*, March 2023. doi: 10.20944/preprints202303.0387.v1. URL <https://doi.org/10.20944/preprints202303.0387.v1>.
- [156] Aurel Schneider, Nicola Stoira, Alexandre Refregier, Andreas J. Weiss, Mischa Knabenhans, Joachim Stadel, and Romain Teyssier. Baryonic effects for weak lensing. Part I. Power spectrum and covariance matrix. *JCAP*, 04:019, 2020. doi: 10.1088/1475-7516/2020/04/019.
- [157] Xiangchong Li, Tianqing Zhang, Sunao Sugiyama, Roohi Dalal, Ryo Terasawa, Markus M. Rau, Rachel Mandelbaum, Masahiro Takada, Surhud More, Michael A. Strauss, Hironao Miyatake, Masato Shirasaki, Takashi Hamana, Masamune Oguri, Wentao Luo, Atsushi J. Nishizawa, Ryuichi Takahashi, Andrina Nicola, Ken Osato, Arun Kannawadi, Tomomi Sunayama, Robert Armstrong, James Bosch, Yutaka Komiyama, Robert H. Lupton, Nate B. Lust, Lauren A. MacArthur, Satoshi Miyazaki, Hitoshi Murayama, Takahiro Nishimichi, Yuki Okura, Paul A. Price, Philip J. Tait, Masayuki Tanaka, and Shiang-Yu Wang. Hyper Suprime-Cam Year 3 results: Cosmology from cosmic shear two-point correlation functions. *Phys. Rev. D*, 108(12):123518, December 2023. doi: 10.1103/PhysRevD.108.123518.
- [158] C Fedeli, M Bartelmann, and L Moscardini. Constraining primordial non-gaussianity with cosmological weak lensing: shear and flexion. *Journal of Cosmology and Astroparticle Physics*, 2012(10):018–018, Oct 2012. ISSN 1475-7516. doi: 10.1088/1475-7516/2012/10/018. URL <http://dx.doi.org/10.1088/1475-7516/2012/10/018>.
- [159] Oliver H. E. Philcox, Morgane J. König, Stephon Alexander, and David N. Spergel. What can galaxy shapes tell us about physics beyond the standard model? *Phys. Rev. D*, 109(6):063541, March 2024. doi: 10.1103/PhysRevD.109.063541.

Appendix A: Deriving the modified Sérsic profile

The canonical Sérsic profile is given by [76]

$$I = I_e \exp \left\{ -b_n \left[\left(\frac{\theta}{\theta_e} \right)^{1/n_s} - 1 \right] \right\} \quad (\text{A.1})$$

where θ_e is the half-light radius, and I_e is the intensity at that radius, and where b_n is approximately $2n - 1/3$. It can be shown that b_n satisfies $\gamma(2n_s; b_n) = \frac{1}{2}\Gamma(2n_s)$, where Γ and γ are the Gamma function and lower incomplete gamma function, respectively. If we define $x \equiv \theta/\theta_e$, then

$$I = I_e \left[e^{-b_n x^{1/n_s}} e^{-b_n} \right] = I_e e^{b_n} e^{-b_n x^{1/n_s}}$$

We define $I_0 \equiv I_e e^{b_n}$ and note that we can write $b_n x^{1/n_s} = (b_n x)^{1/n_s} = (\theta/\theta_e b^{-n_s})$. We then define $\theta_s \equiv \theta_b^{-n_s}$. Thus

$$I = I_0 \exp \left[- \left(\frac{\theta}{\theta_s} \right)^{1/n_s} \right] \quad (\text{A.2})$$

Appendix B: Deriving the Quadrupole-Sérsic Relation

We start by quantifying the *size* of a galaxy image by $a \equiv \sqrt{|Q_{11} + Q_{22}|}$, as given by Eq. (2.14).

Consider the case of a circularly symmetric galaxy, such that

$$a_0^2 = Q_{11}^{(0)} + Q_{22}^{(0)} \iff Q_{11}^{(0)} = Q_{22}^{(0)} = \frac{1}{2}a_0^2 \quad (\text{B.1})$$

where a_0 is the size of a circularly symmetric galaxy, and the superscript (0) on the image moments denotes the assumption of circular symmetry in the light profile of the galaxy. Additionally,

$$\theta = \sqrt{(\theta_1 - \theta_0^1)^2_{\text{circ}} + (\theta_2 - \theta_0^2)^2_{\text{circ}}} \iff (\theta_1 - \theta_0^1)^2_{\text{circ}} = (\theta_2 - \theta_0^2)^2_{\text{circ}} = \frac{1}{2}\theta^2$$

where the subscript “circ” denotes the case of circular symmetry. Then, using Eq. (2.8), we can write

$$\frac{1}{2}a_0^2 = Q_{11}^{(0)} = \frac{\int d^2\theta I(\theta)(\theta_1 - \theta_0^1)^2_{\text{circ}}}{\int d^2\theta I(\theta)} = \frac{1}{2} \frac{\int d^2\theta I(\theta)\theta^2}{\int d^2\theta I(\theta)}$$

We will consider the case of no lensing here, such that the lens and source coordinates are equivalent. Under this assumption, along with the assumption of a circularly symmetric galaxy ($q = 1$), Eq. (2.3) is simply Eq. (2.3) can be written as

$$I(\theta) = I_0 \exp \left[- \left(\frac{\theta}{\theta_s} \right)^{1/n_s} \right]$$

where Eq. (2.4) and (2.5) reduce to $\theta = \sqrt{(\theta_1 - \theta_0^1)^2_{\text{circ}} + (\theta_2 - \theta_0^2)^2_{\text{circ}}}$. Then,

$$a_0^2 = \frac{\int d^2\theta I_0 \exp \left[- \left(\frac{\theta}{\theta_s} \right)^{1/n_s} \right] \theta^2}{\int d^2\theta I_0 \exp \left[- \left(\frac{\theta}{\theta_s} \right)^{1/n_s} \right]}$$

As this is circularly symmetric, we transform to polar coordinates such that $\int d^2\theta = \int_0^\infty d\theta \theta \int_0^{2\pi} d\phi =$

$$2\pi \int_0^\infty d\theta:$$

$$a_0^2 = \frac{2\pi \int_0^\infty d\theta \theta^3 I_0 \exp \left[-\left(\frac{\theta}{\theta_s} \right)^{1/n_s} \right]}{2\pi \int_0^\infty d\theta \theta I_0 \exp \left[-\left(\frac{\theta}{\theta_s} \right)^{1/n_s} \right]} = \frac{\int_0^\infty d\theta \theta^3 \exp \left[-\left(\frac{\theta}{\theta_s} \right)^{1/n_s} \right]}{\int_0^\infty d\theta \theta \exp \left[-\left(\frac{\theta}{\theta_s} \right)^{1/n_s} \right]}$$

Let us make use of the change of variables $u \equiv \theta/\theta_s \implies d\theta = du\theta_s$. Note that the bounds of integration remain the same. Then

$$a_0^2 = \frac{\int_0^\infty du \theta_s(u\theta_s)^3 \exp \left[-u^{1/n_s} \right]}{\int_0^\infty du \theta_s(u\theta_s) \exp \left[-u^{1/n_s} \right]} = \theta_s^2 \frac{\int_0^\infty du u^3 \exp \left[-u^{1/n_s} \right]}{\int_0^\infty du u \exp \left[-u^{1/n_s} \right]}$$

Let us make use of another change of variables: $v \equiv u^{1/n_s} \implies u = v^{n_s} \implies du = n_s v^{n_s-1} dv$.

Again, the bounds of integration remain unchanged. Then

$$a_0^2 = \theta_s^2 \frac{\int_0^\infty dv (n_s v^{n_s-1})(v^{n_s})^3 e^{-v}}{\int_0^\infty dv (n_s v^{n_s-1})(v^{n_s}) e^{-v}} = \theta_s^2 \frac{\int_0^\infty dv v^{4n_s-1} e^{-v}}{\int_0^\infty dv v^{2n_s-1} e^{-v}}$$

The Gamma function is defined as

$$\Gamma(t) \equiv \int_0^\infty dx x^{t-1} e^{-x}. \quad (\text{B.2})$$

Therefore,

$$a_0^2 = \theta_s^2 \frac{\Gamma(4n_s)}{\Gamma(2n_s)} \quad (\text{B.3})$$

We hence have an analytic relationship between θ_s , n_s , q , and quadrupole moments. This is, again, for a circular galaxy. We would like to extend this analytic function to that of an elliptical galaxy ($q \neq 1$). Relaxing the assumption of circular symmetry, but still working under the assumption of no lensing, Eq. (2.4) and (2.5) tell us that

$$\frac{(\theta_1 - \theta_0^1)^2_{\text{non-circ}}}{q^2} = (\theta_1 - \theta_0^1)^2_{\text{circ}}; \quad (\theta_2 - \theta_0^2)^2_{\text{non-circ}} = (\theta_2 - \theta_0^2)^2_{\text{circ}}$$

Revisiting the image moments for the case of a non-circular galaxy, we find that, using Eq. (2.8)

$$Q_{11} = \frac{\int d^2\theta I(\theta)(\theta_1 - \theta_0^1)^2_{\text{non-circ}}}{\int d^2\theta I(\theta)} = \frac{\int d^2\theta I(\theta)q^2(\theta_1 - \theta_0^1)^2_{\text{circ}}}{\int d^2\theta I(\theta)} = q^2 Q_{11}^{(0)} = q^2 \frac{1}{2} a_0^2; \quad Q_{22} = Q_{22}^{(0)} = \frac{1}{2} a_0^2$$

Eq. (2.14) therefore becomes

$$a^2 = Q_{11} + Q_{22} = \frac{1 + q^2}{2} a_0^2$$

Finally, Eq. (B.3) becomes

$$\theta_s = a \sqrt{\frac{2}{1 + q^2} \frac{\Gamma(2n_s)}{\Gamma(4n_s)}} = \sqrt{\frac{2(|Q_{11} + Q_{22}|)\Gamma(2n_s)}{(1 + q^2)\Gamma(4n_s)}}. \quad (\text{B.4})$$

Appendix C: Deriving the Theoretical Two-Point Correlation Functions

C.1 Shear-Shear

It is well known that one can define the convergence power spectrum in the following way under the flat-sky approximation: [4]

$$\langle \tilde{\kappa}(\boldsymbol{\ell}) \tilde{\kappa}^*(\boldsymbol{\ell}') \rangle = (2\pi)^2 \delta_D(\boldsymbol{\ell} - \boldsymbol{\ell}') \mathcal{P}_\kappa(\ell), \quad (\text{C.1})$$

where, due to statistical homogeneity and isotropy, the power spectrum is a function of the modulus of the two-dimensional multipole vector, $\boldsymbol{\ell}$ (the Fourier-conjugate of $\boldsymbol{\theta}$, in the case of flat-sky approximation). Let us consider the case of cosmic shear. In Fourier space, the relationship between shear and convergence is given by [4]

$$\tilde{\gamma}(\boldsymbol{\ell}) = \frac{\ell_1^2 - \ell_2^2 + 2i\ell_1\ell_2}{\ell^2} \tilde{\kappa}(\boldsymbol{\ell}) = e^{2i\beta} \tilde{\kappa}(\boldsymbol{\ell}) \quad (\text{C.2})$$

where β is the polar angle of $\boldsymbol{\ell}$, such that $\boldsymbol{\ell} = (\ell_1, \ell_2) = (\ell \cos \beta, \ell \sin \beta)$. We notice that

$$\langle \tilde{\gamma}(\boldsymbol{\ell}) \tilde{\gamma}^*(\boldsymbol{\ell}') \rangle = e^{2i(\beta-\beta')} \langle \tilde{\kappa}(\boldsymbol{\ell}) \tilde{\kappa}^*(\boldsymbol{\ell}') \rangle = e^{2i(\beta-\beta')} (2\pi)^2 \delta_D(\boldsymbol{\ell} - \boldsymbol{\ell}') \mathcal{P}_\kappa(\ell). \quad (\text{C.3})$$

We will now take the Fourier transform of this. By Eq. (3.12), the left-hand side (LHS) of this expression is simply $\xi_+^{\gamma\gamma}(\theta)$. Thus, we have

$$\xi_+^{\gamma\gamma}(\theta) = \int \frac{d^2\boldsymbol{\ell}}{(2\pi)^2} e^{-i\boldsymbol{\ell}\cdot\boldsymbol{\theta}} \int \frac{d^2\boldsymbol{\ell}'}{(2\pi)^2} \langle \tilde{\gamma}(\boldsymbol{\ell}) \tilde{\gamma}^*(\boldsymbol{\ell}') \rangle = \int \frac{d^2\boldsymbol{\ell}}{(2\pi)^2} e^{-i\boldsymbol{\ell}\cdot\boldsymbol{\theta}} \int \frac{d^2\boldsymbol{\ell}'}{(2\pi)^2} e^{2i(\beta-\beta')} (2\pi)^2 \delta_D(\boldsymbol{\ell} - \boldsymbol{\ell}') \mathcal{P}_\kappa(\ell) \quad (\text{C.4})$$

Upon integration about $\boldsymbol{\ell}'$, the delta function picks out $\boldsymbol{\ell}' = \boldsymbol{\ell}$ and $\beta' = \beta$, leaving us with

$$\xi_+^{\gamma\gamma}(\theta) = \int \frac{d^2\boldsymbol{\ell}}{(2\pi)^2} e^{-i\boldsymbol{\ell}\cdot\boldsymbol{\theta}} P_\kappa(\ell) = \frac{1}{(2\pi)^2} \int_0^\infty d\ell \ell P_\kappa(\ell) \int_0^{2\pi} d\beta e^{-i\ell\theta \cos \beta} \quad (\text{C.5})$$

The Bessel integral can be expressed as

$$J_n(x) = \frac{1}{\pi} \int_0^\pi d\tau \cos(n\pi - x \sin \tau) = \frac{1}{2\pi} \int_{-\pi}^\pi d\tau e^{i(n(-\frac{\pi}{2} + \tau) + x \cos \tau)} = \frac{i^n}{2\pi} \int_0^{2\pi} d\tau e^{-ix \cos \tau} e^{in\tau} \quad (\text{C.6})$$

where the second expression is obtained from the first via Euler's formula, and the third expression is obtained from the second via the substitution of variables $\tau \rightarrow \tau + \pi$ and the relation $(e^{-i\pi/2})^n = i^n$.

We therefore obtain the useful result

$$\int_0^{2\pi} d\beta e^{-i\ell\theta \cos \beta} i^n e^{in\beta} = 2\pi J_n(\ell\theta) \quad (\text{C.7})$$

Using this expression, Eq. (C.5) becomes

$$\xi_+^{\gamma\gamma}(\theta) = \int_0^\infty \frac{d\ell \ell}{2\pi} P_\kappa(\ell) J_0(\ell\theta). \quad (\text{C.8})$$

The next quantity of interest is $\langle \tilde{\gamma}(\boldsymbol{\ell}) \tilde{\gamma}(\boldsymbol{\ell}') \rangle$. First, we note that

$$\langle \tilde{\kappa}(\boldsymbol{\ell}) \tilde{\kappa}(\boldsymbol{\ell}') \rangle = (2\pi)^2 \delta_D(\boldsymbol{\ell} + \boldsymbol{\ell}') \mathcal{P}_\kappa(\ell). \quad (\text{C.9})$$

Upon integration, the delta function will pick out $\boldsymbol{\ell}' = -\boldsymbol{\ell}$, necessarily implying that $\tilde{\kappa}(-\boldsymbol{\ell}) = \tilde{\kappa}^*(\boldsymbol{\ell})$.

Notice that the shear in Fourier space remains unchanged under the transformation

$$\boldsymbol{\ell} \rightarrow -\boldsymbol{\ell} \implies (\ell_1, \ell_2) \rightarrow -(\ell_1, \ell_2) = -(\ell \cos \beta, \ell \sin \beta). \quad (\text{C.10})$$

and hence $\tilde{\gamma}(-\boldsymbol{\ell}) = \tilde{\gamma}(\boldsymbol{\ell})$. Understanding that the delta function will be integrated over, we simply note that

$$\langle \tilde{\gamma}(\boldsymbol{\ell}) \tilde{\gamma}(-\boldsymbol{\ell}) \rangle = e^{4i\beta} (2\pi)^2 \mathcal{P}_\kappa(\ell). \quad (\text{C.11})$$

Upon Fourier transformation, making use of Eq. (3.13), this expression yields

$$\xi_{-}^{\gamma\gamma}(\theta) = \frac{1}{(2\pi)^2} \int_0^\infty d\ell \ell P_\kappa(\ell) \int_0^{2\pi} d\beta e^{-i\ell\theta \cos \beta} e^{4i\beta} = \int_0^\infty \frac{d\ell \ell}{2\pi} P_\kappa(\ell) J_4(\ell\theta). \quad (\text{C.12})$$

C.2 Flexion-Flexion

In Fourier space, the relationship between \mathcal{F} -flexion and convergence is given by [43]

$$\tilde{\mathcal{F}}(\boldsymbol{\ell}) = (i\ell_1 - \ell_2)\tilde{\kappa}(\boldsymbol{\ell}) = i\ell e^{i\beta}\tilde{\kappa}(\boldsymbol{\ell}). \quad (\text{C.13})$$

Following the same lines as for cosmic shear, we can obtain a similar expression for \mathcal{F} -flexion:

$$\langle \tilde{\mathcal{F}}(\boldsymbol{\ell}) \tilde{\mathcal{F}}^*(\boldsymbol{\ell}') \rangle = \ell\ell' \langle \tilde{\kappa}(\boldsymbol{\ell}) \tilde{\kappa}^*(\boldsymbol{\ell}') \rangle = (2\pi)^2 \delta_D(\boldsymbol{\ell} - \boldsymbol{\ell}') \ell\ell' \mathcal{P}_\kappa(\ell) \quad (\text{C.14})$$

Again, upon integration about $\boldsymbol{\ell}'$, the delta function picks out $\boldsymbol{\ell}' = \boldsymbol{\ell}$ and $\beta' = \beta$. Noting this, we can simply write

$$\langle \tilde{\mathcal{F}}(\boldsymbol{\ell}) \tilde{\mathcal{F}}^*(\boldsymbol{\ell}) \rangle = (2\pi)^2 \mathcal{P}_{\mathcal{F}}(\ell) \quad (\text{C.15})$$

where we have used Eq. (3.4). Next, we take a Fourier transform of this expression, which leaves us with

$$\xi_{+}^{\mathcal{F}\mathcal{F}}(\theta) = \frac{1}{(2\pi)^2} \int_0^\infty d\ell \ell \mathcal{P}_{\mathcal{F}}(\ell) \int_0^{2\pi} d\beta e^{-i\ell\theta \cos \beta} = \int_0^\infty \frac{d\ell \ell}{2\pi} \mathcal{P}_{\mathcal{F}}(\ell) J_0(\ell\theta). \quad (\text{C.16})$$

Unlike shear, \mathcal{F} -flexion changes sign in Fourier space under the transformation $\boldsymbol{\ell} \rightarrow -\boldsymbol{\ell}$ (see Eq. (C.13)), such that $\tilde{\mathcal{F}}(-\boldsymbol{\ell}) = -\tilde{\mathcal{F}}(\boldsymbol{\ell})$. Hence, for the quantity $\langle \tilde{\mathcal{F}}(\boldsymbol{\ell}) \tilde{\mathcal{F}}(-\boldsymbol{\ell}) \rangle$, we have

$$\langle \tilde{\mathcal{F}}(\boldsymbol{\ell}) \tilde{\mathcal{F}}(-\boldsymbol{\ell}) \rangle = (2\pi)^2 \ell^2 e^{2i\beta} \mathcal{P}_\kappa(\ell) = (2\pi)^2 e^{2i\beta} \mathcal{P}_{\mathcal{F}}(\ell). \quad (\text{C.17})$$

Taking a Fourier transform of this expression leaves us with

$$\xi_{-}^{\mathcal{F}\mathcal{F}}(\theta) = \frac{1}{(2\pi)^2} \int_0^\infty d\ell \ell \mathcal{P}_{\mathcal{F}}(\ell) \int_0^{2\pi} d\beta e^{-i\ell\theta \cos \beta} e^{2i\beta} = - \int_0^\infty \frac{d\ell \ell}{2\pi} \mathcal{P}_{\mathcal{F}}(\ell) J_2(\ell\theta). \quad (\text{C.18})$$

In Fourier space, the relationship between \mathcal{G} -flexion and convergence is given by

$$\tilde{\mathcal{G}}(\ell) = \frac{i\ell_1^3 - 3i\ell_1\ell_2^2 - 3\ell_1^2\ell_2 + \ell_2^3}{\ell^2} \tilde{\kappa}(\ell) = i\ell e^{3i\beta} \tilde{\kappa}(\ell). \quad (\text{C.19})$$

From here, it is straightforward to derive expressions for $\xi_{\pm}^{\mathcal{G}\mathcal{G}}(\theta)$. However, there is an additional complication for \mathcal{F} - \mathcal{G} cross-correlations. If we analyze the expression $\langle \tilde{\mathcal{F}}(\ell)\tilde{\mathcal{G}}^*(\ell') \rangle$, its Fourier transform is not simply given by Eq. (3.12). Since \mathcal{G}'_1 and \mathcal{G}'_2 have a sign difference relative to the definitions of \mathcal{F}'_1 and \mathcal{F}'_2 (see Eqs. (3.10) and (3.11)), the Fourier transform of $\langle \tilde{\mathcal{F}}(\ell)\tilde{\mathcal{G}}^*(\ell') \rangle$ is actually $-\xi_{+}^{\mathcal{F}\rightarrow\mathcal{G}}(\theta)$. We have:

$$\langle \tilde{\mathcal{F}}(\ell)\tilde{\mathcal{G}}^*(\ell') \rangle = \ell\ell' e^{i(\beta-3\beta')} \langle \tilde{\kappa}(\ell)\tilde{\kappa}^*(\ell') \rangle = (2\pi)^2 \delta_D(\ell - \ell') \ell\ell' e^{i(\beta-3\beta')} \mathcal{P}_{\kappa}(\ell). \quad (\text{C.20})$$

Again, upon integration about ℓ' , the delta function picks out $\ell' = \ell$ and $\beta' = \beta$. Noting this, we can simply write

$$\langle \tilde{\mathcal{F}}(\ell)\tilde{\mathcal{G}}^*(\ell) \rangle = (2\pi)^2 \ell^2 e^{-2i\beta} \mathcal{P}_{\mathcal{F}}(\ell). \quad (\text{C.21})$$

As we stated earlier, the Fourier transform of the LHS is the negative of Eq. (3.12):

$$-\xi_{+}^{\mathcal{F}\rightarrow\mathcal{G}}(\theta) = \frac{1}{(2\pi)^2} \int_0^\infty d\ell \ell \mathcal{P}_{\mathcal{F}}(\ell) \int_0^{2\pi} d\beta e^{-i\ell\theta \cos \beta} e^{-2i\beta} = - \int_0^\infty \frac{d\ell \ell}{2\pi} \mathcal{P}_{\mathcal{F}}(\ell) J_2(\ell\theta) \quad (\text{C.22})$$

and therefore

$$\xi_{+}^{\mathcal{F}\rightarrow\mathcal{G}}(\theta) = \int_0^\infty \frac{d\ell \ell}{2\pi} \mathcal{P}_{\mathcal{F}}(\ell) J_2(\ell\theta). \quad (\text{C.23})$$

\mathcal{G} -flexion changes sign in Fourier space under the transformation $\ell \rightarrow -\ell$ (see Eq. (C.19)), such that $\tilde{\mathcal{G}}(-\ell) = -\tilde{\mathcal{G}}(\ell)$. Hence, for the quantity $\langle \tilde{\mathcal{F}}(\ell)\tilde{\mathcal{G}}(-\ell) \rangle$, we have

$$\langle \tilde{\mathcal{F}}(\ell)\tilde{\mathcal{G}}(-\ell) \rangle = (2\pi)^2 \ell^2 e^{4i\beta} \mathcal{P}_{\kappa}(\ell) = (2\pi)^2 e^{4i\beta} \mathcal{P}_{\mathcal{F}}(\ell). \quad (\text{C.24})$$

Taking a Fourier transform of this expression leaves us with

$$-\xi_-^{\mathcal{F} \rightarrow \mathcal{G}}(\theta) = \frac{1}{(2\pi)^2} \int_0^\infty d\ell \ell \mathcal{P}_{\mathcal{F}}(\ell) \int_0^{2\pi} d\beta e^{-i\ell\theta \cos \beta} e^{4i\beta} = \int_0^\infty \frac{d\ell \ell}{2\pi} \mathcal{P}_{\mathcal{F}}(\ell) J_4(\ell\theta) \quad (\text{C.25})$$

and therefore

$$\xi_-^{\mathcal{F} \rightarrow \mathcal{G}}(\theta) = - \int_0^\infty \frac{d\ell \ell}{2\pi} \mathcal{P}_{\mathcal{F}}(\ell) J_4(\ell\theta). \quad (\text{C.26})$$

One can also compute $\langle \tilde{\mathcal{G}}(\boldsymbol{\ell}) \tilde{\mathcal{F}}^*(\boldsymbol{\ell}) \rangle$ and $\langle \tilde{\mathcal{G}}(\boldsymbol{\ell}) \tilde{\mathcal{F}}(-\boldsymbol{\ell}) \rangle$, which leads to the result $\xi_{\pm}^{\mathcal{G} \rightarrow \mathcal{F}}(\theta) = \xi_{\pm}^{\mathcal{F} \rightarrow \mathcal{G}}(\theta)$.

C.3 Shear-Flexion

Let us consider the correlation $\gamma \rightarrow \mathcal{F}$. First,

$$\langle \tilde{\gamma}(\boldsymbol{\ell}) \tilde{\mathcal{F}}^*(\boldsymbol{\ell}') \rangle = -i\ell' e^{2i\beta - i\beta'} \langle \tilde{\kappa}(\boldsymbol{\ell}) \tilde{\kappa}^*(\boldsymbol{\ell}') \rangle = -(2\pi)^2 \delta_D(\boldsymbol{\ell} - \boldsymbol{\ell}') i\ell' e^{i(2\beta - \beta')} \mathcal{P}_\kappa(\ell) \quad (\text{C.27})$$

Again, upon integration about $\boldsymbol{\ell}'$, the delta function picks out $\boldsymbol{\ell}' = \boldsymbol{\ell}$ and $\beta' = \beta$. Noting this, we can simply write

$$\langle \tilde{\gamma}(\boldsymbol{\ell}) \tilde{\mathcal{F}}^*(\boldsymbol{\ell}) \rangle = -(2\pi)^2 i e^{i\beta} \mathcal{P}_{\kappa\mathcal{F}}(\ell) \quad (\text{C.28})$$

where we have made use of Eq. (3.6). Taking the Fourier transform of this yields

$$\xi_+^{\gamma \rightarrow \mathcal{F}}(\theta) = -\frac{1}{(2\pi)^2} \int_0^\infty d\ell \ell \mathcal{P}_{\kappa\mathcal{F}}(\ell) \int_0^{2\pi} d\beta e^{-i\ell\theta \cos \beta} i e^{i\beta} = - \int_0^\infty \frac{d\ell \ell}{2\pi} \mathcal{P}_{\kappa\mathcal{F}}(\ell) J_1(\ell\theta). \quad (\text{C.29})$$

Next, we consider $\langle \tilde{\gamma}(\boldsymbol{\ell}) \tilde{\mathcal{F}}(\boldsymbol{\ell}') \rangle$. After dropping the delta function, we have

$$\langle \tilde{\gamma}(\boldsymbol{\ell}) \tilde{\mathcal{F}}(-\boldsymbol{\ell}) \rangle = (2\pi)^2 i e^{3i\beta} \mathcal{P}_{\kappa\mathcal{F}}(\ell) \quad (\text{C.30})$$

The Fourier transform gives us:

$$\xi_-^{\gamma \rightarrow \mathcal{F}}(\theta) = \frac{1}{(2\pi)^2} \int_0^\infty d\ell \ell \mathcal{P}_{\kappa\mathcal{F}}(\ell) \int_0^{2\pi} d\beta e^{-i\ell\theta \cos \beta} i e^{3i\beta} = \int_0^\infty \frac{d\ell \ell}{2\pi} \mathcal{P}_{\kappa\mathcal{F}}(\ell) J_3(\ell\theta). \quad (\text{C.31})$$

Finally, one can compute $\langle \tilde{\mathcal{F}}(\ell) \tilde{\gamma}^*(\ell) \rangle$ and $\langle \tilde{\mathcal{F}}(\ell) \tilde{\gamma}(-\ell) \rangle$, which leads to the result $\xi_{\pm}^{\mathcal{F} \rightarrow \gamma}(\theta) = -\xi_{\pm}^{\gamma \rightarrow \mathcal{F}}(\theta)$. Similarly, one can compute the expressions for the \mathcal{G} - γ correlations.

Appendix D: Point-spread function leakage into the cosmic flexion two-point correlation functions

Let a_i^o be some observed spin field, with spin s_a , as in the formalism of Chapter 3, of a galaxy at sky-position ϑ_i , which is related to the intrinsic field a_i^s and the lensing field $a(\vartheta_i)$ by $a_i^o = a_i^s + a(\vartheta_i)$. Similarly, we consider the spin field of another galaxy at position ϑ_j , $b_j^o = b_j^s + b(\vartheta_j)$, such that θ_{ij} is the separation vector between them and φ_{ij} the polar angle. As in Chapter 3, we work in terms of the pair-wise rotated coordinate system, rotated such that the line connecting every galaxy pair (i, j) is taken to be the x -axis, given by Eq. (3.7).

Imagine that for the measurement of each spin-field, there is some point-spread function (PSF) leakage associated with that measurement, δa , such that in the rotated coordinate system,

$$\tilde{a}_{i\alpha}^{o'} = a_{i\alpha}^{o'} + \delta a_{i\alpha}', \quad (\text{D.1})$$

where $\alpha \in \{1, 2\}$. PSF leakage of this kind is described in Sec. 4.2.3. As an illustrative example of PSF leakage in this context, imagine the case of measuring the ellipticity of a galaxy. In addition to the galaxy having some ellipticity (intrinsic ellipticity plus shear), so too does the PSF itself. If one can perfectly account for the ellipticity of the PSF, then upon PSF deconvolution, the measured ellipticity is simply the ellipticity of the galaxy. If the ellipticity is not perfectly accounted for, then some of the ellipticity of the PSF “leaks” into the measured ellipticity of the galaxy. This is similarly the case for flexion.

Let us propagate this PSF leakage into the estimator of the two-point correlation function

(2PCF), $\hat{\xi}_{\pm}^{ab}(\theta)$, given by Eq. (3.36). We will simply analyze the spin-field terms.

$$\begin{aligned}
 \langle \tilde{a}'_{i1} \tilde{b}'_{i1} \rangle \pm \langle \tilde{a}'_{i2} \tilde{b}'_{i2} \rangle &= \langle (a'^o_{i1} + \delta a'_{i1})(b'^o_{j1} + \delta b'_{j1}) \rangle \pm \langle (a'^o_{i2} + \delta a'_{i2})(b'^o_{j2} + \delta b'_{j2}) \rangle \\
 &= (\langle a'^o_{i1} b'^o_{j1} \rangle \pm \langle a'^o_{i2} b'^o_{j2} \rangle) \\
 &\quad + (\langle \delta a'_{i1} b'^o_{j1} \rangle \pm \langle \delta a'_{i2} b'^o_{j2} \rangle + \langle a'^o_{i1} \delta b'_{j1} \rangle \pm \langle a'^o_{i2} \delta b'_{j2} \rangle) \\
 &\quad + (\langle \delta a'_{i1} \delta b'_{j1} \rangle \pm \langle \delta a'_{i2} \delta b'_{j2} \rangle).
 \end{aligned} \tag{D.2}$$

The first term, containing correlations of the true spin fields without PSF leakage, simply belongs to the original 2PCF estimator. I assume that the second term, containing correlations of the form $\langle \delta a_{i\alpha} b_{j\alpha} \rangle$, i.e. cross-correlations between the PSF leakage and the true spin fields of the galaxies, are small. I focus on the final term: the correlations of the PSF leakage. We can work in terms of the unrotated coordinate system – the world coordinate system (WCS) – by the transformation given in Eq. (3.47). We therefore have

$$\begin{aligned}
 \zeta_{\pm}^{\delta a \delta b} &\equiv \langle \delta a'_{i1} \delta b'_{j1} \rangle \pm \langle \delta a'_{i2} \delta b'_{j2} \rangle \\
 &= \langle \delta a_{i1} \delta b_{j1} \rangle \cos(s_a \mp s_b) \varphi_{ij} \pm \langle \delta a_{i2} \delta b_{j2} \rangle \cos(s_a \mp s_b) \varphi_{ij} \\
 &\quad + \langle \delta a_{i2} \delta b_{j1} \rangle \sin(s_a \mp s_b) \varphi_{ij} \mp \langle \delta a_{i1} \delta b_{j2} \rangle \sin(s_a \mp s_b) \varphi_{ij}
 \end{aligned} \tag{D.3}$$

Eq. (D.3) quantifies the amount of PSF leakage propagated into the 2PCFs. The expectation is that PSF leakage is correlated in the WCS frame, not the rotated frame, as the leakage is a function of the PSF modeling in the WCS as well as a function of various effects across the survey footprint. We see for the special case $s_a = s_b$, the “plus” combination becomes

$$\zeta_+^{\delta a \delta a} = \langle \delta a_{i1} \delta a_{j1} \rangle + \langle \delta a_{i2} \delta a_{j2} \rangle \tag{D.4}$$

Therefore, for the 2PCFs $\xi_+^{\gamma\gamma}$, $\xi_+^{\mathcal{FF}}$, and $\xi_+^{\mathcal{GG}}$, any PSF leakage correlations of the form $\langle \delta a_{i\alpha} \delta b_{j\alpha} \rangle$ in the WCS frame are explicitly added to the 2PCFs which are calculated in the rotated frame.

As for all other 2PCFs, all PSF leakage terms have an explicit dependence on the rotated coor-

dinate system, and are therefore expected to be nonzero only if we expect PSF leakage correlations to appear at the pair-wise level in the rotated frame. It is interesting to look at the same terms that appear in the “cross” or EB-mode correlations. For example, following the same analysis as for the 2PCF EE-mode signals above, we find that

$$\begin{aligned}\zeta_{\times 1}^{\delta a \delta b} = & -\langle \delta a_{i1} \delta b_{j1} \rangle \cos s_a \varphi_{ij} \sin s_b \varphi_{ij} + \langle \delta a_{i2} \delta b_{j2} \rangle \sin s_a \varphi_{ij} \cos s_b \varphi_{ij} \\ & - \langle \delta a_{i2} \delta b_{j1} \rangle \sin s_a \varphi_{ij} \sin s_b \varphi_{ij} + \langle \delta a_{i1} \delta b_{j2} \rangle \cos s_a \varphi_{ij} \cos s_b \varphi_{ij}. \end{aligned} \quad (\text{D.5})$$

This is to say that the EE-mode PSF leakage correlations that do not include the special case of the $s_a = s_b$ “plus” combination have similar terms to the EB-mode PSF leakage correlations. Therefore, if those EE-modes are contaminated by PSF leakage, we might expect to see non-zero EB-modes as indicative of that.

Vita

EVAN J. ARENA

RESEARCH INTERESTS

Theoretical astrophysics and cosmology, including general relativity, gravitational lensing, modified gravity, large-scale structure, 21 cm cosmology, dark energy, inflation, dark matter, radio astronomy, and gravitational waves.

EDUCATION

Drexel University

Ph.D. in Physics June 2024

Thesis: “Flexion in gravitation and cosmology”

Advisor: David M. Goldberg, Ph.D., Co-advisor: David. J. Bacon, Ph.D.

M.S. in Physics June 2020

Stony Brook University

B.S. in Physics, second major: Astronomy/Planetary Sciences May 2017

Cum Laude

Departmental Honors in Physics

POSITIONS HELD

Bryn Mawr College

Start Date: 1 August 2024

Lecturer of Physics and Lab Coordinator (title at start of appointment)

Department of Physics

Drexel University

2018 – 2024

Doctoral Research Fellow, Doctoral Teaching Fellow, And CoAS Dean’s Fellow

Department of Physics

Stony Brook University and Brookhaven National Laboratory 2015 – 2019

Research Assistant

SBU Department of Physics & Astronomy and BNL Department of Physics

Brookhaven National Laboratory

2012 – 2013

Intern

Department of Physics

FUNDED GRANTS

National Science Foundation (NSF) Grant №2306989 “Cosmic Flexion” 2023 – 2026

Funded Graduate Student

NSF organization: Division of Astronomical Sciences

NSF program: Extragalactic Astronomy & Cosmology

Award amount: \$359,436.00

Contribution: Wrote significant portion of proposal.

AWARDS AND HONORS

Graduate College Continuing Excellence in Teaching Assistance Award, Drexel University 2023

Graduate College Continuing Excellence in Teaching Assistance Award, Drexel University 2022

Graduate College Continuing Excellence in Teaching Assistance Award, Drexel University 2021

Graduate College Teaching Assistant Excellence Award, Drexel University 2020

Sigma Xi Scientific Research Honor Society Member, Drexel University 2019

College of Arts and Sciences (CoAS) Dean’s Fellowship, Drexel University 2018

Sigma Pi Sigma National Physics Honor Society Member, Stony Brook University 2017

Presidential Scholarship, Stony Brook University 2013

RESEARCH HISTORY

2018 – Present Developed a novel method for measuring the second-order weak gravitational lensing effect known as flexion; Created a full theoretical formalism for “cosmic flexion” – a family of cosmological weak lensing signals originating from the large-scale structure of the universe; Discovered previously unknown cosmological weak lensing signals and posited the existence of non-commutativity

in weak lensing; Measurement of flexion in the Dark Energy Survey, including building the largest flexion catalogue to date as well as making the first ever detection of cosmic flexion; Discovered unique weak lensing signatures for negative mass compact objects and exotic objects such as the Ellis wormhole.

2015 – 2019	Low redshift 21 cm intensity mapping
	Cosmological parameter and modified gravity forecasts for a general 21 cm cosmology experiment, member of the DOE Cosmic Visions Dark Energy 21 cm Working Group, and design and construction of the radio telescope used for the 21 cm Baryon Mapping eXperiment at Brookhaven National Laboratory.
2013	Gravitational waves
	New method for the indirect detection of gravitational waves.
2012	Modified Newtonian Dynamics
	Investigated the plausibility of Modified Newtonian Dynamics on a local scale based on rotation curves of the Milky Way.

REFEREED PUBLICATIONS

4. **Arena, E. J.**, Goldberg, D. M., Bacon, D. J., and the Dark Energy Survey Collaboration, “*Evidence for cosmic flexion in the Dark Energy Survey Year 3 data,*” in preparation.
3. **Arena, E. J.**, “*Weak gravitational flexion in various spacetimes: Exotic lenses and modified gravity,*” Phys.Rev.D **106**, 064019 (2022) [[arXiv:2207.07784](#)]
2. **Arena, E. J.**, Goldberg, D. M., and Bacon, D. J., “*Cosmic flexion,*” Phys.Rev.D **105**, 123521 (2022) [[arXiv:2203.12036](#)]
1. Fabritius, J. M., **Arena, E. J.**, and Goldberg, D. M. “*Shape, color, and distance in weak gravitational flexion,*” Mon.Not.Roy.Astron.Soc. **501**, 4103 (2021) [[arXiv:2006.03506](#)]

CONFERENCE PROCEEDINGS, SCIENCE BOOKS, WHITE PAPERS

3. Timbie, P. et al., including **Arena, E. J.**, “*Research and Development for HI Intensity Mapping,*” ArXiv e-prints (2019) [[arXiv:1907.13090](#)]

2. Slosar, A. et al., including **Arena, E. J.**, “*Packed Ultra-wideband Mapping Array (PUMA): A Radio Telescope for Cosmology and Transients,*”, Bull.Am.Astron.Soc. **51**, 53 (2019) [[arXiv:1907.12559](#)]
1. Cosmic Visions 21 cm Collaboration, including **Arena, E. J.**, “*Inflation and Early Dark Energy with a Stage II Hydrogen Intensity Mapping experiment,*” ArXiv e-prints (2018) [[arXiv:1810.09572](#)]

CONFERENCES AND TALKS

Invited Talks

2. Astro Lunch Seminar at the University of Sussex; “*Constraining the dark universe with light bananas;*” Falmer, East Sussex, United Kingdom; 16 Nov. 2023
1. Colloquium at the Institute of Cosmology and Gravitation, University of Portsmouth; “*Constraining the dark universe with light bananas;*” Portsmouth, Hampshire, United Kingdom; 9 Nov. 2023

Contributed Talks

5. Dark Energy Survey Fall Collaboration Meeting; “*The DES Y3 Weak Lensing Flexion Catalogue;*” NCSA at UI Urbana-Champaign; Urbana-Champaign, Illinois, USA; 10 Oct. 2023
4. AstroPhilly ‘23; “*Constraining the small-scale matter power spectrum with cosmic flexion;*” Villanova University; Villanova, Pennsylvania, USA; 27 July 2023
3. Talk to DES Weak Lensing Working Group; “*Weak gravitational flexion in the Dark Energy Survey;*” Virtual Meeting; 11 May 2022
2. Research talk to incoming graduate students; “*Hybrid analytic image modeling and image moments approach to gravitational lensing;*” Drexel University; Philadelphia, Pennsylvania, USA; 17 Sep. 2019
1. High School Research Program conference; “*Observation of gravitational waves through precision stellar redshift measurement;*” Brookhaven National Laboratory; Brookhaven, New

York, USA; 16 Aug. 2013

Poster Presentations

2. First-year graduate student presentations; “*Hybrid analytic image modeling and image moments approach to gravitational lensing;*” Drexel University; Philadelphia, Pennsylvania, USA; 11 Jun. 2019
1. High School Research Program conference; “*Dark matter and its alternatives;*” Brookhaven National Laboratory; Brookhaven, New York, USA; 27 Nov. 2012

SOFTWARE DEVELOPED

Authored

F-SHARP	Code for computing weak gravitational lensing correlations. <i>Publicly available code written in Python.</i> https://github.com/evanjarena/F-SHARP
Lenser	A tool for measuring weak gravitational flexion. <i>Publicly available code written in Python.</i> https://github.com/DrexelLenser/Lenser
21cmMG	A suite for probing modified gravity with 21 cm cosmology. <i>Publicly available code written in Python.</i> https://github.com/evanjarena/21cmMG
Fisher21cm	Fisher forecast for a general 21 cm experiment. <i>Publicly available code written in Python.</i> https://github.com/evanjarena/Fisher21cm

Contributed

PythonOpenMPI	A generalizable utility for efficient task-based parallel programming using the <code>mpi4py</code> library. <i>Publicly available code written in Python.</i> https://github.com/seanlabean/PythonOpenMPI
LensTools	Useful computing tools for weak lensing analyses. <i>Publicly available code written in Python.</i> https://github.com/apetri/LensTools

TEACHING**Drexel University**

Teaching Assistant (Recitation and Lab Instructor)

PHYS 100, *Preparation for Engineering Studies*

Winter: 2023, 2021, 2020, 2019

This is a basic mathematics foundational course to prepare the students for the beginning sequence of Engineering Physics. Topics include (but are not limited to): linear and quadratic equations, simultaneous equations, basic geometry, use of trigonometric functions, vectors, translational kinematics, and Newton's Laws.

W'23: 3 recitation sections, 65 students total

W'21: 3 recitation sections, 63 students total

W'20: 4 recitation sections, 105 students total

W'19: 3 recitation sections, 86 students total

PHYS 152, *Introductory Physics I*

Spring: 2023, 2022, 2021, 2020, 2019

This class is the first part of a three-course algebra-based sequence that provides a comprehensive introduction to physics and covers the fundamentals of mechanics. Topics include motion in one or more dimensions, Newton's laws, gravitation, energy, momentum, and rotational motion. This course includes in-person labs that are intended to enrich the concepts presented in lecture and recitation section.

S'23: 3 recitation sections, 43 students total

S'22: 3 recitation sections, 50 students total

S'21: 4 recitation section, 87 students total

S'20: 1 recitation section, 70 students total

S'19: 4 recitation sections, 70 students total

PHYS 154, *Introductory Physics III*

Fall: 2022, 2021, 2020, 2019, 2018

This class is the third part of a three-course algebra-based sequence providing a comprehensive introduction to physics and covers the fundamentals of electricity and magnetism. Topics include electric charges, electric fields, electric potential, DC circuits, magnetic induction,

electromagnetic waves, special relativity, and optical interference. This course includes labs that are intended to enrich the concepts presented in lecture and recitation section.

F‘22: 3 recitation sections, 64 students total

F‘21: 3 recitation sections, 58 students total

F‘20: 2 recitation sections and 1 lab section, 84 students total

F‘19: 4 recitation sections, 92 students total

F‘18: 1 recitation section and 1 lab section, 42 students total

Grader

PHYS 131, *Survey of the Universe*

Winter 2022

This is a three-credit elective course that provides an overview of modern astronomy including the scientific method, telescopes, stars and star clusters, stellar evolution, galaxies and the large-scale structure of the universe, and the Big Bang. The online version of this course is designed to engage students in an investigation of astronomy in a more active way; the hope is that, with this interactive video game platform, students will achieve a greater understanding and appreciation of astronomy.

PHYS 231, *Introductory Astrophysics*

Winter 2022

Guest Lecturer

PHYS 231, *Introductory Astrophysics*

Winter 2022

This is an introductory astrophysics course aimed for science majors. Topics include a treatment of orbits, Kepler’s laws, celestial coordinates, light, blackbodies, optics, stellar structure and evolution, galactic formation, and large scale evolution and structure of the universe.

W‘21: 1 Lecture, 25 students total

Stony Brook University

Lecturer

Della Pietra High School Applied Math Program

Spring 2017

PROFESSIONAL ACTIVITIES AND SERVICE

Collaborations	External Collaborator, Dark Energy Survey (DES)
	Member, Packed Ultra-wideband Mapping Array (PUMA) [Inactive]
	Member, Baryon Mapping eXperiment (BMX) [Inactive]
Working Groups	Member, DOE Cosmic Visions Dark Energy 21 cm Working Group [Inactive]

Media Appearances

Appeared on the *Anthony Gargano Show* to discuss the solar eclipse viewing from Philadelphia:
<https://www.youtube.com/watch?v=gkbAUbbIH20> (8 Apr. 2024).

Outreach Activities

- Organized and ran a public solar eclipse viewing at Drexel University (8 Apr. 2024).
- Helped run the Kaczmarczik Lecture Series Open House, hosted by the Drexel University Department of Physics (7 Mar. 2024).
- Free physics tutoring at the Stony Brook University Veterans Student Organization (2023).
- Assist in running the monthly Drexel Physics Department open house, where we open the the Joseph R. Lynch Observatory for public viewing (2018 – Present).
- Invited to appear on the Drexel University Teaching Assistant Orientation Panel, as part of the Teaching Assistant Orientation and Preparation Course GRAD T580 (17 Sep. 2020).
- Helped run the Kaczmarczik Lecture Series Open House, hosted by the Drexel University Department of Physics (14 Nov. 2018).

Committee Work

Treasurer of the Drexel University Physics Graduate Student Association (2020 – 2021).

TECHNICAL SKILLS

Proficient in *Python*.

Proficient in Bash and Linux environments.

Extensive experience with supercomputing clusters and performing parallel computation.

